Dipl.Ing. Mag.art. Robert Winkler, BSc

Fabrication of Functional and Freestanding 3D Nano-Architectures via Focused Electron Beam Induced Deposition

DOCTORAL THESIS

For obtaining the academic degree of
Doktor der technischen Naturwissenschaften

submitted to

Graz University of Technology

Supervisor:

Ass.-Prof. Priv.-Doz. Dipl.-Ing. Dr. techn. Harald Plank

Institute of Electron Microscopy and Nanoanalysis

Graz, January 9th, 2018

AFFIDAVIT

I declare that I have authored this thesis independently, that I have not used other than the declared sources/resources, and that I have explicitly indicated all material which has been quoted either literally or by content from the sources used. The text document uploaded to TUGRAZonline is identical to the present doctoral thesis.

Date

Signature

ABSTRACT

Where 3D-printing meets the ongoing trend for miniaturization of structural elements, novel direct-write nanofabrication techniques are in demand. Focused Electron Beam Induced Deposition (**FEBID**) is a promising candidate as it allows the fabrication of freestanding geometries with structure sizes at the nanoscale. Furthermore, these 3D objects can have various functionalities and can be printed on almost any substrate material and morphology in a single-step process. However, in the past the fabrication of complex geometries was compromised due to unwanted side effects, lack of reliability and cumbersome processing.

This doctoral thesis shows the research route towards the predictable 3D-nanoprinting of functional multi-branch structures via FEBID. Therefore, first an understanding of the dynamically changing working regime for one- and two-dimensional deposits is derived by considering precursor replenishment mechanisms and patterning parameters. In this context, the influence of the patterning sequence on morphology and chemical composition is uncovered as well as shadowing effects by the growing deposit.

Using this knowledge, a reliable approach to fabricate high-fidelity 3D nanoarchitectures is established to upgrade fabrication possibilities of the past. A comprehensive study of process parameters and simulations of the 3D-growth reveal a stable process window for reproducible and artefact-free 3D-nanoprinting. In this context and in particular to fabricate complex 3D geometries, it is suitable to use highest primary beam energies, lowest beam currents, electron limited working conditions and an alternating point sequence at patterning velocities in the range of tens of nm/s. As a representative application, plasmonic activity of such freestanding structures is demonstrated after a successful electron beam assisted purification treatment in water vapor.

In summary, the progress reported in this doctoral thesis significantly expands the 3D-printing capabilities of FEBID and enables a controlled, predictable and reliable fabrication of freestanding, functional and highly complex nano-architectures.

KURZFASSUNG

Wo 3D-Druck auf den anhaltenden Trend zur Miniaturisierung von Bauteilen trifft, sind neue direkte Schreibverfahren auf dem Gebiet der Nanofabrikation gefragt. In diesem Umfeld stellt die direkte Abscheidung mittels fokussierter Elektronenstrahlen (engl. *Focused Electron Beam Induced Deposition*, **FEBID**) eine vielversprechende Methode dar, da sie die Herstellung von freistehenden Geometrien mit Strukturgrößen im Nanometerbereich ermöglicht. Des Weiteren können solche 3D Objekte verschiedene Funktionalitäten aufweisen und in einem einstufigen Prozess auf nahezu jedem Untergrundmaterial und jeder Oberflächenform gedruckt werden. Die Herstellung von Geometrien mit höherer Komplexität war jedoch in der Vergangenheit aufgrund unerwünschter Nebenwirkungen, mangelnder Zuverlässigkeit und aufwendigen Prozessierens beeinträchtigt.

Diese Dissertation präsentiert die Forschungsergebnisse in Richtung vorhersagbarer 3D-Fabrikation von komplexen, funktionellen Nanostrukturen mittels FEBID. Dafür wird zunächst bei ein- und zweidimensionalen Abscheidungen ein Verständnis für das sich dynamisch verändernden Arbeitsregime mittels fundamentaler Überlegungen zu Precursor-Bedeckung und Elektronenstrahlführung erworben. In diesem Zusammenhang werden außerdem der Einfluss der Punktsequenz auf die Morphologie und die chemische Zusammensetzung sowie Abschattungseffekte durch die wachsende Abscheidung aufgedeckt.

Auf dieser Basis wird im Anschluss eine zuverlässige Vorgehensweise zur Fabrikation von 3D Nanoarchitekturen eingeführt, welche die bisherigen Herstellungsmöglichkeiten wesentlich erweitert. Eine umfassende Studie zu Prozessparametern sowie Simulationen zum 3D-Wachstum ermitteln ein stabiles Prozessfenster für reproduzierbares und Artefakt-freies 3D-Nanodrucken. Im Wesentlichen erweisen sich, insbesondere für die Herstellung komplexer 3D Geometrien, höchste Beschleunigungsenergien, niedrigste Strahlströme, Elektronen-limitierte Arbeitsbedingungen und eine abwechselnde Punktfolge bei vergleichsweise hohen Schreibgeschwindigkeiten im Bereich von einigen zehn nm/s als geeignet. Als repräsentative Anwendung wird die plasmonische Aktivität solcher freistehenden Strukturen nach einer erfolgreichen Elektronenstrahl-unterstützten Aufreinigungsbehandlung mittels Wasserdampf demonstriert.

Zusammenfassend hat der Fortschritt, über den diese Doktorarbeit berichtet, die 3D-Druck-Möglichkeiten von FEBID signifikant erweitert und somit die kontrollierte, voraussagbare und verlässliche Herstellung von freistehenden, funktionalen und hochkomplexen Nanoarchitekturen ermöglicht.

ACKNOWLEDGEMENTS

The road to graduation was long and winding, but fortunately not lonesome. Because many people have accompanied, guided and supported me along this path. And because I would not have done all this without them, I dedicate this PhD thesis to them.

First and foremost I would like to thank my parents and my whole family, who supported me unconditionally throughout my studies. I especially thank my girlfriend Claudia, with whom I was able to share successes and setbacks.

A huge part of my gratitude goes to my supervisor Harald Plank. With his motivating mentoring, the constant support and his trust, he has kindled my enthusiasm for science and significantly promoted my personal development. In addition, I am pleased with the honest friendship that has developed over the years.

I would like to sincerely thank my colleagues at the FELMI-ZFE (especially Steffi, Judith, Harald, Robert, Christian, Georg, Luki, Manni, Daniel and all master students) for the fun at coffee breaks, the celebrations and friendships outside of work. This good atmosphere is a reason why I enjoyed work every day. In particular, I thank our workgroup members (Sebastian, Uli 1, Uli 2, Paul, Johannes, Georg, Tom, Angi, Babsi) and my office- and lab-colleagues (Christian, Jürgen, Martina and Roland) for their constant help and discussions.

I am also very grateful for the fruitful collaborations that have developed into personal friendships beyond the scientific cooperation. Here I would like to thank the colleagues from GETec (Ernest, Chris, Tobias, Franz, Marcel) and the Triple-S project (Georg, Melanie, Nahid, Chen, Vlado) and hope that we can continue this great cooperation. I am especially grateful for the joint scientific and personal support from the cooperation partners in Tennessee (Jason, Philip, Bret), in Thun (Ivo, Aleksandra) and in Frankfurt (Michael, Lukas). I am looking forward to more meetings, discussions and projects!

TABLE OF CONTENTS

ABSTRACT **2**

KURZFASSUNG **3**

ACKNOWLEDGEMENTS **4**

LIST OF ABBREVIATIONS **7**

1 INTRODUCTION **8**

1.1 OUTLINE 8
1.2 BASIC PRINCIPLE OF FEBID 9
1.3 WORKING REGIME AND CONTINUUM MODEL 12
1.4 FEBID MATERIALS 13
1.4.1 Functionality *13*
1.4.2 Material property tuning *14*
1.5 3D-NANOPRINTING 16
1.5.1 Definition of 3D *16*
1.5.2 Review on 3BID publications *17*
1.5.3 3BID methodology *21*

2 PUBLICATIONS **25**

2.1 OVERVIEW 26
2.2 PUBLICATION 1 27
2.2.1 Article Details *27*
2.2.2 Executive Summary *27*
2.2.3 Author Contributions *27*
2.3 PUBLICATION 2 28
2.3.1 Article Details *28*
2.3.2 Executive Summary *28*
2.3.3 Preamble – Author Contributions *28*
2.4 PUBLICATION 3 29
2.4.1 Article Details *29*
2.4.2 Executive Summary *29*
2.4.3 Preamble – Author Contributions *29*
2.5 PUBLICATION 4 30
2.5.1 Article Details *30*
2.5.2 Executive Summary *30*
2.5.3 Preamble – Author Contributions *30*
2.6 PUBLICATION 5 31
2.6.1 Article Details *31*
2.6.2 Executive Summary *31*
2.6.3 Preamble – Author Contributions *31*
2.7 PUBLICATION 6 32
2.7.1 Article Details *32*
2.7.2 Executive Summary *32*
2.7.3 Author Contributions *32*

3 SUMMARY **33**

4 CONCLUSIONS AND OUTLOOK **36**

4.1 Conclusions ... 36
4.2 Outlook ... 36
5 References ... 38
6 Appendix ... 47
6.1 Appendix 1 - Publication 1 ... 47
6.2 Appendix 2 - Publication 2 ... 62
6.3 Appendix 3 - Publication 3 ... 91
6.4 Appendix 4 - Publication 4 ... 111
6.5 Appendix 5 - Publication 5 ... 150
6.6 Appendix 6 - Publication 6 ... 194
6.7 Appendix 7 - Curriculum Vitae ... 226

List of abbreviations

3BID … *Three-Dimensional Focused Electron Beam Induced Deposition*

ALD … *Atomic Layer Deposition*

BSE … *backscattered electrons*

DBM … *Dual Beam Microscope*

DEA … *dissociative electron attachment*

DER … *diffusion enhanced regime*

DI … *dissociative ionization*

DT … *dwell time*

EDXS … *Energy-Dispersive X-ray Spectroscopy*

ELR … *electron limited regime*

ESEM … *Environmental Scanning Electron Microscope*

FEBID … *Focused Electron Beam Induced Deposition*

FIB … *Focused Ion Beam*

FIBID … *Focused Ion Beam Induced Deposition*

FSE … *forward scattered electrons*

GIS … *gas injection system*

LAEBID … *Laser Assisted Electron Beam Induced Deposition*

MLR … *molecule limited regime*

PE … *primary electrons*

PoP … *point pitch*

PV … *patterning velocity*

SE … *secondary electrons*

SEM … *Scanning Electron Microscope*

TEM … *Transmission Electron Microscope*

1 INTRODUCTION

1.1 OUTLINE

This doctoral thesis "*Fabrication of Functional and Freestanding 3D Nano-Architectures via Focused Electron Beam Induced Deposition*" describes the route and exploratory work to establish reliable 3D-nanoprinting of complex structures as graphically summarized in Figure 1.

The introduction section gives a general overview of the Focused Electron Beam Induced Deposition (**FEBID**) technique and surveys the status quo of the most relevant aspects for this doctoral thesis. Furthermore, this chapter outlines how the presented results relate to a larger context in the field of additive, direct-write nanofabrication. Particular focus was put on previous findings concerning the main precursor materials used during this study ($MeCpPt^{(IV)}Me_3$ and $Me_2Au(acac)$).

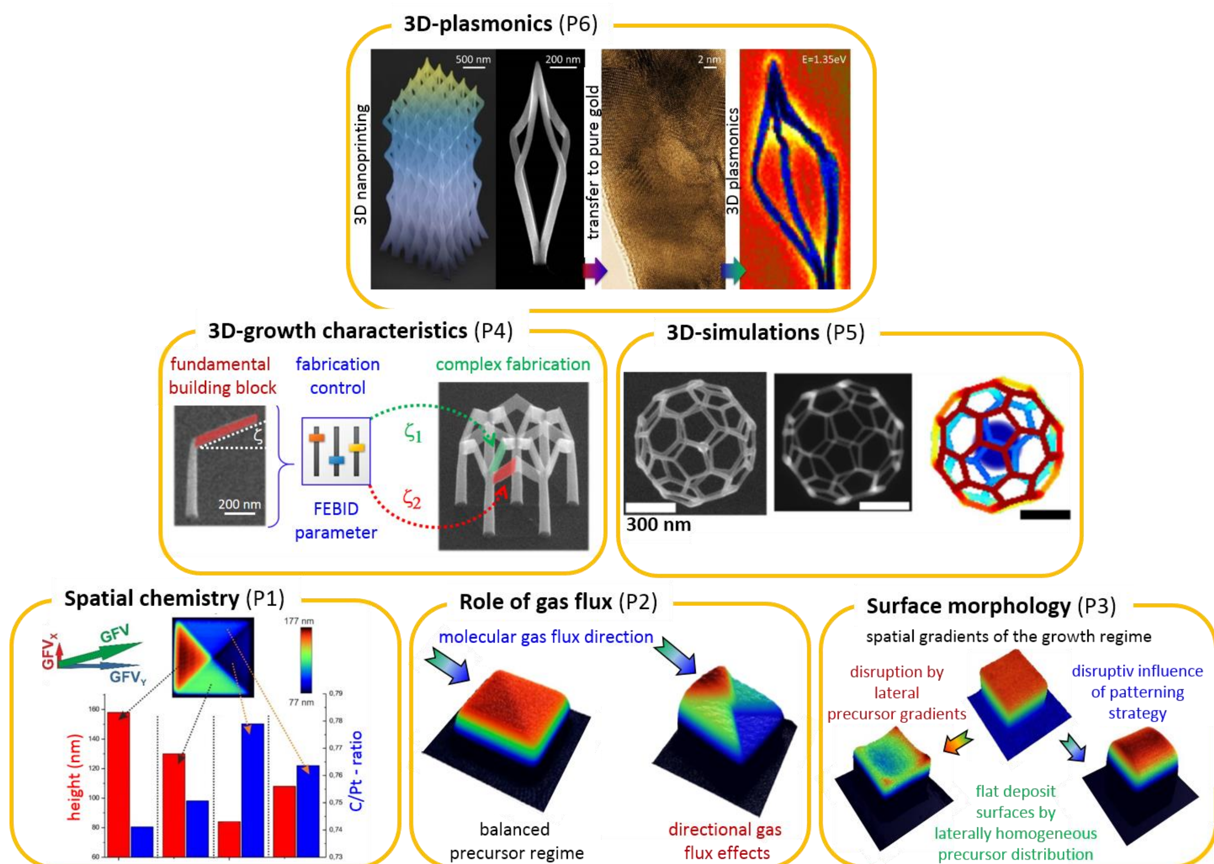

Figure 1: Overview of the development steps to 3D-nanoprinting via FEBID. Publication 1–3 build the groundwork by fundamental studies on important aspects[1–3] in 2D. Publication 4[4] shows the influence of the process parameters on the fabrication of freestanding structures, publication 5[5] simulates the 3D-growth. As application of 3D-nanoprinting the plasmonic activity of purified 3D gold geometries was demonstrated (Publication 6[6]). Figures are taken from the respective publication.

Section 1.2 starts with the basic principle of FEBID, discusses the advantages of this technique and introduces important process parameters. Subsequently, the concept of the working regime that characterizes the balance between electrons and precursor molecules is discussed together with a mathematical model (continuum model) to describe the FEBID process (1.3). Pursuant to the title of this thesis, chapter 1.4.1 reviews potential functionalities of FEBID materials. In this context, several

possibilities to modify the functionalities of as-deposited material using post-deposition procedures are reviewed (1.4.2). Finally, section 1.5 compares previous studies on freestanding 3D FEBID structures and introduces 3D-nanoprinting as developed in the course of this doctoral thesis.

Finally, the most important findings and achievements gathered in this thesis are collected in a summary and complemented by an outlook, including pending questions as well as ideas for future studies and applications.

The appendix contains six journal articles[1–6] written or co-authored by the author of this thesis, which contributed to the development of the discussed 3D-nanoprinting technique. In addition, further important contributions with co-authoring character[7–17] are discussed at appropriate position.

1.2 BASIC PRINCIPLE OF FEBID

Focused Electron Beam Induced Deposition is a direct-write nanofabrication technique in (scanning) electron microscopes, where electrons are used to locally dissociate precursor molecules. The basic principle is illustrated in Figure 2: a gaseous precursor is injected into the vacuum chamber via a gas injection system (**GIS**). The gaseous molecules adsorb and diffuse on the surface followed by desorption after a condition dependent mean residence time. Using an electron beam, the electrons interact with the physisorbed precursor and split the molecules into volatile and non-volatile fragments. While the volatile fragments are pumped out of the chamber, the non-volatile products locally remain on the surface and build up a deposit.

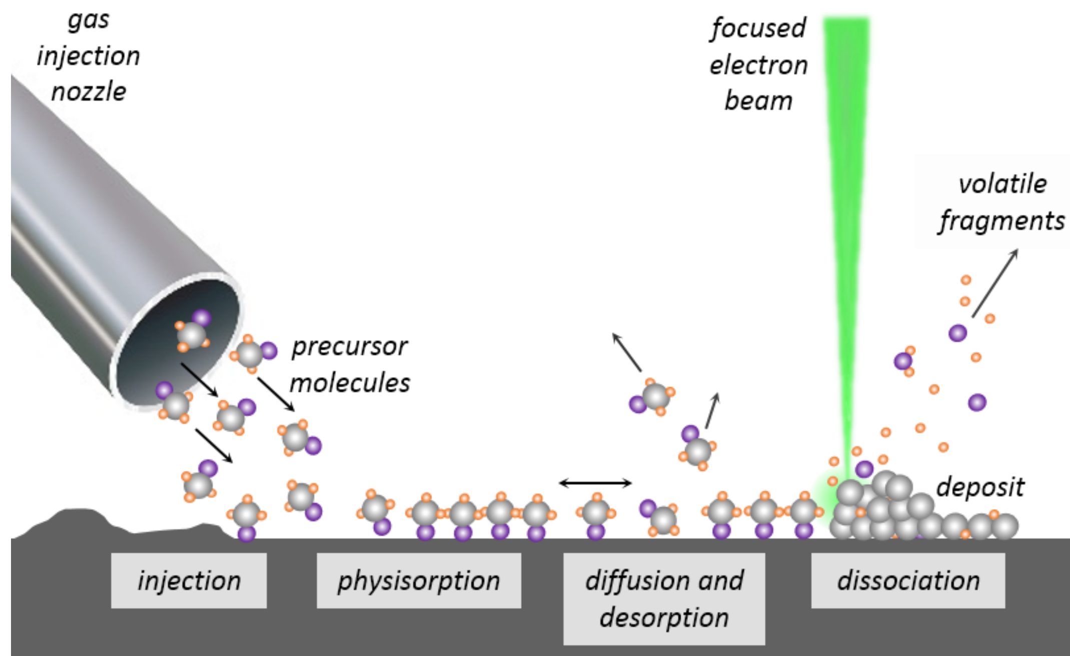

Figure 2: Basic principle of Focused Electron Beam Induced Deposition (FEBID). A gas injection nozzle provides a continuous flow of precursor molecules. The molecules physisorb on the substrate surface where they can diffuse and desorb again. A focused electron beam splits the molecules into volatile fragments, which are pumped out of the chamber, and non-volatile fragments, which stick to the substrate and build up a solid deposit.

As the electron beam can be focused to a spot diameter on the lowest nanoscale, structural dimensions in the sub-10 nm regime can be achieved[18]. Because of the direct-write character of this method, many applications become possible, where other techniques, like lithography, cannot be applied. Furthermore, it is possible to deposit nanostructures on challenging surface morphologies (see publication (**P**) P6) and substrate materials[19]. In contrast to the related Focused Ion Beam Induced Deposition (**FIBID**) technique, the deployment of electrons instead of ions eliminates typical problems like unwanted ion implantation, sputtering effects, and sample heating[8,20]. One of FEBID's unique selling points is the capability to fabricate freestanding 3D geometries on the nanoscale[21], which will be discussed in detail in section 1.5.

Although simple in principle, the FEBID process exhibits a complex interplay between numerous parameters. Those can be categorized into beam, gas, patterning, and other parameters as listed in Table 1 without any claim to completeness.

Table 1: Important parameters during the FEBID process.

beam parameters	gas parameters	patterning parameters	other parameters
primary electron energy	precursor type	dwell time	substrate type
beam current	GIS alignment (X, Y, Z)	pixel-to-pixel distance	surface temperature
convergence angle	precursor flux	patterning sequence	stage stability
beam diameter	GIS type	patterning direction	surface morphology
lens abberations	precursor temperature	total exposure time	…
…	chamber pressure	precursor refresh time	
	…	…	

Before we discuss the most important parameters in more detail, we have to take a closer look at the electron/solid interactions. Figure 3 shows possible paths and scattering events for electrons after impinging a solid pillar. As the precursor molecules are located at the surface, only electrons at those areas are contributing to the deposition process. Furthermore, most of the precursor materials are preferentially decomposed by low-energy electrons, therefore, secondary electrons are predominantly responsible for the deposit growth[22] (see also section 1.3). Following the considerations above, the effect of different primary electron energies, which are typically between 1 keV and 30 keV, can be examined. Highest growth efficiency is found for low primary electron energies as the reduced penetration depth of the electrons results in a high number of secondary electrons close to the surface. Thus, a variation of the primary electron energy has consequences on volume growth rate (see P1), resolution[23] and the amount of unwanted deposition at surrounding areas (proximity deposition)[10] due to scattered electrons. P1 demonstrates that the primary electron energy and beam current have also an implication on the deposit chemistry and by that on the final functionality.

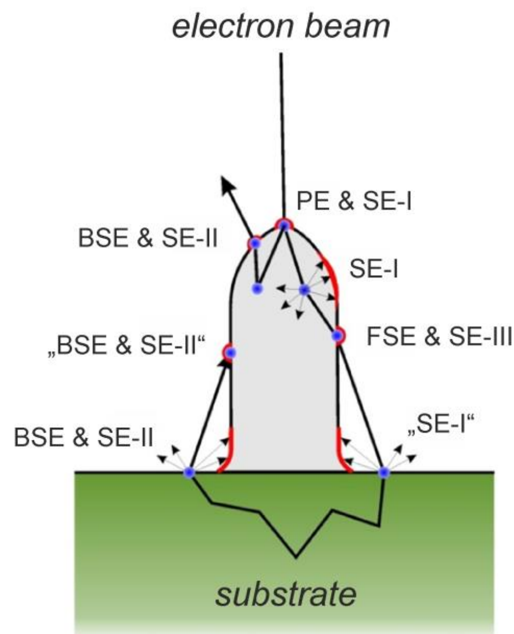

Figure 3: Illustration of electron trajectories after impingement of an electron beam on a pillar[24]. Primary electrons (PE) are scattered in the solid (the blue dots indicate scattering events). Elastically scattered electrons that exit the pillar at the side walls in forward direction are denoted as forward scattered electrons (FSE); reflected electrons (either from the deposit or the substrate) are called backscattered electrons (BSE). All three types (PE, FSE, and BSE) are scattered inelastically on their path through the solid, resulting in the emission of low-energy secondary electrons (SE). Depending on the initiating high-energy electrons, they are called SE-I (triggered by PE), SE-II (triggered by BSE) and SE-III (triggered by FSE). Please note, deposition can only take place at surface areas, which are indicated as red areas in the figure.

Another important beam parameter is the beam current. By definition, higher beam currents lead to a higher number of electrons available for dissociation. However, there is no linear relationship between beam current and volume growth rates per se, but mostly a saturation tendency for high beam currents because of the strong precursor depletion and limited precursor replenishment. For the reliable fabrication of freestanding 3D FEBID structures, high beam currents turned out as unsuited as shown in detail in P4. In most cases, the growth-limiting factor is the replenishment with new precursor molecules.

Therefore, a detailed look at the gas parameters (see Table 1, 2nd column) is essential. As discussed in literature[25,26] and in particular in P2, the alignment of the gas injection nozzle has a major implication on the growth rate. In this context, the direction of patterning in relation to the orientation and position of the GIS is also of importance for both morphology and chemistry (see P1–P3).

From a practical point of view, the patterning parameters (see Table 1, 3rd column) are more accessible than other parameters. The most important patterning parameters are the pixel-to-pixel distance (point pitch, **PoP**) and the dwell time (**DT**), which play an essential role in particular for 3D-fabrication (see 1.5). As a central element of this thesis, the patterning strategy has been studied in detail. The effects of different patterning sequences shown in Ps 1–6 build the fundament for high-fidelity deposition in 2D, as well as in 3D.

Due to the high number of interdependent process parameters, it is advantageous to describe the FEBID process by more general concepts (working regime, continuum model) explained in the following section.

1.3 Working Regime And Continuum Model

As mentioned in the previous section, the interdependence of numerous process parameters makes it difficult to decouple all influences. As most parameters locally change either the number of electrons and / or the number of precursor molecules, the overall system can be described as the ratio between both, defining the respective working regime. Three different regimes can be distinguished[27]: **1)** *electron limited regime* (**ELR**, also called reaction rate limited), where the number of electrons limits the growth. This in turn implies that sufficient precursor molecules are available. **2)** *molecule limited regime* (**MLR**, also called mass transport limited regime, adsorbate limited regime[28]) describes working conditions, where the local amount of precursor molecules limits the growth. Consequently, this implies an excess of electrons compared to precursor molecules. In the transition between ELR and MLR conditions, the so called **3)** diffusion enhanced regime (**DER**) evolves. This regime arises, when surface diffusion significantly contributes as replenishment mechanism because of a strong precursor gradient. As shown by Utke et al.[29], a single dot fabricated in ELR condition exhibits a Gaussian shape, therefore mimicking the beam profile. A single dot fabricated in MLR exhibits a flat top shape as the surplus of electrons in the center of the Gaussian beam profile do not find any new precursor molecules apart from those directly adsorbing from the gas flux. In other words, the flat top directly reflects the gas adsorption rate, which is laterally constant. In DER, molecules outside of the beam spot diffuse towards the heavily depleted areas, but are dissociated on their way to the beam center by electrons from the beam tails. This results in an indent shape. Typical FEBID setups usually provide MLR conditions, as a high precursor coverage is complicated to achieve. Mathematically, the change of *local precursor molecules* $n(r,t)$ over *space r* and *time t* is described via a continuum model[29–31]

$$\frac{\partial n(r,t)}{\partial t} = \underbrace{sJ\left(1-\frac{n(r,t)}{n_0}\right)}_{adsorption} - \underbrace{\frac{n(r,t)}{\tau}}_{desorption} - \underbrace{\sigma f(r) n(r,t)}_{decomposition} + \underbrace{D\left(\frac{\partial^2 n(r,t)}{\partial r^2} + \frac{1}{r}\frac{\partial n(r,t)}{\partial r}\right)}_{diffusion}$$

The number of locally available precursor molecules $n(r,t)$ changes due to four processes: **1)** adsorption, **2)** desorption **3)** decomposition, and **4)** diffusion.

1) The first term takes adsorption of precursor molecules via the *sticking probability s* into account, which depends on the interaction of precursor and substrate. The *molecular flux J* describes the direct delivery of new molecules from the GIS nozzle. This value already combines several process parameters like GIS alignment, crucible temperature and base pressure in the vacuum chamber. The term with the *number of molecules in a complete monolayer* n_0 in the denominator furthermore accounts for the maximum coverage of precursors.

2) The second term $\frac{n(r,t)}{\tau}$ reduces precursor coverage as it considers that molecules desorb after a *specific average residence time* τ. In P2, τ was calculated to 60 – 100 µs for $MeCpPt^{(IV)}Me_3$ for our setup. Please note that desorbing molecules can re-adsorb at the region of interest (see Figure 8c in P2). Assuming isotropic desorption directions, this leads to a diffuse gas pressure component as used for example in P5 to match experiments and simulations.

3) The decomposition term describes the electron induced deposition process itself. The *beam distribution* $f(r)$ represents the electron flux profile and is a combination of various beam parameters (primary energy, beam current, beam diameter, …). Electrons with an energy *E* dissociate a precursor molecule with a specific probability, described by the *net cross section* σ. Data for dissociation cross sections as a function of electron energy are of high importance (e.g. for simulation of the evolving structure), but complicated to extract as the results depend on the precursor chemistry and environmental conditions. For $MeCpPt^{(IV)}Me_3$, the highest dissociation cross section was found around 150 eV[32,33]. However, taking the significantly higher number of secondary electrons (**SE**, energy < 50 eV), as a consequence of inelastic electron-solid interaction, into account[34], the SE can be considered as dominant species for the deposition process[22]. Nevertheless, primary electrons (**PE**), backscattered (**BSE**) and forward scattered electrons (**FSE**) also contribute to some extent. Among others[35], the most important electron stimulated reaction pathways are dissociative electron attachment (**DEA**) and dissociative ionization (**DI**). For $MeCpPt^{(IV)}Me_3$, DEA leads to a loss of preferentially one, DI to a dissociation of 2–3 methyl ligands, respectively[22]. Exposing the precursor to electrons below 30 eV already immobilize the platinum containing fragment[36], leaving behind a deposit with high carbon content. The low metal content is also a problem for $Me_2Au(acac)$ and for metal-acetylacetonates in general[37].

4) The last term of the continuum model considers the precursor replenishment path via surface diffusion with the *surface diffusion coefficient D*. In P2 values from 0.09 – 0.65 µm²/s are calculated for $MeCpPt^{(IV)}Me_3$, recently a confined value of 0.42 µm²/s[38] was reported, where *D* is a function of the substrate temperature[38]. Under strong ELR conditions, almost no precursor coverage gradients emerge. As a result, the last term can be neglected and by that diffusive contribution[38] in such regime conditions, which obviously simplifies both, real experiments and mathematical description.

Because the experimental conditions are different for each system (precursor type, GIS alignment, …) the universal concept of the working regime is necessary to give a more general description of individual results. In this thesis, the concept of the working regime was applied to explain growth rates (P1 – P4), chemical composition (P1), resolution (P4), morphologies (P1 – P3), and local effects (P2 – P4).

1.4 FEBID MATERIALS

Another aspect of this thesis concerns the material properties of the deposited structures. The following section reviews the relevant functionalities of FEBID materials together with respective applications demonstrated in the past.

1.4.1 FUNCTIONALITY

The precursor chemistry determines the final material properties of FEBID deposits. Depending on the demands, the various properties of FEBID materials (e.g. insulating, metallic) can be used to realize different applications as discussed below.

For some application fields the properties of FEBID materials are of minor importance and only the precise morphology is of relevance. For example, in Dual Beam Microscopes (**DBM**), FEBID is typically used for the preparation of lamellas for Transmission Electron Microscope (**TEM**) investigations[39]. Firstly, to provide a protection layer for the region of interest and secondly, to solder the lamella for the lift-out. Other important applications are repairing lithographic masks[40] or modifying tips for Atomic Force Microscopy (**AFM**) [41,42]. Another approach is to use FEBID structures as a template, followed by a coating with the material of the desired functionality. Examples are Atomic Layer Deposition (**ALD)** coatings of freestanding FEBID geometries to enhance mechanical stiffness[43] or a coating/decoration of FEBID-antennas with silver or gold to achieve plasmonic activity[44,45]. Coating FEBID surfaces with bio-molecules might also allow interesting sensing applications in future as it could introduce a variable specificity concerning the target species.

In contrast to the examples discussed so far, many applications require conductive FEBID materials, e.g. for circuit repair in the semiconductor industry[46]. The capability to electrically contact nanowires or carbon nanotubes in a direct-write fashion with nanoscale resolution is one of FEBID's unique selling points[47]. Unfortunately, FEBID materials typically suffer from low purity and their resistivity is usually orders of magnitude higher than that of the corresponding bulk metals. This issue is addressed in 1.4.2, in P1 and P6, including workarounds by using suitable post-processing methods.

While typical carbon incorporations are problematic for some applications, the resulting nanogranular composition of FEBID materials can also be used as advantage. For example, a stress/strain induced change in the grain-to-grain distance can be used as a strain sensor[48]. Kolb et al.[49] demonstrated a humidity sensor based on the separation of platinum grains in a carbon matrix that acts as a transducer. For a thin platinum/carbon deposit, the presence of polar molecules on the surface changes the electrical field within the matrix. That improves the hopping probability of electrons from one platinum grain to the next, resulting in a detectable current increase through the device.

FEBID with magnetic materials is also very promising for applications. Gavagnin et al.[50] demonstrated magneto-logic modules with ferromagnetic elements from the $Fe(CO)_5$ precursor, and very recently, Keller et al.[14] showed an artificial spin ice system using the precursor $HCo_3Fe(CO)_{12}$. As no magnetic material was used during this thesis, I refer to the literature for further information[51–57].

FEBID materials can also be used for optical applications[58]. For example, insulating SiO_x has the suitable dielectric constant for the fabrication of a spiral phase plate for vortex beams[11]. In addition, arranging FEBID structures in an array enables interesting photonic applications[59,60]. Finally, as shown in P6, single purified gold structures exhibit plasmonic behavior[6]. By demonstrating plasmonic activity for FEBID materials, the developments in this thesis have added a new functionality to the FEBID portfolio.

1.4.2 MATERIAL PROPERTY TUNING

As mentioned in the previous section, FEBID materials in the as-deposited state often do not comply with the required functionalities. Especially organometallic precursors, which are used throughout this thesis, exhibit a massive incorporation of carbon in the deposited material due to the incomplete dissociation of precursor molecules. The desired element is deposited together with ligand groups, typically forming a carbonaceous matrix with nanometer-sized metal grains[6,7,61,62].

The development of suitable precursors for FEBID is a challenging task, as they have to fulfill several requirements. On one hand, high purity of the final deposit is desired. On the other hand, the precursor should also be volatile under reasonable conditions and dissociable via an electron induced process. Furthermore, handling, shelf stability, price and toxicity have to be considered for general use. Most carbon-free precursors[63] have not gained relevance yet because of such restrictive criteria.

Another approach is to change the material property in a second step after deposition. For instance, electron-beam curing is a simple post-processing method[48,64]. In absence of new precursor gas, the deposit is irradiated with electrons. By this, further ligands are detached from the incompletely dissociated precursor molecules. As a result, the metal grains are slightly growing[65], and a graphitization of the carbon matrix takes place with increasing curing dose[48]. With that method, the resistivity can be improved by about three orders of magnitude[65] and mechanical stability of freestanding structures is notably improved[66].

For higher material purity, several purification methods for different precursor types have been proposed. A comprehensive review is found in Botman et al.[63]. In the following, some purification approaches for the very common FEBID precursors $MeCpPt^{(IV)}Me_3$ and $Me_2Au(acac)$ are compared, as these precursors are used in this thesis.

For both precursors, thermal annealing (500 °C) under O_2 atmosphere increases the metal content to 60 at% (Au) and 70 at% (Pt), respectively[67]. In 2012, Riazanova et al. reported a gold content of 92 at%[68] by annealing for 1 hour in air at 600 °C, Höflich et al. purified freestanding Au-C structures in ozone for 3 hours at a temperature of 175 °C[69]. Please note that heating the whole substrate to such high temperatures might be critical for many applications. A combination of O_2 exposure, electron irradiation and temperatures of 120 °C was introduced by Mehendale et al., resulting in high Pt content, but also porous structures if applied on thick deposits[70].

An approach at low temperatures (50 °C) under electron beam exposure and O_2 injection, reported by Plank et al.[71], revealed compact and pure platinum deposits. This study suggests that the electron beam dissociates the O_2 molecules into atomic oxygen, which removes the carbon from the $Pt-C_X$ structure. This assumption was confirmed recently[15] directly by injecting atomic oxygen. The purification takes place only at the surface layers (around 15 nm) in agreement with the previously mentioned study[71]. Atomic hydrogen does not show significant purification effects for $MeCpPt^{(IV)}Me_3$[15]. In contrast, for $Me_2Au(acac)$ a sequential combination of atomic oxygen and atomic hydrogen treatment is capable to fully remove carbon and oxygen[72] from the deposits.

The purification towards compact metal structures has the consequence that all structures lose about 2/3rd of the initial volume[6,7]. Performing a simultaneous purification during the FEBID writing process has the advantages that this volume loss does not need to be considered upfront and a quasi-1-step process can be maintained. Laser annealing is a possible *in situ* process, for which a laser pulse in between each FEBID step leads to a thermal desorption of residual fragments[73]. Combining this procedure with O_2 co-flow further improves the purity of the deposit[9,74,75]. This Laser Assisted Electron Beam Induced Deposition (**LAEBID**) approach is also applicable for 3D structures[12]. However, for LAEBID locally high temperatures can occur, which are problematic for sensitive substrates.

In 2014 Geier et al.[7] demonstrated a purification method at room temperatures for $MeCpPt^{(IV)}Me_3$. In this approach, the FEBID structure is exposed to water vapor at a pressure of 10 Pa in an Environmental

Scanning Electron Microscope (**ESEM**) and further irradiated with electrons. It is assumed that the H_2O molecules permeate the nanogranular deposit and are dissociated by the scanning electron beam. Radicals are formed, which attack the remaining carbon in the structure[7]. With this electron-beam assisted water purification method pure and compact platinum structures with excellent shape retention were achieved. While the electron-beam assisted O_2 purification is limited to the surface layers due to the limited permeability depth of oxygen, the Pt-C_X soaks up H_2O like a sponge and thicker deposits can be purified[9] as well. P6 shows that deposits fabricated from the $Me_2Au(acac)$ precursor can also be treated with this electron-beam assisted H_2O process, resulting in pure and compact gold 2D as well as 3D structures.

1.5 3D-NANOPRINTING

1.5.1 DEFINITION OF 3D

One of the most striking advantages of FEBID is the possibility to create freestanding structures on the nanoscale. There is an ambiguity in the perception of “3D” in literature, therefore, we first have to clarify the terminology.

In some instances, “non-flat” deposits with geometric expansions in all three dimensions (X, Y and Z) are denoted as “3D structure”. As in principle all FEBID structures have more or less a physical expansion in height, this definition is only justified for layer-by-layer printing of a desired 3D morphology, e.g. a FEBID miniature model of the Matterhorn[13]. We do not follow this interpretation of 3D in this thesis, and add the criterion “freestanding” or “meshed-style” to exclude bulky structures.

Other FEBID studies entitled “3D” are describing a straight pillar geometry[50,76–78]. The fabrication of such pillars is comparably straightforward by using spot exposure. Single pillars or pillar arrays are still of high interest for applications[50,59,66,79], as one can take advantage of the enormous aspect ratios and the flexibility to synthesize those site-specifically. Furthermore, this simple 3D geometry is perfectly suited for fundamental studies[1,77,80–83]. An important study on pillars with respect to 3D-fabrication was reported by Burbridge et al.[80]. Bending of previously prepared pillars occurs due to proximity effects by scattered electrons from subsequent fabricated structures. This problem explains the difficulties in printing of multi-branch 3D geometries in the past and emphasizes the importance of an appropriate patterning sequence. To circumvent this intrinsic problem and to enable 3D-nanoprinting of structures with higher complexity it is therefore necessary to use a 3D-interlacing patterning strategy presented in detail in P4, P5 and P6, as well as in chapter 1.5.3.

Another possibility to manufacture quasi-3D structures is to deposit a straight pillar on an inclined surface. With a combination of subsequent stage tilts and rotations, freestanding geometries can be realized[44,84]. In contrast to 3D-nanoprinting as introduced in the following, the branches show a typical cylindrical cross section. Furthermore, this “stationary beam on inclined surfaces” - method is restricted to simple geometries with only a few and straight branches.

To delimit from the above-described definitions of 3D-nanoprinting via FEBID, the name “**3BID**” (**3**-dimensional Focused Electron **B**eam **I**nduced **D**eposition) is introduced throughout this doctoral thesis for the following 3D-printing approach, schematically depicted in Figure 4. 3BID uses a non-stationary, moving electron beam. To realize the beam guidance, a patterning generator controls

deflection coils. The patterning velocity (**PV**, also called (lateral) scan(ning) speed[5,85–87], horizontal speed[84], scan rate[47]) is defined by the ratio of the pixel-to-pixel distance (point pitch, PoP) and the dwell time per pixel (DT).

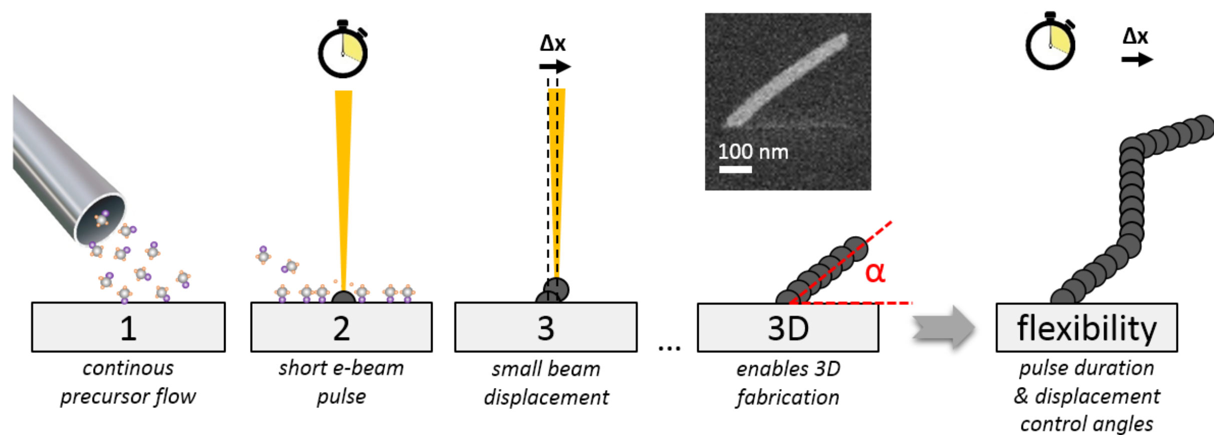

Figure 4: Basic principle for the fabrication of freestanding, 3-dimensional nanostructures via Focused Electron Beam Induced Deposition (3BID). (1) A gas nozzle continuously injects precursor molecules during the whole fabrication process. (2) The focused electron beam is turned on for a short dwell time and converts precursor molecules into a solid deposit. (3) Subsequently, the electron beam is shifted for a small distance Δx (point pitch) and the next electron beam exposure starts. (3D) By continuing this procedure, a segment with a certain inclination angle α grows. By adjusting the patterning velocity (PV = point pitch/dwell time), the inclination angle can be varied (→ flexibility).

The following chapter gives a comprehensive review of 3BID studies.

1.5.2 Review on 3BID publications

This chapter lists, to my best knowledge, all publications on 3BID in Table 2 and Table 3. Although similar in basic principle, studies on freestanding 3D structures fabricated in Transmission Electron Microscopes[88–90] are excluded as the process parameters and growth characteristics significantly differ from the typical FEBID process in Scanning Electron Microscopes (**SEM**), ESEMs or Dual Beam Microscopes . Because of the different fundamental growth characteristics and material properties, 3D-printing with ion beams (**FIBID**) is not discussed at this point either. In this context, Igaki et al.[91] and Esposito et al.[60] demonstrated the differences between 3D-nanoprinting via FEBID and FIBID in a direct comparison of both techniques with identical setup and test structure. Beside thicker wire diameter (130 nm vs. 50 nm for FIBID and FEBID, respectively), the implantation of ions can cause major changes in material functionality[60]. Nevertheless, I want to refer to some FIBID publications, showing remarkable 3D structures[92–96].

Table 2 lists journal articles of other work groups in which freestanding 3D FEBID structures are fabricated. Beside different precursor materials, a large variety of combinations concerning the process parameters (primary beam energy, beam currents, patterning velocities) is used. The number of individual segments reflects the complexity of these 3D structures. Many publications show only one inclined branch[97–104]. This relatively simple single element is suitable to extract fundamental growth characteristics[47,105] or to connect two electrodes with a suspended nanowire[101–104]. In the following, important findings concerning 3D-fabrication are highlighted.

Several articles investigate the influence of the patterning velocity on the inclination angle[47,99,105–107]. The reported values are typically in the range between 2 nm/s and 50 nm/s. These patterning velocities are relatively low, compared to those gained in our experiments (see Table 3 and P4), even if identical precursor material is used. Furthermore, most of the studies apply high beam currents, which results in unwanted co-deposition and side branching[47,98,99,106].

Mølhave et al.[47] and Gazzadi et al.[105] performed a variation of primary beam energy (5–20 keV), and both noted an increase of structural width of the freestanding nanowires in top view for lower beam energies. Due to that fact and because of less unwanted side branching below the intended wire, the first study concludes that higher primary energies might be beneficial for 3BID. The study of Gazzadi et al.[105] also considers different beam currents by normalizing the patterning velocity with the electron dose. As shown, a lower value of the *electron charge deposited per unit length* results in smaller branch dimensions.

Throughout a series of three studies[99,107,108] Bret et al. investigated the electron trajectories when impinging on a freestanding element. The findings explain the evolution of co-deposition below an inclined branch as well as the current drop in the sample stage current signal for growing structures due to wide-angle scattered electrons[99]. With these considerations, a correlation between sample current signal and 3D-growth becomes possible. Monitoring the stage current is very helpful to evaluate whether a branch is still growing or has already collapsed (see 1.5.3). One of these studies furthermore revealed a strong influence of the beam scan direction[107] in relation to the GIS orientation. Higher growth rates were reported by patterning towards the gas flux. The same article demonstrated that this behavior compromises the fabrication of more complex 3D structures for the used setup. In numerous dedicated experiments, no such significant influence of the gas flux and patterning direction has been observed (see supplement 3 in P4) for our typical setting as it has already been optimized. Nevertheless, P5 (Supplement 10 and 11) mimicked the described behavior in simulations by taking the major differences compared to our 3BID setup (beam current, precursor material, surface coverage) into account.

In 2004, Ueda and Yoshimura[109] reported an unorthodox approach to fabricate 3D meshed structures. Instead of injecting a precursor gas, residual gas (hydrocarbon) is used to deposit nanowires by moving the focused beam manually from a protrusion into the vacuum. Despite the by far highest number of single elements in Table 2, the manual fabrication character is probably critical in terms of reliability.

In several studies[47,60,91,107,110–112] helical structures were fabricated. In 2015, Esposito et al.[60] pointed out that there are problems with proximity effects within one helix, resulting in a thickening of lower parts due to transmitted and forward scattered electrons. Arranged in an array, this problem, together with lateral precursor coverage gradients and shadowing effects, led to inhomogeneous vertical growth rates. Despite the high carbon content in the fabricated structures, the promising measurements clearly demonstrate 3BID's potential for optical applications.

Other application ideas for 3BID structures (discussed or already demonstrated in literature) are field emitter tips or special shaped tips for STM and AFM probes[61,113]. Due to the nearly independency in choice of substrate material or morphology, the latter can be easily pinpointed on a cantilever. Edinger et al.[114] and Rangelow et al.[41] used this flexibility to fabricate a 3BID bridge as a scanning thermal probe, a concept that we are already pursuing at our institute.

Table 2: List of journal publications on 3D-nanoprinting via FEBID from other work groups. In some studies, primary beam energy (U), beam current (I) or patterning velocity (PV) were not specified (n.a., not available). The last column shows the maximum number of individual segments of the 3D object.

year	first author	precursor	U [keV]	I [pA]	PV [nm/s]	segments
1993	Koops[110]	$Me_2Au(tfac)$	10	1000	2–18	2
1994	Koops[61]	$CpPtMe_3$	20	400	n.a.	8
1994	Kretz[113]	$Me_2Au(tfac)$	25	n.a.	n.a.	3
1995	Koops[115]	$CpPtMe_3$	20	660	n.a.	2
2001	Edinger[114]	$MeCpPtMe_3$	n.a.	n.a.	n.a.	4
2001	Rangelow[41]	$MeCpPtMe_3$	n.a.	n.a.	n.a.	3
2002	Lau[116]	$Co_2(CO)_8$	25	183–10700	n.a.	2
2002	Utke[106]	(hfac)Cu(VTMS)	25	500	11.6–23.2	1
2003	Fujita[117]	$C_{14}H_{10}$	15	60	10–20	4
2003	Mølhave[47]	$Me_2Au(acac)$ $Mo(CO)_6$	5, 10, 20	200	50	1
2004	Ueda[109]	residual gas	5, 10, 15	n.a.	n.a.	113
2004	Bret[99]	(hfac)Cu(VTMS)	25	500	15–50	1
2004	Luisier[98]	$Cu(hfac)_2$ (hfac)Cu(VTMS) (hfac)Cu(MHY) (hfac)Cu(DMB)	25	500	35	1
2005	Takeguchi[118]	$Fe(CO)_5$	30	800	2–3	5
2005	Okada[100]	$C_{14}H_{10}$	15	50	2.5–13	1
2005	Bret[107]	(hfac)Cu(VTMS)	25	500	10–30	1
2006	Frabboni[102]	TEOS	15	45	n.a.	1
2006	Frabboni[101]	$MeCpPtMe_3$	15	90	25–83	1
2006	Igaki[91]	$C_{14}H_{10}$	5	160	n.a.	1
2006	Bret[108]	(hfac)Cu(VTMS) $[RhCl(PF_3)_2]_2$	25	500 100	n.a.	3
2007	Gazzadi[105]	$MeCpPtMe_3$ TEOS	5, 10, 15	24, 32, 42	3–27	5
2009	Gazzadi[103]	$MeCpPtMe_3$	15	90	40	1
2011	Höflich[111]	$Me_2Au(acac)$	15	140	n.a.	1
2013	Fernandez-Pacheco[112]	$Co_2(CO)_8$	3	21	n.a.	1
2015	Esposito[60]	$MeCpPtMe_3$	10	17	n.a.	1
2015	Gazzadi[104]	$Co_2(CO)_8$	15	67	143–500	1

Application ideas by using magnetic 3BID geometries are collected in a review by Fernández-Pacheco et al.[77] and already topic of intensive research[14].

In a historical context, one can observe from Table 2 that there has been a high interest in 3BID in the years 2001–2006 (16 journal articles), while there were only 6 articles published on this topic in the years 2007–2015. Furthermore, about 2/3rd of the 3BID publications are linked with four workgroups/scientists: 4 publications by Koops/Kretz/Weber et al. (1993, 1994, 1994, 1995), 5 publications by Utke/Bret/Luisier/Hoffmann et al. (2002, 2004, 2004, 2005, 2006), 3 publications by Matsui/(Fujita/Okada/Igaki) et al. (2003, 2005, 2006) and 5 publications by Gazzadi/Frabboni (2006, 2006, 2007, 2009, 2015). Beside the journal articles in Table 2, the 3D works of the mentioned groups (except Matsui) are summarized and expanded in the book by Utke, Moshkalev and Russell[31] in the sections Introduction 1 (Utke and Koops), chapter 22 (Gazzadi), and chapter 12 (Utke et al.).

Table 3 expands the list of 3BID publications with articles from our workgroup and cooperation partners, which are based on the development of this doctoral thesis to some extent. While much less has been reported in the previous ten years on this topic (6 articles), the recent evolutionary development steps have led to a renaissance in this area with 6 articles already 2017; more will follow soon.

Table 3: Journal publications on 3BID with contributions by the author of this thesis. For each, the range of the fabrication parameters primary beam energy (U), beam current (I) and patterning velocity (PV) are listed. The last column shows the maximum number of individual segments for the respective meshed 3D architecture.

year	first author (contribution of thesis author)	precursor	U [keV]	I [pA]	PV [nm/s]	segments
2016	Fowlkes[5] (P5, co-author)	$Me_2Au(acac)$ $MeCpPtMe_3$ $W(CO)_6$	30	21	20–333	90
2017	Winkler[6] (P6)	$Me_2Au(acac)$ $MeCpPtMe_3$	30	21	11–250	1296
2017	Lewis[12] (co-author)	$MeCpPtMe_3$ $W(CO)_6$	30	21.	10–96	20
2017	Winkler[4] (P4)	$Me_2Au(acac)$ $MeCpPtMe_3$ $W(CO)_6$ TEOS	1, 2, 5, 10, 15, 20, 30	1.4–150	20–333	360
2017	Keller[14] (co-author)	$HCo_3Fe(CO)_{12}$ $MeCpPtMe_3$	20	13	100	88
2017	Lewis[43] (cooperation partner)	$MeCpPtMe_3$	30	21	not specified	64
2017	Fowlkes[16] (co-author)	$MeCpPtMe_3$	30	31	20–200	51

Our 3BID approach differs in several aspects in comparison to previous reported studies. Therefore, the next section gives a detailed description of the 3BID methodology, established in this thesis. This approach may also act as guide how to fabricate 3D nanostructures in a reliable way.

1.5.3 3BID METHODOLOGY

Although there are dedicated method sections in each of the enclosed publications, this section expands and explains in more detail how 3BID – as developed during this doctoral thesis – was performed. In particular, aspects that are not explicitly discussed in the publications are addressed. Furthermore, this section should point out, which evolutionary steps in 3D-nanoprinting were taken compared to previous studies (see 1.5.2), resulting in highly complex, reliable, and tunable architectures.

First, some technical issues have to be considered to ensure reproducible results. In this context, it is very important to establish conditions close to the electron limited regime (see in particular P4). This can be achieved by using low beam currents, high precursor coverage and strong dynamic replenishment. The two latter points are maximized with an appropriate GIS setup, which is discussed in detail in P1–P4. In summary and as illustrated in Figure 5, it is beneficial to bring the GIS nozzle at a steep angle to the substrate (**a**), to reduce the distance between nozzle and surface (**b**) and to minimize the lateral distances to the deposition area in X and Y direction (**c**). The gas flux is linked to the temperature of the precursor crucible. Except for demonstration purposes in P4, the crucible was heated to 45 °C for the Pt precursor and to 30° for the Au precursor for at least 2 hours in all experiments. Furthermore, the gas valves were opened for at least 3 minutes prior to any deposition in order establishes equilibrium gas conditions.

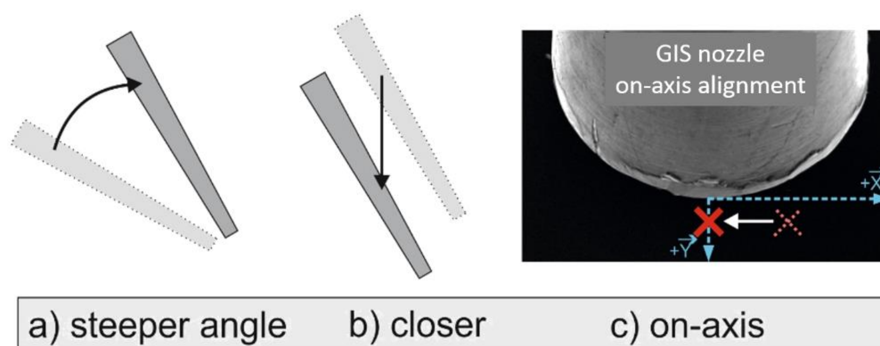

Figure 5: Steps for an optimized alignment of the gas injection nozzle.

Please note that stage drift can compromise a stable 3D-fabrication (see Figure 7 left) especially for structures with long exposure times (see for example Figure S5 in P4). While a stage settling time of about 15 minutes after stage movements is required at the FIB Nova 200 at the FELMI-ZFE (AUT), no problematic stage drift was observed at a FIB Nova 600 at the Oak Ridge National Laboratories (US). It is not recommended to use the electronic beam deflection via the beam shift coils (beam shift option) because it led to unpredictably lowered growth rates on both microscopes, most likely due to unwanted beam distortion (P4).

Beside a proper technical setup, a reliable beam alignment is indispensable to ensure reproducible results. For that, a two-step alignment procedure is recommended. In a first step, a pillar is deposited in spot mode for five seconds. Thereafter, the test spot can be inspected in top view, followed by careful optimization of beam focus and correction of astigmatism. The pillar diameter inevitably grows during inspection because of residual gas deposition; therefore, a new pillar has to be fabricated from time to time until the pillar diameter falls below a certain value. The second alignment step is shown in Figure 6. An array of several diving board structures (pillar + segment, see Figure 6a) is fabricated

using a critical range of patterning velocities for the growth of horizontal segments. During deposition, the current through the sample stage is monitored to determine, which segments are growing on top of the pedestal (Figure 6c). In this way, the critical patterning velocity can be determined, which corresponds to the highest possible patterning velocity for stable segment growth. Above that critical patterning velocity, 3D-growth cannot be guaranteed for these focal settings. To retain the same conditions in all experiments, one has to ensure that the same segment is always stable. If that is not the case, step 1 (spot optimization) has to be repeated. This alignment procedure can be quite time-consuming but establishes almost identical conditions for each experiment.

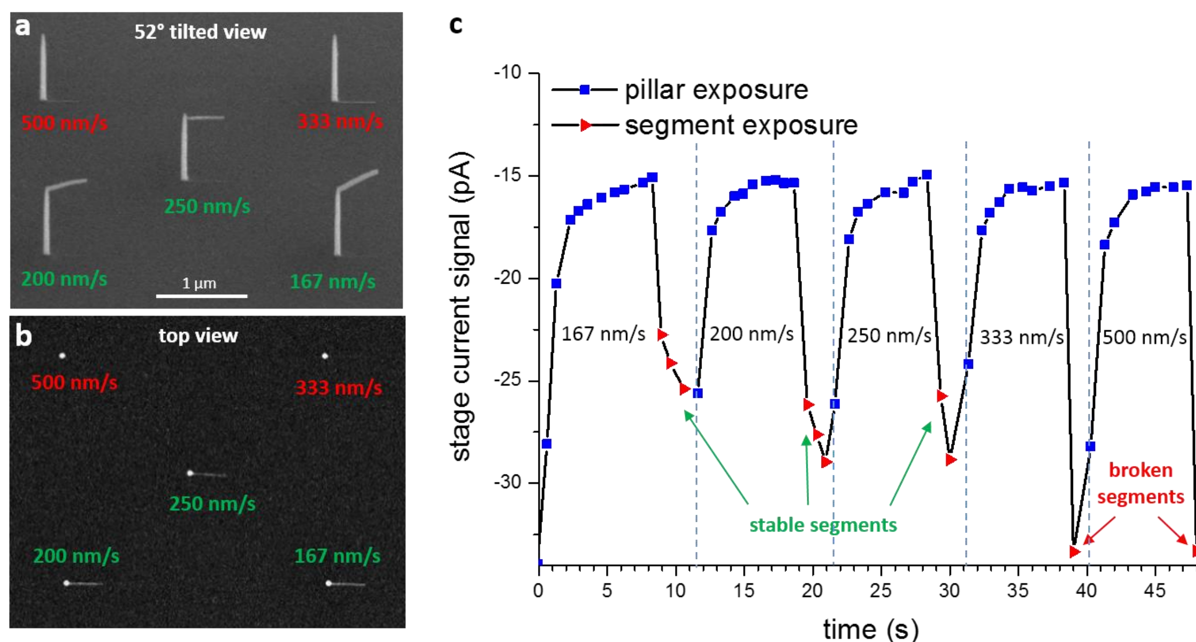

Figure 6: Setup procedure to establish reproducible conditions for 3D-fabrication. Diving board structures are deposited as shown in 52° tilted view in (a), and in top view in (b). The vertical pillars are fabricated in spot mode for 8 seconds. For the segment growth a point pitch of 1 nm and dwell times between 2 ms and 6 ms are used, resulting in patterning velocities between 167 nm/s and 500 nm/s. During fabrication, the stage current signal can be monitored (c) to evaluate, if a segment (red triangles) is connected to the pillar (blue squares). The vertical dashed lines mark the start of a new diving board.

With such a reproducible setup, one has to evaluate the inclination angles of segments fabricated with different patterning velocities once, resulting in a calibration curve (see P4 – Figure 3, P4 – Supplement 1 and P5 – Figure 4b). With that, a reliable growth of desired segment angles, specified in this calibration curve is ensured. For highest reliability the conditions have to be as close as possible to the calibration conditions (precursor flux, temperature, PoP, ...). Furthermore, it should be mentioned that we recently developed a CAD-based 3BID-generator[16] as an essential part of our publication series on 3BID, which has already included compensation mechanisms for several growth peculiarities (i.e. proximity deposition, growth rate differences for long branches). Please note, each change of the system (primary beam energy, beam current, precursor type, GIS alignment) results in an individual calibration curve and consequently in an individual critical patterning velocity and test spot size.

The deposition specification for our system at 30 keV, 21 pA and the platinum precursor are for example: critical patterning velocity = 333 nm/s; test spot size = 52 nm. The segment angle is sensitively affected by any deviation of beam focus (P4 – Figure 4), astigmatism or precursor supply, in particular close to the critical patterning velocity. In general, the alignment procedure proposed here is perfectly

suited for any FEBID experiment. Reporting for example the critical patterning velocities will facilitate the reproducibility of results and provides a practical number to describe beam and precursor conditions.

A comparison of Table 2 and Table 3 shows that we were able to increase the complexity of 3BID structures dramatically. The most important aspect in this context was the implementation of an alternating point sequence. This patterning strategy is named “3D-interlacing”, referring to the interlacing strategy, which was successfully applied for ion milling of polymers[8] and higher deposition rates of 2-dimensional FEBID pads[119]. Instead of a continuous point sequence, the beam alternates between individual segments of a multi-branch structure. As discussed and demonstrated in more detail in P6, this is advantageous for printing of complex 3D geometries in three aspects: **1)** non-isotropic bending due to proximity effects is minimized; **2)** drift problems at merging points are reduced; **3)** additional refresh times shift the working regime towards electron limited conditions while the beam is processing the other branches. Figure 7 displays the different outcome by rearranging the point sequence from continuous to 3D-interlaced.

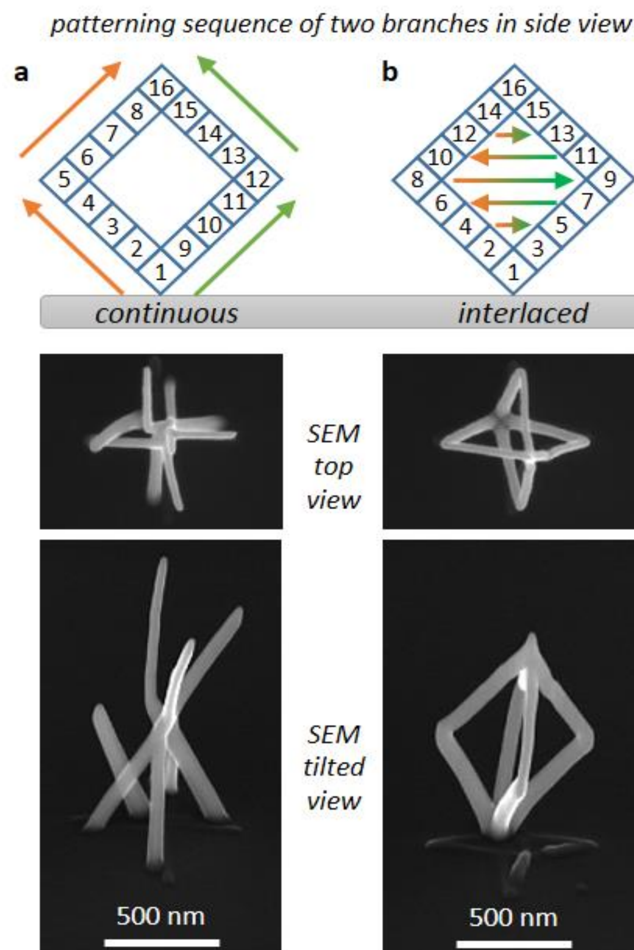

Figure 7: Advantages of the interlaced (b) in contrast to a continuous patterning sequence (a) on the same tetragonal-bipyramid geometry. The top row schematically shows the differences in the point sequence, the SEM images display the results of both strategies. Despite on-purpose drift, the branches merged at the final point by using the 3D-interlacing strategy. Images are taken from P6 (Figure 2).

To realize such an advanced 3D-interlacing point sequence, the integrated patterning possibilities of the microscope software are not sufficient. One gains the necessary flexibility by loading a list of pixel

coordinates and exposure times in a so-called "stream file". For that purpose, a code in C++ was written, to enable complex 3D geometries with such an alternating patterning sequence (see for example Figure S5b, d, e, f, j in P6). During the course of P5, a Matlab based graphical user interface was introduced to gain flexibility, reliability and simple generation of a stream file. This 3D-generator was then tested and improved, resulting in a user-friendly computer-aided-design software package called "3BID" (Fowlkes et al.[16]) that calculates the appropriate coordinates and dwell times for such 3D-interlaced 3BID exposure files for even highly complex architectures (see e.g. Figure 9 and cover page in P6).

Of high importance for 3BID is the selection of the primary beam energy and the beam current. While almost the whole range of possible values were used in the past (see Table 2), P4 elaborated the advantages of high beam energies and low beam currents, resulting in high patterning velocities and thinnest, artifact-free 3D structures at the same time (P4 – Figure 2). Low primary energies lead to thicker, however more symmetrical branches as demonstrated in Figure 8.

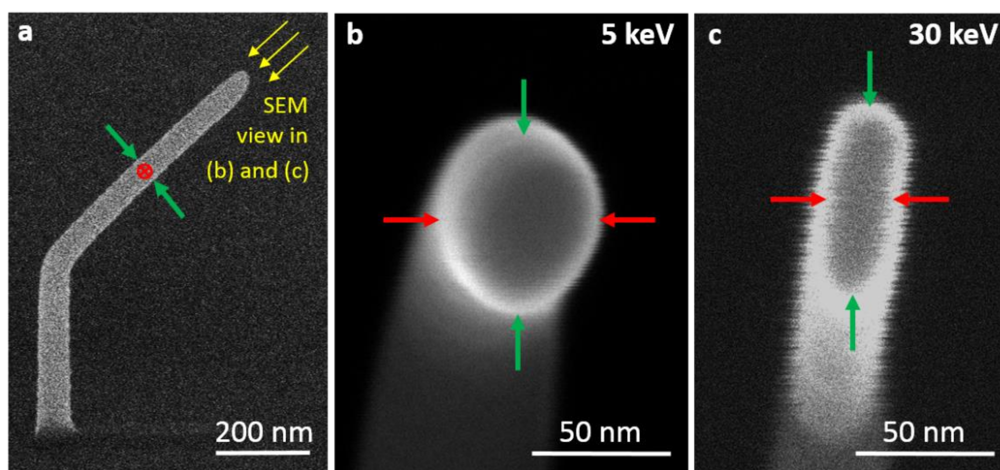

Figure 8: Shape analysis of 3BID elements fabricated at a primary electron energy of 5 keV (a, b) and 30 keV (c). The SEM image in (a) shows a diving board geometry in 52° tilted view. The yellow arrows indicate the inspection direction for the cross section shape analysis in (b) and (c). The green and red arrows display the height and the width, respectively, of the inclined segments. A blade-like cross section shape with a height-to-width ratio of 2.9 was found for 30 keV (c), while the cross section shape for 5 keV is almost circular (height-to-width ratio = 1.1).

To fabricate segments with a defined inclination angle one has to record a calibration curve for a given setup (primary energy, beam current, precursor type, GIS alignment) upfront (see P4 and P5). With that, a certain segment angle is achieved by using a certain patterning velocity. This velocity is defined as ratio of point pitch and dwell time. P4 validates that it is not only reliable but also more precise to keep a fixed value for the PoP and to vary the DT accordingly. To give numbers for our setup (30 keV, 21 pA, Pt-precursor), for the most of the experiments in this thesis typically a PoP of 1 nm and DTs starting from 3 ms upwards were used, resulting in patterning velocities of 333 nm/s or lower. A more detailed discussion and interpretation can be found in the subsequent publications.

To sum up this section, by considering the manifold influences during 3D-growth (P4, P5) a reliable methodology has been demonstrated to establish reproducible 3BID experiments. Even further, a user-friendly software package[16] for general use has been presented to enable the construction of highly complex 3D architectures.

2 PUBLICATIONS

In this chapter, the enclosed publications for this cumulative doctoral thesis are briefly summarized. How the articles correlate to each other is shown in a general overview (2.1). Furthermore, Table 4 and Table 5 give a quick survey of the topics. Basic data about title, authors and journal are mentioned in this chapter, while the original journal articles are attached in the appendix. An executive summary conflates the experiments and results briefly and concisely. Furthermore, an author's contribution section is provided for each publication with emphasis on the contributions by the author of this thesis. A final summary and conclusion of all papers is given in chapter 3 and 4, summarizing the novel and relevant aspects.

Table 4: Overview of the enclosed publications concerning research area, precursor type, material tuning, used methods and dimensionality of the fabricated FEBID structures. Furthermore, the essential output of each publication is listed briefly. Abbreviations and microscopes: FIB…Focused Ion Beam (FEI Nova 200, FEI Nova 600); AFM…Atomic Force Microscope (Bruker Dimension 3100, Bruker Fast Scan Bio), EDXS…Energy Dispersive X-ray Spectroscopy (Bruker Xflash 4010, EDAX XL-30); 3BID…CAD-Software for 3D-nanoprinting[16]; EBL…Electron Beam Lithography (Raith e-line); ESEM…Environmental Scanning Electron Microscope (FEI Quanta 200); TEM/BF…Transmission Electron Microscopy/Bright Field imaging mode (FEI Technai TF20); STEM-EELS…Scanning Transmission Electron Microscopy based Electron Energy Loss Spectroscopy (FEI Technai TF20 + Gatan Imaging Filter).

	publication					
	1	2	3	4	5	6
research area	fundamental	fundamental	fundamental	fundamental	simulation	application
precursor material	$MeCpPtMe_3$	$MeCpPtMe_3$	$MeCpPtMe_3$	$MeCpPtMe_3$ $Me_2Au(acac)$ $W(CO)_6$ TEOS	$MeCpPtMe_3$ $Me_2Au(acac)$ $W(CO)_6$	$Me_2Au(acac)$ $MeCpPtMe_3$ TEOS
chemistry tuning	via parameters					purification (H_20 + electron beam)
methods	FIB, AFM, EDXS	FIB, AFM, finite differences simulations	FIB, AFM, finite differences simulations, continuum model calculations	FIB	FIB, AFM hybrid Monte-Carlo continuum simulations	3BID, FIB, EBL, ESEM, TEM-BF, STEM-EELS
dimensionality footprint	1D, 2D	2D	2D	3D	3D	3D
essential output	role of fabrication parameters on chemical composition	shadowing effects and optimization of the GIS alignments	top surface morphologies for different patterning strategies /parameters	evaluation of numerous process parameters and growth characteristics for 3BID	mimicking and describing 3D-growth in simulations	showing plasmonic activity of FEBID material in 2D and 3D after purification

2.1 OVERVIEW

In the following, six peer reviewed journal articles are presented, which constitute the fundament for reliable 3D-nanoprinting of functional nanostructures via FEBID. Simulations and calculations from our cooperation partners (Oak Ridge National Laboratories, University of Tennessee and EMPA) complemented the experimental results. In short, P1 – P3 discuss one- and two-dimensional deposits and not freestanding 3D structures per se, but they revealed highly important findings, enabling reliable 3D-nanoprinting. Therefore, those publications serve as gateway to a more fundamental understanding of diffusion processes, dynamically changing working regimes, chemical tuning of deposits, as well as technical aspects like GIS alignments and patterning challenges. P4 comprehensively evaluates the influence of numerous process parameters on the 3BID process and is the central 3BID publication in this thesis. P5 introduces a simulation of the 3D-growth, which enables predictability and a simplified generation of FEBID exposure files. P6 finally demonstrates the plasmonic activity of 3BID geometries and thus fulfills a long lasting promise in this field. Briefly, the presented approach demonstrates how to leverage classical and more planar plasmonics into the third dimension with an enormous degree of design flexibility beyond previous limitations.

Table 5: Overview of investigated/varied process parameters in each publication. The parameters are categorized into the four topics beam parameters, gas parameters, patterning parameters and other parameters.

	publication					
	1	**2**	**3**	**4**	**5**	**6**
beam parameters	primary energy, beam current	beam current	beam current	primary energy, beam current, beam quality, convergence angle, beam shift		purification: primary energy, beam current and dose
gas parameters	GIS alignment	gas flux		GIS alignment, precursor temperature, precursor type	precursor type, diffuse and directed gas component	purification: H_2O pressure
patterning parameters	dwell time, patterning strategy, pattering direction, loops	dwell time, patterning strategy, patterning direction, loops	dwell time, patterning strategy, patterning direction, loops	PoP, dwell time, patterning direction, refresh time, patterning engine accuracy	dwell time, patterning direction	patterning strategy, purification: PoP, dwell time
other parameters				drift	voxel size, number of sampled electron trajectories	disk size

2.2 PUBLICATION 1

2.2.1 ARTICLE DETAILS

- Spatial Chemistry Evolution during Focused Electron Beam-Induced Deposition: Origins and Workarounds.
- Winkler, R.; Geier, B.; Plank, H.
- *Appl. Phys. A Mater. Sci. Process.* (invited) **2014**, *117* (4), 1675–1688.
- Full article can be found in appendix 1

2.2.2 EXECUTIVE SUMMARY

Incomplete dissociation of $MeCpPt^{(IV)}Me_3$ precursor molecules results in an incorporation of carbon in FEBID materials. In this article, we show that by using different process parameters the amount of carbon can vary within the deposit. Interpreting previously reported data on growth rates and chemical composition for quasi-1D pillar structures[81], lowest carbon content was found for working conditions between the electron limited regime (ELR) and the molecule limited regime (MLR). While less electrons (ELR) support an incomplete dissociation, excess of electrons (MLR) leads to polymerization of fragments[81]. On that base, the origins of the observed spatially differing metal contents for pads with 4x4 μm^2-footprint via EDXS analysis are discussed. Within the first 100 nm deposit height, the electron interaction volume shifts from the substrate into the deposit. In consequence of the higher density of the FEBID material a greater number of electrons is generated locally and the Pt content increases. A variation of the beam current shows that higher beam currents result in higher metal content. This statement seems to be in contradiction to results for 1D pillars but is explained by including considerations of the very different precursor replenishment times in both cases. To evaluate the influence of replenishment mechanisms, the scan strategy is varied as well as the scan direction in relation to the gas injection system. As result, a higher metal content and higher growth rates are found by patterning with the slow scan axis in the direction of the gas flux. These findings emphasize the importance of a suitable scan strategy and a proper alignment of the gas injection system. Finally, to correlate the chemical composition with material properties, the resistivity of deposits fabricated at different working regimes is measured in the as-deposited state and after electron beam curing.

2.2.3 AUTHOR CONTRIBUTIONS

R.W. and H.P. designed this study to resolve arising questions and to prove assumptions from previous findings of both authors concerning a correlation of process parameters and deposit chemistry. H.P. supervised the work, performed and analyzed all experiments on 1D pillars (section 2.1) and did the electrical resistivity measurements (section 2.2.4). For all 2D footprints (section 2.2 – 2.2.3), R.W. carried out stream file preparation, fabrication via FEBID, characterization with EDXS as well as AFM and data analysis. R.W. executed Monte-Carlo simulations to evaluate electron interaction volumes and BSE coefficients via CASINO. B.G. helped with EDXS data quantification as well as with calculation of Pt/C ratio by providing a Matlab script. R.W. and H.P. discussed and interpreted all data. R.W. drafted the manuscript, which was improved in several iterations with H.P. and the final feedback by B.G.

2.3 PUBLICATION 2

2.3.1 ARTICLE DETAILS

- The Nanoscale Implications of a Molecular Gas Beam during Electron Beam Induced Deposition.
- Winkler, R.; Fowlkes, J.; Szkudlarek, A.; Utke, I.; Rack, P. D.; Plank, H.
- *ACS Appl. Mater. Interfaces* **2014**, *6* (4), 2987–2995.
- Full article and Supporting Information can be found in appendix 2

2.3.2 EXECUTIVE SUMMARY

This study reveals the effects of a directed gas beam on deposition rates. To describe the precursor flux from the gas injection system (GIS), we first introduce the gas flux vector (GFV). We prove through experiments, calculations and simulations that the growing nanostructure itself is able to cast a shadow for the directed gas flux. Replenishment in the shaded area is only driven by surface diffusion (from substrate or deposit) and re-adsorption, resulting in lower growth rates. The impact of the shadowing effect is then demonstrated for several patterning strategies/directions and pattern rotations in relation to the GFV. Performing experiments with variations of beam currents and dwell times at constant total exposure times show that, for higher currents and/or higher dwell times, the deposits also increase and the shadowing effect is therefore more pronounced. A comprehensive supplementary section expands the main findings with further simulations, calculations and experiments. In summary, this study demonstrates the need for **1)** an optimized GIS alignment, **2)** the selection of a suitable patterning strategy (serpentine towards the GFV) and **3)** balanced dwell time/beam current settings.

2.3.3 PREAMBLE – AUTHOR CONTRIBUTIONS

H.P. and I.U. initiated this study to evaluate the impact of different patterning strategies. H.P. supervised the project. R.W. wrote a C++ code for flexible stream file generation, performed all deposition experiments and did the characterization via Atomic Force Microscopy. R.W. hypothesized a shadowing effect as origin for the unexpected deposit morphologies. Following the joint discussion between H.P., P.D.R., J.D.F., and R.W. about the experimental findings, J.D.F. conducted finite differences simulations to support the hypothesized model (Figure 2c, 3b,c, 8d,e, Supplement 4 and 7). A.S. calculated the ratio of diffusive replenishment vs. directed gas flux adsorption replenishment (Figure 7c) and wrote Supplement 8. I.U. supervised the work of A.S. and provided the Gas flux simulator, which R.W. used for the interpretation of the precursor gradient experiments in Supplement 1. R.W. performed single dots deposition experiments needed for the calibration of the calculations in Supplement 8. H.P. wrote the first draft of the main manuscript, R.W. drafted the Supplement section. Together, H.P. and R.W elaborated the final manuscript, which was commented by all co-authors.

2.4 PUBLICATION 3

2.4.1 ARTICLE DETAILS

- Toward Ultraflat Surface Morphologies During Focused Electron Beam Induced Nanosynthesis: Disruption Origins and Compensation.
- Winkler, R.; Szkudlarek, A.; Fowlkes, J. D.; Rack, P. D.; Utke, I.; Plank, H.
- *ACS Appl. Mater. Interfaces* **2015**, *7* (5), 3289–3297.
- Full article and Supporting Information can be found in appendix 3

2.4.2 EXECUTIVE SUMMARY

This study reveals that during deposition of 2-dimensional pads locally different growth rates occur, which can lead to distortion of the top surface morphology. Firstly, we test several patterning strategies (raster, spirals and serpentine) and analyze the evolving morphology via AFM. This reveals patterning related instabilities (chair-type, trenches, tunnel-shape), with the best and most symmetrical results being achieved with serpentine strategies. For interpretation, the dynamically changing working regime at the respective patterning pixel is considered, which consistently explains the significant differences for the investigated patterning sequences. Exploring the parameter space with a dwell time and beam current variation for the beneficial serpentine strategy (raster is shown in the supplements), four characteristic top surface shapes were found. The concave shape for low dwell times and low beam currents evolves due to preferential coverage at the pad borders because of surface diffusion. A tunnel shape arises for short DT/high currents due to depletion at turning points. Proximity deposition of forward scattered electrons at high DT and high currents is responsible for the slanted morphology. Flat shapes are obtained for low beam currents and high DT. Continuum model calculations confirmed the interpretations. A closer look at the edges and corners of a flat shaped deposit reveals rounded edges/corners as a consequence of a reduced number of adjacent patterning points. The thereby lower number of electrons can be compensated by a suitable dwell time correction, resulting in almost perfectly flat top surfaces with steep side walls.

2.4.3 PREAMBLE – AUTHOR CONTRIBUTIONS

H.P. and R.W. devised the conceptual ideas in this manuscript that based on morphological peculiarities. Such unexpected surface features were found in preliminary experiments by R.W. All deposition experiments, AFM characterizations and data analysis, as well as advanced stream file generation (special patterning strategies, edge/corner compensation) were executed by R.W. All authors critically reviewed H.P.'s and R.W.'s interpretation of the data. A.S. mimicked the experimental shapes with continuum model calculations (Fig. 4a–c) and I.U. supervised her results. J.D.F. performed Monte-Carlo simulations at deposit borders (Fig. 4d). R.W. elaborated the idea of edge/corner compensation strategy. H.P. supervised the whole study, reviewed all results and performed supplementary Monte-Carlo simulation with CASINO software package. R.W. wrote the first version of the manuscript and the supplements; H.P. and R.W. discussed and improved the paper together. All authors contributed to the final version with their critical comments.

2.5 PUBLICATION 4

2.5.1 ARTICLE DETAILS

- High-Fidelity 3D-Nanoprinting using a Focused Electron Beam: Growth Characteristics.
- Winkler, R.; Lewis, B. B.; Rack, P. D.; Fowlkes, J. D.; Plank, H.
- *ACS Nano* **2017**, in review
- Full article and Supporting Information can be found in appendix 4

2.5.2 EXECUTIVE SUMMARY

This article comprehensively elaborates the role of numerous process parameters for 3D-nanoprinting. As test structure we use a diving board geometry where the inclination angle is measured. A variation of beam parameters reveals that high primary beam energies and low beam currents are advantageous. In addition, the beam focal settings turn out to be crucial. Next, the patterning velocity is deconvolved in point pitch and and dwell time. In this context, a better reproducibility of a certain segment angle was achieved by fixing the point pitch and changing the dwell times accordingly. While the patterning direction does not have major impact on the angles, additional refresh times and other actions to shift the working regime towards electron limited conditions (GIS alignment, temperature increase of the crucible) increase the vertical growth rate. Furthermore, several precursor materials are compared, results for different convergence angles are analyzed and technical issues (beam shift, thermal equilibrium conditions and drift, patterning accuracy) are covered. The experimental data are then interpreted in particular in the context of the working regime and a strategy for reliable 3D-nanoprinting is given in the end.

2.5.3 PREAMBLE – AUTHOR CONTRIBUTIONS

R.W. and H.P. conceived the study, H.P. supervised the whole project. R.W. designed the experiments in accordance with H.P., prepared the samples, generated the stream files, fabricated all 3D-FEBID structures and analyzed the results. J.D.F. and P.D.R. were involved in planning and supervising the work at Oak Ridge National Laboratories. B.B.L. did the tungsten deposition in Figure 9 and assisted R.W. during 3D-fabrication and the analysis of the data for Figure 7, Figure 9 and Supplement 5 at the Nova 600 Dual Beam Microscope at the CNMS/ORNL. R.W. and H.P. primarily interpreted all data, J.D.F., B.B.L. and P.D.R. contributed to the discussion. J.D.F. provided a CAD-based 3D-software (3BID[16]) for the generation of the 3D-FEBID exposure file for the pyramid structures shown in Figure S5. R.W. summarized the results and wrote the main draft and supplements. H.P. critically reviewed and refined the manuscript; both H.P. and R.W. iteratively improved the paper for the final version after critical review from all authors.

2.6 PUBLICATION 5

2.6.1 ARTICLE DETAILS

- Simulation-Guided 3D Nanomanufacturing via Focused Electron Beam Induced Deposition.
- Fowlkes, J. D.; Winkler, R.; Lewis, B. B.; Stanford, M. G.; Plank, H.; Rack, P. D.
- *ACS Nano* **2016**, *10* (6), 6163–6172.
- Full article and Supporting Information can be found in appendix 5

2.6.2 EXECUTIVE SUMMARY

In this article hybrid Monte-Carlo – continuum-model simulations are presented to describe the 3D-growth via Focused Electron Beam Induced Deposition. Starting with a Monte-Carlo simulation of the electron trajectories the interaction volume is superimposed with the evolving 3D-object. In the next step, the evaluation of surface electrons is combined with a rate equation solver, which also includes directional and diffuse precursor replenishment separately. This hybrid simulation of Monte-Carlo and continuum model is then successfully tested on its robustness on a 2-dimensional deposit, for which the experiments revealed morphological peculiarities due to shadowing effects. Proceeding to three-dimensional objects, the simulation is calibrated with a set of diving board structures for different precursors. After its successful calibration, a CAD-based software is introduced that enables the comfortable creation of exposure files including an alternating point sequence. That allows the predictable fabrication of 3D FEBID geometries beyond trial-and-error approaches. As examples, highly complex meshed nanoarchitectures (cubic frame, truncated icosahedron) are simulated and successfully fabricated afterwards with remarkable conformance of predictions and experiments. In addition, a comprehensive supplementary section describes in detail the development of the 3D-code and previously reported 3D-experiments[107] are reproduced via simulations.

2.6.3 PREAMBLE – AUTHOR CONTRIBUTIONS

J.D.F., H.P. and P.D.R. created the idea to mimic the 3D-growth of freestanding FEBID structures via simulations. R.W. proposed the segment geometries for proper calibration of the simulations and introduced B.B.L., M.G.S. and J.D.F. to 3D-nanoprinting during the visit at ORNL. J.D.F. developed hybrid Monte-Carlo – continuum-model simulations to replicate experimental FEBID segments. On that base, J.D.F. wrote a Matlab based CAD-program to simplify the stream file generation for complex 3D structures, which was tested by R.W. and B.B.L and iteratively improved by their inputs. H.P. supervised the work of R.W. and both were involved in the discussion and interpretation during the whole process. Based on preliminary work, R.W. suggested beam- and patterning parameters and fabricated the calibration segments for the $MeCpPt^{(IV)}Me_3$ and $Me_2Au(acac)$ precursors (Figure 3), B.B.L. showed responsible for similar segments from the $W(CO)_6$ precursor (Figure 3 inset). J.D.F. tested the applicability of the 3D-simulation code to 2D structures (Figure 2), and R.W. performed the fabrication, characterization and analysis of the spiral-out prism shown in Figure 2a and 2d. R.W. also printed the cube-structure shown in Figure 5a. R.W. and B.B.L. performed several rotation experiments to evaluate the influence of patterning direction in relation to the gas supply, leading to the discussion shown in supplement 11. J.D.F. wrote the manuscript with input from all authors.

2.7 PUBLICATION 6

2.7.1 ARTICLE DETAILS

- Direct-Write 3D Nanoprinting of Plasmonic Structures.
- Winkler, R.; Schmidt, F.-P.; Haselmann, U.; Fowlkes, J. D.; Lewis, B. B.; Kothleitner, G.; Rack, P. D.; Plank, H.
- *ACS Appl. Mater. Interfaces* **2017**, *9* (9), 8233–8240.
- Full article and Supporting Information can be found in appendix 6

2.7.2 EXECUTIVE SUMMARY

This article combines previous achievements in terms of 3D-nanoprinting and purification to demonstrate FEBID's first plasmonically active, pure gold nanostructures. In detail, we report the strong plasmonic activity of FEBID gold structures in 2D and 3D after the introduction of a suitable purification step for $Me_2Au(acac)$. For that, we adapt our electron beam assisted purification approach in water vapor at room temperature[7] to gold FEBID deposits, resulting in pure and compact gold disks. STEM-EELS measurements on such disks with different diameters reveal all expected surface plasmon modes in well agreement with Electron Beam Lithography based reference disks. Next, we demonstrate new possibilities in 3D-nanoprinting via FEBID and discuss the required alternating patterning sequence. The here shown nano-architectures exhibit the highest degree of complexity for FEBID structures to date. To facilitate plasmonic activity, the above-described purification approach has been adapted to freestanding 3D-printed structures to prevent their collapse. The finally achieved 3D structures maintain their shape, consisting of pure and compact gold branches that were shrunken in thickness. The measurements of spatial electron energy losses via STEM-EELS confirm high plasmonic activity, with electron energy loss peaks visible even in the raw data and enhanced plasmonic behavior especially at the tip and merging regions.

2.7.3 AUTHOR CONTRIBUTIONS

H.P. conceived the idea to this study that was refined in discussion with R.W., P.D.R. and G.K.. H.P. supervised the investigations. R.W. installed the gold precursor and supported U.H. during FEBID-disk synthesis at the FIB and during the water assisted purification at the ESEM. F-P.S. carried out all investigation at the TEM (STEM-EELS measurements) under participation of U.H. (for FEBID-disks) and R.W. (for tetragonal-bipyramids). F-P.S. synthesized and characterized the EBL-disks (bottom row in Figure 3a and Figure 3c right graph) and executed a careful deconvolution of STEM-EEL maps (in Figure 3a, 5 and 6, Supporting video) via a self-made analysis program. U.H. fabricated all 2D FEBID deposits, while R.W. printed all freestanding 3D structures. For the design of the 3D architectures in Figure 1a,e as well as for the structures in Supporting Figure 5c,d,g,h R.W. utilized a CAD-software provided by J.D.F.. Otherwise, R.W. created and manipulated the stream files with a self-written C++ code. For 2D FEBID structures, U.H. performed purification experiments, EDX and AFM analysis (Figure 1i,j; Figure 3a, Supplement 3). R.W. did purification pretesting, optimization and fabrication of tetragonal-bipyramids on a TEM-grid. R.W. evaluated the EEL spectra under guidance from F-P.S.. Under the lead of H.P. all authors discussed the results and contributed to the interpretation. R.W. wrote the manuscript and Supporting Information with consultation of U.H. and F-P.S. The final version was optimized and jointly prepared by H.P. and R.W. and commented by all authors in the end. R.W. created the cover art graphic for the journal cover page.

3 SUMMARY

The achievements of this doctoral thesis contribute to the field of Focused Electron Beam Deposition (**FEBID**) based 3D nanofabrication especially in two aspects: ***1)*** a deeper fundamental understanding of the interdependencies of process parameters during FEBID; and ***2)*** the development of reliable 3D-nanoprinting via FEBID further called 3BID. In the following summary, the most important results from the enclosed publications are highlighted.

Starting from a technical point of view, one necessary requirement was the creation of a program code to generate FEBID process files (stream files) beyond the limitations of the integrated software solutions of the microscopes. The code was written in C++ and improved stepwise including proper 3D-interlacing point sequence for 3BID.

This acquired flexibility in patterning allowed the study of influences that occurred with different scanning strategies. The assumption that the point sequence has an implication on growth rates was hypothesized and calculated upfront. However, the conducted experiments revealed unexpected effects on the deposit morphology. Here, P2 demonstrated in a comprehensive experimental study that the growing deposit itself is able to shadow the directed precursor flux from the GIS nozzle. This shadowing effect was more or less prominent, depending on the used patterning strategy, direction and pattern rotation in relation to the gas nozzle. In particular, for spiral scan sequences, the implications are obvious as these strategies combine four scan directions within one pad. Consequently, the importance of the GIS-alignment became evident and on that basis, rules for a proper nozzle setup were deduced. Furthermore, a variation of dwell time revealed that, despite identical total pixel doses, different effects can lead to unexpected deposit morphologies. This is a consequence of inhomogeneous growth rates in a single pad due to variations in precursor coverage and different replenishment paths. Cooperation partners from Thun (EMPA; CH), Oak Ridge and Knoxville (ORNL, UT; US) supported the interpretations with calculations and simulations. Beside several other aspects, the main take-away messages are the benefits of an improved GIS alignment (as close as possible, high angle port, on-axis setup) and a patterning in serpentine lines towards the GIS nozzle for highest volume growth rates.

P1 demonstrated that these varying growth rates are accompanied by a change of chemical compositions within the deposit as well. EDXS characterization revealed a higher platinum content by patterning towards the gas nozzle. For the discussion of the working regime, considerations of BSE yields during early growth stages were included, in particular to explain the decreasing and then saturating behavior of volume growth rates and C / Pt ratios, respectively. Changes in working regime conditions during pillar growth are responsible for changes in composition and growth rates especially during the deposition of the first few nanometers. For 2D pads, a platinum content of 12 – 18 at% was found, depending on the fabrication parameters.

P3 utilized different pattern strategies to elaborate the dynamically changing working regime within one pad. Because of spatial precursor coverage inhomogeneity during patterning of 2D pads, different types of top surface morphologies evolved. The responsible disruption effects that cause deviations from the ideal flat top shape were investigated in detail. For interpretation, precursor replenishment channels were analyzed for each patterning strategy. As practical guide to the fabrication of flat deposit surfaces, the serpentine patterning strategy was proposed and studied in detail by varying the

dwell time and beam current. The results were summarized in a parameter map and an ideal parameter space for flat deposits was found. The change in either the dwell time or the beam current resulted in different top surface shapes (tunnel, concave, slanted). Although an unfavourable strategy, a discussion of unwanted surface features for spirals and raster strategies was provided in the supplements of P3. Finally, in order to compensate rounded edges and corners even at optimal settings, a correction approach via adaption of dwell times was demonstrated.

The first three publications paved the way for 3BID as they provided several essential components. Firstly, they enabled a flexible patterning via stream file generation and manipulation. Secondly, an optimized GIS setup was elaborated, advantageous for reproducible 3D-nanoprinting. Most importantly, a deeper understanding of changes in the working regime was achieved.

P4 – P6 are part of our overall strategy to leverage 3BID into the status of a reliable and user-friendly 3D-printer for complex nanostructures. Together with our scientific partners in the US we cover several complementary aspects, starting with a comprehensive experimental parameter study (P4), continuing with fundamental simulations concerning the growth characteristics (P5), demonstration of plasmonic 3BID structures for optical applications (P6), laser assisted purification of 3D structures[12], to a user-friendly CAD based design package to create exposure files[16].

P4 evaluated the implications of numerous process parameters on the 3D-growth characteristics in a comprehensive manner. A diving board geometry was used as test structure, which can be considered as fundamental building block for more complex 3D structures. Best results were found for high primary energies (30 keV) and low beam currents (21 pA) as these beam settings avoid many disadvantages reported in the past (side branching, co-deposition, strong scan direction dependency). In addition, influences of further beam parameters (focus, astigmatism, beam shift, convergence angle), gas parameters (GIS alignment, precursor type and temperature), patterning parameters (point pitch, dwell time, patterning direction, refresh time) and other aspects (drift, patterning engine accuracy, thermodynamic equilibrium of the crucible) were investigated and discussed in particular in the context of the working regime. The generic description via the working regime, the comprehensive consideration of the process parameters and complementary experiments on different microscopes led to a strategy guide for reliable 3D-nanoprinting.

P5 simulated the growth process in 3D via a Monte-Carlo simulation of the electron trajectories in combination with the finite differences method to calculate the evolving 3D deposit. The simulations were first calibrated with experiments. In addition, key aspects such as proximity deposition and dynamically changing precursor coverages were implemented in the calculations. Then, the simulations predicted specific 3D geometry, which were validated in 3BID experiments afterwards. Although the 3D-code was developed specifically for 3D structures, it is also applicable for 2D fabrication. P5 also discussed the 3D-interlacing patterning strategy, as this is the key for complex 3D manufacturing, as demonstrated in P6.

P6 indicated the potential of 3BID for plasmonic applications. To get to this point, several hurdles had to be overcome first. For plasmonic activity, pure gold deposits are required. Here, we demonstrated the purification of $Me_2Au(acac)$ in H_2O vapor of 10 Pa with the same approach as we reported previously[7] for $MeCpPt^{(IV)}Me_3$. Using an electron dose of 28 C/cm² for purification, compact and pure gold disks were obtained, which was confirmed by EELS measurements. Mapping the spatial electron energy losses, plasmonic modes (dipole, quadrupole, hexapole, and breathing mode) of FEBID deposits

were shown. For 3D architectures, adapted purification parameters were elaborated (purification doses about 3–8 times higher, low purification currents), leading to compact and pure, but still stable tetragonal bi-pyramid geometries. STEM-EELS confirmed their plasmonic activity, with strong plasmonic peaks already visible in the raw data. With this publication, plasmonic activity can be included in the list of FEBID functionalities for 2D structures but also for freestanding 3D geometries that cannot be fabricate with other techniques. Finally, the unique 3D-printing capabilities of 3BID were illustrated in a set of SEM-images showing complex multi-branch architectures.

4 CONCLUSIONS AND OUTLOOK

4.1 CONCLUSIONS

The developments described in this doctoral thesis enabled the reliable fabrication of functional and freestanding 3D nanoarchitectures via Focused Electron Beam Induced Deposition.

In short, publication 1 revealed a spatial varying chemical composition in dependency on the local working regime, publication 2 revealed shadowing effects of the growing deposit arising due to the directional nature of the gas flux, and publication 3 interpreted characteristic top surface shapes as consequence of pattern or parameter related issues. Beyond that, P1 – P3 provided the essential foundation for 3D-nanoprinting by the following achievements: **1)** a deeper understanding of the dynamic changes in the working regime has been gained, **2)** the effects of gas replenishment mechanisms have been uncovered; **3)** an optimized GIS alignment has been proposed, **4)** full control and flexibility regarding the electron beam movement has been achieved, and **5)** the required experimental expertise has been obtained.

In particular, publications 4–6 have significantly improved FEBID's 3D-nanoprinting capabilities. In this context, publication 4 acts as central study, as it comprehensively evaluates the involved process parameters and provides a strategy guide for reproducible 3D-nanofabrication. In publication 5, the 3D-growth was simulated consistently, and a CAD-based design simplified the generation of process files for complicated 3D architectures. After demonstrating a purification method for 2D and 3D FEBID gold structures at room temperature, those structures exhibited plasmonic activity (publication 6).

Summarizing all advancements, an evolutionary step forward towards a unique 3D-printer for highly complex architectures on the nanoscale has been taken. Novel aspects are in particular **1)** the complexity of the fabricated 3D geometries, **2)** the fundamental insights into the 3D-growth characteristics, **3)** the comprehensive evaluation of process parameters, **4)** the deduction of a practical guide for reliable 3D-nanoprinting, **5)** the full purification of 3D structures, and **6)** the demonstration of their plasmonic activity.

4.2 OUTLOOK

While a huge step for reliable 3D-printing of complex nanostructures via FEBID has been taken, there are still many interesting fundamental questions open for future investigations.

Already work in progress is the analysis of cross sectional shapes of freestanding elements. In this context, Figure 8 showed a strong dependency on the primary electron energy. Simulations by our collaboration partners will complement this study, with the aim to extract design rules and strategies to tune the branch thicknesses arbitrarily.

Furthermore, we observed a change of growth rates with increasing structure height. There are indications that surface diffusion and depth of focus play a central role, but also re-adsorption and heating effects are under suspicion. A separation of the mentioned aspects is planned in the near future and is expected to improve reliability of the fabrication of very high 3D structures.

Future applications for 3BID also depend on the functionalities of the available precursor material. In this context, the 3D-growth characteristics for many precursors are still an open task. Furthermore,

different purification approaches for 3D structures have to be tested. As shown by Shawrav et al.[120] for a different gold precursor ($Me_2Au(tfac)$), it is possible to implement the water vapor purification step already during the fabrication for flat deposits. Adapting this approach, pure metal deposition in one single step might get possible also for 3D structures. That would furthermore eliminate issues with shrinking or collapsing 3D architectures or temperature induced problems during 3D-LAEBID[12].

As discussed in 1.5.2, the sample stage current signal provides live information about the 3D-growth[121]. As already successfully demonstrated for FIBID[95], this can be used as feedback to adapt the deposition process right during fabrication. The development of such a feedback control is already work in progress and should allow defined growth even for long and high structures.

Beside such fundamental studies, 3BID has a high potential for novel application concepts or miniaturization of existing devices. The direct-write fabrication of freestanding, complex 3D structures with structural dimensions on the nanoscale is one of FEBID's unique selling points[21]. With the help of the published work on 3BID[4–6,12,14,16] in the course of this thesis and last but not least with the release of the 3BID CAD software[16], a major impulse on the FEBID community is expected in near future.

Especially, applications of 3D structures with magnetic materials could be of high interest. For example, Keller et al.[14] already demonstrated an artificial spin-ice system on magnetic 3D FEBID structures. In addition, mechanical properties of designed 3D architectures[43] are promising for diverse applications. Our working group already showed the proof of principle of a thermal nanoprobe via a 3D tetrapod, fabricated on an AFM tip. We will pursue this route in a national laboratory starting in 2018.

As shown in P6, plasmonic applications are another promising field for 3BID. The fabrication of designed structures for TERS (Tip-enhanced Raman spectroscopy) might provide completely new possibilities.

Assuming that many application fields are still not foreseeable, I hope that 3BID can provide important impulses for the nanofabrication community in the future. And I would be delighted, if I were able to make a modest contribution to that.

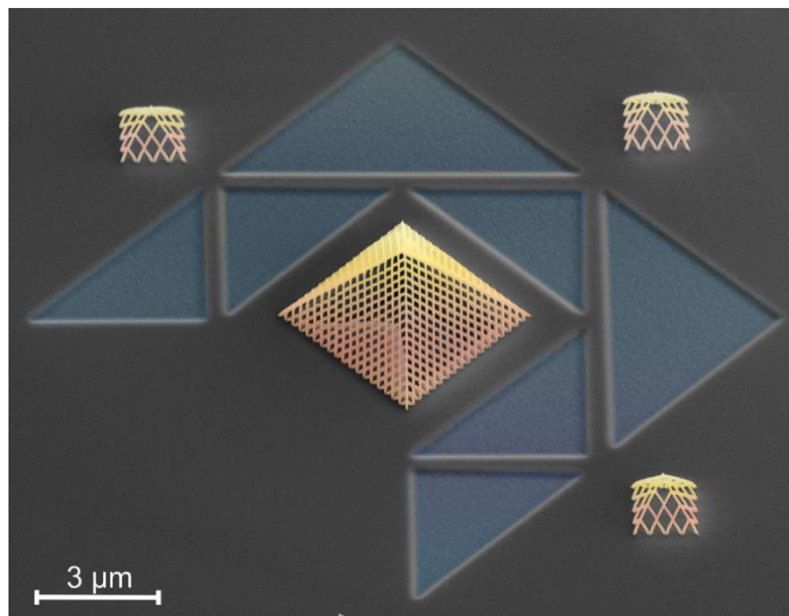

Figure 9: 3BID Pt-C_X model of the glass pyramid of the Louvre on a FIB structured silicon surface.

5 REFERENCES

(1) Winkler, R.; Geier, B.; Plank, H. Spatial Chemistry Evolution during Focused Electron Beam-Induced Deposition: Origins and Workarounds. *Appl. Phys. A Mater. Sci. Process.* **2014**, *117* (4), 1675–1688.

(2) Winkler, R.; Fowlkes, J.; Szkudlarek, A.; Utke, I.; Rack, P. D.; Plank, H. The Nanoscale Implications of a Molecular Gas Beam during Electron Beam Induced Deposition. *ACS Appl. Mater. Interfaces* **2014**, *6* (4), 2987–2995.

(3) Winkler, R.; Szkudlarek, A.; Fowlkes, J. D.; Rack, P. D.; Utke, I.; Plank, H. Toward Ultraflat Surface Morphologies During Focused Electron Beam Induced Nanosynthesis: Disruption Origins and Compensation. *ACS Appl. Mater. Interfaces* **2015**, *7* (5), 3289–3297.

(4) Winkler, R.; Lewis, B. B. B.; Fowlkes, J. D.; Rack, P. D.; Plank, H. High-Fidelity 3D-Nanoprinting Using a Focused Electron Beam: Growth Characteristics. *ACS Nano* **2017**, *in review*.

(5) Fowlkes, J. D.; Winkler, R.; Lewis, B. B.; Stanford, M. G.; Plank, H.; Rack, P. D. Simulation-Guided 3D Nanomanufacturing via Focused Electron Beam Induced Deposition. *ACS Nano* **2016**, *10* (6), 6163–6172.

(6) Winkler, R.; Schmidt, F.-P.; Haselmann, U.; Fowlkes, J. D.; Lewis, B. B.; Kothleitner, G.; Rack, P. D.; Plank, H. Direct-Write 3D Nanoprinting of Plasmonic Structures. *ACS Appl. Mater. Interfaces* **2017**, *9* (9), 8233–8240.

(7) Geier, B.; Gspan, C.; Winkler, R.; Schmied, R.; Fowlkes, J. D.; Fitzek, H.; Rauch, S.; Rattenberger, J.; Rack, P. D.; Plank, H. Rapid and Highly Compact Purification for Focused Electron Beam Induced Deposits: A Low Temperature Approach Using Electron Stimulated H2O Reactions. *J. Phys. Chem. C* **2014**, *118* (25), 14009–14016.

(8) Orthacker, A.; Schmied, R.; Chernev, B.; Fröch, J. E.; Winkler, R.; Hobisch, J.; Trimmel, G.; Plank, H. Chemical Degradation and Morphological Instabilities during Focused Ion Beam Prototyping of Polymers. *Phys. Chem. Chem. Phys.* **2014**, *16* (4), 1658–1666.

(9) Fowlkes, J. D.; Geier, B.; Lewis, B. B.; Rack, P. D.; Stanford, M. G.; Winkler, R.; Plank, H. Electron Nanoprobe Induced Oxidation: A Simulation of Direct-Write Purification. *Phys. Chem. Chem. Phys.* **2015**, *17* (28), 18294–18304.

(10) Schmied, R.; Fowlkes, J. D.; Winkler, R.; Rack, P. D.; Plank, H. Fundamental Edge Broadening Effects during Focused Electron Beam Induced Nanosynthesis. *Beilstein J. Nanotechnol.* **2015**, *6* (1), 462–471.

(11) Béché, A.; Winkler, R.; Plank, H.; Hofer, F.; Verbeeck, J. Focus Electron Beam Induced Deposition as a Tool to Create Electron Vortices. *Micron* **2015**, *80*, 34–38.

(12) Lewis, B. B.; Winkler, R.; Sang, X.; Pudasaini, P. R.; Stanford, M. G.; Plank, H.; Unocic, R. R.; Fowlkes, J. D.; Rack, P. D. 3D Nanoprinting via Laser-Assisted Electron Beam Induced Deposition: Growth Kinetics, Enhanced Purity, and Electrical Resistivity. *Beilstein J. Nanotechnol.* **2017**, *8*, 801–812.

(13) Yang, C.; Winkler, R.; Dukic, M.; Zhao, J.; Plank, H.; Fantner, G. E. Probing the Morphology and Evolving Dynamics of 3D Printed Nanostructures Using High-Speed Atomic Force Microscopy. *ACS Appl. Mater. Interfaces* **2017**, *9* (29), 24456–24461.

(14) Keller, L.; Mamoori, M. K. I. Al; Pieper, J.; Gspan, C.; Stockem, I.; Schröder, C.; Barth, S.; Winkler, R.; Plank, H.; Pohlit, M.; Müller, J.; Huth, M. Direct-Write of Free-Form 3D Nanostructures with Controlled Magnetic Frustration. *Nat. Commun.* **2017**, *accepted*.

(15) Spencer, J. A.; Barclay, M.; Gallagher, M. J.; Winkler, R.; Unlu, I.; Wu, Y.-C.; Plank, H.; McElwee-White, L.; Fairbrother, D. H. Comparing Postdeposition Reactions of Electrons and Radicals with Pt Nanostructures Created by Focused Electron Beam Induced Deposition. *Beilstein J. Nanotechnol.* **2017**, *8*, 2410–2424.

(16) Fowlkes, J. D.; Winkler, R.; Lewis, B. B.; Fernández-Pacheco, A.; Skoric, L.; Sanz Hernandez, D.; Stanford, M.; Mutunga, E.; Rack, P. D.; Plank, H. High-Fidelity 3D-Nanoprinting Using a Focused Electron Beam: Computer-Aided Design (CAD). *ACS Appl. Nano Mater.* **2017**, *submitted*.

(17) Ganner, T.; Sattelkow, J.; Rumpf, B.; Eibinger, M.; Reishofer, D.; Winkler, R.; Nidetzky, B.; Spirk, S.; Plank, H. Direct-Write Fabrication of Cellulose Nano-Structures via Focused Electron Beam Induced Nanosynthesis. *Sci. Rep.* **2016**, *6*, 32451.

(18) van Oven, J. C.; Berwald, F.; Berggren, K. K.; Kruit, P.; Hagen, C. W. Electron-Beam-Induced Deposition of 3-Nm-Half-Pitch Patterns on Bulk Si. *J. Vac. Sci. Technol. B Microelectron. Nanom. Struct.* **2011**, *29* (6), 06F305.

(19) Peinado, P.; Sangiao, S.; Teresa, J. M. De. Focused Electron and Ion Beam Induced Deposition on Flexible and Transparent Polycarbonate Substrates. *ACS Nano* **2015**, *9* (6), 6139–6146.

(20) Schmied, R.; Fröch, J. E.; Orthacker, A.; Hobisch, J.; Trimmel, G.; Plank, H. A Combined Approach to Predict Spatial Temperature Evolution and Its Consequences during FIB Processing of Soft Matter. *Phys. Chem. Chem. Phys.* **2014**, *16* (13), 6153.

(21) Hirt, L.; Reiser, A.; Spolenak, R.; Zambelli, T. Additive Manufacturing of Metal Structures at the Micrometer Scale. *Adv. Mater.* **2017**, 1604211.

(22) Thorman, R. M.; Ragesh Kumar, T. P.; Howard Fairbrother, D.; Ingólfsson, O. The Role of Low-Energy Electrons in Focused Electron Beam Induced Deposition: Four Case Studies of Representative Precursors. *Beilstein J. Nanotechnol.* **2015**, *6* (1), 1904–1926.

(23) Arnold, G.; Timilsina, R.; Fowlkes, J. D.; Orthacker, A.; Kothleitner, G.; Rack, P. D.; Plank, H. Fundamental Resolution Limits during Electron Induced Direct Write Synthesis. *ACS Appl. Mater. Interfaces* **2014**, *6*, 7380–7387.

(24) Plank, H. Focused Electron Beam Induced Deposition: From Fundamentals towards Applications., TU Graz, 2014.

(25) Bret, T.; Utke, I.; Hoffmann, P. Influence of the Beam Scan Direction during Focused Electron Beam Induced Deposition of 3D Nanostructures. *Microelectron. Eng.* **2005**, *78*, 307–313.

(26) Friedli, V.; Utke, I. Optimized Molecule Supply from Nozzle-Based Gas Injection Systems for Focused Electron- and Ion-Beam Induced Deposition and Etching: Simulation and Experiment. *J. Phys. D. Appl. Phys.* **2009**, *42* (12), 125305.

(27) Utke, I.; Hoffmann, P.; Melngailis, J. Gas-Assisted Focused Electron Beam and Ion Beam Processing and Fabrication. *J. Vac. Sci. Technol. B Microelectron. Nanom. Struct.* **2008**, *26* (4), 1197–1276.

(28) Utke, I.; Moshkalev, S.; Russell, P. *Nanofabrication Using Focused Ion and Electron Beams: Principles and Applications*; 2012.

(29) Utke, I.; Friedli, V.; Purrucker, M.; Michler, J. Resolution in Focused Electron- and Ion-Beam Induced Processing. *J. Vac. Sci. Technol. B* **2007**, *25* (6), 2219–2223.

(30) Toth, M.; Lobo, C.; Friedli, V.; Szkudlarek, A.; Utke, I. Continuum Models of Focused Electron Beam Induced Processing. *Beilstein J. Nanotechnol.* **2015**, *6* (1), 1518–1540.

(31) Utke, I.; Moshkalev, S.; Russell, P. E. *Nanofabrication Using Focused Ion and Electron Beams: Principles and Applications.*; Utke, I., Moshkalev, S., Russell, P. E., Eds.; Oxford University Press: New York, 2012.

(32) van Dorp, W. F.; Wnuk, J. D.; Gorham, J. M.; Fairbrother, D. H.; Madey, T. E.; Hagen, C. W. Electron Induced Dissociation of Trimethyl (Methylcyclopentadienyl) Platinum (IV): Total Cross Section as a Function of Incident Electron Energy. *J. Appl. Phys.* **2009**, *106* (7), 74903.

(33) Botman, A.; de Winter, D. A. M.; Mulders, J. J. L. Electron-Beam-Induced Deposition of Platinum at Low Landing Energies. *J. Vac. Sci. Technol. B Microelectron. Nanom. Struct.* **2008**, *26* (6), 2460–2463.

(34) Reimer, L. *Scanning Electron Microscopy: Physics of Image Formation and Microanalysis*, 2nd comple.; Springer Series in Optical Sciences; Springer: Heidelberg, 1998.

(35) Moore, J. H.; Swiderek, P.; Matejcik, S.; Allan, M. Fundamentals of Interactions of Electrons with Molecules. In *Nanofabrication Using Focused Ion and Electron Beams*; Utke, I., Moshkalev, S., Russell, P., Eds.; Oxford University Press: New York, 2012; pp 184–225.

(36) Hedhili, M. N.; Bredehöft, J. H.; Swiderek, P. Electron-Induced Reactions of MeCpPtMe 3 Investigated by HREELS. *J. Phys. Chem. C* **2009**, *113* (30), 13282–13286.

(37) Warneke, J.; Van Dorp, W. F.; Rudolf, P.; Stano, M.; Papp, P.; Matejčík, Š.; Borrmann, T.; Swiderek, P. Acetone and the Precursor Ligand Acetylacetone: Distinctly Different Electron Beam Induced Decomposition? *Phys. Chem. Chem. Phys.* **2015**, *17* (2), 1204–1216.

(38) Cullen, J.; Lobo, C. J.; Ford, M. J.; Toth, M. Electron-Beam-Induced Deposition as a Technique for Analysis of Precursor Molecule Diffusion Barriers and Prefactors. *ACS Appl. Mater. Interfaces* **2015**, *7* (38), 21408–21415.

(39) Krueger, R. Dual-Column (FIB–SEM) Wafer Applications. *Micron* **1999**, *30* (3), 221–226.

(40) Liang, T.; Frendberg, E.; Lieberman, B.; Stivers, A. Advanced Photolithographic Mask Repair Using Electron Beams. *J. Vac. Sci. Technol. B Microelectron. Nanom. Struct. Process. Meas. Phenom.* **2005**, *23* (6), 3101–3105.

(41) Rangelow, I. W.; Gotszalk, T.; Grabiec, P.; Edinger, K.; Abedinov, N. Thermal Nano-Probe. *Microelectron. Eng.* **2001**, *57–58*, 737–748.

(42) Utke, I.; Hoffmann, P.; Berger, R.; Scandella, L. High-Resolution Magnetic Co Supertips Grown by a Focused Electron Beam. *Appl. Phys. Lett.* **2002**, *80* (25), 4792–4794.

(43) Lewis, B. B.; Mound, B. A.; Srijanto, B.; Fowlkes, J. D.; Pharr, G. M.; Rack, P. D. Growth and Nanomechanical Characterization of Nanoscale 3D Architectures Grown via Focused Electron Beam Induced Deposition. *Nanoscale* **2017**, *9* (42), 16349–16356.

(44) Höflich, K.; Becker, M.; Leuchs, G.; Christiansen, S. Plasmonic Dimer Antennas for Surface Enhanced Raman Scattering. *Nanotechnology* **2012**, *23* (18), 185303.

(45) Kosters, D.; De Hoogh, A.; Zeijlemaker, H.; Acar, H.; Rotenberg, N.; Kuipers, L. Core-Shell

Plasmonic Nanohelices. *ACS Photonics* **2017**, *4* (7).

(46) Utke, I.; Hoffmann, P.; Melngailis, J. Gas-Assisted Focused Electron Beam and Ion Beam Processing and Fabrication. *J. Vac. Sci. Technol. B Microelectron. Nanom. Struct.* **2008**, *26* (4), 1197.

(47) Mølhave, K.; Madsen, D. N.; Rasmussen, A. M.; Carlsson, A.; Appel, C. C.; Brorson, M.; Jacobsen, C. J. H.; Bøggild, P. Solid Gold Nanostructures Fabricated by Electron Beam Deposition. *Nano Lett.* **2003**, *3* (11), 1499–1503.

(48) Porrati, F.; Sachser, R.; Schwalb, C. H.; Frangakis, A. S.; Huth, M. Tuning the Electrical Conductivity of Pt-Containing Granular Metals by Postgrowth Electron Irradiation. *J. Appl. Phys.* **2011**, *109* (6), 063715–063717.

(49) Kolb, F.; Schmoltner, K.; Huth, M.; Hohenau, A.; Krenn, J.; Klug, A.; List, E. J. W.; Plank, H. Variable Tunneling Barriers in FEBID Based PtC Metal-Matrix Nanocomposites as a Transducing Element for Humidity Sensing. *Nanotechnology* **2013**, *24* (30), 305501.

(50) Gavagnin, M.; Wanzenboeck, H. D.; Wachter, S.; Shawrav, M. M.; Persson, A.; Gunnarsson, K.; Svedlindh, P.; Stöger-Pollach, M.; Bertagnolli, E. Free-Standing Magnetic Nanopillars for 3D Nanomagnet Logic. *ACS Appl. Mater. Interfaces* **2014**, *6* (22), 20254–20260.

(51) Gabureac, M.; Bernau, L.; Utke, I.; Boero, G. Granular Co-C Nano-Hall Sensors by Focused-Beam-Induced Deposition. *Nanotechnology* **2010**, *21* (11), 115503–115505.

(52) Gabureac, M. S.; Bernau, L.; Boero, G.; Utke, I. Single Superparamagnetic Bead Detection and Direct Tracing of Bead Position Using Novel Nanocomposite Nano-Hall Sensors. *IEEE Trans. Nanotechnol.* **2013**, *12* (5), 668–673.

(53) de Teresa, J. M.; Fernández-Pacheco, A.; Córdoba, R.; Serrano-Ramón, L.; Sangiao, M.; Ibarra, M. R. Review of Magnetic Nanostructures Grown by Focused Electron Beam Induced Deposition (FEBID). *J. Phys. D. Appl. Phys.* **2016**, *49* (24), 243003.

(54) Serrano-Ramón, L.; Córdoba, R.; Rodríguez, L. A.; Magén, C.; Snoeck, E.; Gatel, C.; Serrano, I.; Ibarra, M. R.; De Teresa, J. M. Ultrasmall Functional Ferromagnetic Nanostructures Grown by Focused Electron-Beam-Induced Deposition. *ACS Nano* **2011**, *5* (10), 7781–7787.

(55) De Teresa, J. M.; Fernández-Pacheco, A. Present and Future Applications of Magnetic Nanostructures Grown by FEBID. *Appl. Phys. A* **2014**, *117* (4), 1645–1658.

(56) Huth, M.; Porrati, F.; Schwalb, C.; Winhold, M.; Sachser, R.; Dukic, M.; Adams, J.; Fantner, G. Focused Electron Beam Induced Deposition: A Perspective. *Beilstein J. Nanotechnol.* **2012**, *3*, 597–619.

(57) Fernández-Pacheco, A.; Streubel, R.; Fruchart, O.; Fischer, P.; Cowburn, R. P.; Fern, A.; Streubel, R.; Fruchart, O.; Hertel, R.; Fischer, P. Three-Dimensional Nanomagnetism. *Nat. Commun.* **2017**, *8*, 15756.

(58) Perentes, A.; Bachmann, A.; Leutenegger, M.; Utke, I.; Sandu, C.; Hoffmann, P. Focused Electron Beam Induced Deposition of a Periodic Transparent Nano-Optic Pattern. *Microelectron. Eng.* **2004**, *73*, 412–416.

(59) Koops, H. W. P.; Hoinkis, O. E.; Honsberg, M. E. W.; Schmidt, R.; Blum, R.; Böttger, G.; Kuligk, A.; Liguda, C.; Eich, M. Two-Dimensional Photonic Crystals Produced by Additive Nanolithography with Electron Beam-Induced Deposition Act as Filters in the Infrared. *Microelectron. Eng.* **2001**,

57–*58*, 995–1001.

(60) Esposito, M.; Tasco, V.; Cuscuná, M.; Todisco, F.; Benedetti, A.; Tarantini, I.; Giorgi, M. De; Sanvitto, D.; Passaseo, A. Nanoscale 3D Chiral Plasmonic Helices with Circular Dichroism at Visible Frequencies. *ACS Photonics* **2015**, *2* (1), 105–114.

(61) Koops, H. W. P.; Kretz, J.; Rudolph, M.; Weber, M.; Dahm, G.; Lee, K. L. Characterization and Application of Materials Grown by Electron-Beam-Induced Deposition. *Jpn. J. Appl. Phys.* **1994**, *33* (Part 1, No. 12B), 7099–7107.

(62) Plank, H.; Gspan, C.; Dienstleder, M.; Kothleitner, G.; Hofer, F. The Influence of Beam Defocus on Volume Growth Rates for Electron Beam Induced Platinum Deposition. *Nanotechnology* **2008**, *19* (48), 485302.

(63) Botman, A.; Mulders, J. J. L.; Hagen, C. W. Creating Pure Nanostructures from Electron-Beam-Induced Deposition Using Purification Techniques: A Technology Perspective. *Nanotechnology* **2009**, *20* (37), 372001.

(64) Schwalb, C. H.; Grimm, C.; Baranowski, M.; Sachser, R.; Porrati, F.; Reith, H.; Das, P.; Müller, J.; Völklein, F.; Kaya, A.; Huth, M. A Tunable Strain Sensor Using Nanogranular Metals. *Sensors* **2010**, *10* (11), 9847–9856.

(65) Plank, H.; Kothleitner, G.; Hofer, F.; Michelitsch, S. G.; Gspan, C.; Hohenau, A.; Krenn, J. Optimization of Postgrowth Electron-Beam Curing for Focused Electron-Beam-Induced Pt Deposits. *J. Vac. Sci. Technol. B* **2011**, *29* (5), 51801–51807.

(66) Arnold, G.; Winkler, R.; Stermitz, M.; Orthacker, A.; Sax, S.; Klug, A.; Noh, J. H.; Fowlkes, J. D.; Rack, P. D.; Plank, H. Free-Standing Quasi-1D Resonators for Gas-Sensing Applications. *Adv. Funct. Mater.* **2017**, in review.

(67) Botman, A.; Mulders, J. J. L.; Weemaes, R.; Mentink, S. Purification of Platinum and Gold Structures after Electron-Beam-Induced Deposition. *Nanotechnology* **2006**, *17* (15), 3779–3785.

(68) Riazanova, A. V; Rikers, Y. G. M.; Mulders, J. J. L.; Belova, L. M. Pattern Shape Control for Heat Treatment Purification of Electron-Beam-Induced Deposition of Gold from the Me2Au(acac) Precursor. *Langmuir* **2012**, *28* (14), 6185–6191.

(69) Höflich, K.; Yang, R. Bin; Berger, A.; Leuchs, G.; Christiansen, S. The Direct Writing of Plasmonic Gold Nanostructures by Electron-Beam-Induced Deposition. *Adv. Mater.* **2011**, *23* (22–23), 2657–2661.

(70) Mehendale, S.; Mulders, J. J. L.; Trompenaars, P. H. F. A New Sequential EBID Process for the Creation of Pure Pt Structures from MeCpPtMe3. *Nanotechnology* **2013**, *24* (14), 145303–145307.

(71) Plank, H.; Noh, J. H.; Fowlkes, J. D.; Lester, K.; Lewis, B. B. B.; Rack, P. D. Electron-Beam-Assisted Oxygen Purification at Low Temperatures for Electron-Beam-Induced Pt Deposits: Towards Pure and High-Fidelity Nanostructures. *ACS Appl. Mater. Interfaces* **2014**, *6* (2), 1018–1024.

(72) Wnuk, J. D.; Gorham, J. M.; Rosenberg, S. G.; Madey, T. E.; Hagen, C. W.; Fairbrother, D. H. Atomic Radical Abatement of Organic Impurities from Electron Beam Deposited Metallic Structures. *J. Vac. Sci. Technol. B, Nanotechnol. Microelectron. Mater. Process. Meas. Phenom.* **2010**, *28* (3), 527–537.

(73) Roberts, N. A.; Fowlkes, J. D.; Magel, G. A.; Rack, P. D. Enhanced Material Purity and Resolution via Synchronized Laser Assisted Electron Beam Induced Deposition of Platinum. *Nanoscale* **2013**, *5* (1), 408–415.

(74) Stanford, M. G.; Lewis, B. B.; Noh, J. H.; Fowlkes, J. D.; Roberts, N. A.; Plank, H.; Rack, P. D. Purification of Nanoscale Electron-Beam-Induced Platinum Deposits via a Pulsed Laser-Induced Oxidation Reaction. *ACS Appl. Mater. Interfaces* **2014**, *6* (23), 21256–21263.

(75) Lewis, B. B.; Stanford, M. G.; Fowlkes, J. D.; Lester, K.; Plank, H.; Rack, P. D.; Huth, M.; Gölzhäuser, A. Electron-Stimulated Purification of Platinum Nanostructures Grown via Focused Electron Beam Induced Deposition. *Beilstein J. Nanotechnol.* **2015**, *6*, 1883–1885.

(76) Pablo-Navarro, J.; Magén, C.; de Teresa, J. M. Three-Dimensional Core–shell Ferromagnetic Nanowires Grown by Focused Electron Beam Induced Deposition. *Nanotechnology* **2016**, *27* (28), 285302.

(77) Pablo-Navarro, J.; Sanz-Hernández, D.; Magén, C.; Fernández-Pacheco, A.; De Teresa, J. M. J. M. Tuning Shape, Composition and Magnetization of 3D Cobalt Nanowires Grown by Focused Electron Beam Induced Deposition (FEBID). *J. Phys. D. Appl. Phys.* **2017**, *50* (18), 18LT01.

(78) Córdoba, R.; Sharma, N.; Kölling, S.; Koenraad, P. M.; Koopmans, B. High-Purity 3D Nano-Objects Grown by Focused-Electron-Beam Induced Deposition. *Nanotechnology* **2016**, *27* (35), 355301.

(79) Hao, T.; Shen, T. H.; Li, W.; Song, C.; Xu, Z.; Jin, A.; Jin, L.; Li, J.; Bai, X. Platinum Composite Nanowires for Ultrasensitive Mass Detection. **2017**, *143102* (110).

(80) Burbridge, D. J.; Gordeev, S. N. Proximity Effects in Free-Standing EBID Structures. *Nanotechnology* **2009**, *20* (28), 285308.

(81) Plank, H.; Haber, T.; Gspan, C.; Kothleitner, G.; Hofer, F. Chemical Tuning of PtC Nanostructures Fabricated via Focused Electron Beam Induced Deposition. *Nanotechnology* **2013**, *24* (17), 175305–175308.

(82) Belić, D.; Shawrav, M. M.; Gavagnin, M.; Stöger-Pollach, M.; Wanzenboeck, H. D.; Bertagnolli, E. Direct-Write Deposition and Focused-Electron-Beam-Induced Purification of Gold Nanostructures. *ACS Appl. Mater. Interfaces* **2015**, *7* (4), 2467–2479.

(83) Bret, T.; Utke, I.; Bachmann, A.; Hoffmann, P. In Situ Control of the Focused-Electron-Beam-Induced Deposition Process. *Appl. Phys. Lett.* **2003**, *83* (19), 4005–4007.

(84) Koops, H. W. P. Constructive Three-Dimensional Lithography with Electron-Beam Induced Deposition for Quantum Effect Devices. *J. Vac. Sci. Technol. B Microelectron. Nanom. Struct.* **1993**, *11* (6), 2386.

(85) Van Dorp, W. F.; Hagen, C. W. A Critical Literature Review of Focused Electron Beam Induced Deposition. *J. Appl. Phys.* **2008**, *104* (8), 81301–81342.

(86) Gazzadi, G. C.; Frabboni, S.; Menozzi, C. Suspended Nanostructures Grown by Electron Beam-Induced Deposition of Pt and TEOS Precursors. *Nanotechnology* **2007**, *18* (44), 445709.

(87) Ishida, J. F.; Ichihashi, T.; Matsui, Y. O. K. Carbon Nanopillar Laterally Grown with Electron Beam-Induced Chemical Vapor Deposition Carbon Nanopillar Laterally Grown with Electron Beam-Induced Chemical Vapor Deposition. **2003**, *2990*.

(88) Kislov, N. A. Direct STEM Fabrication and Characterization of Self-Supporting Carbon Structures for Nanoelectronics. *Scanning* **1993**, *15* (4), 212–218.

(89) Aristov, V. V; Kasumov, A. Y.; Kislov, N. A.; Kononenko, O. V; Matveev, V. N.; Tulin, V. A.; Khodos, I. I.; Gorbatov, Y. A.; Nikolaichik, V. I. A New Approach to Fabrication of Nanostructures. *Nanotechnology* **1995**, *6* (2), 35–39.

(90) Jesse, S.; He, Q.; Lupini, A. R.; Leonard, D. N.; Oxley, M. P.; Ovchinnikov, O.; Unocic, R. R.; Tselev, A.; Fuentes-Cabrera, M.; Sumpter, B. G.; Pennycook, S. J.; Kalinin, S. V.; Borisevich, A. Y. Atomic-Level Sculpting of Crystalline Oxides: Toward Bulk Nanofabrication with Single Atomic Plane Precision. *Small* **2015**, *11* (44), 5895–5900.

(91) Igaki, J.; Kanda, K.; Haruyama, Y.; Ishida, M.; Ochiai, Y.; Fujita, J.; Kaito, T.; Matsui, S. Comparison of FIB-CVD and EB-CVD Growth Characteristics. *Microelectron. Eng.* **2006**, *83* (4–9), 1225–1228.

(92) Kometani, R.; Ishihara, S. Nanoelectromechanical Device Fabrications by 3-D Nanotechnology Using Focused-Ion Beams. *Sci. Technol. Adv. Mater.* **2009**, *10* (3), 34501.

(93) Guo, D.; Kometani, R.; Warisawa, S.; Ishihara, S. Three-Dimensional Nanostructure Fabrication by Controlling Downward Growth on Focused-Ion-Beam Chemical Vapor Deposition. *Jpn. J. Appl. Phys.* **2012**, *51* (6 PART 1), 65001.

(94) Guo, D.; Warisawa, S.; Ishihara, S.; Kometani, R. Mechanical Characteristics of Ultra-Long Horizontal Nanocantilevers Grown by Real-Time Feedback Control on Focused-Ion-Beam Chemical Vapour Deposition. *J. Micromechanics Microengineering* **2015**, *25* (12), 125028.

(95) Guo, D.; Kometani, R.; Warisawa, S.; Ishihara, S. Growth of Ultra-Long Free-Space-Nanowire by the Real-Time Feedback Control of the Scanning Speed on Focused-Ion-Beam Chemical Vapor Deposition. *J. Vac. Sci. Technol. B Microelectron. Nanom. Struct.* **2013**, *31* (6), 61601.

(96) Li, W.; Gu, C.; Cui, A.; Fenton, J. C.; Jiang, Q.; Warburton, P. A.; Shen, T. H. Three-Dimensional Nanostructures by Focused Ion Beam Techniques: Fabrication and Characterization. *J. Mater. Res.* **2013**, *28* (22), 3063–3078.

(97) Utke, I.; Luisier, A.; Hoffmann, P.; Laub, D.; Buffat, P. A. Focused-Electron-Beam-Induced Deposition of Freestanding Threedimensional Nanostructures of Pure Coalesced Copper Crystals. *Appl. Phys. Lett.* **2002**, *81* (17), 3245–3247.

(98) Luisier, A.; Utke, I.; Bret, T.; Cicoira, F.; Hauert, R.; Rhee, S.-W.; Doppelt, P.; Hoffmann, P. Comparative Study of Cu Precursors for 3D Focused Electron Beam Induced Deposition. *J. Electrochem. Soc.* **2004**, *151* (8), C535.

(99) Bret, T.; Utke, I.; Gaillard, C.; Hoffmann, P. Periodic Structure Formation by Focused Electron-Beam-Induced Deposition. *J. Vac. Sci. Technol. B Microelectron. Nanom. Struct.* **2004**, *22* (5), 2504.

(100) Okada, S.; Mukawa, T.; Kobayashi, R.; Fujita, J.; Ishida, M.; Ichihashi, T.; Ochiai, Y.; Kaito, T.; Matsui, S. Growth Manner and Mechanical Characteristics of Amorphous Carbon Nanopillars Grown by Electron-Beam-Induced Chemical Vapor Deposition. *Jpn. J. Appl. Phys.* **2005**, *44* (7B), 5646–5650.

(101) Frabboni, S.; Gazzadi, G. C.; Felisari, L.; Spessot, A. Fabrication by Electron Beam Induced Deposition and Transmission Electron Microscopic Characterization of Sub-10-Nm Freestanding Pt Nanowires. *Appl. Phys. Lett.* **2006**, *88* (21), 213113–213116.

(102) Frabboni, S.; Gazzadi, G. C.; Spessot, A. Transmission Electron Microscopy Characterization and Sculpting of Sub-1 Nm Si-O-C Freestanding Nanowires Grown by Electron Beam Induced Deposition. *Appl. Phys. Lett.* **2006**, *89* (11), 1–4.

(103) Gazzadi, G. C.; Frabboni, S. Structural Evolution and Graphitization of Metallorganic-Pt Suspended Nanowires under High-Current-Density Electrical Test. *Appl. Phys. Lett.* **2009**, *94* (17).

(104) Gazzadi, G. C.; Frabboni, S. Structural Transitions in Electron Beam Deposited Co-Carbonyl Suspended Nanowires at High Electrical Current Densities. *Beilstein J. Nanotechnol.* **2015**, *6* (1), 1298–1305.

(105) Gazzadi, G. C.; Frabboni, S.; Menozzi, C. Suspended Nanostructures Grown by Electron Beam-Induced Deposition of Pt and TEOS Precursors. *Nanotechnology* **2007**, *18* (44), 445709.

(106) Utke, I.; Luisier, A.; Hoffmann, P.; Laub, D.; Buffat, P. A. Focused-Electron-Beam-Induced Deposition of Freestanding Three-Dimensional Nanostructures of Pure Coalesced Copper Crystals. *Appl. Phys. Lett.* **2002**, *81* (17), 3245–3247.

(107) Bret, T.; Utke, I.; Hoffmann, P. Influence of the Beam Scan Direction during Focused Electron Beam Induced Deposition of 3D Nanostructures. *Microelectron. Eng.* **2005**, *78–79*, 307–313.

(108) Bret, T.; Utke, I.; Hoffmann, P.; Abourida, M.; Doppelt, P. Electron Range Effects in Focused Electron Beam Induced Deposition of 3D Nanostructures. *Microelectron. Eng.* **2006**, *83* (4–9), 1482–1486.

(109) Ueda, K.; Yoshimura, M. Fabrication of Nanofigures by Focused Electron Beam-Induced Deposition. *Thin Solid Films* **2004**, *464*, 331–334.

(110) Koops, H. W. P. Constructive Three-Dimensional Lithography with Electron-Beam Induced Deposition for Quantum Effect Devices. *J. Vac. Sci. Technol. B Microelectron. Nanom. Struct.* **1993**, *11* (6), 2386.

(111) Höflich, K.; Yang, R. Bin; Berger, A.; Leuchs, G.; Christiansen, S. The Direct Writing of Plasmonic Gold Nanostructures by Electron-Beam-Induced Deposition. *Adv. Mater.* **2011**, *23* (22–23), 2657–2661.

(112) Fernández-Pacheco, A.; Serrano-Ramón, L.; Michalik, J. M.; Ibarra, M. R.; De Teresa, J. M.; O'Brien, L.; Petit, D.; Lee, J.; Cowburn, R. P. Three Dimensional Magnetic Nanowires Grown by Focused Electron-Beam Induced Deposition. *Sci. Rep.* **2013**, *3*, 1492–1495.

(113) Kretz, J.; Rudolph, M.; Weber, M.; Koops, H. W. P. Three-Dimensional Structurization by Additive Lithography, Analysis of Deposits Using TEM and EDX, and Application to Field-Emitter Tips. *Microelectron. Eng.* **1994**, *23* (1–4), 477–481.

(114) Edinger, K.; Gotszalk, T.; Rangelow, I. W. Novel High Resolution Scanning Thermal Probe. *J. Vac. Sci. Technol. B* **2001**, *19* (6), 2856–2860.

(115) Koops, H. W. P.; Kaya, A.; Weber, M. Fabrication and Characterization of Platinum Nanocrystalline Material Grown by Electron-beam Induced Deposition. *J. Vac. Sci. Technol. B Microelectron. Nanom. Struct. Process. Meas. Phenom.* **1995**, *13* (6), 2400–2403.

(116) Lau, Y. M.; Chee, P. C.; Thong, T. L.; Ng, V. Properties and Applications of Cobalt-Based Material Produced by Electron-Beam-Induced Deposition. *J. Vac. Sci. Technol. A* **2002**, *20*, 1295–1302.

(117) Fujita, J.; Ishida, M.; Ichihashi, T.; Ochiai, Y.; Kaito, T.; Matsui, S. Carbon Nanopillar Laterally Grown with Electron Beam-Induced Chemical Vapor Deposition. *J. Vac. Sci. Technol. B* **2003**, *21*, 2990–2993.

(118) Takeguchi, M.; Shimojo, M.; Furuya, K. Fabrication of Magnetic Nanostructures Using Electron

Beam Induced Chemical Vapour Deposition. *Nanotechnology* **2005**, *16*, 1321–1325.

(119) Plank, H.; Smith, D. A.; Haber, T.; Rack, P. D.; Hofer, F.; Proximity, F.; Electron, F.; Induced, B. Fundamental Proximity Effects in Focused Electron Beam Induced Deposition. *ACS Nano* **2012**, *6* (1), 286–294.

(120) Shawrav, M. M.; Taus, P.; Wanzenboeck, H. D.; Schinnerl, M.; Stöger-Pollach, M.; Schwarz, S.; Steiger-Thirsfeld, A.; Bertagnolli, E. Highly Conductive and Pure Gold Nanostructures Grown by Electron Beam Induced Deposition. *Sci. Rep.* **2016**, *6* (1), 34003.

(121) Bret, T.; Utke, I.; Bachmann, A.; Hoffmann, P. In Situ Control of the Focused-Electron-Beam-Induced Deposition Process. *Appl. Phys. Lett.* **2003**, *83* (19), 4005–4007.

6 APPENDIX

6.1 APPENDIX 1 - PUBLICATION 1

Publication 1

Spatial Chemistry Evolution during Focused Electron Beam-Induced Deposition: Origins and Workarounds.

Winkler, R.; Geier, B.; Plank, H.

Appl. Phys. A Mater. Sci. Process. (invited) **2014**, *117* (4), 1675–1688.

Appl. Phys. A (2014) 117:1675–1688
DOI 10.1007/s00339-014-8496-y

Applied Physics A
Materials Science & Processing

Spatial chemistry evolution during focused electron beam-induced deposition: origins and workarounds

Robert Winkler · Barbara Geier · Harald Plank

Received: 28 April 2014 / Accepted: 4 May 2014 / Published online: 28 May 2014
© Springer-Verlag Berlin Heidelberg 2014

Abstract The successful application of functional nanostructures, fabricated via focused electron-beam-induced deposition (FEBID), is known to depend crucially on its chemistry as FEBID tends to strong incorporation of carbon. Hence, it is essential to understand the underlying mechanisms which finally determine the elemental composition after fabrication. In this study we focus on these processes from a fundamental point of view by means of (1) varying electron emission on the deposit surface; and (2) changing replenishment mechanism, both driven by the growing deposit itself. First, we revisit previous results concerning chemical variations in nanopillars (with a quasi-1D footprint) depending on the process parameters. In a second step we expand the investigations to deposits with a 3D footprint which are more relevant in the context of applications. Then, we demonstrate how technical setups and directional gas fluxes influence final chemistries. Finally, we put the findings in a bigger context with respect to functionalities which demonstrates the crucial importance of carefully set up fabrication processes to achieve controllable, predictable and reproducible chemistries for FEBID deposits as a key element for industrially oriented applications.

R. Winkler · B. Geier · H. Plank (✉)
Graz Centre for Electron Microscopy, Steyrergasse 17, 8010 Graz, Austria
e-mail: harald.plank@felmi-zfe.at

H. Plank
Institute for Electron Microscopy and Nanoanalysis, Graz University of Technology, 8010 Graz, Austria

1 Introduction

During the past decade focused electron-beam-induced deposition (FEBID) has attracted increasing attention due to its capability to fabricate functional nanostructures with sub-10 nm spatial resolution [1–4]. Furthermore, FEBID allows fabrication on even non-flat surfaces without any pre- or post-processing steps giving this technique a direct-write character as one of the major advantages compared to classical lithographic structuring methods. FEBID is based on the electron-induced, local decomposition of gaseous precursor molecules which are injected into the vacuum chamber of scanning electron or dual-beam microscopes via a localized gas injection system (GIS) [1]. More specifically, the precursor molecules adsorb and diffuse on the surface for a typical residence time after which the again desorb from the surface if they are not dissociated via appropriate electron species. The balance between precursor molecules on the surface and available electrons, denoted as precursor working regime, can influence growth rates, deposit shapes and the deposit chemistry [1–3, 5–7]. Based on the precursor chemistry a variety of functionalities can be achieved ranging from insulating, semi-conducting and conductive towards magnetic [8]. After a period of more fundamentally oriented investigation, a diverse range of applications has been demonstrated during the past years such as magnetic storage or sensing [9–13], nanooptics [14, 15], (nano)lithography [16, 17], lithography-mask repair [18–20], atomic-layer-deposition seeding [21], stress–strain nanosensors [22, 23], nanoscale gas sensors [24] and others [10–13]. One of the main issues for FEBID applications, however, are chemical impurities as electron-induced depositions typically suffer from severe carbon contents up to 90 at.%, often reducing or even masking the intended functionalities [1, 8, 22–24]. Hence,

in context of applications, these impurities can be the knock-out criteria since defined, predictable and reproducible chemistries are not only a benefit but absolutely necessary for industrial oriented applications. A straightforward solution is the application of precursor allowing pure deposits such as carbon-free precursor or ideally dissociating molecules [25–28]. Although a few examples of pure materials after deposition have been demonstrated [29, 30] most efforts have focused on additional in situ and/or post-growth purification processes including: fabrication on hot substrates [31, 32], co-flow with reactive gases [33], synchronized laser assisted FEBID [34, 35], or other in-situ/ex-situ processes [9, 36–43]. Latest breakthroughs use e-beam assisted post-growth treatments together with room temperature H_2O vapour which allow entire carbon removal at very high purification rates of better than 5 min nA^{-1} μm^{-2} [44]. This approach is furthermore capable of maintaining the original footprint (minimal lateral shrinking) of even 3D surface features which is absolutely essential considering high-performance FEBID devices on the lower nanoscale. From these developments it can be concluded that highly pure, FEBID-based nano-deposits can be achieved via post-growth treatments and the problem seems to be solved. At this point, however, the authors would like to draw the attention to the very special internal structure of FEBID deposits: typically, such structures show a metal-matrix composition consisting of nano-sized metal grains (1–5 nm) which are homogeneously embedded in an insulating (hydro)carbon matrix [1, 3, 6–8, 23, 24, 40, 41]. Although often considered as highly unwanted in the FEBID community many other research fields put much effort into the fabrication of such composites. Some FEBID activities already used these special properties as advantage by means of tunable metals [22–24, 38, 39, 41] for fundamental physics or as nano-sized gas sensors where the carbon matrix acts as variable tunnelling barrier to detect adsorbed species [24]. Furthermore, current activities of the authors comprise this special metal-matrix structure to achieve tunable mechanical properties of electrodynamically driven (nano)sensor concepts [45]. For such applications, as well as for situations in which the above-mentioned post-growth purification cannot be applied, it is crucial to understand the evolving chemistry depending on the process parameters from a fundamental point of view. Furthermore, only little attention has been placed on the spatial evolution of the chemistry during growth which is expected to vary based on the complex interplay between available surface electrons and precursor molecules.

In this article, we focus, therefore, on the spatial chemistry distribution in FEBID deposits using ($MeCpPt^{IV}Me_3$) precursor as test vehicle to demonstrate possible effects. In more detail, this study first summarizes previous findings of the authors concerning chemical variations in nanopillars with a quasi-1D footprint [7]. Based on these results we then expand the investigations to micrometer-sized 3D footprints and demonstrate how the chemistry vertically varies within the first 200 nm height growth. Next we provide a systematic parameter variation including beam current, beam energy, dwell times and patterning strategies which allow to attribute varying chemistries mainly to (1) the increasing number of electrons on the surface caused by the traversing interaction volume from the substrate to the deposit; and (2) decreasing surface coverage by means of diffusive replenishment from surrounding areas as the growing deposit represents a dynamically increasing morphological barrier. Finally, the results are put in context to the functionality of Pt based deposits derived from previous studies [22–24, 38, 39, 41]. This will demonstrate that the varying chemistry can entail an electrical resistivity variation up to one order of magnitude within the first 100 nm. The study is complemented by a comprehensive discussion of all results revisited and presented here involving counteracting strategies for more constant spatial distribution of chemistries/functionalities during deposition. The study spans from fundamental considerations determining final chemistries towards applicable workarounds providing more homogeneous functionalities in all three deposit dimensions as a crucial element towards more defined, predictable and reproducible properties. As this article is a semi-review on previous results but also presents new findings, we conclude each section individually for more clarity. A final discussion section is then given to put the found results in a bigger context for combination of previous and new findings.

2 Morphology-induced chemical variations

In the following we focus on spatial chemistry variations of Pt based FEBID deposits depending on its geometry and the process parameters used. As we will show the growing deposit itself is responsible for the chemical variation as it can be considered as dynamically changing morphological barrier. The consequence is a variation of surface diffusion-related replenishment (SDR) components which shifts the precursor working regime. As a result the chemistry also changed which demonstrates the importance of careful parameter setup including patterning alignment to achieve spatially homogeneous and predictable chemistries.

In the following we start with nanopillars, exhibiting a quasi-1D footprint, to demonstrate the regime shifts and its chemical consequences. Subsequently, we expand the considerations to more complex deposits with three-dimensional footprints and derive the correlation between

working regime and the growing deposit in a more general way. Finally, we discuss the findings in the context of functionality on Platinum-based FEBID deposits.

2.1 Quasi-1D

As starting point, the chemical composition of $MeCpPt^{IV}Me_3$ based quasi-1D nanopillars is re-visited, discussed in detail by Plank et al. [7]. The main essence of the study is (1) varying chemistry during vertical pillar growth, (2) strong chemical variations depending on the main process parameters beam current, dwell time, replenishment time and (3) the existence of two types of carbon matrices mainly consisting of incompletely dissociated precursor molecules or polymerized carbon fragments stemming from precursor fragments and chamber residue [7, 41].

As presented in Fig. 1a, the volume growth rate (VGR) shows an initial increase caused by the traversing interaction volume from the substrate into the Pt–C nanopillar. As the densities are strongly different (1.74 → 7.96 g/cm^3 for SiO_2 and PtC_5, respectively) the according interaction volume is considerably reduced within the deposit [46, 50, 52]. The consequence is a stronger areal reemission of all electron species, namely back-scattered-electrons (BSE), forward-scattered-electrons (FSE) and secondary electrons type-I [SE-I, primary electron (PE) related], type-II (SE-II, BSE related) and type-III (SE-III, FSE related). This in turn leads to increasing dissociation rates which explain the initial VGR increase. In order to simplify further discussions we collectively denote reemitted electrons as surface electrons. Once the interaction volume is entirely within the quasi-1D Pt–C nanopillar the total emission of surface electrons is widely constant which seems to be in contradiction with the subsequent VGR decay in Fig. 1a. At this point we need to consider the precursor working regime. Local replenishment of precursor molecules basically occurs via two processes: (1) gas flux-related replenishment (GFR) by means of direct adsorption from the gas phase; and (2) SDR from the surrounding regions. As it will be important for discussions later, we further split the latter into SDR components from (i) the substrate (SDR-S); and (ii) from deposit regions (SDR-D) which is closely related to the GFR component at respective areas. As the quasi-1D nanopillar grows, GFR is practically constant for all heights while SDR-S contributions are strongly decaying. This is the consequence of the very narrow pathway from the substrate to the pillar tip (<100 nm in diameter but several microns long) together with the comparable short mean free path of about 25 nm [1, 47]. Therefore, the replenishment mechanism for a growing nanopillar changes from GFR + SDR at the beginning towards GFR (including low SDR-D contributions). This explains the decaying VGR Fig. 1a as well as the saturating and non-

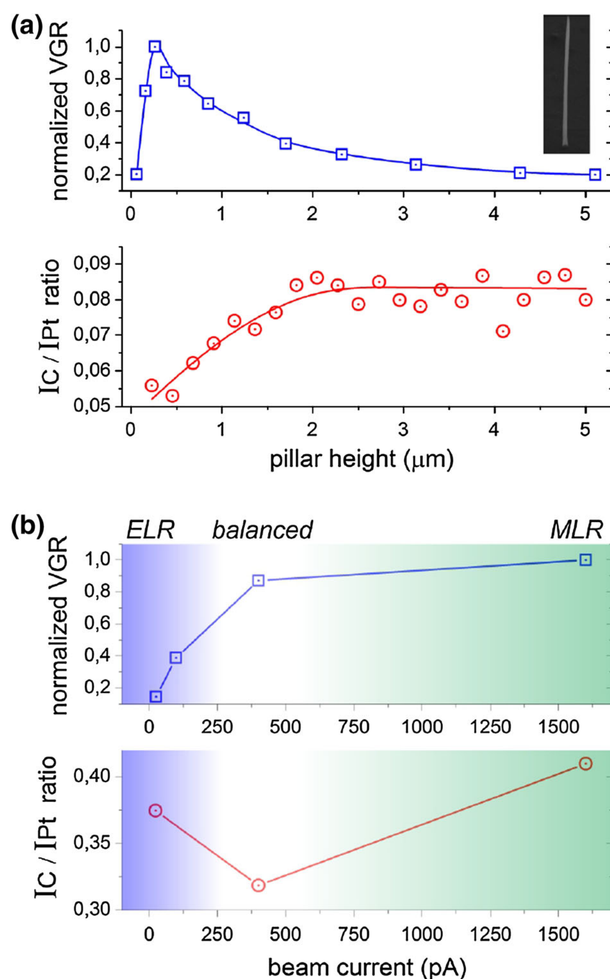

Fig. 1 **a** Normalized vertical volume growth rate (VGR, *upper panel*) for a nanopillar fabricated at 5 keV, 98 pA, 100 µs DT and 100 µs refresh time in between subsequent beam pulses. The *small inset* gives a SEM side view image. The *lower panel* gives the intensity ratio I_C/I_{Pt} determined by STEM EELS measurements visualizing the chemical evolution during pillar growth. **b** correlated VGR and I_C/I_{Pt} variation (taken at a pillar height of 2.7 µm) during a beam current sweep while DT and refresh time were kept constant [7]

zero VGR for high pillar which has also been predicted via simulations in the past [6, 7, 56]. This transition can also be understood as shift towards more molecule-limited regime (MLR) conditions describing a lack of precursor molecules compared to available surface electrons. As a consequence, the local chemistry is affected similar to the VGR as shown in Fig. 1a (lower panel) by C/Pt intensity ratios accessed via scanning transmission electron microscopy based electron energy loss spectroscopy (STEM-EELS) as discussed in detail by Plank et al [7]. The essential result, however, is that the carbon content increases due to reduced precursor coverage. The study comprised then a systematic parameter variation performed at pillar heights predominantly replenished via GFR components. It was found that lowest carbon contents can be achieved neither

for strong molecule limited (MLR) nor for strong electron limited regimes (ELR) as representatively shown for a beam current sweep in Fig. 1b (bottom). Lowest carbon contents are always found for regime conditions in between ELR and MLR where an ideal balance between surface electrons and precursor coverage is established (see indications of Fig. 1b). Lack of electrons (ELR) leads to a high number of incompletely dissociated precursor molecules while an excess of electrons (MLR) polymerizes precursor fragments and possible chamber residue. Hence, both extremes lead to an increased carbon content, however, due to different reasons which also affect the functionality of the deposit as will be shown later. As a more practical result of this study it was found that the balanced situation can roughly be identified via the VGR behaviour revealing strongest curvature in the respective parameter range (compare upper and lower panel in Fig. 1b and also Plank et al [7] for full-parameter investigation). As essence it can be concluded that lowest carbon contents are found for a balanced precursor working regime in between ELR and MLR conditions. The existence of two different carbon types in the matrices is also important for the discussion later.

2.2 3D

In a second step we expand our investigations to more relevant deposits with a 3-dimensional footprint. We start the discussion with the vertical evolution of deposit chemistries and investigate then the influence of process parameters which influence the precursor working regime. Afterwards, we focus on the influence of patterning strategies which will turn out as important parameter often considered as less significant in the past. Finally, we connect the chemical variations to the deposit functionalities which will reveal how strong the properties can change during growth of the first 200 nm.

2.2.1 Vertical chemistry evolution

For further experiments we increased the deposit footprint from quasi-1D (ϕ <100 nm) to a micrometer-sized 3D footprint (4 × 4 μm^2) keeping in mind the (1) traversing interaction volume from the substrate into the Pt–C deposit followed by (2) decreasing precursor coverage on deposit surfaces due to more complicated diffusive replenishment from the surrounding substrate (SDR-S) as the growing deposit represents a morphological barrier. Figure 2a shows the atomic force microscopy (AFM) based VGR evolution (blue squares, left axis) for FEBID deposits fabricated at 5 keV, 400 pA with 13 nm pixel point pitch (further denoted as PoP), 50 µs dwell time (DT) and a serpentine patterning strategy (SP). Figure 2b gives the according chemical

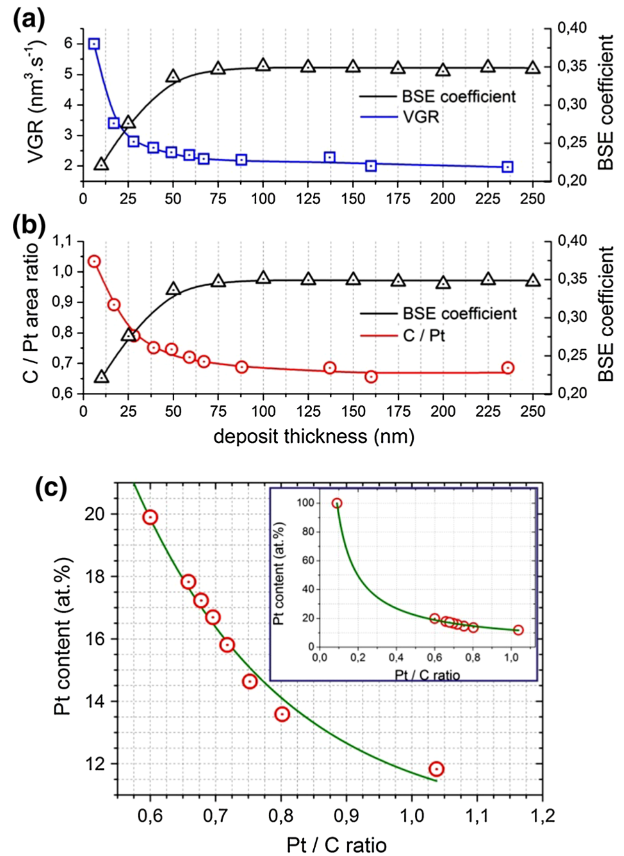

Fig. 2 Vertical evolution of volume growth rate VGR (**a**) and EDXS-based C/Pt area ratios (**b**) together with Monte-Carlo based BSE yield variation (*black triangles* in **a** and **b**) during growth of a Pt–C deposit fabricated at 5 keV, 400 pA, 50 µs DT, 13 nm PoP via serpentine patterning. **c** correlation between EDXS-based C/Pt area ratios and ZAF corrected quantification on sufficiently thick Pt deposits fabricated at different process parameters. The *inset* gives the overview towards pure Pt at C/Pt values of 0.08

analyses via energy dispersive X-ray spectroscopy (EDXS). As absolute quantification is complicated for thin layers [46] we follow an approach introduced by Mehendale et al. [42] and further used by Plank et al. [43], and Geier et al. [44] by monitoring the areal peak ratio C/Pt (see also methodology). While as-deposited FEBID Pt–C structures typically give C/Pt ratios between 0.6 and 2 (depending on the exact chemistry) pure Pt shows a ratio of 0.08 as the Pt N-peak overlaps with the C–K peak [42–44]. Nevertheless, to estimate the absolute Pt contents we have performed ZAF corrected quantification [46] on sufficiently thick FEBID deposits fabricated at strongly different parameters. The correlation between Pt contents and C/Pt ratios is shown in Fig. 2c for the relevant range in this study while the inset shows the entire range up to pure Pt. According curve fitting gives a correlation function of $c_{Pt} = 12.04 \times r_{C/Pt}^{-0.879}$ with the Pt concentration c_{Pt} in at.% and the C/Pt ratio $r_{C/Pt}$ determined via EDXS based areal ratios. As shown by red circles

in Fig. 2b, the C/Pt ratio is around 1.05 (~ 12 ± 1 at.% Pt) at the beginning followed by a quick decrease towards a stable value around 0.65 (18 ± 1 at.% Pt) after the first 100 nm growth. In a general picture, this decreasing carbon content can be explained by more ELR conditions at the beginning leading to incorporation of incompletely dissociated precursor molecules as discussed in the quasi-1D section [7]. As the interaction volume traverses from the substrate into the deposit, the number of surface electrons increases due to the smaller interaction volume. To investigate this effect in more detail, we have conducted Monte Carlo simulations (CASINO [48]) assuming differently thick Pt–C layers on the substrate with respective chemistries found via EDXS. The key parameter is the thickness dependent BSE yield which is overlaid in Fig. 2a and b by black triangles. Please note, as the cross section for the used Pt precursor molecule is known to be highest for low energies [1–3, 5, 7, 49–58], we expect PE-related SE-I and more importantly BSE-related SE-II as predominant electron species during dissociation as described by van Dorp et al. and Arnold et al. recently [1, 3, 57, 58]. As can be seen the BSE yield initially increases and saturates around 100 nm deposit thickness meaning a widely constant number of surface electrons for thicknesses above. The initial BSE increase is also in agreement with the general interpretation of a regime shift as the enhanced number of surface electrons leads to improved dissociation and by that to lower carbon contents (see Fig. 2b). Concerning the replenishment situation we consider the general VGR decrease at early growth stages (Fig. 2a) which reflects a decreasing surface coverage once the deposit starts growing as it acts as morphological barrier. For thicknesses above 100 nm, the number of surface electrons is widely stable and the replenishment is a combination of SDR-S, SDR-D and GFR components. Together with the fact of a decreasing carbon content (Fig. 2b) these results strongly support the assumption of more ELR conditions at the beginning followed by a regime shift towards more balanced electron-to-precursor ratios. Hence, it can be concluded that the chemistry is always affected by (1) the increasing number of surface electrons and further influenced by (2) decreasing replenishment components due to the growing deposit itself which acts as morphological barrier. The main aspect of these experiments, however, is that the chemistry considerably changes within the first 100 nm (up to 7 at.%) which affects (1) predictable overall chemistries for different deposit thicknesses and more importantly, (2) final functionalities which will be discussed later.

2.2.2 *Process parameters*

Reconsidering Fig. 1c, it is obvious that the chemical composition of quasi-1D structures strongly depend on the

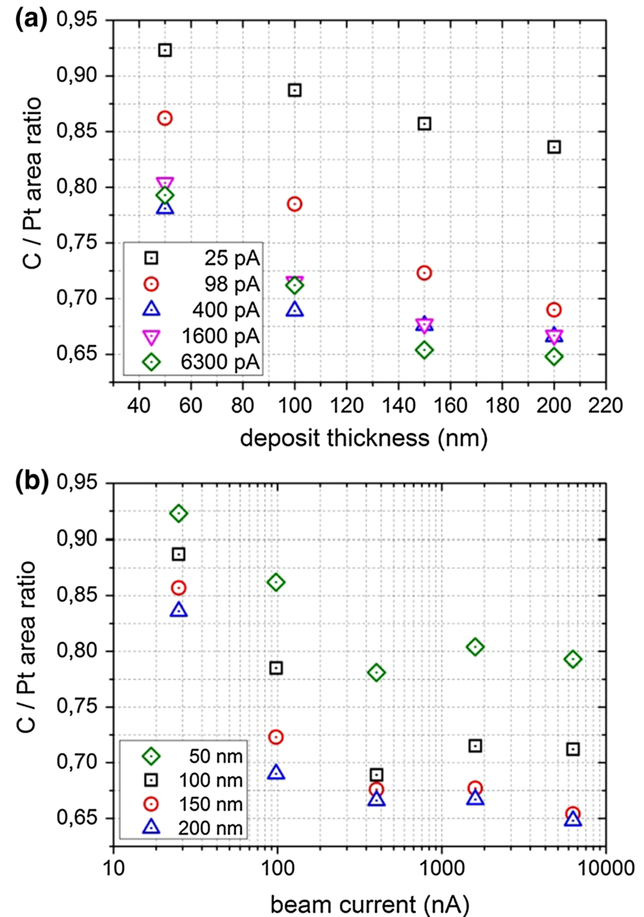

Fig. 3 C/Pt ratios versus deposit thickness (**a**) and beam currents (**b**) for 5 keV, 50 µs DT, 13 nm PoP and serpentine patterning strategies

used beam currents and lowest carbon contents are found for intermediate ranges. To investigate whether this observation also holds for deposits with 3D footprints, the chemical evolution is investigated depending on applied beam currents (25 → 6,300 pA) for different deposit heights (50 → 200 nm). To provide comparability, PoPs (13 nm), DTs (50 µs), primary energies (5 keV) and SP were kept constant. The results are summarized in Fig. 3a depending on the deposit thicknesses for different beam currents (see legend). Lowest beam currents of 25 pA (black squares) reveal generally the highest carbon contents as expected (more ELR like conditions) but show a continuous decay behaviour even for thicknesses above 100 nm where the number of surface electrons is widely constant (black triangles in Fig. 2). Hence, this detail directly reflects the decreasing surface coverage due to decreasing diffusive replenishment from the surrounding substrate (SDR-S) caused by the dynamically growing morphological barrier. The result is a decreasing number of precursor molecules at constant surface electron densities

which is equal to a regime shift towards more balanced electron-to-precursor ratios leading to decreasing carbon contents. On the other hand, GFR and SDR-D components are widely constant due to the comparable large footprints of 4 × 4 μm^2 which increasingly dominate the local replenishment rate relevant for further growth.

In contrast, very high beam currents already start with improved dissociation reflected by generally lower C/Pt ratios in Fig. 3a. During growth, the carbon content is further reduced up to a thickness of about 140 nm (see e.g. 6,300 pA beam current) followed by widely stable C/Pt ratios in agreement with the stable electron yield for higher thicknesses. The latter two details, however, strongly suggest a transition towards more MLR conditions as sufficient electrons are available for high dissociation degrees. To visualize the current dependency in more detail the same plot is given as function of the beam current for different thicknesses (Fig. 3b). As can be seen for beam currents of 400 pA and higher the according C/Pt ratios start to saturate widely independently on the respective thickness. This suggests that for beam currents of 400 pA or higher a sufficient number of electrons are available to achieve highest dissociation degree reflected by lowest C/Pt ratios.

As discussed for the quasi-1D nanopillars, increasing beam currents first lead to decreasing carbon contents in agreement with the findings for 3D footprint deposits based on the more balanced electron-to-precursor situation. For highest beam currents, quasi-1D nanopillars show again increasing carbon contents attributed to a strong excess of electrons leading to polymerization of precursor fragments and possible chamber residue. However, this behaviour is not found for the 3D as can be seen in Fig. 3b. To investigate this absence of an again increasing carbon content in more detail we have performed single pass dwell time sweeps ranging from 20 to 1,000 µs at high beam currents of 1,600 pA while primary energies (5 keV), PoPs (13 nm) and SP have been kept identical. Please note, higher currents and longer dwell times both result in a pad lift-off from the surface and are, therefore, not relevant. As shown in Fig. 4a the C/Pt composition strongly decreases from 1.38 to 0.78 equivalent to Pt contents of (9 ± 1) and (15 ± 1) at.% for 20 and 500 µs, respectively. Highest dwell times of 1000 µs, however, show a weak increasing tendency (C/Pt of 0.82; 15 ± 1.0 at.% Pt) which might indicate an excess of surface electrons leading to polymerization effects. The key aspect, however, is the absence

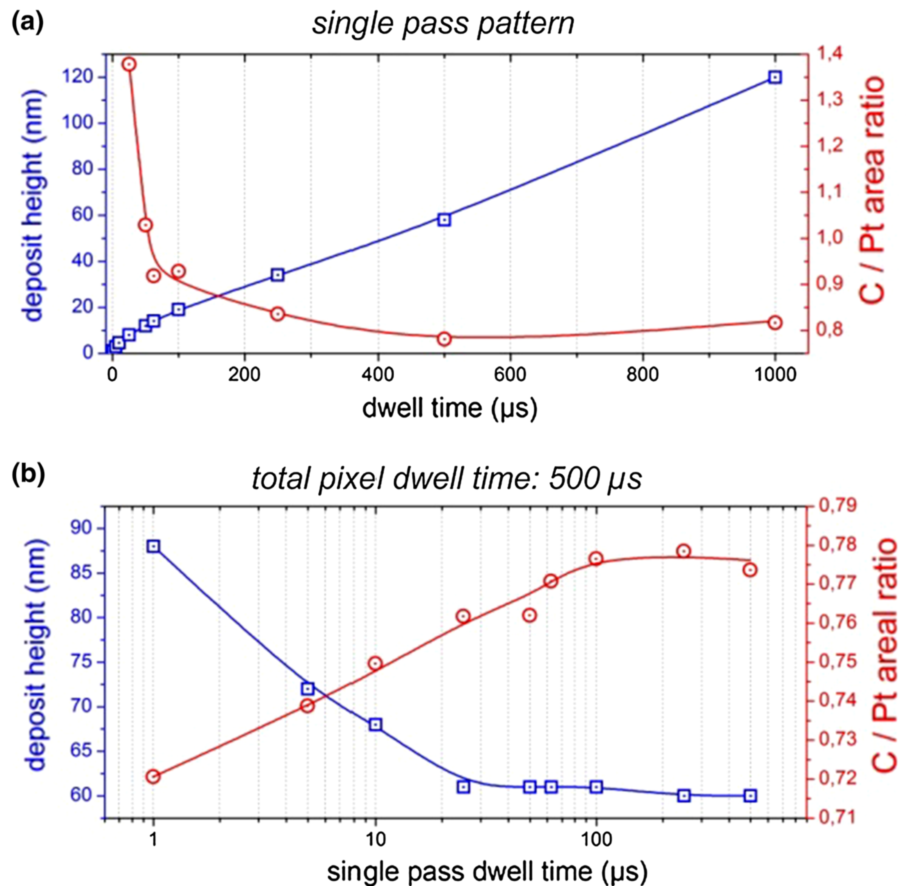

Fig. 4 Deposit heights (*squares, left axis*) and EDXS-based C/Pt area ratios (*circles, right axis*) for increasing dwell times fabricated via single passes (**a**) and a constant total pixel dwell time of 500 µs via multiple loops (**b**). Further, deposition parameters were 5 keV, 1,600 pA, 13 nm PoP via serpentine patterning

of strongly increasing carbon contents even for highest dwell times used as observed for nanopillars discussed before and presented in previous studies [7, 56]. To clarify the situation the geometrical differences between quasi-1D and 3D footprints have to be taken into account as well. Surface diffusion-related replenishment from the substrate is practically eliminated for nanopillars due to their enormous aspect ratio in combination with the short diffusion radius [7, 56–58]. Furthermore, the extremely thin pillars are replenished via the gas flux only on one side which faces the GIS. This leads to a very low areal adsorption rate from the gas flux which, in combination with high beam currents, leads to a very strong excess of surface electrons. In contrast, the 3D pads investigated here show a footprint of 4 × 4 μm^2 which is constantly replenished via the gas flux supported from deposit-related surface diffusion SDR-D. The results are higher local replenishment rates compared to the nanopillar situation which prevents a regime shift towards a massive excess of surface electrons required for polymerization effects. This might explain the wide absence of again increasing carbon content for highest currents (Fig. 3b) and longest dwell times (Fig. 4a).

To separate the influence of deposit heights and dwell times on final chemistries the electron dose per patterning point (equivalent to 500 μs pixel dwell time) was kept constant while the incremental dwell time was decreased, compensated by an increasing number of patterning loops (1 pass for 500 μs → 500 passes for 1 μs). Figure 4b shows the height evolution (blue squares, left axis) together with corresponding C/Pt ratios (red circles, right axis) revealing increasing growth rates for decreasing DTs caused by the reduced local depletion during deposition as expected. The chemistry, on the other hand, showed also a small decrease of C/Pt—ratios from 0.78 to 0.72 equivalent to an increase of the Pt content of about 1 at.%. This, however, correlates well with the enhanced growth rates and can, therefore, be attributed to the increasing surface electrons due to increased deposits heights.

Finally, the beam energy is changed from 5 to 30 keV. Due to the much larger interaction volume a stable number of surface electrons is expected for larger heights, hence, leading to a much more constant chemistry for early sub-50 nm growth stages. While the PoP (13 nm), the DT (50 μs) and the scanning strategy (SP) were kept identical, the beam current was increased to 2,400 pA due to technical reasons. Figure 5a shows a direct height comparison (blue squares, left axis) together with the evolving chemistry (red circles, right axis) for 5 keV (1,600 pA) and 30 keV (2,400 pA) as indicated by the legend. It can be seen that the expected more homogeneous chemistry cannot be achieved for growing 30 keV deposits; instead again a quick decay of the C/Pt—ratio within the first 40 nm was observed. The

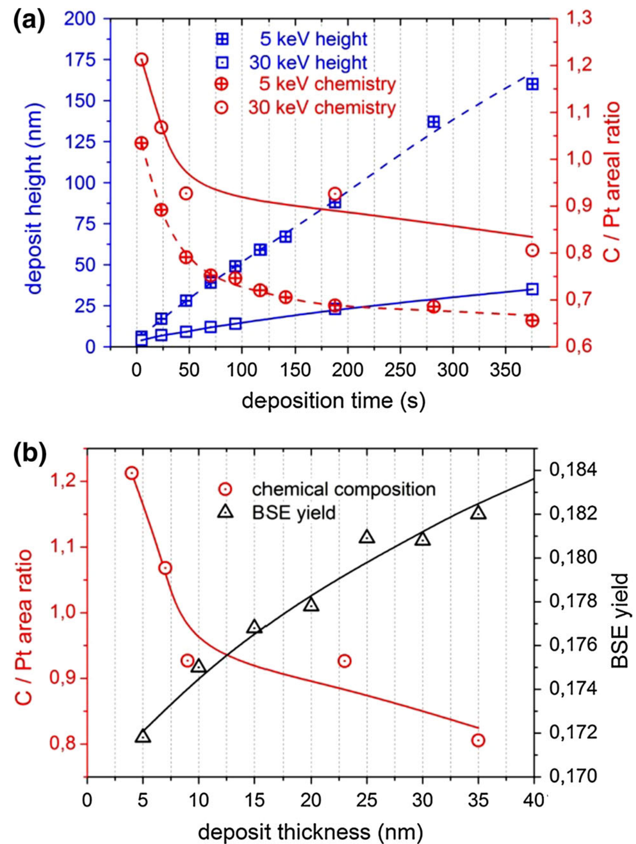

Fig. 5 **a** Height (*squares*) and C/Pt ratios (*circles*) as function of exposure time for 5 keV (*centre cross*) and 30 keV (*centre dot*) using 1,600 and 2,400 pA, respectively (50 μs DT, 13 nm PoP, serpentine patterning). **b** C/Pt area ratios (*circles, left axis*) versus deposit thickness together with according BSE yields (*triangles, right axis*) for deposition at 30 keV

according BSE yield is almost linearly increasing in this height range as summarized in Fig. 5b using Monte Carlo simulation-based data. Both details indicate an influence of decreasing SDR components from the substrate surface (SDR-S) as they depend only on the evolving morphology (together with the occurring local depletion) and not from the used primary energy.

To conclude this section it can be stated that for 3D pads a parameter-dependent chemical gradient of up to 8 at.% is found within the first 100 nm layer growth. This effect is caused by (1) an increasing number of surface electrons due traversing interaction volume and (2) a decreasing replenishment rate mainly caused by the decaying surface diffusion from the substrate (SDR-S) while gas flux replenishment GFR and deposit related diffusion SDR-D are widely constant.

Compared to the quasi-1D situation, two differences have been found. First, decreasing carbon contents for higher deposits, explained by much better replenishment rates due to the more planar deposit/substrate situation.

Nevertheless, it could be shown that there exists a replenishment decay for higher 3D deposits as they act as dynamically increasing morphological barrier. The second difference concerns higher beam current which does not show the ELR (high C) → balanced (low C) → MLR (high C) transition as observed for quasi-1D nanopillars. Even high beam currents of 6,300 pA or highest possible dwell times result in a widely stable chemistry with lowest carbon contents once the number of surface electrons is constant. This strongly suggests only the "ELR → balanced" transition and that the strong lack of precursor molecules, required for strong MLR conditions, cannot be achieved due to the improved replenishment situation for deposits with larger 3D footprints. However, as we will see in the next section, improperly aligned patterns can reveal more MLR-like conditions which further complicates predictable and reproducible chemistries in FEBID deposits.

2.2.3 Directional gas flux effects

So far we have considered the influence of the growing deposit on (1) the number of surface electrons and (2) diffusive related replenishment components. The constant in this picture was the gas flux-related adsorption rate which is practically independent of the deposit height. However, as we will show in the next sections, there is another crucial element by means of directional gas flux components due to the geometrical arrangement of GIS. As a consequence the gas flux adsorption is spatially varying which can strongly influence both, volume growth rate and final chemistries. At first we will describe the problem itself and demonstrate then how the patterning orientation influences the chemical composition of a deposit.

2.2.3.1 Alignment and shadowing effect In a first step the influence of the arrangement of the GIS is elucidated. For this study two different GIS alignments were used to show the impact on growth rates and final chemistry. Figure 6a shows the previously used "off-axis"-alignment [5] where deposition areas are shifted 200 μm to the right (e-beam centre). Figure 6b shows the ideal alignment ("on-axis") of deposition area on the main axis of the GIS (red cross). Tilt angles and nozzle-to-sample distances are indicated in both images.

The basic difference between these two arrangements is the net-direction of the gas flux vector (GFV) at the deposition area as indicated on the right of Fig. 6a and b, respectively. While for ideal situations (Fig. 6b) the resulting GFV has only a *Y* component, the off-axis arrangement (Fig. 6a) introduces an additional *X* component as confirmed via experiments and simulations by Winkler et al. [47]. The consequences are morphological

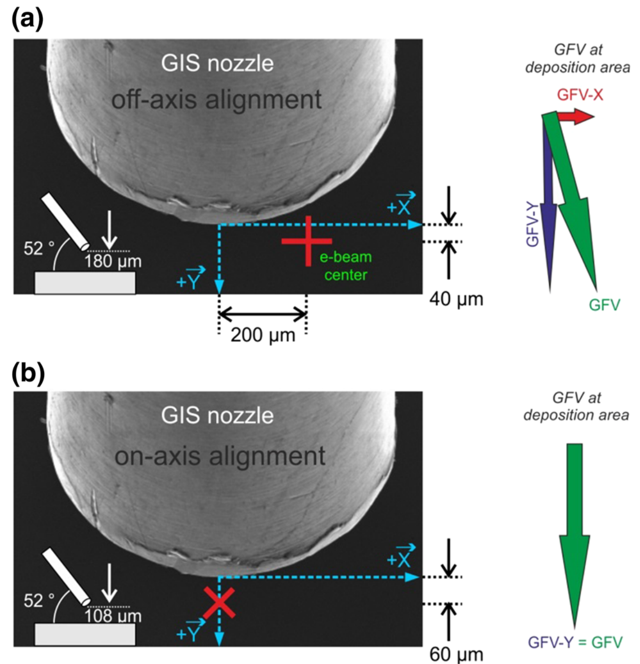

Fig. 6 Schematic arrangements of gas injection system (GIS) and deposition area (*red crosses*) for off-axis (**a**) [47] and on-axis (**b**) alignment. Vertical distances and tilt angles are indicated at the *bottom left* while the resulting gas flux vector at the deposition areas are given at the *right*

instabilities mainly caused by geometrical shadowing. The origin of this effect is the non-perpendicular GFV with respect to the surface (52° instead of 90°) which leads to shadowed regions as a function of deposit heights. Those areas are not directly replenished via the gas flux (GFR) but mainly via surface diffusion (SDR) from the deposit surface (SDR-D) and from the surrounding substrate (SDR-S). The latter, however, is a function of deposit heights as the shadowing radius competes with the average diffusion length of precursor molecules [5]. Hence, the only constant is the SDR-D component which leads to a complex VGR and chemistry dependency not only on the height but also on the patterning direction as will be shown in the following.

2.2.3.2 Patterning orientation To simplify the discussion we start with the ideal "on-axis" GIS arrangement as shown in Fig. 6b where no additional GFV-*X* components are present. This alignment was used for all experiments in the former sections. To exclude refresh time influences, all patterns have been processed via serpentine single passes using 5 keV, 1,600 pA, 1,000 μs DT and 13 nm PoP. To demonstrate the influence of the directional gas flux, the patterning orientation relative to the GIS was systematically rotated by 90° as indicated in Fig. 7a. As shown by the blue bars in Fig. 7b, highest deposits are achieved for 180° arrangements where the growing front is always

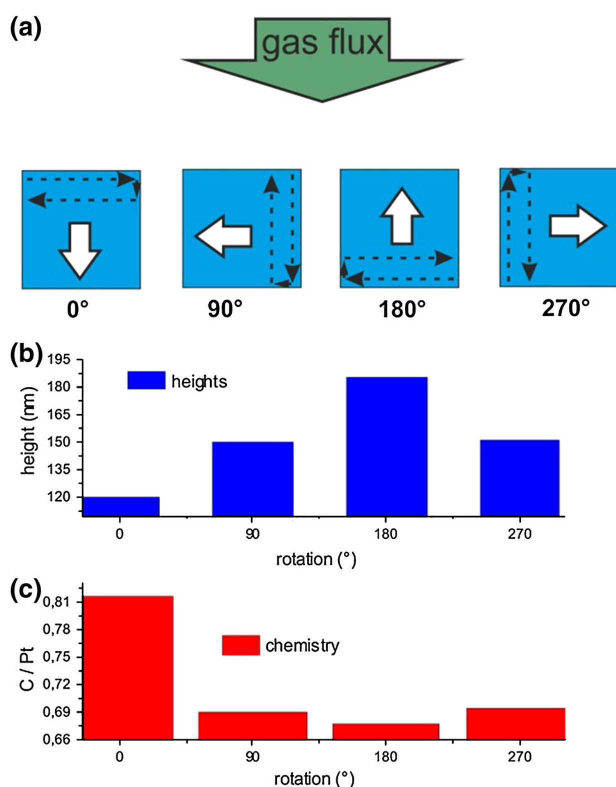

Fig. 7 **a** Rotation of patterning directions (see *white arrows*) relative to the gas flux direction (*green arrow*) using serpentine strategies (see *black arrows*) using 5 keV, 1,600 pA, 1,000 µs DT and 13 nm PoP via single pass patterning. **b**, **c** Give the respective heights and the according C/Pt ratios for all four patterning orientations shown in **a**

directed towards to the gas flux. Subsequently, the gas flux directly replenishes the growing front face leading to highest growth rates as discussed in detail by Winkler et al. for the off-axis alignment [47]. In contrast, when patterning away from the gas flux (0° arrangement) previously deposited barriers entails geometrical shadowing where the gas flux cannot replenish the growing deposit front. However, SDR from the deposit surface (SDR-D) as well as from the surrounding areas (SDR-S) can replenish the relevant areas. While the former is widely constant, the latter is a function of barrier heights and starts to decrease for heights above 50 nm [47]. Considering the final thickness of about 120 nm it follows that the replenishment mechanism is mostly related to the smallest SDR-D components during patterning away from the gas flux (0°). For patterning perpendicular to the GIS (90° and 270° arrangements), the growing front face is partly replenished from the GFV, however, not as efficient as for the 180° situation. This is in agreement with the finding of identical deposit heights for 90° and 270° as well as their final height in between the extremes (0° and 180°). For further discussion it is essential to note that the number of surface electrons is widely constant for all deposits above 120 nm which has been found to be sufficient for constant BSE yields (see Fig. 2). The essential part is the chemical results by means of C/Pt ratios as shown in Fig. 7c. It can be seen that highest carbon contents are found for 0° arrangements (away from the GIS) while lowest C/Pt values emerge for patterning towards the GIS (180°). The latter suggests a sufficient number of electrons leading to high dissociation degrees towards a Pt content of about (17 ± 1) at.%. However, when patterning away from the GIS (0°) shadowing occurs which decreases the VGR (see Fig. 7b). Considering previous findings that SDR-S components for thicknesses above 50 nm are strongly decreased [47] and GFR is practically zero, it is obvious that downwards diffusion from the substrate surface (SDR-D) is the predominant replenishment mechanism. Since the used parameters of 1,600 pA and 1,000 µs beam current and dwell time, respectively, lead to strong local depletion [1–3, 7, 55–57], it follows that the replenishment rate via SDR-D is comparably small. This, in turn, shifts the local working regime towards stronger excess of surface electrons compared to available precursor molecules which finally initiates polymerization effects in agreement with the increased carbon content. This effect has strongly been observed for the quasi-1D nanopillars and weakly for 3D pads fabricated at highest dwell times (Fig. 4) as discussed in the previous section. This completes the picture of ELR → balanced → MLR shifts during parameter variation and patterning orientation. Considering the absolute range of C/Pt ratios it is obvious that for 3D pads the last regime shift from balanced towards MLR is not as dominant as for quasi-1D footprints which were attributed to the very different replenishment rates discussed in the previous section.

In conclusion, these finding demonstrate the high importance of patterning directions with respect to the GIS directions as geometrical shadowing effects can become striking even for sub-100 nm deposit thicknesses. The consequences of different patterning orientations can be (1) varying VGRs and more importantly (2) chemical variations up to 3 at.% in addition to the spatial variations during growth evolution discussed in the previous section. Finally, it is also found that special situations (strong shadowing, long dwell times at high beam currents) can initiate polymerization effects of precursor fragments and possible chamber/substrate residue resulting in increased carbon contents.

2.2.3.3 Off-axis effects In the previous section we have used the ideal GIS arrangement where deposition areas are aligned on the long GIS axis, which effectively eliminates predominant *X* directions of the GFV (Fig. 6). To demonstrate how a slightly off-axis alignment, as shown in Fig. 6a, can influence final growth rates and chemical composition,

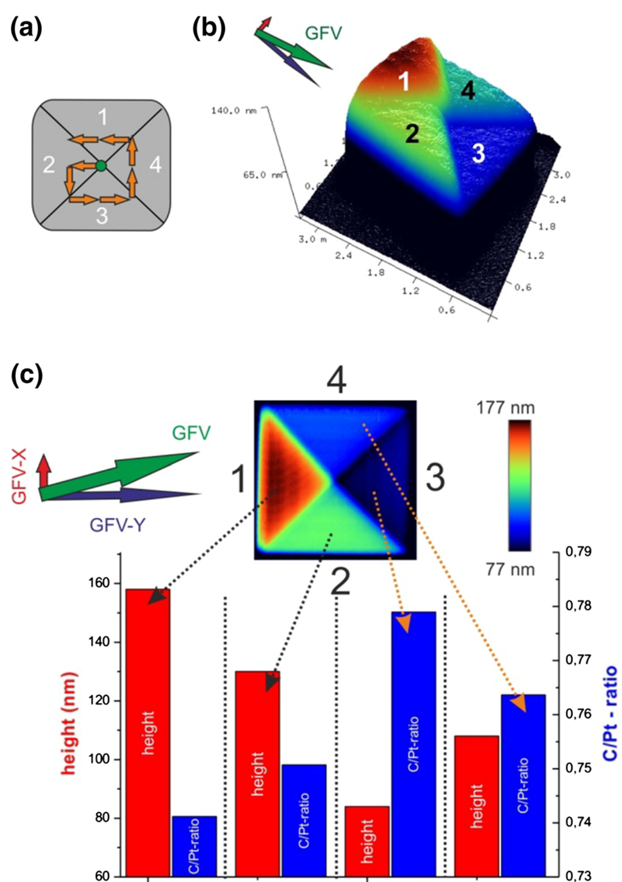

Fig. 8 **a** Spiral out patterning strategy together with the segment definition. **b** 3D AFM height image for a FEBID deposit fabricated via single passes at 5 keV, 1,600 pA, 1,000 µs and 13 nm PoP. The correctly aligned gas flux vector GFV is given *top left*. **c** AFM height image (*centre*) together with the correctly aligned GFV and its *X* and *Y* components. The *bottom panel* gives the according heights (*red*) and C/Pt area ratios (*blue*) for each segment

we have used a special spiral out (SO) patterning strategy (Fig. 8a) which allows visualization of all effects within one single pattern [47]. Again, we used 5 keV, 1,600 pA, 13 nm PoP, 1,000 µs DT with a single-pass pattern to provide comparability to previous sections. As can be seen by an AFM height image in Fig. 8b, all four segments show different heights, again as the consequence of the shadowing effect discussed before and in detail by Winkler et al [47]. However, there is also a height difference between the lateral segments 2 and 4 which can also be seen in the 2D AFM height image in Fig. 8c. In detail, segment 2 is directly replenished by GFV-*X* component (compare to GFV in Fig. 8c) while segment 4 lies in its shadowed region (a detailed discussion can be found in [47, 51]). As described in the previous section, the front segment 1 shows highest growth rates as it is directly replenished by the strong GFV-*Y* component, while back-segment 3 is in its shadowed region leading to lowest VGRs. Considering the chemistry (Fig. 8c) a similar picture emerges as found for the on-axis orientation discussed in the previous section. Patterning towards the gas flux gives lowest carbon contents due to a sufficient number of dissociating surface electrons for the used parameters (5 keV, 1,600 pA, 1,000 µs DT and 13 nm PoP). In contrast, back-segments show highest carbon contents as they are strongly depleted (predominant SDR-D) leading to polymerization of carbon fragments from the precursor and possible chamber/substrate residue. Please note the enlarged nozzle-to substrate distance for the off-axis alignment, which shifts the working regime towards MLR.

The main finding is the lateral asymmetry for VGR and chemical composition between segments 2 and 4. This is the consequence of the slight off-axis alignment between deposition area and GIS main axis. Hence, it is obvious that careful geometrical alignment (this section) and careful selection of patterning direction (previous section) are important parameters to push this technique further towards its intrinsic limits.

2.2.4 Functionality

So far we have discussed the spatial chemical distribution for growing deposits depending on patterning parameters and technical GIS setups. In this section we briefly discuss the implications of a varying chemistry on the functionality of Pt based deposits. Basically, we start with the electrical resistivity of as-deposited structures. As indicated by the squares in Fig. 9b, electrical resistivities of 8×10^6 µΩ cm are found for deposits fabricated at 5 keV, 1,600 pA, 1,000 µs DT and 13.5 nm PoP. Similar parameters are also used for the 180° situation in Fig. 7 (patterning towards the GIS). As discussed above such parameters lead to a balanced number of electrons compared to available precursor molecules resulting in a high degree of dissociation (C/Pt ~0.68, equivalent to about (17 ± 1) at.% Pt). On the other hand, we found electric resistivities of 6×10^7 µΩ cm for as-deposited structures fabricated in much more electron limited conditions as discussed in detail by Plank et al [7, 22–24, 41]. As observed for quasi-1D pillars [7] and for 3D pads in this article, ELR conditions lead to higher carbon contents due to incorporation of incompletely dissociated precursor molecules. This explains the higher electrical resistivities and demonstrates the huge influence by almost one order of magnitude between ELR conditions and a more balanced situation. Keeping this in mind it is clear that a regime shift during growth can lead to an enormous vertical functionality variation of up to one order of magnitude.

However, Porrati et al. and Plank et al. demonstrated an approach to improve the functionality [22–24, 41] which is further denoted as curing. They have shown that post-growth treatment with an electron beam can decrease electrical resistivities by more than two orders of

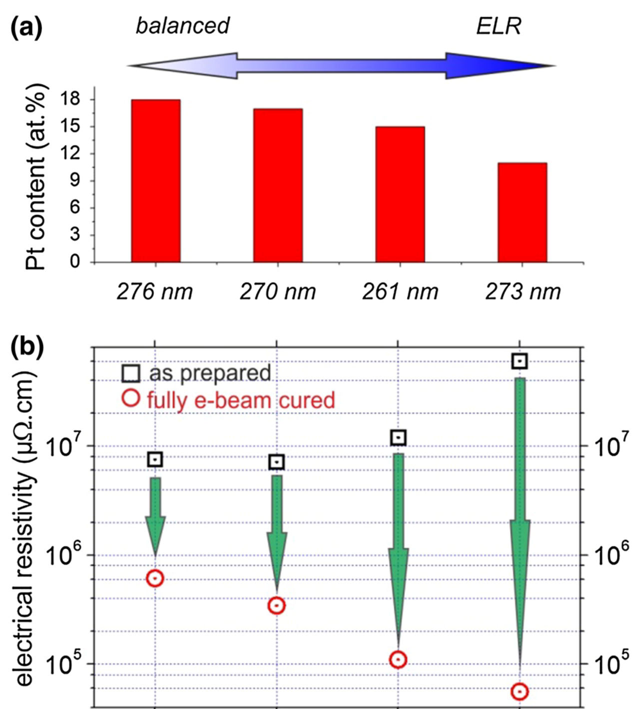

Fig. 9 **a** Chemical analysis of FEBID deposits fabricated at different parameters [41] ranging from more ELR conditions (*right*) to more balanced regime conditions (*left*) together with final thicknesses (*bottom*). **b** Electrical resistivity for as-deposited structures (*black squares*) and after full curing via electron beam assisted post-growth treatment (*red cirles*)

magnitude. The underlying effect is a slight growth of the Pt nanograins while the relative grain positions are maintained. This reduces the intergrain distance which improves the intergranular tunnelling probability and by that decreases the electrical resistivity [22–24, 41]. By performing such an e-beam post-growth-treatment (PGT) on deposits fabricated at different precursor working regimes, a tendency can be found as shown by squares in Fig. 9. The chemical composition after deposition is given in Fig. 9a together with regime tendencies indicated by the top arrow. As evident, lowest electric resistivities are found for more balanced regime conditions for highest Pt contents, in agreement with previous discussions. On the other hand, more ELR-like conditions (large point pitches, short dwell times and strong beam defocus; see Reference [7]) give highest electrical resistivities after deposition based on the higher number of incompletely dissociated precursor molecules. As described in detail by Porrati et al. and Plank et al. [22–24, 41], the e-beam PGT leads to finalization of the dissociation process which explains the above-mentioned particle growth while the overall chemistry widely remains. For more balanced situations the initial degree of dissociation is much higher, which reduces the effect of a post-growth treatment by the electron beam. This, in turn, explains the smallest resistivity decrease for such deposits. In the following, we are summarizing the data and put them in a bigger context to derive a few approaches which improves both, predictability and reproducibility of chemical properties for FEBID deposits.

3 Discussion

As demonstrated for quasi-1D nanopillars, there are two different kinds of carbon matrices rich in (1) incompletely dissociated precursor molecules for strong ELR conditions; and (2) polymerized carbon stemming from precursor fragments and possible chamber residue for strong MLR conditions. In between this transition there exists a balanced situation of electrons and precursor molecules which results in high dissociation degrees and by that in lowest carbon contents.

However, as most FEBID applications do not use such quasi-1D structures, a closer look was given on similar effects for 3D structures fabricated on flat substrates. The chemistry can change up to 8 at.% within the first 100 nm growth leading to functional gradients of up to one order of magnitude with respect to electrical resistivity. The underlying effect can be described by two main components: (1) increasing number of electrons on the surface; and (2) decreasing coverage due to reduced diffusive replenishment from the substrate. The former is caused by the interaction volume which traverses from the substrate into the deposit, which has very different densities in most cases. In this study we considered Si substrates and Pt–C deposits where the backscatter yield increases and saturates within growth of the first 100 nm deposit thickness using 5 keV primary electron energy (see Fig. 2). The increasing BSE number is associated with SE-II cascades which are energetically favourable for dissociation on the surface. In terms of working regime this effect implies a regime shift from ELR towards MTL conditions.

On the other hand, the local replenishment situation has to be considered which consists of three components: (1) direct gas flux replenishment (GFR); (2) surface diffusion replenishment from the substrate (SDR-S); and (3) SDR from the deposit surface itself (SDR-D). While GFR is independent on deposit heights, SDR-D components depend on the available area around actual deposition and are closely related to the GFR. Although small in magnitude, these SDR-D components are widely constant over time. The sensitive component is replenishment from the substrate as the growing deposit represents an increasing morphological barrier which precursor molecules have to overcome in order to contribute to local replenishment. Hence, SDR-S components can strongly decrease during growth depending on the geometry of the deposits (e.g. quasi-1D nanopillars). In terms of precursor working

regimes, a SDR decrease is equivalent to shift from ELR towards MLR conditions.

While the number of surface electrons gets widely stable after a certain deposit thickness ($\sim$100 nm for the used parameter), SDR is continuously decaying, leading to strong gradual chemical variations during growth (see 25 pA experiments in Fig. 3). By varying the DT, especially by changing the beam current, different VGR as well chemical composition can be achieved (Figs. 3 and 4). For example, high beam currents allow establishment of a widely balanced situation (low carbon contents) once the interaction volume is within the deposit (see Fig. 3). Although this approach provides widely stable chemistry for thicker deposits, the first 100 nm shows gradually changing chemistry. If thin deposits are of interest it is beneficial to use low beam currents which keep the working regime closer to ELR-like conditions making the varying SDR contributions less relevant (see Fig. 3). For Pt-based FEBID deposits the latter approach is highly beneficial considering the functionality tuning. For deposits fabricated in more ELR conditions, post-growth-treatment via the e-beam gives highest improvement rates (see Fig. 9) making this strategy ideal for high resolution (due to smallest beam diameters for lowest currents) with spatially constant chemistries (only weak regime changes) allowing for highest functionalities (e-beam post-growth treatment).

Another compensation approach could be the application of substrates with similar densities as the final deposit. This could reduce the variation of surface electrons, but cannot prevent the decaying SDR components as exemplarily demonstrated for high energy electrons (see Fig. 5). However, as the substrate can often not be chosen freely, process parameters have to be used for compensation.

Beside this general effect of varying chemistry within the first layers patterning alignment is found to be crucial. Geometrical shadowing can occur on the deposit backside caused by the tilted arrangement of the GIS. This effect prevents the direct replenishment via the gas flux (GFR) which is partly compensated by SDR from the deposit surface (SDR-D) and from the surrounding substrate (SDR-S). The latter is further decreased for deposit heights above 50 nm (for the given precursor and GIS-alignment) which reduces local replenishment mechanism to the weak SDR-D components. Hence, when patterning is performed away from the gas flux, the growing deposit front is weakly replenished leading to low volume growth rates. Depending on the process parameters, this situation can lead to MLR conditions, similar to quasi-1D nanopillars, where a strong excess of electrons can lead to polymerization of precursor fragments and chamber/substrate residue resulting in higher carbon contents.

The ideal arrangement is, therefore, patterning towards the gas flux where growing deposit fronts are directly replenished by the gas flux supported from SDR-S and SDR-D components. As the influence of the patterning direction on the platinum content can be up to 4 at.% this effect should be kept in mind when considering reproducibility. In addition, off-axis alignments should be avoided as this can lead to lateral asymmetries as shown in detail by Winkler et al [47].

4 Conclusions and outlook

The main essence of this article is the improved understanding of strongly varying chemistries during growth of the first 100–200 nm layer thicknesses, using $MeCpPt^{IV}Me_3$ related Pt–C deposits as test vehicle. Two main components have been found as responsible factors, namely (1) varying number of surface electrons due to different chemistries of substrate and deposit; and (2) reduced (diffusive) replenishment mechanisms caused by the dynamically growing deposit acting as morphological barrier. A systematic parameter study based on previous (quasi-1D nanopillars) and new results (3D footprints) revealed that both effects are basically unavoidable but reducible in their strength leading to more controlled deposit chemistries by choosing ideal fabrication parameters. Furthermore, it was demonstrated that the patterning alignment itself also affects final chemistries due to directional gas fluxes which has often be considered as less important in the past. Although of general relevance in terms of a fundamental understanding, the presented findings are of particular importance for applications which use the unique metal-matrix nanostructures of FEBID deposits. Hence, this study spans from fundamental aspects towards applicable strategies to achieve improved spatial homogeneity of chemistry as absolutely essential step on the road towards industrially oriented applications.

5 Methodology

The FEBID deposits were fabricated with dual beam system (FEI NOVA 200, FEI, The Netherlands) using a $MeCpPt^{IV}Me_3$ precursor, inserted via a FEI gas injections system which was preheated to 45 °C for at least 30 min. The stage was not moved for at least 15 min and the gas flux was turned on for at least 3 min before patterning. Two different GIS alignments were used as described in the main text. The inner and outer diameters of the injection nozzle are 500 and 830 μm, respectively. As substrate 10×10 mm Si samples with 3 nm of SiO_2 were prepared

in a laminar flow box and transferred to the dual-beam microscope chamber immediately. The distance of the final lens to the substrate was set to 5 mm for all experiments and the deposition site selected in a way that the gas nozzle does not intersect the substrate edges. The electron beam movement was controlled via stream files, generated with Matlab (release 2010b, MathWorks, USA).

After deposition the chamber was pumped for at least 2 h to get minimized chamber contaminations during the EDX measurements. Those were performed by a Bruker Xflash 4010 EDX-system (Bruker AXS). For the acquisition of the spectra an area of 2 × 2 μm within the deposition was exposed for 100 s with a beam current of 1.6 nA and a beam energy of 5 keV. During this time an input of 1.5–4.3 counts per seconds and a dead time of 4–6 % were achieved. For subtraction of the background signals the mean values of 3 spectra taken from the substrate were used. The energy values of peak integration were selected as 120–330 eV for the C K-line peak overlapping with Pt N-line and 1,950–2,220 for the platinum M-lines peak. The height measurements were performed on a second identical set of depositions with an atomic force microscope (Dimension 3100, Bruker AXS, US, operation with a Nanoscope IVa controller) using Olympus OMCL TS-160/TS-240 cantilever in tapping mode.

Acknowledgments The authors gratefully acknowledge the valuable support provided by Prof. Dr. Ferdinand Hofer, Prof. Dr. Gerald Kothleitner, Prof. Dr. Werner Grogger, Prof. Dr. Philip D. Rack, Dr. Jason Fowlkes, Dr. Ivo Utke, Dr. Julian Wagner, DI Roland Schmied, Alexander Melischnig, Laura Resch, and Martina Dienstleder. Special gratitude is given to Angus Young, Malcom Young, Phil Rudd, Cliff Williams, and Brian Johnson for constant inspiration. The authors also thank the FFG Austria (base project Nr. 830186), the European Union (EUROSTARS project E! 8213) and the COST funding (Nr. CM 1301) for their financial support.

References

1. I. Utke, S. Moshkalev, P.E. Russell, *Nanofabrication Using Focused Ion and Electron Beams: Principles and Applications*, 1st edn. (Oxford University Press, New York, 2012)
2. S.J. Randolph, J.D. Fowlkes, P.D. Rack, Crit. Rev. Sol. State **31**, 55 (2006)
3. W.F. van Dorp, C.W. Hagen, J. Appl. Phys. **104**, 081301 (2008)
4. W.F. van Dorp, T.W. Hansen, J.B. Wagner, J.T.B. De Hosson, Beilstein J. Nanotechnol. **4**, 474 (2013)
5. I. Utke, U. Gölzhäuser, Angew. Chem. Int. Ed. **49**, 9328 (2010)
6. H. Plank, C. Gspan, M. Dienstleder, G. Kothleitner, F. Hofer, Nanotechnology **19**, 485302 (2008)
7. H. Plank, T. Haber, C. Gspan, G. Kothleitner, F. Hofer, Nanotechnology **24**, 1753605 (2013)
8. A. Botman, J.J.L. Mulders, C.W. Hagen, Nanotechnology **20**(1), 372001 (2009)
9. M. Gavagnin, H.D. Wanzenboeck, D. Belić, E. Bertagnolli, ACS Nano **7**(1), 777 (2013)
10. M. Gabureac, L. Bernau, G. Boero, I. Utke, IEEE Trans. Nanotechnol. **12**(5), 668 (2013)
11. L. Serrano-Ramon, R. Cordoba, L.A. Rodriguez, C. Magen, E. Snoeck, C. Gatel, I. Serrano, M.R. Ibarra, J.M. De Teresa, ACS Nano **5**(10), 7781 (2001)
12. A. Fernandez-Pacheco, J.M. De Teresa, R. Cordoba, M.R. Ibarra, D. Petit, D.E. Read, L. O'Brien, E.R. Lewis, H.T. Zeng, R.P. Cowburn, Appl. Phys. Lett. **94**(19), 192509 (2009)
13. M. Gabureac, L. Bernau, I. Utke, G. Boero, Nanotechnology **21**, 115503 (2010)
14. A. Perentes, A. Bachmann, M. Leutenegger, I. Utke, C. Sandu, P. Hoffmann, Microelectron. Eng. **73–74**, 412 (2004)
15. I. Utke, M.G. Jenke, C. Röling, P.H. Thiesen, V. Iakovlev, A. Sirbu, A. Mereuta, A. Caliman, E. Kapon, Nanoscale **3**(7), 2718 (2011)
16. C.T.H. Heerkens, M.J. Kamerbeek, W.F. van Dorp, C.W. Hagen, J. Hoekstra, Microelectron. Eng. **86**, 961 (2009)
17. Y. Guan, J.D. Fowlkes, S.T. Retterer, M.L. Simpson, P.D. Rack, Nanotechnology **19**, 505302 (2008)
18. M.G. Lassiter, T. Liang, P.D. Rack, J. Vac. Sci. Technol. B **26**, 963 (2008)
19. T. Liang, E. Frendberg, B. Lieberman, A. Stivers, J. Vac. Sci. Technol. B **23**, 3101 (2005)
20. K. Edinger, H. Becht, J. Bihr, V. Boegli, M. Budach, T. Hofmann, H.W.P. Koops, P. Kuschnerus, J. Oster, P. Spies, B. Weyrauch, J. Vac. Sci. Technol. B **22**, 2902 (2004)
21. A.J.M. Mackus, J.J.L. Mulders, M.C.M. van de Sanden, W.M.M. Kessels, J. Appl. Phys. **107**, 116102 (2010)
22. F. Porrati, R. Sachser, C.H. Schwalb, A.S. Frangakis, M. Huth, J. Appl. Phys. **109**, 0637151 (2011)
23. M. Huth, F. Porrati, C. Schwalb, M. Winhold, R. Sachser, M. Dukic, J. Adams, G. Fantner, Beilstein J. Nanotechnol. **3**, 597 (2012)
24. F. Kolb, K. Schmoltner, M. Huth, A. Hohenau, J. Krenn, A. Klug, E.J.W. List, H. Plank, Nanotechnology **24**, 305501 (2013)
25. A. Botman, M. Hesselberth, J.J.L. Mulders, Microelectron. Eng. **85**(5–6), 1139 (2008)
26. S. Wang, Y.-M. Sun, Q. Wang, J.M. White, J. Vac. Sci. Technol. B **22**(4), 1803 (2004)
27. M.H. Ervin, D. Chang, B. Nichols, A. Wickenden, J. Barry, J. Melngailis, J. Vac. Sci. Technol. B **25**(6), 2250 (2007)
28. M. Takeguchi, M. Shimojo, K. Furuya, Appl. Phys. A **93**(2), 439 (2008)
29. A. Fernandez-Pacheco, J.M. De Teresa, R. Cordoba, M.R. Ibarra, J. Phys. D Appl. Phys. **42**(05), 055005 (2009)
30. K.L. Klein, S.J. Randolph, J.D. Fowlkes, L.F. Allard, H.M. Meyer, M.L. Simpson, P.D. Rack, Nanotechnology **19**(34), 345705 (2008)
31. J.J.L. Mulders, L.M. Belova, A. Riazanova, Nanotechnology **22**(05), 055302 (2011)
32. R. Cordoba, J. Sese, J.M. De Teresa, M.R. Ibarra, Microelectron. Eng. **87**(5–8), 1550 (2010)
33. R.M. Langford, D. Ozkaya, J. Sheridan, R. Chater, Microsc. Microanal. **10**, 1122 (2004)
34. N.A. Roberts, J.D. Fowlkes, G.A. Magel, P.D. Rack, Nanoscale **5**(1), 408 (2013)
35. N.A. Roberts, G.A. Magel, C.D. Hartfield, T.M. Moore, J.D. Fowlkes, P.D. Rack, J. Vac. Sci. Technol. A **30**(4), 041404 (2012)
36. V. Gopal, V.R. Radilovic, C. Daraio, S. Jin, P. Yang, E.A. Stach, Nano Lett. **4**(11), 2059 (2004)
37. R.M. Langford, T.X. Wang, D. Ozkaya, Microelectron. Eng. **84**(5–8), 784 (2007)
38. F. Porrati, R. Sachser, C.H. Schwalb, A.S. Frangakis, M. Huth, J. Appl. Phys. **109**(6), 063715 (2011)
39. C.H. Schwalb, C. Grimm, M. Baranowski, R. Sachser, F. Porrati, H. Reith, P. Das, J. Muller, F. Volklein, A. Kaya, M. Huth, Sensors **10**, 9847 (2010)
40. S. Frabboni, G.C. Gazzadi, L. Felisari, A. Spessot, Appl. Phys. Lett. **88**(21), 213116 (2006)

41. H. Plank, G. Kothleitner, F. Hofer, S.G. Michelitsch, C. Gspan, A. Hohenau, J. Krenn, J. Vac. Sci. Technol. B **29**(5), 051801 (2011)
42. S. Mehendale, J.J.L. Mulders, P.H.F. Trompenaars, Nanotechnology **24**(14), 145303 (2013)
43. H. Plank, J.H. Noh, J.D. Fowlkes, K. Lester, B.B. Lewis, P.D. Rack, ACS Appl. Mater. Interfaces **6**(2), 1018 (2014)
44. B. Geier, C. Gspan, R. Winkler, R. Schmied, J.D. Fowlkes, H. Fitzek, S. Rauch, J. Rattenberger, P.D. Rack, H. Plank, J. Appl. Chem. C (2014) (in review)
45. M. Stermitz, S. Nau, J.H. Noh, R. Winkler, A. Orthacker, S. Rauch, G. Kothleitner, P.D. Rack, S. Sax, E.J.W. List-Kratochvil, H. Plank, Adv. Mater. (2014) (in review)
46. J. Goldstein, D. Newbury, D. Joy, C. Lyman, P. Echlin, E. Lifshin, L. Sawyer, J. Michael, *Scanning Electron Microscopy and X-Ray Microanalysis*, 4th edn. (Springer, New York, 2003)
47. R. Winkler, J.D. Fowlkes, A. Szkudlarek, I. Utke, P.D. Rack, H. Plank, ACS Appl. Mater. Interfaces **6**, 2987 (2014)
48. D. Drouin, A.R. Couture, D. Joly, X. Tastet, V. Aimez, R. Gauvin, Scanning **29**(3), 92 (2007)
49. I. Utke, V. Friedli, M. Purrucker, J. Michler, J. Vac. Sci. Technol. B **25**, 2219 (2007)
50. J.D. Fowlkes, P.D. Rack, ACS Nano **4**, 1619 (2010)
51. D.A. Smith, J.D. Fowlkes, P.D. Rack, Small **4**, 1382 (2008)
52. J.D. Fowlkes, S.J. Randolph, P.D. Rack, J. Vac. Sci. Technol. B **23**, 2825 (2005)
53. W.F. van Dorp, J.D. Wnuk, J.M. Gorham, H.D. Fairbrother, T.E. Madey, C.W. Hagen, J. Appl. Phys. **106**, 74903 (2009)
54. J.D. Wnuk, J.M. Gorham, S.G. Rosenberg, W.F. van Dorp, T.E. Madey, C.W. Hagen, H.D. Fairbrother, J. Phys. Chem. C **113**, 2487 (2009)
55. H. Plank, D.A. Smith, T. Haber, P.D. Rack, F. Hofer, ACS Nano **6**, 286 (2012)
56. D.A. Smith, J.D. Fowlkes, P.D. Rack, Nanotechnology **19**, 415704 (2008)
57. G. Arnold, R. Timilsina, J. Fowlkes, A. Orthacker, G. Kothleitner, P. D. Rack, H. Plank, Fundamental resolution limitations during electron induced direct write synthesis. Appl. Mater. Interfaces (2014). doi:10.1021/am5008003
58. W.F. van Dorp, A. Beyer, M. Mainka, U. Gölzhäuser, T.W. Hansen, J.B. Wagner, C.W. Hagen, J.T.M. De Hosson, Nanotechnology **24**, 345301 (2013)

6.2 APPENDIX 2 - PUBLICATION 2

Publication 2

The Nanoscale Implications of a Molecular Gas Beam during Electron Beam Induced Deposition.

Winkler, R.; Fowlkes, J.; Szkudlarek, A.; Utke, I.; Rack, P. D.; Plank, H.

ACS Appl. Mater. Interfaces **2014**, *6* (4), 2987–2995.

ACS APPLIED MATERIALS & INTERFACES
Research Article
www.acsami.org

The Nanoscale Implications of a Molecular Gas Beam during Electron Beam Induced Deposition

Robert Winkler,[†] Jason Fowlkes,[‡] Aleksandra Szkudlarek,[§] Ivo Utke,[§] Philip D. Rack,[‡,||] and Harald Plank*[,†,⊥]

[†]Center for Electron Microscopy, Steyrergasse 17, 8010 Graz, Austria
[‡]Center for Nanophase Materials Sciences, Oak Ridge National Laboratory, Oak Ridge, Tennessee 37831, United States
[§]EMPA, Swiss Federal Laboratories for Materials Science and Technology, Laboratory for Mechanics of Materials and Nanostructures, Feuerwerkerstrasse 39, 3602 Thun, Switzerland
[||]Department of Materials Science and Engineering, University of Tennessee, Knoxville, Tennessee 37996, United States
[⊥]Institute for Electron Microscopy and Nanoanalysis, Graz University of Technology, 8010 Graz, Austria

Supporting Information

ABSTRACT: The gas flux direction in focused electron beam induced processes can strongly destabilize the morphology on the nanometer scale. We demonstrate how pattern parameters such as position relative to the gas nozzle, axial rotation, scanning direction, and patterning sequence result in different growth modes for identical structures. This is mainly caused by nanoscale geometric shadowing, particularly when shadowing distances are comparable to surface diffusion lengths of $(CH_3)_3$-Pt-$CpCH_3$ adsorbates. Furthermore, two different adsorbate replenishment mechanisms exist and are governed by either surface diffusion or directional gas flux adsorption. The experimental study is complemented by calculations and dynamic growth simulations which successfully emulate the observed morphology instabilities and support the proposed growth model.

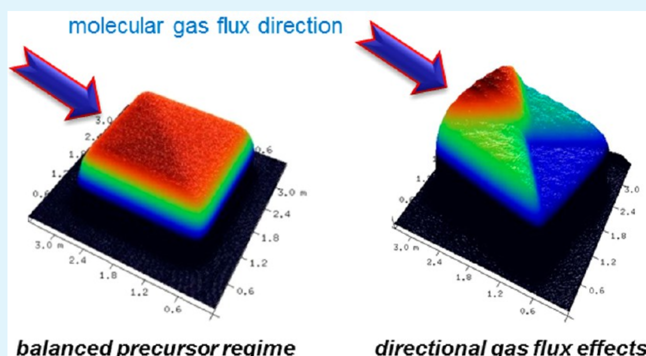

KEYWORDS: *focused electron beam induced deposition, nanofabrication, platinum, simulation*

INTRODUCTION

Electron beam induced deposition (EBID) provides a unique method to direct write functional 3D nanostructures[1−3] on almost any substrate material or shape. EBID mostly uses gaseous precursors which are injected into the vacuum chamber via a localized gas injection system (GIS) close to the point of deposition. Alternative strategies implementing liquid phase precursors/media have also recently emerged.[4] Gaseous precursors consist mainly of organometallic precursor molecules[5] which adsorb and diffuse on the surface and eventually desorb after a residence time if not consumed/decomposed by the electron beam.[1,3,6−10] The deposition is based on electron beam induced decomposition which dissociates the precursor molecules into immobilized functional condensates and volatile fragments which are pumped away from the chamber.[1−3,11] Thus, very small (3D) structures can be fabricated on even nonflat surfaces with spatial resolutions below 10 nm.[12] In recent years, an increasing number of applications have been demonstrated, ranging from passive applications such as nano optics,[13] lithography-mask repair,[14] nanolithography,[15,16] vapor−liquid−solid nanowire growth templating,[17] atomic-layer-deposition seeding,[18] advanced scanning probe microscopy probes,[19] and diodes[20] toward active devices such as magnetic storage, sensing and logic applications,[21] nanoscale strain sensors,[22,23] and gas sensors.[24] Most of the applications have two main performance demands: (1) high morphological control to allow reproducible fabrication of required geometries and (2) defined chemistry for proper functionality. Both of these requirements depend strongly on the precursor working regime during deposition which can be described by the balance between dissociating electrons and available precursor adsorbates[1,3,9,11,25,26] with two extremes: (i) more adsorbates than electrons, which is typically referred to as reaction rate limited (RRL), and (ii) more electrons than adsorbates, which is referred to as mass transport limited (MTL). It is known that a regime change not only changes the volumetric growth rate and resolution[1,9,11,27] but also the chemistry/composition.[28−30] Hence, control of the working regime is critical to define and reproduce the morphology and functionality. Regarding the chemistry, several ex and in situ strategies have been developed in order to modify the functionality, such as parameter optimization,[7,28] heated substrates,[31,32] reactive gases,[33,34] in

Received: December 5, 2013
Accepted: February 6, 2014
Published: February 6, 2014

 © 2014 American Chemical Society

situ laser assist,[35,36] thermal postgrowth annealing,[37,38] postgrowth e-beam curing,[39] and other combined processes.[38,40,41] On the basis of this progress in functional material tuning, advanced industrial applications are a step closer to reality. However, the final device performance depends strongly on both the shape fidelity and chemistry, which is therefore a primary gateway for potential applications.

In this study, we focus on the influence of the inhomogeneous molecular gas flux on final deposit shapes and the dependence on position, orientation, and electron scanning sequences used during electron beam patterning. It is demonstrated that the inhomogeneous gas flux including shadowing effects[42−45] leads to a directional replenishment component which can destabilize the growth mode. Finally, counterstrategies via beam current and pixel dwell time variations are presented which reveal the existence of two different types of MTL conditions dominated by (1) the gas flux and (2) surface diffusion. The study is complemented by calculations and finite difference growth simulations revealing excellent agreement with the experimental findings.

■ EXPERIMENTS

Gas Flux Vector. The experimental setup of our system uses an FEI gas injection system (GIS) with an angle of 52° with respect to the sample surface. The electron beam scan rotation was used to align the GIS main axis (along the needle) in the imaging window (see Figure 1a). All deposits were synthesized at a distance of 40 μm with respect

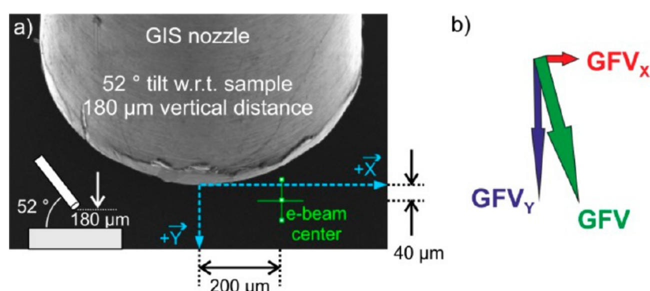

Figure 1. (a) SEM image of the gas injection system (GIS) relative to the center of the electron beam (green cross) at a distance of 200 and 40 μm for X and Y, respectively. The inset in the bottom left shows the vertical distance and the GIS angle. The blue dashed arrows define X and Y axes used for the discussion. (b) Gas flux vector (GFV) derived from simulations and experiments (see main text) including its individual X and Y components GFV_X and GFV_Y, respectively, for the given setup in part a.

to the GIS (defined as the Y direction) and 200 μm from the GIS main axis (defined as the X direction), as shown by the green cross in Figure 1a. Please note that the off-axis alignment of 200 μm was deliberately chosen to demonstrate the effects of the gas flux direction. Friedli et al. showed that, as a consequence of the finite nozzle diameter, sample surface distance, and tilted GIS arrangement, the molecular adsorption rate is site-specific due to the spatially varying gas flux $GF(x, y, z)$.[42,45,46] In the following, we reduced this expression to $GF(x, y)$ due to the flat substrates and comparably flat deposits less than 200 nm thick. The gas flux simulator (GFS) by Friedli and Utke et al.[46] was used to simulate the relative flux ratio J/J_{TOT}. The GFS results were compared to quasi 1D nanopillar experiments where surface diffusion from the substrate is minimized and the growth rates limited by local gas flux adsorption (shown in Supplement 1, Supporting Information). Importantly, the main gas flux vector (GFV) with respect to the X axis was determined to be ∼72 and ∼75° by simulations and experiments, respectively (shown in Supplement 1, Supporting Information). For convenience, X and Y directional components, GFV_X and GFV_Y, of the main GFV are used, as shown in Figure 1b.

Scan Directions. First, experiments with 3D pads were performed with high beam currents (1600 pA) and long DTs (1000 μs) via single pass patterning (2 × 2 μm^2 footprint, 13 nm point pitch). These parameters were chosen to increase precursor depletion in the beam area and its proximity as observed in previous studies which revealed reduced coverage in a radius of about 60 nm for comparable conditions and low DTs.[47] The reduced coverage is due to adsorbate consumption during long beam pulses with high electron flux. This is experimentally demonstrated via VGR experiments for increasing DTs which show an initial decay followed by a constant value (see Supplement 2, Supporting Information, and refs 1, 3, 7, 27, and 28). The nonzero steady state volume growth rate (VGR) reflects the constant gas flux replenishment which is independent of the DTs used.[47] Thus, to simplify our interpretation and directly infer the gas flux dependent growth, we performed experiments at high currents together with high DTs (see also Supplement 2, Supporting Information).

Initially, serpentine (SP) scans were used, as schematically shown in Figure 2a. We define the scanning direction along consecutive patterning points as the fast scan axis (FSA), while the slow scan axis (SSA) is the direction perpendicular to the FSA, as indicated by solid arrows in Figure 2a. Note the alignment of the gas flux vector GFV and its X and Y components (GFV_X, GFV_Y) relative to the scan axes. In order to elucidate the effect of the SSA with respect to the GFV, the serpentine patterns were rotated, as indicated in the four segments in Figure 2a (denoted as SP1, SP2, SP3, and SP4). AFM measurements reveal flat structures for all these patterning directions (representatively shown in Figure 2b) and enable quantitative volume analyses. The solid red bars in Figure 2c show their relative VGRs for all four orientations, revealing variations up to 35%. Comparing the different orientations, several details emerge: (1) the highest VGRs occur when the SSA vector points toward the strongest gas flux component GFV_Y (SP3), and (2) patterning away from the GFV_Y direction gives the lowest VGRs (SP1). A similar trend is observed with respect to the weaker gas flux component GFV_X. Further experiments with reversed FSA directions were conducted, revealing identical height distributions (see Supplement 3, Supporting Information). Thus, it was concluded that the relative orientation of patterning direction and gas flux vector GFV can influence the growth.

Special Patterning Strategies. In order to visualize gas flux vector effects within one single pad, a spiral-out (SO) patterning strategy was introduced which conveniently scans consecutively in different directions relative to the gas flux vector GFV. Figure 3a shows a 3D AFM height image of a deposit fabricated by an SO strategy (bottom left) with a single pass (identical parameters relative to the previous section). Although each patterning point was exposed to the electron beam once, the deposit shows a terraced structure in contrast to the widely flat deposits achieved with the serpentine patterns, as shown in Figure 2b.

Besides the strong height difference of the front (1) and back segments (3), slightly different heights are also found for the lateral segments (2 and 4) (higher and lower, respectively). To mimic the experiments, a finite difference algorithm was written and executed to estimate the dynamic surface coverage and EBID deposit heights using identical SO patterning conditions as those used for Figure 3a (details can be found in the Methodology section and in Supplement 4, Supporting Information). To simplify, only the y-component of the gas flux vector GFV was simulated perpendicular to the deposit front edge. Figure 3b shows the simulated deposit heights, which is very similar to what was observed experimentally (Figure 3a). Figure 3c reveals that the highest adsorbate surface coverage is realized on the front side with respect to the gas flux vector GFV (dark parts), while the lowest coverage exists on the deposit back side (yellow regions). Interestingly, surface coverage "crevices" are observed at the boundaries of the four segments, as noted in Figure 3c. A detailed look at the temporal coverage evolution reveals furthermore that the height difference between the lateral segments (2, 4) and the back segment (3) starts to increase with a larger spiral diameter (see the

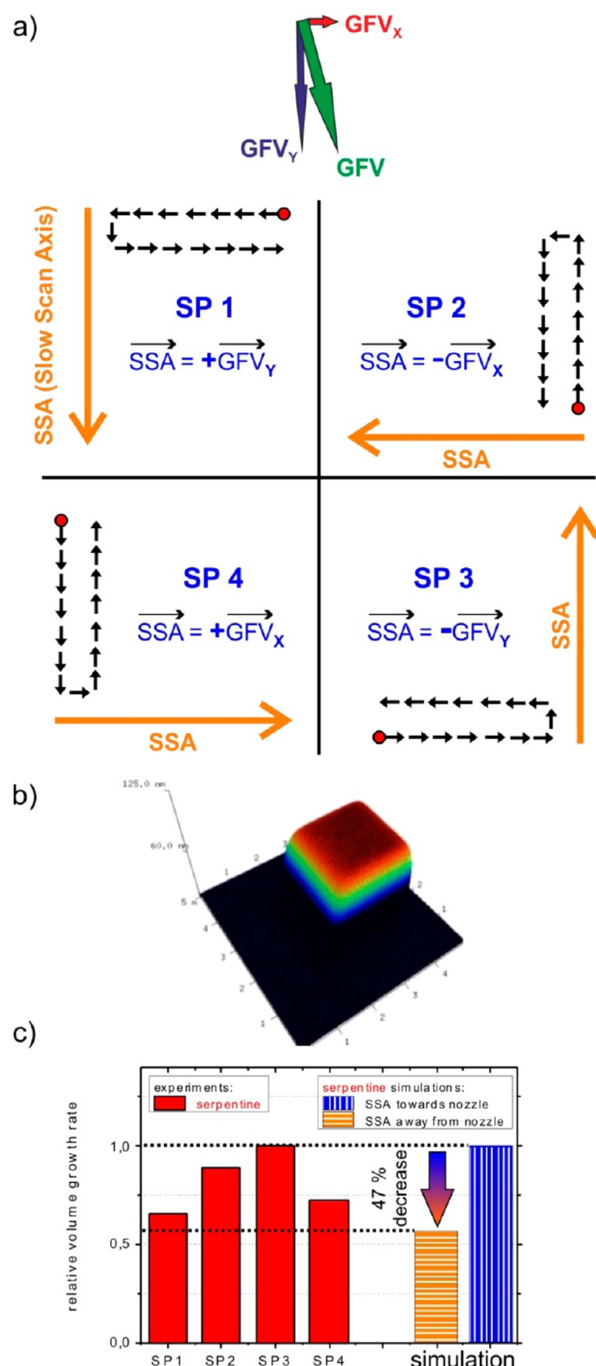

Figure 2. Variable serpentine patterns: (a) basic patterning strategy including the slow scan axis vector SSA. The four segments show the SSA orientation for SP1, SP2, SP3, and SP4 relative to the gas flux vector GFV (see Figure 1) and its X and Y components (GFV_X, GFV_X). (b) Representative AFM height image of a deposit fabricated via the serpentine pattern. (c) Relative VGRs for different pattern orientations defined in part a for serpentine strategies (solid bars, highest VGR used as reference value). Simulation results are shown by the two bars at the right with SSA orientation toward (vertical stripes and analogous to SP3) and away from the gas flux (horizontal stripes and analogous to SP1), revealing 47% decrease in VGR which is in good agreement with the experimental trend (see dotted lines).

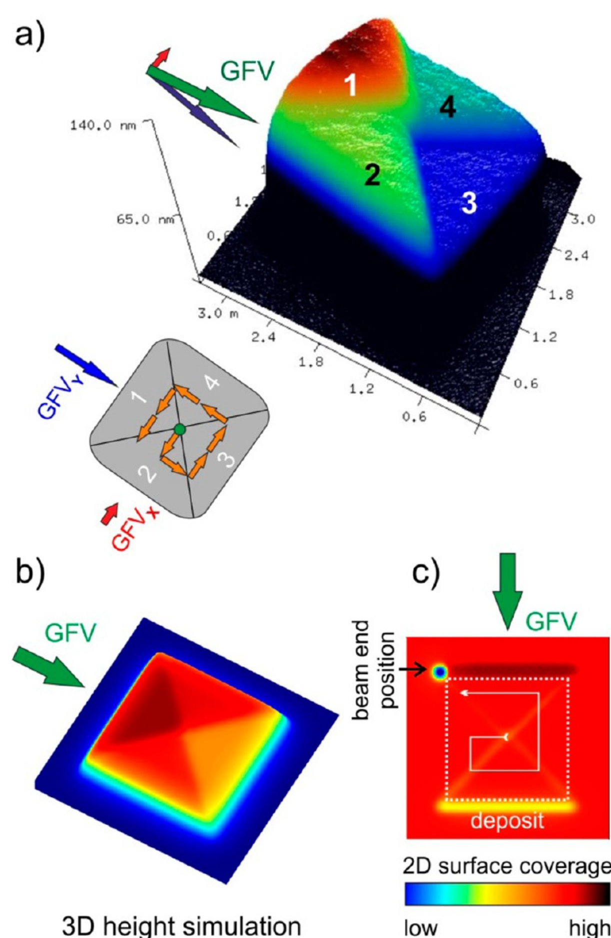

Figure 3. (a) AFM height image of a spiral-out deposit fabricated with a single pass. The relative orientation of the gas flux vector and its components are shown in the top left. The scanning strategy is indicated in the bottom left together with the individual gas flux components GFV_X and GFV_Y. (b) Simulation results using the same process parameters as those for the deposit in part a, however, with only the GFV_y component oriented perpendicular to the deposit front (see green arrow). Due to the missing GFV_X component, segments 2 and 4 have the same simulated height. (c) Simulated surface coverage after one complete spiral-out scan. The lowest coverage is observed on the back segment, and the highest, on the front segment (facing the GFV). Please note the small coverage crevices behind the segments (slightly brighter). The patterning box frame (dotted line) and the scanning strategy used (solid arrows) are also indicated.

movie in the Supporting Information) as a consequence of the triangularly shaped front segment. Note that the spiral-out patterns were also investigated in the opposite scanning directions where the beam travels clockwise and showed identical results (see Supplement 5, Supporting Information).

Pattern Rotation. As discussed in the previous section, the SO deposit shows also a lateral asymmetry in height (segments 2 and 4 in Figure 3a), which was not found for the simulations. The symmetry observed in the simulations is due to the small X component of the gas flux vector which was ignored. In order to investigate the relation between the GFV_X component and the observed asymmetry, the SO patterns were experimentally rotated in 15° increments. As observed in Figure 4, the height distribution for four segments varies depending on the orientation relative to the GFV and the height variations scale with the magnitude of GFV_X and GFV_Y. Interestingly, at 30° rotation, the GFV is parallel with the square diagonal and the front two segments have equivalent heights which are thicker than the back two segments which also have equivalent thickness. At 75°, the gas flux vector GFV is perpendicular to one of the square edges (see Supplement 1, Supporting Information). Similar to the simulation, in this case, the side segments are of equivalent thickness and the front and back have

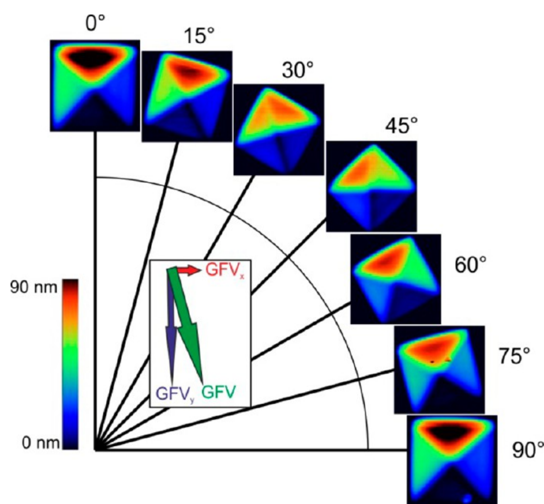

Figure 4. Pattern rotation for spiral-out patterning (counterclockwise) using the same electron beam parameters used in Figure 3. The gas flux vector is shown relative to the pattern orientation.

the largest thickness variation. The relative magnitudes of the GFV components clearly and systematically affect each segment thickness and illustrate the influence it has on the growth modes.

Separation of Gas Flux and Diffusive Replenishment. To separate between gas flux and surface diffusion related replenishment mechanisms, growth experiments without the gas flux were performed. Initially, the GIS system was opened for 3 min to achieve coverage equilibrium at the surface. Then, the GIS valve was closed and retracted before electron beam patterning was started (within less than 3 s). Note that this strategy eliminates the directed gas flux adsorption, while homogeneous precursor adsorption from the chamber volume still occurs as the monitored chamber pressure decays on a larger time scale than the patterning time. The results for SO patterns with identical electron beam parameters revealing thin (sub 5 nm) and flat deposits (see Supplement 6, Supporting Information) without any terraced segments compared to gas flux assisted deposition are shown in Figure 3a. However, even for such high dwell times, the pads are laterally symmetric. To investigate the influence of diffusion related replenishment from the substrate via simulations, the spiral-out experiments summarized in Figure 3 were repeated with a very small diffusion coefficient of 1×10^{-11} cm^2 s^{-1} with an associated diffusion length of less than 0.4 Å. The simulations reveal practically identical results in terms of morphological shapes, absolute heights, temporal behavior, and surface coverage (see Supplement 7, Supporting Information). Together with the GIS-off experiments, it can therefore be concluded that the directed gas flux is responsible for the asymmetrically terraced morphology (Figures 3a and 4). Furthermore, it shows that the surface coverage is widely constant in the deposition area, which is in agreement with the initial 1-D pillar growths (see Supplement 1, Supporting Information).

Beam Current Variation. In order to investigate the influence of the precursor working regime on final morphologies, the electron beam current was varied from 6300 to 5 pA (constant beam energy), while single pass SO patterning was used at a constant dwell time of 1000 μs (decreasing total dose). As shown in the AFM height images in Figure 5, decreasing beam currents lead to stabilized morphologies. The flatter structures emerge due to less gas depletion at lower currents. As a quantitative measure of the decreasing terrace formation, the relative height ratio between the lowest (3) and highest (1) segments is plotted vs the beam current in the center of Figure 5. As can be seen both for highest and lowest currents, the relative height

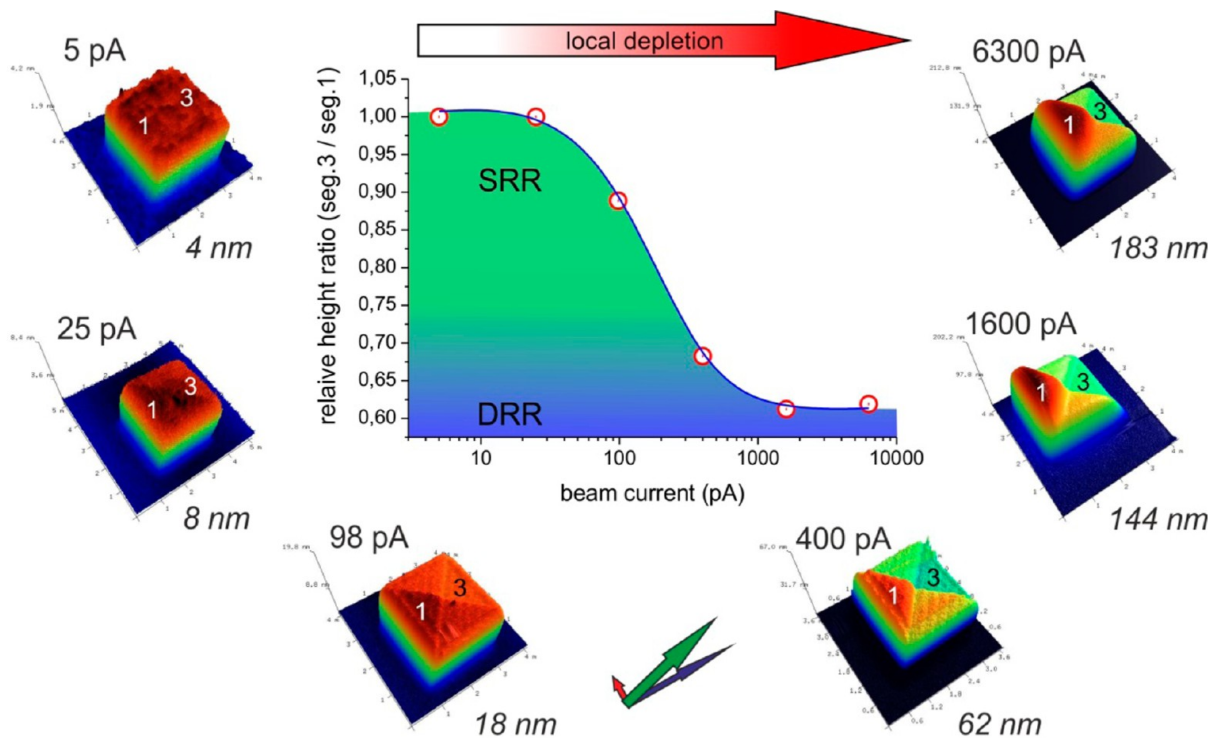

Figure 5. Beam current variation using spiral-out strategies for identical patterning conditions of 5 keV, 13 nm point pitch and 1000 μs pixel exposure via single pass patterning (2×2 μm^2 footprint), leading to increasingly flatter structures at lower current. The correctly oriented GFV and its components are also indicated together with the maximum deposit heights (segment 1). The relative height ratio between back and front segments versus beam current (central graph) is a qualitative measure for the surface coverage. For the highest currents, deposit related replenishment (DRR) dominates, while decreasing currents reveal the transition to predominant surface related replenishment (SRR) due to lower depletion and incremental growth heights.

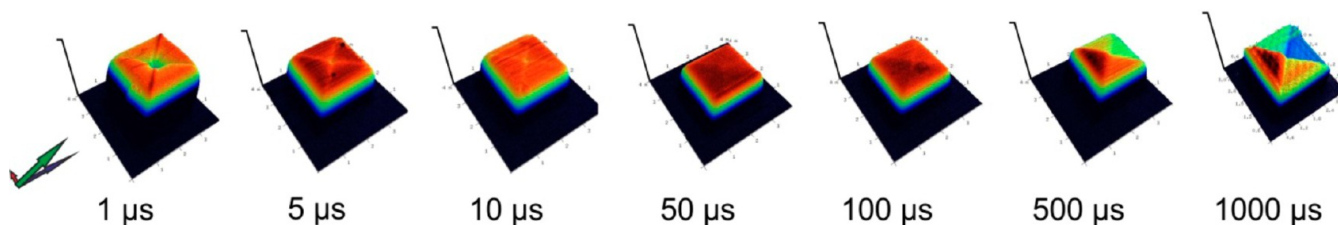

Figure 6. Dwell time variation using spiral-out strategies with adapted patterning loop numbers to keep the total exposure time constant. Color settings are adapted to clearly reveal surface variations. All deposits have the same footprint of 2×2 μm^2, and all vertical scale bars are 200 nm.

difference saturates, which indicates widely constant but very different regime conditions, as will be discussed later.

Pixel Dwell Time Variation. As an alternative to the previously discussed beam current variation, the pixel dwell time was also used to control the local precursor regime. Therefore, SO experiments were conducted with varying pixel dwell times ranging from 1000 to 1 μs, while the number of patterning loops was adapted to maintain the total exposure time (and thus electron dose). Such a DT sweep for 1600 pA is shown in Figure 6 by 3D AFM images which reveal that decreasing dwell times lead to flatter deposits. For very short dwell times of 10 μs and less, additional features appear in terms of a diagonal trench and an even deeper central indent (see the 1 μs deposit in Figure 6).

To correlate the process parameters with the unstable morphology, AFM based height histograms were taken from all deposits. For defined shapes, the histogram shows very sharp peaks, as shown for the 50 μs deposit in Figure 7a (center). For the terraced 1000 μs deposit, as shown in Figure 3a, the histogram shows four distinct peaks, as can be seen in Figure 7a on the right. The trench and indent formation for the 1 μs deposit is accompanied by an asymmetric peak, as shown in Figure 7a on the left. When measuring the base widths of these histogram peaks and plotting vs dwell times for different currents, one obtains the diagram shown in Figure 7b. As can be seen, the morphology destabilizes for high and low dwell times, however, for very different reasons as will be discussed below.

DISCUSSION

As discussed and summarized in Figure 2, the VGR was highest when patterning was performed toward gas flux vector components GFV_X (SP2) and GFV_Y (SP3) where new deposition areas are efficiently replenished by the gas flux. In contrast, when patterning away from the gas flux components, deposition occurs in the geometric shadow of the deposit[42−45] which inhibits replenishment, as schematically shown in Figure 8a. For the given geometry, we can estimate the most beneficial geometric shadowing radius Δr_S on the back side of the deposit as a function of the deposit height h to >20% ($\Delta r_S = 0.2{*}h$) assuming straight molecule trajectories between the GIS and substrate/deposit. This suggests a geometric shadowing radius Δr_S of a minimum 20−30 nm for the deposits SP1−SP4 (see Figure 2). On the basis of a diffusion constant D_0 of 6.5×10^{-9} to 8.5×10^{-10} $cm^2 \cdot s^{-1}$ and a typical residence time τ of 60−100 μs, this results in a radial diffusion length $\langle r \rangle$ between 2 and 25 nm according to $\langle r \rangle = (4{*}D_0{*}\tau)^{1/2}$ assuming 2D random surface diffusion (details about D_0 and τ can be found in Supplement 8, Supporting Information).[1,3,7,9] A shadowing radius of at least 20 nm suggests that the back side of the deposits cannot be efficiently replenished via diffusion of molecules that adsorb outside the shadowing radius because they desorb before reaching the deposit back side. A certain fraction of these desorbing molecules, however, are assumed to readsorb on the deposit back side and contribute to the precursor population. Both replenishment mechanisms, diffusion and readsorption, are further denoted as *substrate related replenishment* (SRR) throughout the manuscript. On the other hand, for molecules which adsorb on top of the deposit, close to the growing front, it is possible to diffuse "downwards" and contribute to the growth which we denote as *deposit related replenishment* (DRR). Note that the estimations given above are based on the 20% criterion for the shadowing radius related to the most beneficial angle, while a majority of trajectories show higher shadow radii illustrated by green and red lines in Figure 8a, respectively. On the basis of these estimations, the observed VGR dependency on the SSA orientation with respect to GFV

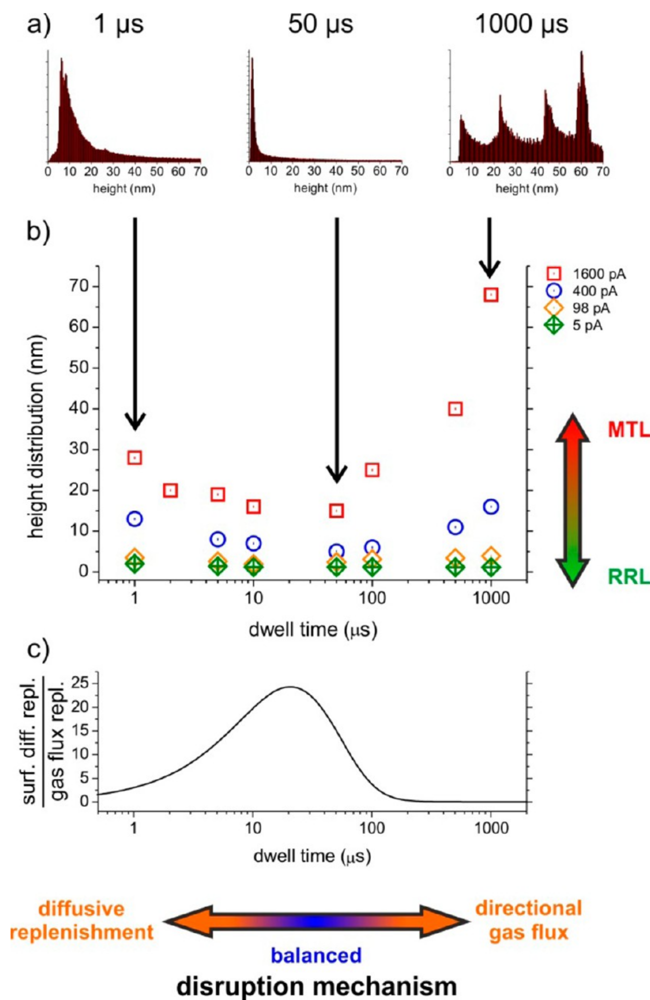

Figure 7. (a) Comparison of AFM pixel height histograms from experimental deposits for selected dwell times. (b) Summary of the histogram peak base widths as a function of dwell time and beam current. (c) Calculated ratio of diffusive replenishment vs gas flux adsorption replenishment at the center of the electron beam as a function of the same dwell time range as for part b with a current of 1600 pA (compare to red squares in part b).

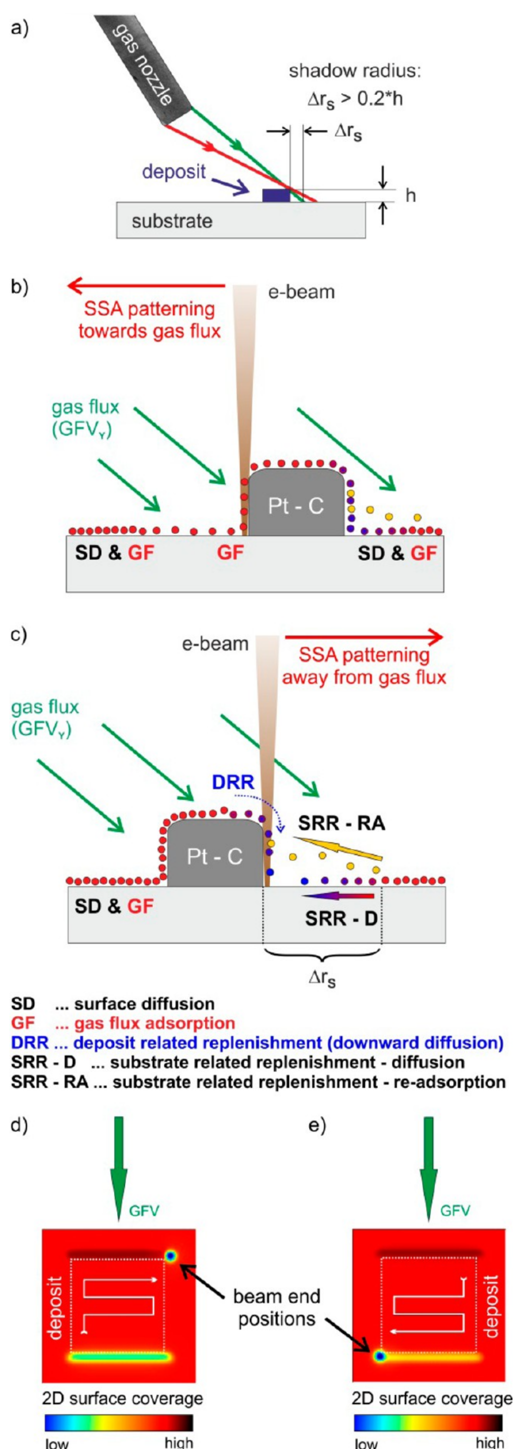

Figure 8. (a) Schematic of geometrical shadowing as a consequence of the GIS tilt angle and its distance to deposit. The suggested coverage and replenishment mechanism during patterning toward and away from the gas flux are shown in side view schemes in parts b and c, respectively. The 2D plots in parts d and e show simulations of the surface coverage at the termination of a beam dwell cycle from a top view, revealing higher and lower precursor population on the deposit front and back side, respectively. For as explanation, please consult the main text.

can be interpreted as follows: when patterning with the SSA toward the GFV_Y gas flux component (SP3 in Figure 2), as illustrated in Figure 8b, the front side of the growing deposits gets directly replenished by the gas flux, while substrate related replenishment is reduced as a result of the high dwell times used. To further investigate this hypothesis, finite difference simulations were performed for the purpose of estimating the dynamic surface coverage and deposit heights (details can be found in the Methodology section and in Supplement 4, Supporting Information) using a similar geometrical setup as described in the "Scan Directions" section and shown in Figure 2. The surface coverage distributions are shown by 2D top view plots in Figure 8d and 8e and reveal an increased molecular coverage on the front side due to direct gas flux replenishment (dark areas) and relatively low coverage at the back side as the consequence of geometrical shadowing (yellow areas). In contrast, when patterning is performed away from the GFV_Y component (SP1), as shown in Figure 8c, new deposition takes place in the geometrical shadow region where direct gas flux replenishment is restricted to the topmost edge areas of the structures. Due to the nonzero VGR, deposit related replenishment via downward diffusion is assumed to predominantly populate the evolving deposition front, as indicated by the DRR labeled arrow in Figure 8c. Substrate related replenishment (SRR) is assumed to be reduced as the precursor molecules tend to desorb before they diffuse through the shadowing radius Δr_S toward the growing deposit (see SRR-D path in Figure 8c), while readsorption can slightly contribute to the growth (SRR-RA path). Complementary surface coverage simulations (Figure 8e) reveal again that deposition takes place in areas of lower surface coverage (yellow areas), which explains the lower VGRs when patterning away from the gas flux. Quantitative simulation analyses of the VGRs suggest a VGR decay of 47% when patterning away from the gas flux (Figure 2c). A similar argument holds for SP2 and SP4 patterns relative to the GFV_X component. The fact that $GFV_y > GFV_x$ explains why higher VGRs are found for SP3 (toward Y) compared to SP2 (toward X), as summarized in Figure 2c. From these experiments, it can be concluded that a *directional gas flux replenishment component* is caused by (1) the GIS position with respect to the deposit (absolute X direction) together with (2) a geometric shadowing effect which depends on the absolute Y distance and the GIS tilt angle, as previously described by Friedli et al.[42−45]

The spiral-out (SO) patterning strategy allows one to visualize both directional gas flux replenishment components with one pattern. The terraced deposit shown in Figure 3a can be explained by directional gas flux effects: during patterning in segment 1, the strongest gas flux component GFV_Y replenishes the growing deposit front. Subsequently, during growth within segment 2, the replenishment situation is determined by the weaker gas flux component GFV_X. The decreased VGR results in a lower segment height, which furthermore induces geometrical shadowing, as suggested by the simulations (see surface coverage plot in Figure 3c). Both effects together explain the decreasing height for segment 2 in Figure 3a and b. When moving into segment 3, geometrical shadowing further decreases the replenishment of the growing back side (Figure 8c), leading to the lowest segment height which is also in agreement with the coverage simulations shown in Figure 8e. Finally, segment 4 evolves similarly to segment 2 but with the experimental difference that the gas flux component GFV_X is reduced and thus is the slightly reduced height compared to segment 2 (see Figure 3a). Finally, the experiments with a retracted and closed GIS system demonstrate that the destabilized morphology for SO strategies can be attributed

to the gas flux, while surface diffusion effects from surrounding areas are of minor relevance.

On the basis of the previous discussion, it follows that reducing the local depletion should decrease the influence of directional gas flux components. This can be done by two different approaches: (1) reducing the beam current and (2) decreasing the pixel dwell time. As shown in Figure 5, the highest beam currents have a saturated height ratio between front and back segments (central graph), which indicates constant replenishment conditions. Considering the estimated minimum shadowing radius Δr_S = 45 nm (6300 pA deposit), substrate related replenishment via diffusion and readsorption is assumed to be negligible. This explains the lower plateau for the highest currents where downward diffusion of molecules (DRR) is assumed to be the dominant replenishment mechanism (blue areas in Figure 5). As the beam current decreases, the back side replenishment increases via SRR (Figure 8c) due to (1) reduced local depletion (and a shift toward RRL-like conditions) and (2) reduced geometric shadowing as a result of decreased growth height. Once the surface coverage equilibrates over the entire deposit, the height ratio between segments 3 and 1 approaches 1 (upper plateau in Figure 5) and the directional gas flux components have no further implication. Alternatively, the pixel dwell times can be reduced while the number of patterning loops is increased accordingly, which should again lead to reduced local depletion. As shown in Figure 6 for SO strategies (constant beam current), the deposits get flatter for decreasing pixel dwell times for the same reasons as for decreasing beam currents. The central indent and the diagonal trenches, observed for lowest dwell times, are a result of the SO patterning strategy. Both effects indicate locally higher depletion due to more stationary beam movements at the center (starting point) and at directional changes at the diagonals (>25 nm FWHM beam diameter compared to 13 nm point pitch). To allow the assignment of indent/trench formation to insufficient surface diffusion, SO patterns have been fabricated for shortest dwell times with a retracted and closed GIS, leading to the same central indents and diagonal trenches (see Supplement 6, Supporting Information), which excludes the directional gas flux as the origin of these features. Taking these mechanisms into account, the morphological destabilization for very low and very high pixel dwell times, summarized in Figure 7b, can both be understood as a consequence of a regime shift toward more MTL-like conditions, however, due to different reasons: while the directional gas flux dominates for high dwell times (directional replenishment and shadowing), insufficient diffusive replenishment leads to the observed instabilities for low dwell times (see horizontal arrow in Figure 7c). When the beam current is reduced, the deposits become more flat (see Figure 5b) as a consequence of a regime shift toward more RRL conditions (vertical arrow in Figure 7b) where the number of adsorbates density is comparable to the electron flux.

To investigate this situation in more detail, numerical calculations of the local surface replenishment were conducted by considering surface related diffusion and gas flux adsorption individually. The results for the 1600 pA beam current are shown in Figure 7c (calculation details can be found in Supplement 8, Supporting Information). Starting from the longest dwell times, it can be seen that the surface diffusion related replenishment is increasing for decreasing dwell times while the impinging gas flux is constant. The highest surface diffusive replenishment coincides with flat deposits for DTs between 10 and 100 μs (see Figure 6). This increasing SDR contribution results in the more balanced situation between locally available precursor molecules and electrons, leading to widely flat surface structures. Further decreased dwell times lead to reduced depletion and thus to smaller concentration gradients, resulting in lower diffusive replenishment contributions, as shown in Figure 7c.

■ CONCLUSIONS

The study demonstrates how the inhomogeneous molecular gas flux which results from a standard gas injection system can significantly influence the growth modes during focused electron beam induced deposition processes. We demonstrate that the gas flux vector and the patterning strategy in terms of the absolute arrangement, axial rotation, point sequence, and patterning direction during EBID can significantly change the resultant growth rate and can give rise to interesting growth instabilities and morphologies. In the context of applications, it should be kept in mind that spatially varying precursor working regimes might entail different deposit compositions.[28] This, in turn, implies undefined and inhomogeneously distributed deposit functionality which is highly unwanted for potential applications. Together with destabilized morphologies, the study points out the importance of a careful adaption of geometrical setup, beam parameters, and patterning strategies to exploit the full potential of EBID on its way to real applications. Considering the main advantages of this method as a direct-write 3D nanostructuring tool, understanding these interactions is critical to enhancing resolution and maintaining high-fidelity 3D nanopatterns.

■ METHODOLOGY

Deposition experiments were performed with an FEI NOVA 200 (FEI, The Netherlands) dual beam system equipped with an FEI gas injection system (GIS) for Pt−C deposition using a $MeCpPt(IV)Me_3$ precursor. The GIS has an inner and outer diameter of 500 and 830 μm, respectively, and in this study, the distance between the lower edge of the GIS needle and the sample was set at 180 ± 10 μm. 15 × 15 mm^2 Si samples with 3 nm of SiO_2 were used and prepared in a laminar flow box for experiments. After immediate transfer of the samples to the dual beam microscope chamber, a background pressure of at least 9×10^{-6} mbar was established before any experiment was conducted. The precursor was preheated to 45 °C for at least 30 min. Beam focusing and optimization were performed on different areas than the final experiments in order to prevent any cross-contamination. Prior to any deposition, the GIS nozzle was opened for at least 3 min to provide a stable equilibrium between adsorption and desorption. The chamber pressure typically increased to a stable value of 3×10^{-5} mbar during deposition. Lateral positioning was always done in such a way that the GIS nozzle opening is not intersected with substrate edges which could disturb the molecular flux. The electron column sample distance was 5 mm for all experiments. Stage movements to defined areas have been performed with a blanked e-beam followed by deposition and an additional stage movement away from the actual deposition area. All patterns used stream files which have been generated via Matlab (release 2010b, MathWorks, U.S.) and double checked for errors in the point sequence. After successful deposition, the structures were characterized via atomic force microscopy (AFM) performed with a Dimension 3100 microscope (Bruker AXS, U.S.) operated with a Nanoscope IVa controller and equipped with an XYZ Hybrid scan head using an Olympus OMCL TS-160/TS-240 cantilever in tapping mode. Analyses were performed using NanoScope Analysis software (v1.4, Bruker AXS, U.S.). A detailed description of the finite difference simulation is given in Supplement 4 (Supporting Information).

■ ASSOCIATED CONTENT

Supporting Information

Detailed comparisons between gas flux simulations and experiments to derive the gas flux vector for the technical setup used; dwell time dependent volume growth rate investigations to demonstrate precursor regime shifts toward MTL-like conditions for high dwell times for high beam currents; mirrored serpentine strategies to investigate VGR variation for different patterning directions; detailed description of finite difference simulations; mirrored spiral-out experiments including systematic patterning rotation to determine segment specific volume growth rates; experiments with a retracted and turned off gas injection system at different dwell times and varying loop numbers to differ between surface diffusion and gas flux related influences; finite difference simulations with extremely low diffusion coefficients; diffusion coefficient determination via numerical methods and correlated experiments; and video showing temporal coverage evolution. This material is available free of charge via the Internet at http://pubs.acs.org.

■ AUTHOR INFORMATION

Corresponding Author

*E-mail: harald.plank@felmi-zfe.at. Phone: +43 316 873 8821.

Notes

The authors declare no competing financial interest.

■ ACKNOWLEDGMENTS

The authors gratefully acknowledge the valuable support provided by Prof. Dr. Ferdinand Hofer, DI Roland Schmied, DI Angelina Orthacker, Martina Dienstleder, and DI Florian Kolb. The authors also thank FFG Austria and the Federal Ministry of Economy, Family and Youth of Austria for their financial support. A portion of this research was conducted at the Center for Nanophase Materials Sciences, which is sponsored at Oak Ridge National Laboratory by the Scientific User Facilities Division, Office of Basic Energy Sciences, U.S. Department of Energy.

■ REFERENCES

(1) *Nanofabrication Using Focused Ion and Electron Beams: Principles and Applications*; Utke, I., Moshkalev, S., Russell, P., Eds.; Oxford University Press: New York, 2012.

(2) Randolph, S. J.; Fowlkes, J. D.; Rack, P. D. *Crit. Rev. Solid State Mater. Sci.* **2006**, *31*, 55−89.

(3) van Dorp, W. F.; Hagen, C. W. *J. Appl. Phys.* **2008**, *104*, 081301−1−081301−42.

(4) (i) Donev, E. U.; Hastings, J. T. *Nanotechnology* **2009**, *20*, 505302. (ii) Donev, E. U.; Hastings, J. T. *Nano Lett.* **2009**, *9*, 2715−2718. (iii) Schardein, G.; Donev, E. U.; Hastings, J. T. *Nanotechnology* **2011**, *22*, 015301.

(5) Botman, A.; Mulders, J. J. L.; Hagen, C. W. *Nanotechnology* **2009**, *20* (1), 372001.

(6) Smith, D. A.; Fowlkes, J. D.; Rack, P. D. *Nanotechnology* **2007**, *18*, 265308.

(7) Fowlkes, J. D.; Rack, P. D. *ACS Nano* **2010**, *4*, 1619−1629.

(8) Smith, D. A.; Fowlkes, J. D.; Rack, P. D. *Nanotechnology* **2008**, *19*, 415704.

(9) Smith, D. A.; Fowlkes, J. D.; Rack, P. D. *Small* **2008**, *4*, 1382−1389.

(10) Fowlkes, J. D.; Randolph, S. J.; Rack, P. D. *J. Vac. Sci. Technol., B* **2005**, *23*, 2825−2832.

(11) van Dorp, W.; Hansen, T. W.; Wagner, J. B.; De Hosson, J. T. B. *Beilstein J. Nanotechnol.* **2013**, *4*, 474−480.

(12) (i) van Dorp, W. F.; van Someren, B.; Hagen, C. W.; Kruit, P.; Crozier, P. A. *Nano Lett.* **2005**, *5*, 1303−1307. (ii) Bret, T.; Utke, I.; Hoffmann, P.; Abourida, M.; Doppelt, P. *Microelectron. Eng.* **2006**, *83*, 1482−1486. (iii) van Dorp, W. F.; Hagen, C. W.; Crozier, P. A.; van Someren, B.; Kruit, P. *Microelectron. Eng.* **2006**, *83*, 1468−1470. (iv) Córdoba, R.; Baturina, T. I.; Sesé, J.; Yu Mironov, A.; De Teresa, J. M.; Ibarra, M. R.; Nasimov, D. A.; Gutakovskii, A. K.; Latyshev, A. V.; Guillamón, I.; Suderow, H.; Vieira, S.; Baklanov, M. R.; Palacios, J. J.; Vinokur, V. M. *Nat. Commun.* **2013**, *4*, 1437. (v) van Dorp, W.; Zhang, X.; Feringa, B. L.; Hansen, T. W.; Wagner, J. B.; De Hosson, J. T. B. *ACS Nano* **2012**, *6* (11), 10076−10081.

(13) (i) Perentes, A.; Bachmann, A.; Leutenegger, M.; Utke, I.; Sandu, C.; Hoffmann, P. *Microelectron. Eng.* **2004**, *73*−*74*, 412−416. (ii) Utke, I.; Jenke, M. G.; Iakovlev, V.; et al. *Nanoscale* **2011**, *3* (7), 2718−2722.

(14) (i) Lassiter, M. G.; Liang, T.; Rack, P. D. *J. Vac. Sci. Technol., B* **2008**, *26* (3), 963−967. (ii) Liang, T.; Frendberg, E.; Lieberman, B.; Stivers, A. *J. Vac. Sci. Technol., B* **2005**, *23* (6), 31013105. (iii) Edinger, K.; Becht, H.; Bihr, J.; Boegli, V.; Budach, M.; Hofmann, T.; Koops, H. W. P.; Kuschnerus, P.; Oster, J.; Spies, P.; Weyrauch, B. *J. Vac. Sci. Technol., B* **2004**, *22* (6), 2902−2906.

(15) Heerkens, C. T. H.; Kamerbeek, M. J.; van Dorp, W.; Hagen, C. W.; Hoekstra, J. *Microelectron. Eng.* **2009**, *86*, 961−964.

(16) Guan, Y.; Fowlkes, J. D.; Retterer, S. T.; Simpson, M. L.; Rack, P. D. *Nanotechnology* **2008**, *19* (50), 505302.

(17) Jenke, M. G.; Lerose, D.; Niederberger, C.; Michler, J.; Christiansen, S.; Utke, I. *Nano Lett.* **2011**, *11*, 4213−4217.

(18) Mackus, A. J. M.; Mulders, J. J. L.; van de Sanden, M. C. M.; Kessels, W. M. M. *J. Appl. Phys.* **2010**, *107* (11), 116102−1−116102−3.

(19) (i) Noh, J. H.; Nikiforov, M.; Kalinin, S. V.; Vertegel, A. A.; Rack, P. D. *Nanotechnology* **2010**, *21* (36), 365302. (ii) (19) Roberts, N. A.; Noh, J. H.; Lassiter, M. G.; Guo, S.; Kalinin, S. V.; Rack, P. D. *Nanotechnology* **2012**, *23* (14), 145301. (iii) Utke, I.; Hoffmann, P.; Berger, R.; Scandella, L. *Appl. Phys. Lett.* **2002**, *80* (25), 47924794.

(20) Miura, N.; Ishii, H.; Shirakashi, J. I.; Yamada, A.; Konagai, M. *Appl. Surf. Sci.* **1997**, *269*−*273*, 113−114.

(21) (i) Fernandez-Pacheco, A.; De Teresa, J. M.; Cordoba, R.; Ibarra, M. R.; Petit, D.; Read, D. E.; O'Brien, L.; Lewis, E. R.; Zeng, H. T.; Cowburn, R. P. *Appl. Phys. Lett.* **2009**, *94*, 192509−1−192509−3. (ii) Serrano-Ramon, L.; Cordoba, R.; Rodriguez, L. A.; Magen, C.; Snoeck, E.; Gatel, C.; Serrano, I.; Ibarra, M. R.; De Teresa, J. M. *ACS Nano* **2001**, *5* (10), 7781−7787. (iii) Gavagnin, M.; Wanzenboeck, H. D.; Belić, D.; Bertagnolli, E. *ACS Nano* **2013**, *7* (1), 777−784. (iv) Gabureac, M.; Bernau, L.; Boero, G.; Utke, I. *IEEE Trans. Nanotechnol.* **2013**, *12* (5), 668−673. (v) Gabureac, M.; Bernau, L.; Utke, I.; Boero, G. *Nanotechnology* **2010**, *21*, 115503.

(22) Huth, M.; Porrati, F.; Schwalb, C.; Winhold, M.; Sachser, R.; Dukic, M.; Adams, J.; Fantner, G. *Beilstein J. Nanotechnol.* **2012**, *3*, 597−619.

(23) Porrati, F.; Sachser, R.; Schwalb, C. H.; Frangakis, A. S.; Huth, M. *J. Appl. Phys.* **2011**, *109*, 0637151−1−063715−7.

(24) Kolb, F.; Schmoltner, K.; Huth, M.; Hohenau, A.; Krenn, J.; Klug, A.; List, E. J. W.; Plank, H. *Nanotechnology* **2013**, *24*, 305501.

(25) Utke, I.; Gölzhäuser, I. *Angew. Chem., Int. Ed.* **2010**, *49*, 9328−9330.

(26) Utke, I.; Friedli, V.; Purrucker, M.; Michler, J. *J. Vac. Sci. Technol., B* **2007**, *25* (6), 2219−2223.

(27) Plank, H.; Gspan, C.; Dienstleder, M.; Kothleitner, G.; Hofer, F. *Nanotechnology* **2008**, *19*, 485302.

(28) Plank, H.; Haber, T.; Gspan, C.; Kothleitner, G.; Hofer, F. *Nanotechnology* **2013**, *24*, 1753605.

(29) Gabureac, M.; Bernau, L.; Utke, I. *J. Nanosci. Nanotechnol.* **2011**, *11* (1−6), 7982−7987.

(30) Bernau, L.; Gabureac, M.; Erni, R.; Utke, I. *Angew. Chem., Int. Ed.* **2010**, *49*, 8880−8884.

(31) Cordoba, R.; Sese, J.; De Teresa, J. M.; Ibarra, M. R. *Microelectron. Eng.* **2010**, *87* (5−8), 1550−1553.

(32) Mulders, J. J. L.; Belova, L. M.; Riazanova, A. *Nanotechnology* **2011**, *22* (05), 055302.
(33) Langford, R. M.; Ozkaya, D.; Sheridan, J.; Chater, R. *Microsc. Microanal.* **2004**, *10*, 1122−1123.
(34) Miyazoe, H.; Utke, I.; et al. *J. Vac. Sci. Technol., B* **2010**, *28* (4), 744−750.
(35) Roberts, N. A.; Fowlkes, J. D.; Magel, G. A.; Rack, P. D. *Nanoscale* **2013**, *5* (1), 408−415.
(36) Roberts, N. A.; Magel, G. A.; Hartfield, C. D.; Moore, T. M.; Fowlkes, J. D.; Rack, P. D. *J. Vac. Sci. Technol., A* **2012**, *30* (4), 041404−041406.
(37) (i) Gopal, V.; Radilovic, V. R.; Daraio, C.; Jin, S.; Yang, P.; Stach, E. A. *Nano Lett.* **2004**, *4* (11), 2059−2063. (ii) Botman, A.; Mulders, J. J. L.; Weemaes, R.; Mentink, S. *Nanotechnology* **2006**, *17* (15), 3779−3785. (iii) Langford, R. M.; Wang, T. X.; Ozkaya, D. *Microelectron. Eng.* **2007**, *84* (5−8), 784−788.
(38) Mehendale, S.; Mulders, J. J. L.; Trompenaars, P. H. F. *Nanotechnology* **2013**, *24* (14), 145303.
(39) Porrati, F.; Sachser, R.; Schwalb, C. H.; Frangakis, A. S.; Huth, M. *J. Appl. Phys.* **2011**, *109* (06), 063715.
(40) Frabboni, S.; Gazzadi, G. C.; Felisari, L.; Spessot, A. *Appl. Phys. Lett.* **2006**, *88*, 213116-1−213116-3.
(41) Plank, H.; Noh, J. H.; Fowlkes, J. D.; Lewis, B.; Rack, P. D. *ACS Appl. Mater. Interfaces* **2014**, *6* (2), 1018−1024.
(42) Friedli, V.; Utke, I. *J. Phys. D: Appl. Phys.* **2009**, *42*, 125305.
(43) Bret, T.; Utke, I.; Hoffmann, P. *Microelectron. Eng.* **2005**, *78*−*79*, 307−313.
(44) DeMarco, A. J.; Melngailis, J. *J. Vac. Sci. Technol., B* **1999**, *17*, 3154−3157.
(45) Friedli, V. Focused electron- and ion-beam induced processes: in situ monitoring, analysis and modelling. Ph.D. Thesis, Ecole Polytechnique Féderale de Lausanne, 2008.
(46) Friedli, V.; Utke, I. http://www.empa.ch/GISsimulator; 2009.
(47) Plank, H.; Smith, D. A.; Haber, T.; Rack, P. D.; Hofer, F. *ACS Nano* **2012**, *6*, 286−294.

Supplement 1

In this supplement we use the gas flux simulator[46] (**GFS**) to simulate the molecular gas adsorption distribution and compare the results with experiments in order to derive a gas flux vector. As shown in the literature, the volume growth rate (**VGR**) for 1D pillars typically shows a strong initial increase followed by decay towards a constant value with increasing pillar height (growth time) (see Figure S 2). This is based on a varying replenishment situation via surface diffusion from the base substrate from 2-D towards quasi 1-D as the growing pillar provides an increasingly one-dimensional pathway towards the tip where new deposition takes place[1,6,7,10,9,10]. Hence, the growth rates of sufficiently tall pillars are mainly determined by direct replenishment from the gas flux which is reflected by the widely stable and non-zero VGR in Figure S 2. This allows the use of 1D pillars, grown at a constant deposition times (5 keV, 98 pA, 100 sec), to be an indicator for lateral gas flux distributions suggested by the GFS. A 7x7 matrix (49 pillar deposits) equal spaced in a square box with a side length of 120 µm (blue frame in Figure S 1a) has been used for experimental determination of the relative gas flux distribution J/J_{TOT}. The relative variation of the pillar heights is shown in Figure S 1b by a 3D plot together with the typical deposition area that will be used later in this study (shown by the grey 20 x 20 µm square). The graph below shows a direct comparison of the relative height variation in the experiment (circles) with the simulated gas flux result (triangles) which reveals very good agreement. Please note, the shown comparison has been done along the matrix diagonal as indicated by the black arrow in Figure S 1b. Similar comparisons in X and Y directions also showed very good agreement of between experiment and simulation. Similar experiments have been performed with an array of 3D pads of 2 x 2 µm ranging from 100 – 300 µm along the X direction at Y = 40 µm as indicated by the red arrow in Figure S 1a. Deposition has been performed at low currents and short pixel dwell times (**DT**) of 25 pA and 1 µs, respectively, to keep local precursor depletion and by that also the adsorbate concentration gradients low which prevents locally varying surface diffusion.

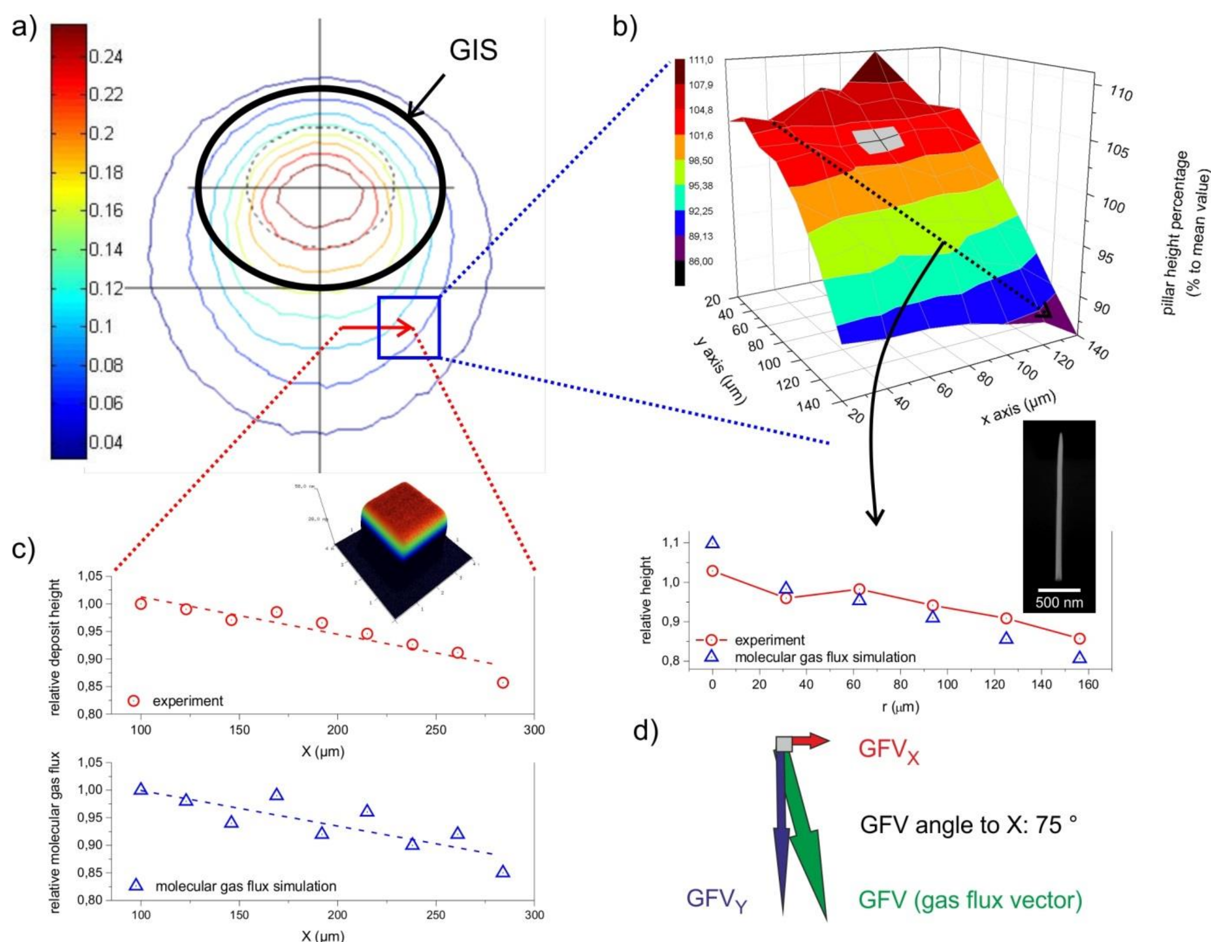

Figure S 1: verification of the gas flux simulation (a) by means of nanopillar (b) and 3D pad growth (c) which enables the definition of the gas flux main vector (d) to be approximately 75° tilted with respect to the X axis (green arrow).

The VGR analysis of such pads therefore allows an insight of the lateral adsorbate coverage distribution established by the varying gas flux. Figure S 1c compares experimental growth rates (circles) and simulated gas flux (triangles), which again reveals very good agreement. From these investigations it can be concluded that ***1)*** the GFS is capable of predicting the spatially dependent relative molecule flux $J_{\mathbf{X}}/J_{\mathbf{TOT}}$ (1D experiments); and ***2)*** the local surface coverage is similar to the gas flux distribution (3D experiments). Furthermore, the latter result shows that for the areas of interest, the surface coverage is clearly below one monolayer (= 100 %) as expected (typically around 30 %[1,3,9,1]). Finally, we can derive the gas flux vector (**GFV**) as the tangent normal on equal flux ratios J/J_{TOT}. For the deposition center used in this study (see green cross in Figure 1a) the GFV has an angle of ~ 72 ° with respect to the X axis. Analysing the experimentally determined gradients in the X- and Y- direction reveals a ratio of 1 :

3.8 which equals a GFV angle of 75 ° which is in excellent agreement with the GFS results. For further discussion, it is convenient to split this vector in its X and Y directional components GFV_X and GFV_Y as shown in Figure S 1d. As discussed in the main article, high DTs shift the replenishment mechanism to a regime dominated by direct adsorption from the gas phase while substrate related replenishment is clearly reduced (see also Supplement 2). Furthermore, initial experiments concerning the lateral molecule adsorption from the gas phase revealed very low variations of less than 1 % within a 5x5 µm area around the deposit which exclude coverage gradient related effects.

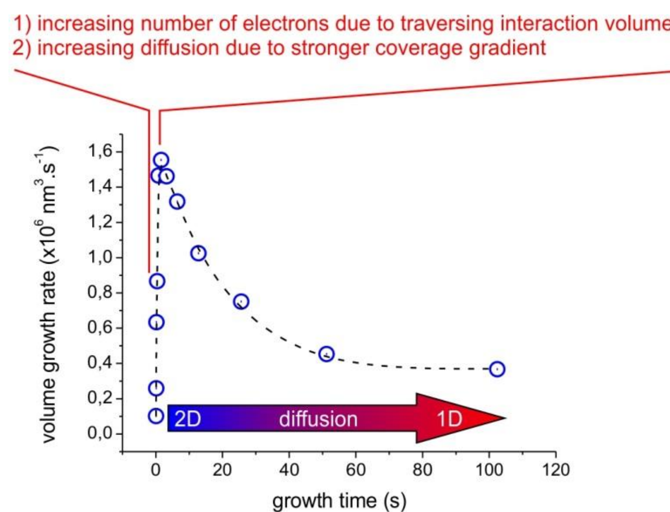

Figure S 2: volume growth rate (VGR) vs. growth time of a Pt-C nanopillar deposited at X = 200 µm and Y = 40 µm (see also Figure 1 and Figure S 1). The initial increase indicates two effects: *1)* the traversing interaction volume from the substrate into the deposit, which increases the number of dissociating electron species; and *2)* an increasing 2D diffusion towards the point of new deposition as the consequence of the increasing concentration gradient due to the stronger local depletion. Afterwards, the decreasing VGR reflects the decreasing contribution by diffusion related replenishment from the substrate as a consequence of the very narrow pathway (~ 100 nm in diameter but several micrometers long) which can be understood as a transition from 2D towards 1D diffusion. The fact that a constant and non-zero value is approached is based on the constant replenishment from the gas phase. Hence, the observed VGRs for sufficiently long 1D nanopillars is rather governed by direct gas flux replenishment.

Supplement 2

Figure S 3 shows the volume growth rate (**VGR**) vs. dwell time for 5 keV, 1600 pA, 13 nm point pitch, 2x2 µm for a constant total exposure time of ~ 23 sec (9.47 nC.µm^2). As can be seen the VGR decreases for increasing dwell times as the consequence of increasing precursor consumption during each pulse. At DTs of ~50 µs the VGR becomes widely constant which reflects the achievable growth rate based on direct replenishment from the gas flux assisted by surface diffusion before the molecules desorb again. Hence, high DTs allow the investigation of a widely gas flux determined replenishment mechanism with clearly reduced contributions by diffusion related replenishment from the substrate. Please note, the absence of the initial VGR increase as observed for 1D nanopillars (see Supplement 1) is explained by the high current used (1600 pA) and the entailed excess of electrons (MTL regime). When the interaction volume traverses from the substrate towards the deposit, the entailed increase of dissociating electrons has no effect as the local areas are depleted already.

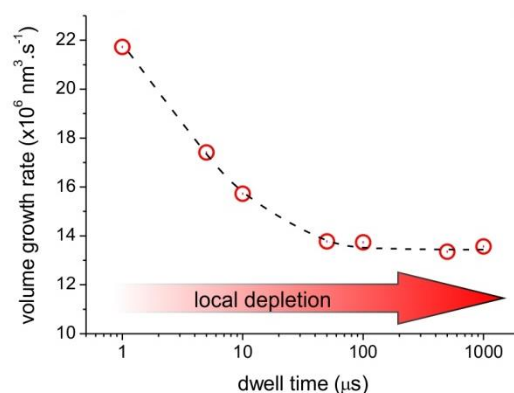

Figure S 3: volume growth rate (VGR) vs. dwell time for 5 keV, 1600 pA, 13 nm point pitch, 2x2 µm for a constant total exposure time of ~ 23 sec (9.47 nC.µm^2).

Supplement 3

In order to exclude effects by means of differently oriented fast scan axes (**FSA**) the originally used serpentine patterns have been reversed or mirrored while the slow scan axis (**SSA**) remains the same (a) which is summarized in Figure S 4. As can be seen in the VGR summary (c) by red (regular) and blue (mirrored) bars, no difference could be found for different SSA orientations.

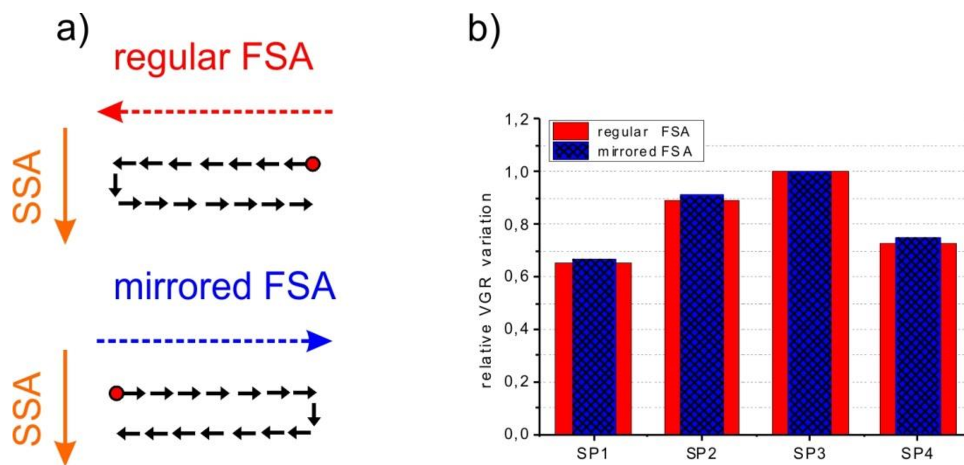

Figure S 4: patterning mirror experiments for serpentine strategies.

Supplement 4

4.1 Simulation framework for emulating scanning EBID

The time evolution of the adsorbed precursor gas coverage during EBID was estimated by the application of an explicit finite differencing numerical scheme to solve the following PDE;

$$\frac{\partial P(x,y,t)}{\partial t} = \delta\Phi_P(x,y)\Delta x^2 P(x,y,t) - \frac{\delta\Phi_P(x,y)}{s_P}P(x,y,t) - \frac{P(x,y,t)}{\tau} + D_P\left(\frac{\partial^2 P(x,y,t)}{\partial x^2} + \frac{\partial^2 P(x,y,t)}{\partial y^2}\right) - \delta_{SE_I}\Phi_{e^-}(x,y,t)\sigma P(x,y,t) \quad [\textbf{equation } 1]$$

where *P(x,y,t)* is the number of gas molecules per pixel of edge length Δx and surface area (Δx^2), δ is the impinging precursor gas sticking probability to the surface, s_P is the precursor gas surface density at maximum monolayer coverage, D_p is the surface diffusion coefficient of the precursor gas on the surface, $\delta_{SE(I)}$ is the number of secondary electrons emitted per incident primary electron, Φ_{e-} is the flux of the impinging primary electron beam and σ is the mean dissociation cross-section for the dissociation of absorbed precursor gas by the emitted secondary electrons. This methodology is similar to what we have reported recently[7] as well as by others in the past[2,3] with the addition of a space–dependent precursor flux term that will be described in detail below. Regarding the various terms in equation 1, terms #1 and #2 describe the change in precursor coverage due to the impinging precursor flux, term #3 describes the change in adsorbed precursor coverage due to precursor desorption, term #4 considers changes due to surface diffusion and finally term #5 which captures the dissociation of the adsorbed precursor by an impinging electron flux. The electron beam irradiates the surface at normal incidence leading to the following Gaussian approximation of the primary electron beam's flux on the substrate/deposit surface;

$$\Phi_{e^-}(x,y,t) = \frac{i_B}{2\pi q a^2} e\left(-\frac{(x-x_o(t))^2 + (y-y_o(t))^2}{2a^2}\right) \quad [equation\ 2]$$

where a is related to the full–width at half–maximum (*FWHM*) of the impinging electron beam according to $2a(2ln2)^{0.5}$=FWHM [4], i_B is the primary electron beam current and q is the charge of the electron. Electron beam motion was introduced into the simulation through the variables $x_o(t)$ and $y_o(t)$ facilitating either the serpentine or spiral pattern geometries of interest here. The beam is set to stationary at a specified location according to the beam dwell time then immediately moves to the next pixel.

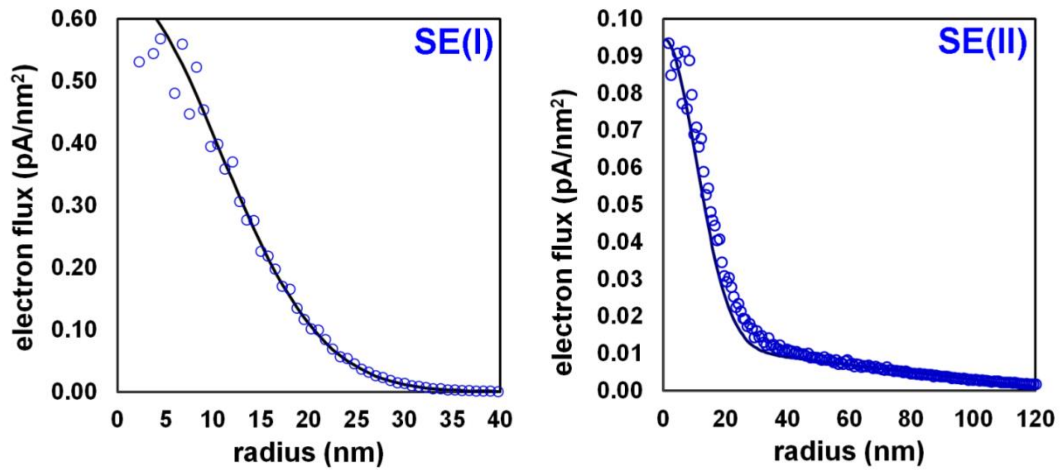

Figure S 5: Monte Carlo simulations (o) of electron surface emission profiles for a 5keV electron beam (FWHM=25nm, left) impinging a flat, 50nm semi–infinite slab of material with an average composition of PtC_5. The superimposed profile fits (black curves) were used in the simulation. The fit of the SE(II) distribution was estimated by way of the summation of a Gaussian (FWHM=33nm, i = $\delta_{SE(II)}$*η*i_B) and a simple linear function in radius (slope = $-1x10^{-4}$ pA/nm^3 and y–intercept = 0.013 pA/nm^2).

The height of the growing deposited was estimated according to;

$$\frac{dh(x,y)}{dt} = \frac{t_{ML}}{s_d \Delta x^2} \delta_{SE_I} \Phi_{e^-}(x,y,t) \sigma P(x,y,t) \quad [equation\ 3]$$

where t_{ML} is the thickness of a deposited monolayer and s_d is the surface density of a deposited monolayer. ***It is important to note that the height does not couple back in to the precursor coverage equation 1.*** Thus, the diffusion of precursor on the surface does not account for the change in height among adjacent pixels. As a result, the simulation in valid only for small deposit heights and becomes less accurate as the deposit grows in height. Nonetheless, for the relatively small pad aspect ratios studied here the simulation results were deemed an appropriate approximation of the experimental problem. The mean dissociation cross section σ for *MeCpPt(IV)Me* was estimated over the energy range *10–50 eV* using;

$$\sigma = \frac{\sum_{i=10eV}^{50eV} n_{SE}(E(i)) * \sigma\big(E(i)\big)}{\sum_{i=10eV}^{50eV} n_{SE}(E(i))} \quad [\textbf{\textit{equation}}\ 4]$$

where $\sigma(E(i))$ was estimated by fitting a curve to (Figure 6 in (5)), $n_{SE}(E(i))$ was derived from the Monte Carlo simulation[6] described above and the results are shown in Figure S 6.

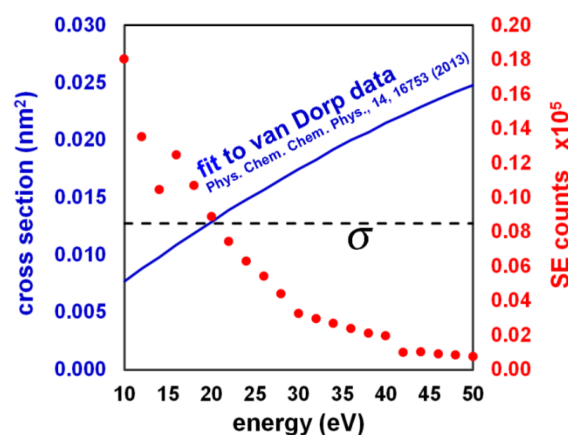

Figure S 6: the mean dissociation cross section (σ ~ 0.013 nm²) was estimated over the energy range from 10–50 eV using equation 4 which resulted in the hatched black line shown superimposed in the figure.

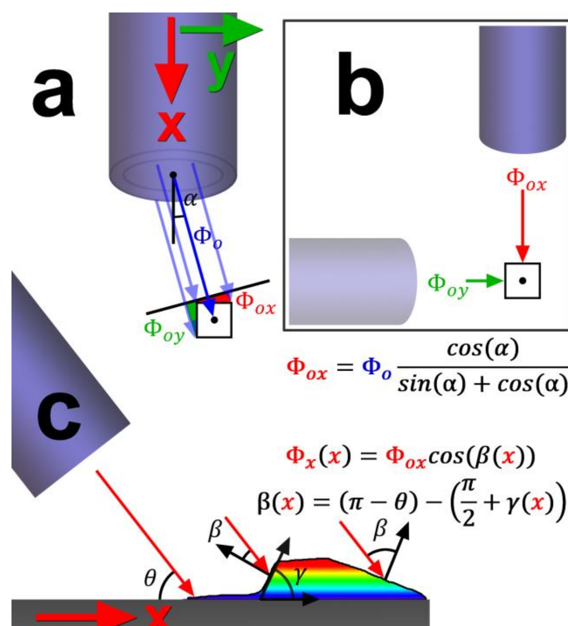

Figure S 7: (a) the geometric method used to partition the impinging precursor flux into *x*– and *y*– components. For example, the percentage of gas molecules striking the deposit (square black box) face were partitioned into a *y*– directed flux in the simulation (green area). (b) The approximation shown in (a) is analogous to having an additional, virtual precursor source along the *y*–direction as demonstrated schematically here. (c) The local precursor flux at the pixel level is modified in the simulation to account for the orientation of the pixel surface normal with respect to the impinging precursor vector according to the superimposed equations. This schematic shows the case for the x– direction. The same treatment was applied also in the y–direction.

4.2 Impinging precursor flux variations

The impinging precursor flux in the simulation domain was calculated according to;

$$\Phi_P = 3.513x10^{14} \frac{P}{\sqrt{MW * T_P}} \left[\frac{molecules}{\mu m^2 s}\right] \quad [equation\ 5]$$

where P is the local surface pressure, MW is the molecular weight of the precursor molecule and T_P is the temperature of the gas. In addition, the impinging precursor flux Φ_P was assumed to irradiate the surface at 52° with respect to a surface vector, parallel to the substrate plane, oriented along the *x*–direction of the simulation domain. *Inherent to the simulation is the assumption that all impinging gas*

molecules strike the surface along the same orientation over the 1 μm x 1 μm domain (see the blue vectors in Figure S 7a); effectively a 'beam'. This is clearly not the case, as shown by *Utke et-al*[51,6], where significant gas divergence occurs due partly to the large inside diameter of the precursor nozzle. However, the paraxial precursor flux assumption used here was adequate to reproduce several experimental observations.

Simulations revealed that the orientation of the local surface normal vector, with respect to the impinging gas flux vector, played a critical role in the evolution of h(x,y). The following procedure was implemented to approximate the effect of the angle of local gas impingement on the deposit surface and the role it plays in affecting *h(x,y)*. The impinging flux was partitioned into x (red shaded region, Figure S 7a) and y (green shaded region, Figure S 7a) components by the procedure illustrated in Figure S 7a and which was based on the spatial orientation of the deposit with respect to the orientation of the incident flux vector. This approach is complementary to the approximation of two virtual gas nozzles as shown in Figure S 7b. Once the Φ_{ox} is determined, the spatial dependence of the impinging precursor flux may be calculated as illustrated in Figure S 7c. β in turn depends on γ which ultimately imposes the *x* dependence on the problem. For example, γ appears in the simulation as;

$$\gamma_{(n,m,q)} = atan\left(\frac{h_{(n+1,m,q)} - h_{(n-1,m,q)}}{2\Delta x}\right) \quad [\textbf{equation } 6]$$

where only relatively short deposits are considered with respect to the width of the final box thereby avoiding problems, e.g., with steep sidewalls. The (*q*) index in equation 6 captures the time step where the space–dependent height changes with each time step in response to EBID. The pixel index (*n*) was used for the *x*–direction in the simulation while the index (*m*) was used to iterate in the *y*–direction. The angle θ is an input parameter.

Ultimately, the angle β was found to be the most critical parameter toward determining the final box deposit *h(x,y)* map. This angle represents the angle between a vector extended normal to the local substrate surface and the impinging flux vector (Figure S 7c). With regards to equation 1, the final flux term was;

$$\Phi_p(x,y) = \Phi_o\left[\cos(\beta(x))\frac{\cos(\alpha)}{\sin(\alpha)+\cos(\alpha)} + \cos(\delta(y))\frac{\sin(\alpha)}{\sin(\alpha)+\cos(\alpha)}\right] \cdot \boldsymbol{S}(\boldsymbol{x},\boldsymbol{y}) \quad [equation\ 7]$$

where δ is the matching angle to β but in the *y*–direction. Lastly, the variable ***S(x,y)*** is a two–dimensional array spanning the *x*– and *y*–directions that accounts for precursor shadowing that occurs when the deposit blocks precursor from striking the surrounding surface. An illustration of the shadowing effect is shown in Figure S 8.

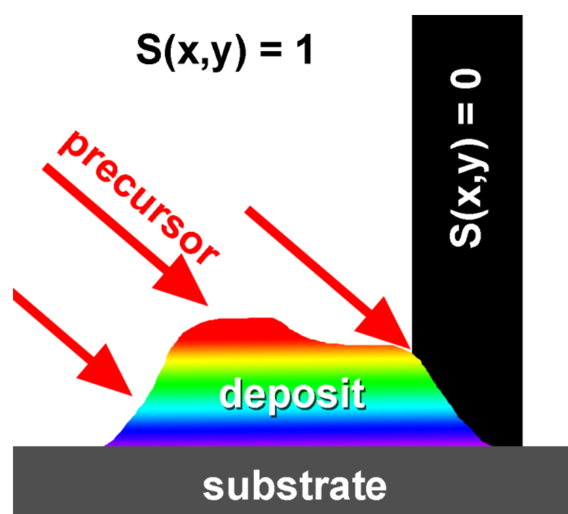

Figure S 8: the projected delivery of a precursor beam to the region of dissociation leads to the formation of a depleted zone on the opposite facing surface of the deposit. The process exhibits positive feedback exacerbating the shadowing effect for longer deposition times.

A representative explicit finite-difference equation to solve for *P(n,m,q+1)* where *q* is the time index.

$$P(n,m,q+1) = \frac{D_p \Delta t}{\Delta x^2}[P(n+1,m,q) + P(n-1,m,q) + P(n,m+1,q) + P(n,m-1,q) - 4P(n,m,q)]$$

$$- \frac{\sigma \Delta t}{q}\left[\frac{\delta_{SE(I)} i_B}{2\pi a_{SE(I)}^2} e^{-\left(\frac{(x(n)-x_o(t))^2+(y(m)-y_o(t))^2}{2a_{SE(I)}^2}\right)} + \frac{\delta_{SE(II)} \eta i_B}{2\pi a_{SE(II)}^2} e^{-\left(\frac{(x(n)-x_o(t))^2+(y(m)-y_o(t))^2}{2a_{SE(II)}^2}\right)} + m_{SE(II)}\sqrt{(x(n)-x_o(t))^2 + (y(m)-y_o(t))^2} + b_{SE(II)}\right] P(n,m,q)$$

$$- \frac{\delta \Delta t}{s_p}\left\{3.515x10^{14} \frac{P}{\sqrt{MW \cdot T_P}}\left[\frac{\cos(\alpha)}{\sin(\alpha)+\cos(\alpha)} \cos\left(\frac{\pi}{2} - \theta - atan\left(\frac{h(m+1,n,q) - h(m-1,n,q)}{2\Delta x}\right)\right) + \frac{\sin(\alpha)}{\sin(\alpha)+\cos(\alpha)} \cos\left(\frac{\pi}{2} - \theta - atan\left(\frac{h(m,n+1,q) - h(m,n-1,q)}{2\Delta x}\right)\right)\right]\right\} P(n,m,q) \cdot S(n,m) - \frac{\Delta t}{\tau} P(n,m,q)$$

$$+ \Delta t \delta \Delta x^2 \left\{3.515x10^{14} \frac{P}{\sqrt{MW \cdot T_P}}\left[\frac{\cos(\alpha)}{\sin(\alpha)+\cos(\alpha)} \cos\left(\frac{\pi}{2} - \theta - atan\left(\frac{h(m+1,n,q) - h(m-1,n,q)}{2\Delta x}\right)\right) + \frac{\sin(\alpha)}{\sin(\alpha)+\cos(\alpha)} \cos\left(\frac{\pi}{2} - \theta - atan\left(\frac{h(m,n+1,q) - h(m,n-1,q)}{2\Delta x}\right)\right)\right]\right\}$$

$$+ P(n,m,q) \quad [\,\textit{equation}\ 8]$$

Regarding the color coding in equation 8 above; **diffusion term**, **beam consumption terms**, **desorption term** and **adsorption terms**.

primary electron beam current	i_B	1600	*pA*
electron beam dwell time per pixel	τ_{dwell}	500	*µs*
precursor pressure at deposit	P_{local}	15	*mTorr*
precursor surface diffusion coefficient	D_P	0.65	$\mu m^2/s$
precursor sticking coefficient	δ	1	*[0-1]*
precursor mean residence time	τ	100	*µs*
precursor temperature	T_P	45	^oC
mean dissociation cross-section (10-50 eV)	σ	0.013	nm^2
maximum precursor surface density	s_P	2.8	PtC_9/nm^2
deposit surface density	s_d	9.6	PtC_5/nm^2
deposit monolayer thickness	t_{ML}	0.53	*nm*
simulation pixel size	Δx	5	*nm*
simulation time step	Δt	2.89	*µs*
simulation domain edge length (x and y)	x_{Sim}	1000	*nm*
deposit box edge length (x and y)	x_{Box}	494	*nm*
spacing between dwell points	Δx_{Scan}	13	*nm*
Precursor flux with respect to the x-direction	α	0°	*deg*
Nozzle angle with respect to the substrate surface	θ	52°	*deg*
BSE coefficient (PtC_5, 5keV)	η	0.28	*[0-1]*
SE(I) coefficient (PtC5, 5keV)	$\delta_{SE(I)}$	0.30	
SE(II) coefficient (PtC5, 5keV)	$\delta_{SE(II)}$	0.24	
FWHM, SE(I) beam	$a_{SE(I)}$	25	*nm*
FWHM, SE(II) beam	$a_{SE(II)}$	33	*nm*
SE(II) linear beam tail approximation slope	$m_{SE(II)}$	$(-)1x10^{-4}$	pA/nm^3
SE(II) linear beam tail approximation y-intercept	$b_{SE(II)}$	0.013	pA/nm^2

Table S 1: simulation parameters

Supplement 5

Figure S 9 shows the results for mirror experiments for spiral-out patterns to exclude directional scanning influences. Both patterns are shown in a) together with 2D AFM height images in b) revealing no difference of the levelled features. Additional rotation experiments (c) reveal, in agreement with Figure 4, two symmetrical situations at 30° and 75°, which excludes scan direction dependent effects.

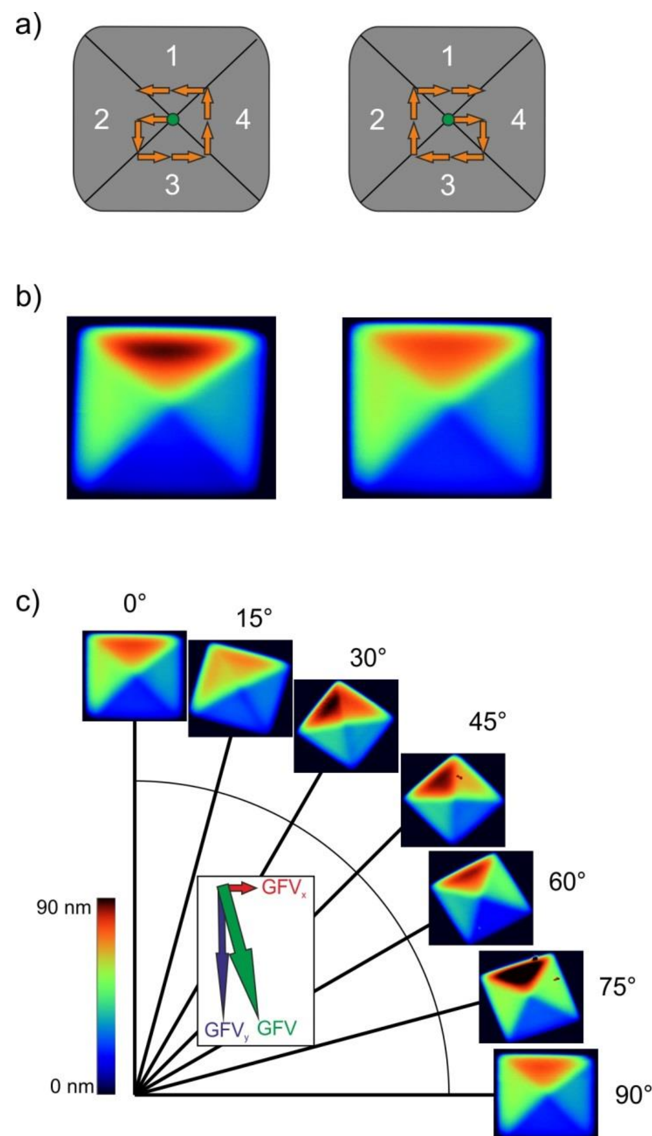

Figure S 9: mirror experiments for clockwise spiral-out patterns to exclude directional scanning influences.

Supplement 6

In order to exclude gas flux related effects and estimate the influence of surface diffusion, deposition experiments have been done with a retracted and turned off GIS before patterning was started. As can be seen in Figure S 10, the resulting pad is entirely flat which suggests that the gas flux is strongly involved in the morphological destabilization during deposition. Increasing the pixel dwell time from 1000 µs to 5000 µs results in a slight pyramidal shape (see Figure S 10) which reflects the decreasing precursor coverage over time as the beam moves outwards. However, even for such high dwell times the pads are laterally symmetric and do not show any terraced structure. Please note, complementary experiments without any precursor exposure revealed very low carbon deposition based on chamber residual which confirms the structures shown in Figure S 10 as Pt-C deposits.

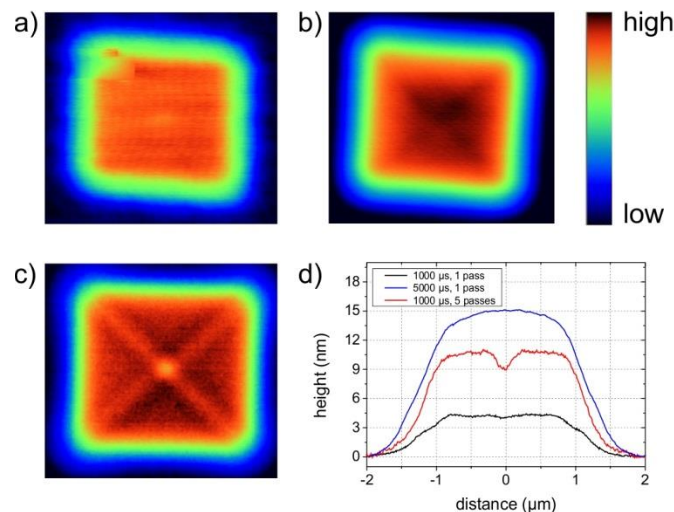

Figure S 10: AFM height images of deposits fabricated via spiral-out strategies as shown in Figure 3a but with the GIS gas flux turned off. Different dwell times of 1000 µs (a) and 5000 µs (b) have been used via single pass patterning while (c) shows a deposit grown at 1000 µs via 5 passes (5 keV, 1600 pA, 13 nm point pitch). Height cross sections of all deposits are shown in (d) (taken across central areas). Please note, the scale bar top right gives only qualitative height information since the used Z scales have been adapted to reveal morphological variations (image widths are 2.4 µm).

Supplement 7

Figure S 11 shows simulated height growth (left curves) for high ($6.5x10^{-9}$ $nm^2.s^{-1}$) and very low ($1x10^{-11}$ $nm^2.s^{-1}$) surface diffusion (upper and lower graph) revealing very similar growth evolution. More importantly, however, are the very similar morphologies for high (top green panel) and very low (bottom red panel) surface diffusion as well as practically identical the surface coverage distributions (bottom right plots). These comparisons confirm from a simulation point of view that surface diffusion is negligible for long dwell times and directional gas flux adsorption and geometrical shadowing is mainly responsible for the morphological instabilities.

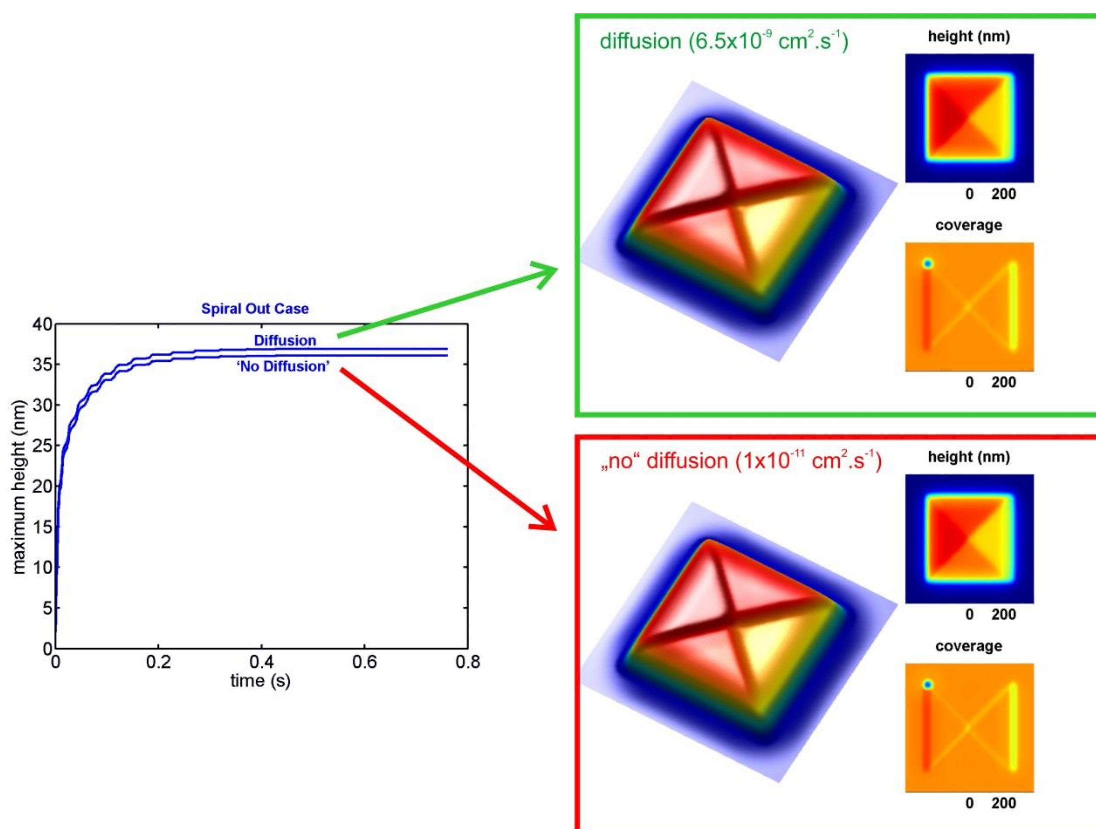

Figure S 11: simulated height growth (left curves) for high ($6.5x10^{-9}$ $cm^2.s^{-1}$) and very low ($1x10^{-11}$ $nm^2.s^{-1}$) surface diffusion (upper and lower graph).

Supplement 8

Figure S 12 summarizes the specification of diffusion coefficient from a series of pulsed FEBID experiments. The surface kinetics parameters determine the deposit profile in a stationary state for a given beam conditions. Three generic distinguishable shapes: Gaussian, Indent, Flat-top - corresponding to different process regimes - are predicted by simulations and observed in experiments (a). Starting from the MTL regime and decreasing the dwell time values DT, the transition between Flat-top and Gaussian profiles occurs (b). As in this regime the contribution of diffusion is negligible, the residence time of adsorbate and the net-dissociation cross section can be fitted to the growth rate function. In the next step the beam is adjusted to observe the indent shape (c). The indent value - IND_{DIFF} once the rest process parameters are known, depends on surface diffusion coefficient - D_P , which can be derived by numerically solving the equation of adsorbates concentration in continuum model[7]. From a series of pulsed FEBID experiments for $MeCpPt(IV)Me_3$ used as a precursor IND_{DIFF} = 0.07, which corresponds $D_P = 8.5 \times 10^{-10}$ $cm^2 s^{-1}$. The same equation allows to calculate the contribution of diffusion replenishment vs. flux replenishment, as a function of DT. The rate of incoming adsorbates due to the surface diffusion vs. due to the adsorption from gas phase is expressed by a formula:

$$\frac{D_P\left(\frac{1}{r}\frac{\partial n(r,t)}{\partial r}+\frac{\partial^2 n(r,t)}{\partial r^2}\right)}{sJ_{TOT}}$$

where *n(r,t)* is the concentration of adsorbates at the time - *t*, at a given distance from the beam center - *r*, *s* – sticking probability and J_{TOT} –impinging molecular flux.

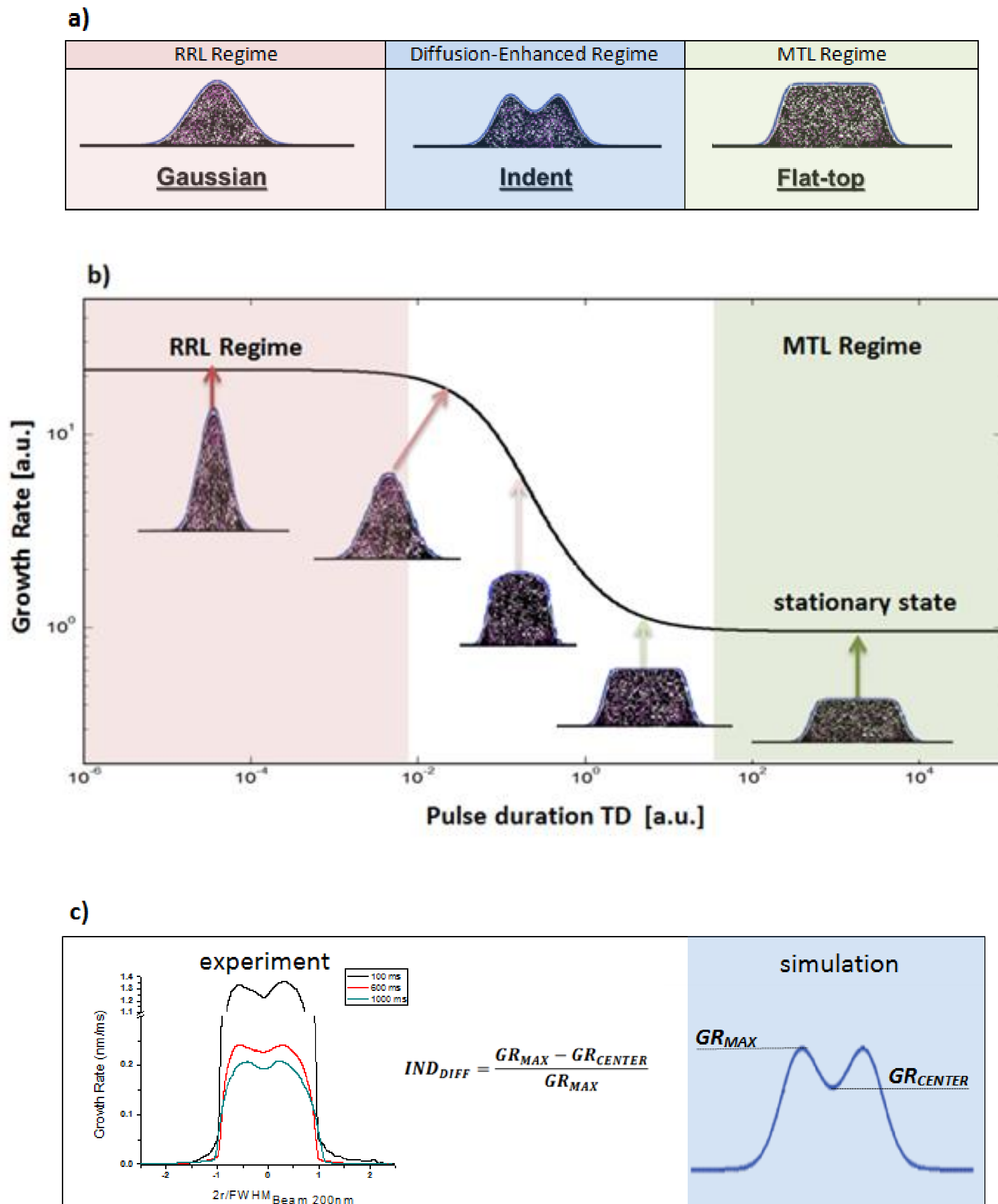

Figure S 12: Specification of diffusion coefficient from a series of pulsed FEBID experiments.

References

(1) Alkemade, P. F. A.; Miro, H.; van Veldhoven, E.; Maas, D. J.; Smith, D. A.; Rack, P. D. *J. Vac. Sci. Technol. B* **2011,** *29 (6),* 06FG05-1.

(2) Lobo, C. J.; Toth, M.; Wagner, R.; Thiel, B. L.; Lysaght, M. *Nanotechnology* **2008,** *19,* 025303.

(3) Rykaczewski, K.; White, W. B.; Fedorov, A. G. *J Appl Phys* **2007,** *101,* 054307.

(4) Utke, I.; Hoffmann, P.; Melngailis, J. *J Vac Sci Technol B* **2008,** *26,* 1197-1276.

(5) van Dorp, W. F. *Phys. Chem. Chem. Phys.* **2012,** *14,* 16753-16759.

(6) Utke, I.; Friedli, V.; Amorosi, S.; Michler, J.; Hoffmann, P. *Microelectron. Eng.* **2006,** *83,* 1499-1502.

(7) Szkudlarek, A.; Gabureac, M.; Utke, I. *J. Nanosci. Nanotechnol.* **2011,** *11 (9),* 8074-8078.

6.3 Appendix 3 - Publication 3

Publication 3

Toward Ultraflat Surface Morphologies During Focused Electron Beam Induced Nanosynthesis: Disruption Origins and Compensation.

Winkler, R.; Szkudlarek, A.; Fowlkes, J. D.; Rack, P. D.; Utke, I.; Plank, H.

ACS Appl. Mater. Interfaces **2015**, *7* (5), 3289–3297.

ACS APPLIED MATERIALS & INTERFACES
Research Article
www.acsami.org

Toward Ultraflat Surface Morphologies During Focused Electron Beam Induced Nanosynthesis: Disruption Origins and Compensation

Robert Winkler,[†] Aleksandra Szkudlarek,[‡,§] Jason D. Fowlkes,[‖,⊥] Philip D. Rack,[‖,⊥] Ivo Utke,[‡] and Harald Plank*,[†,#]

[†]Graz Centre for Electron Microscopy, Steyrergasse 17, 8010 Graz, Austria

[‡]EMPA, Swiss Federal Laboratories for Materials Science and Technology, Laboratory for Mechanics of Materials and Nanostructures, Feuerwerkerstrasse 39, 3602 Thun, Switzerland

[§]AGH University of Science and Technology, Academic Centre for Materials and Nanotechnology, A. Mickiewicza 30, 30-059 Krakow, Poland

[‖]Center for Nanophase Materials Sciences, Oak Ridge National Laboratory, Oak Ridge, Tennessee 37831, United States

[⊥]Department of Materials Science and Engineering, University of Tennessee, Knoxville, Tennessee 37996, United States

[#]Institute for Electron Microscopy and Nanoanalysis, Graz University of Technology, Steyrergasse 17, 8010 Graz, Austria

S *Supporting Information*

ABSTRACT: Emerging applications for nanoscale materials demand precise deposit shape retention from design to deposition. This study investigates the effects that disrupt high-fidelity shapes during focused electron beam induced nanosynthesis. It is shown that process parameters, patterning strategies and deposit topography can impose lateral precursor coverage gradients during growth resulting in unwanted topographic artifacts. The study classifies the evolving surface shapes into four general types and explains the formation and transition from a fundamental point of view. Continuum model calculations and simulations expand the experimental results to provide a comprehensive insight into understand the disruption mechanism. The findings demonstrate that the well-established concept of growth regimes has to be expanded by its lateral gradients as they strongly influence final shape fidelities. Finally, the study is complemented by a compensation strategy that improves the edge fidelity on the lower nanoscale to further push this technique toward the intrinsic limitations.

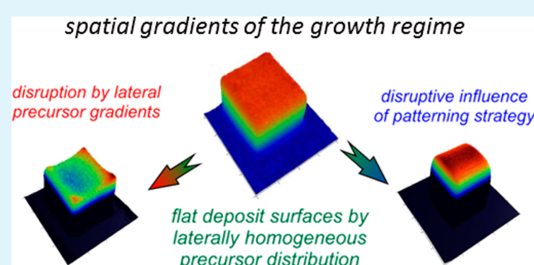

KEYWORDS: *focused electron beam induced deposition, patterning, morphology, platinum*

1. INTRODUCTION

Focused electron beam induced deposition (FEBID) relies on a highly localized nanosynthesis of functional precursor molecules via a nanometer sized, focused electron beam.[1−5] An injected gaseous precursor physisorbs on the specimen surface and is locally decomposed by an electron beam. Together with the very accurate and flexible positioning capabilities of the e-beam, FEBID represents a mask-less, additive direct-write method with spatial nanometer resolution, even on nonflat surfaces where classical resist based lithography is complicated or even impossible.[2,3,5−9] As different precursor chemistries provide a wide range of materials functionalities,[1,3] several application concepts have successfully been demonstrated including magneto-logics, storage or sensing[10,11] for magnetic deposits, strain sensors,[12] hall sensors,[13] and gas sensors.[14] While the long-lasting issue of unwanted carbon impurities in Co- and Pt-based deposits has recently been solved by different approaches,[9,15−20] topographic errors by means of missing flatness and/or edge sharpness still limits FEBID applications in which the morphology is an essential element (e.g., plasmonics, thin-film multilayer devices or high-resolution sensor gaps). Although progress has been made in the fundamental understanding of broadening effects which ultimately limits the achievable lateral resolution,[7,8,21−26] surface related aspects are rarely investigated with respect to its underlying mechanisms.[8,24] Such knowledge, however, is indispensable considering the industrial applications and their demand for predictable and reproducible shape fidelity on the lower nanoscale.

In this work, we therefore focus on the surface morphology of FEBID deposits, study disruption effects under different process conditions and link the experimental findings to lateral gradients in the precursor working regime. We demonstrate how surface morphologies of PtC deposits change as a function of process parameters, patterning strategies, and deposit thicknesses, leading to the identification of four basic morphologies. Continuum model calculations and finite difference simulations reveal that experimentally observed

Received: November 18, 2014
Accepted: January 15, 2015
Published: January 15, 2015

ACS Publications © 2015 American Chemical Society

DOI: 10.1021/am508052k
ACS Appl. Mater. Interfaces 2015, 7, 3289−3297

surface shapes can consistently be rationalized by lateral gradients of the precursor coverage during growth. By that, it becomes evident that the well-established concept of the growth regime has to be expanded to account for, albeit subtle, lateral gradients as they strongly influences final shape fidelity. Based on this fundamental understanding, we finally introduce a compensation strategy that sharpens the edges of nanoscale deposits toward ultraflat, high-fidelity morphologies of FEBID structures, which we surmise are critical for many applications.

2. RESULTS

In the following, we start with the influence of the patterning strategy on the morphology. On the basis of the findings, we then use the most appropriate patterning type for a systematic study of other relevant FEBID process parameters. This results in the classification of four basic morphologies, which are described in detail and whose formation is explained in the Discussion section and rationalized with calculations and simulations.

2.1. Patterning Strategy. The considerations start with the influence of different patterning strategies, namely, raster (RA) and serpentine (SP) scanning. Atomic force microscopy (AFM) height images in Figure 1 reveal the morphologies for raster and serpentine strategies, which become apparent for the shortest dwell times (DT) and highest beam currents, as will be discussed in the next subsection. A chair-like morphology evolves for raster scanning with the highest features at the starting points of each scanning line (arrows). In contrast, serpentine strategies lead to a tunnel-like morphology in which lowest deposit heights evolve at the reversal points of the e-beam (arrows). A more detailed comparison of cross-sectional height profiles is shown in the following section. As discussed by Winkler et al.,[17] alternative patterning strategies by means of spiral-in (SI) or spiral-out (SO) can be used; however, they lead to diagonal features (trench and ridge) at the turning point of the e-beam (Supplement 1, Supporting Information) and are therefore not suitable alternatives when aiming for flat surfaces. Considering the unfavorable lateral asymmetry of raster patterns (Figure 1a) further experiments have been conducted with serpentine patterning strategies as the most promising candidate toward flat deposit surfaces.

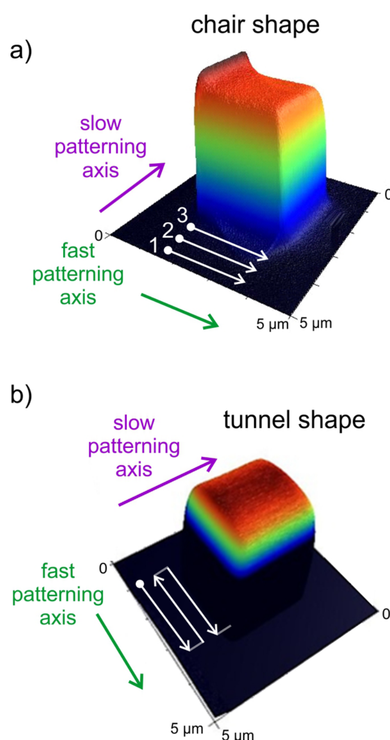

Figure 1. 3D-AFM height images of FEBID deposits fabricated via (a) raster and (b) serpentine patterning strategies resulting in chair- and tunnel-like morphologies, respectively. Both deposits were fabricated at 5 keV, 1600 pA, 1 μs dwell time, and 13 nm point pitch via 1000 patterning loops. The white arrows indicate the patterning sequence that defines the fast and slow patterning axes as indicated.

2.2. Patterning Parameters. Serpentine patterning was investigated over the processing range of beam current (25−6300 pA) and pixel dwell times (1−1000 μs) while the point pitch was kept constant at 13 nm. To provide constant total exposure times for each patterning pixel, we compensated decreasing DTs with an increasing number of patterning loops. On the basis of detailed AFM investigations, we divided the evolving surface morphologies into four different types for the investigated parameter space, as summarized in Figure 2: (1) flat, (2) concave, (3) slanted, and (4) patterning dependent. Representative 3D AFM height images are also shown to give a qualitative impression of the evolving morphologies. Note: The transition between these classifications varies, and the AFM images reveal the most pronounced results. In the following, a more detailed morphological description is given for all four types.

As a starting point, we consider the flat morphology (green range in Figure 2), which strongly suggests a steady-state precursor coverage gradient during patterning. As shown in the AFM height cross sections in Figure 3a, the deposits exhibit a fairly flat surface along the fast (parallel to the scan direction) and slow (orthogonal to the scan direction) patterning axes, as schematically shown in Figure 3e together with the gas flux direction.[17,27] The only deviations from an ideal situation are the nonvertical sidewall slopes and, in particular, the rounded upper edges. As discussed by Schmied et al.[24] and Arnold et al.[8] the former relies on a complex interplay between back- and forward scattered electrons from the substrate and the deposit itself. The latter, however, can be compensated toward sharper edges, as will be discussed later.

When the DTs were lowered, a concave shape evolved, as shown by a representative 3D AFM image in Figure 2 (yellow) and by AFM height cross sections in Figure 3b. Detailed analyses revealed the corners as the highest heights, edges as the intermediate heights, and central areas as the lowest heights that form the concave shape. Central cross-sectional profiles reveal no difference between fast and slow scan axes, as can be seen by essentially identical profiles in Figure 3b. As described in literature based on experiments, calculations, and simulations, it is well-known that lowest DTs lead to the lowest local precursor consumption and by that to the smallest lateral concentration gradients and low proximity depletion.[8,25,26,28,29] Intuitively, such a situation should then lead to most flat surfaces, which contradicts the observed concave shapes. However, it has to be kept in mind that very short DTs imply very short loop times, which strongly decreases the replenishment times in between two consecutive pulses at the same patterning pixel. This circumstance ultimately induces a lateral precursor gradient reflected by the concave morphology, as will be explained in detail in the Discussion section.

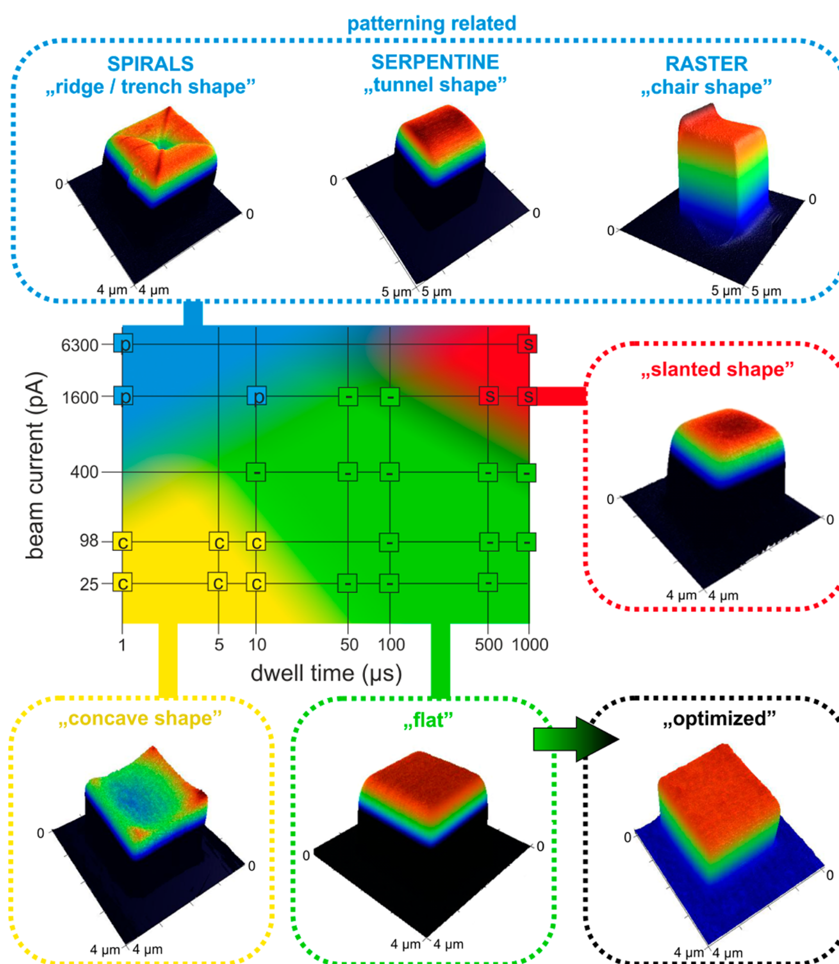

Figure 2. Classification of the morphology types obtained for serpentine/raster/spiral as a function of pixel dwell time (*x* axis) and beam current (*y* axis) for constant total exposure times at a primary electron energy of 5 keV: (green) flat, (yellow) concave, (red) slanted, and (blue) patterning related, which change shapes depending on the strategy used. AFM height images give a visualization of the four morphology types for the most illustrative parameter sets. (Bottom right) Representative image of a fully optimized patterning strategy within the flat regime (detailed explanation can be found in the main text).

In contrast, for very high beam currents and long dwell times (red area in Figure 2) a slanted morphology evolves. As evident by the AFM cross-sectional profiles in Figure 3c, the slant evolves only in the slow patterning axis (solid red), while widely flat surfaces are found along the fast patterning axis (dashed blue). Also, as evident on the right-hand side of the red cross-sectional profile and in the representative 3D AFM height image at the center (arrow) the final front is not as steep and smooth as the other three slopes. A similar effect has been reported for decreasing point pitches by van Dorp et al.,[30] who attributed this feature to enhanced secondary electron emission at the front slopes, which then increase the deposition rates, leading to ascending morphologies. Considering the very high beam currents, which entail higher local depletion, we expand this interpretation and suggest forward scattered electrons due to the thick deposits as discussed in detail later. Note: To rule out the influence of gas flux direction, we systematically rotated the pattern. The results revealed the slant is independent of the gas flux (Supplement 3, Supporting Information) which further supports the assignment to a FSE/SE-III related effect.

Finally, we again consider the blue range in Figure 2, which shows very different morphologies for different patterning strategies as discussed in the previous subsection. Here, we only discuss the most promising serpentine strategy within the investigated parameter space (details for raster strategy are in Supplement 5, Supporting Information). As can be seen by AFM height cross sections in Figure 3d, the surface is widely flat in the slow patterning direction (solid red) but strongly rounded at both edges along the fast patterning direction (dashed blue) which ultimately forms the tunnel shape (see representative 3D AFM inset). The dynamic evolution of this morphology is related to the turning points of the e-beam at the pattern edges as discussed in detail in the following section.

3. DISCUSSION

To correlate the experimentally found surface morphologies with lateral precursor gradients, we first need to consider different mechanisms of precursor replenishment during growth, following the notation and explanation by Winkler et al.[17] Three main components are involved in the local precursor replenishment for each patterning pixel: (1) gas flux replenishment (GFR) which is laterally constant, (2) surface diffusion replenishment from the deposit (SDR-D) following gas flux adsorption on the deposit surface, and (3) surface diffusion replenishment from the surrounding substrate (SDR-S). The two SDR components differ in that SDR-D components rely on the GFR contribution after local depletion due to the e-beam pulse while the surrounding substrate is

DOI: 10.1021/am508052k
ACS Appl. Mater. Interfaces 2015, 7, 3289−3297

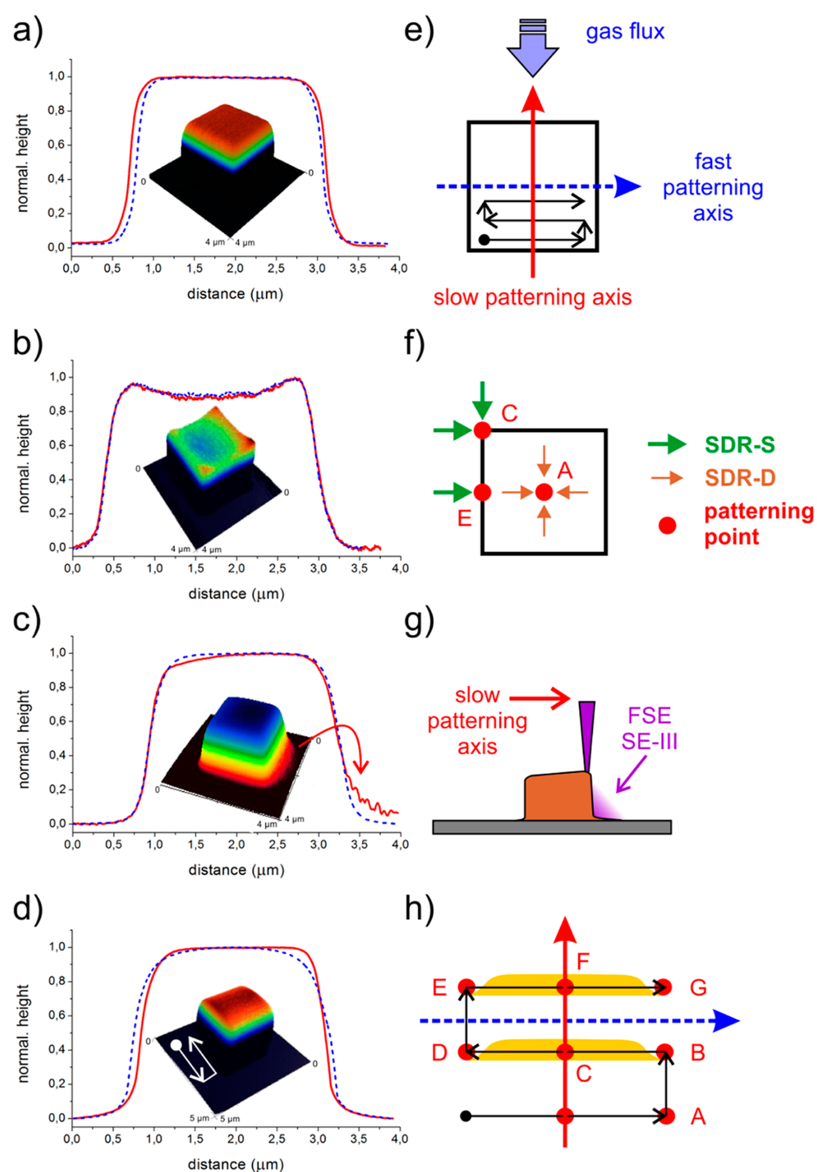

Figure 3. AFM height cross sections for (a) flat, (b) concave, (c) slanted, and (d) tunnel shapes, together with (insets) representative AFM 3D images. (e) Pattern footprint (black square) together with the serpentine strategy (black arrows) relative to the gas flux direction. The dashed blue and solid red lines indicate the directions of the AFM height cross sections along the fast and slow patterning axis, respectively, valid for all graphs in this figure. (f) Schematic representation of the different precursor adsorbate supply directions for surface diffusive replenishment (SDR) split into deposit related SDR-D and substrate related SDR-S components for three different patterning points (see text for details). (g) Scheme illustrating the deposit cross section and (purple) scanning e-beam and FSE/SE-III contributions leading to proximity growth,[8,24] as discussed in the text and simulated in Figure 4d. (h) Scheme illustrating the patterning process in detail for several pixel positions (red points) to explain the tunnel shape via different replenishment degrees, as indicated by the yellowish bars for two scan lines (see text for details).

unexposed, hence, having a higher virtually constant equilibrium coverage. Therefore, depending on the local depletion degree, SDR-S components (from outside the deposit) can be stronger than SDR-D contributions (from the deposit area itself) during replenishment. Furthermore, as shown by Winkler et al.[17] in detail, the slow patterning direction with respect to the incoming gas flux direction is essential.[17,27,31]

With this framework, we consider the four basic morphologies together with related patterning parameters and reveal, in conjunction with calculations and simulations, how laterally varying precursor regimes disrupt the intended surface morphology.

3.1. Surface Shapes. As a starting point, the flat morphologies are reconsidered and strongly suggest lateral homogeneous precursor coverage due to a local equilibrium between depletion and GFR, SDR-D, and SDR-S. For very short DTs, the dynamic situation during growth has to be considered. During the first patterning loop, a certain degree of local depletion occurs. While the gas flux replenishment component is constant, surface diffusion toward subsequently exposed patterning pixel plays an essential role as schematically shown in Figure 3f. For an edge point E the SDR-S component is stronger than the SDR-D component as the former supply path stem from unexposed, higher coverage regions. In contrast, a central patterning point A (Figure 3f) can mainly be replenished by GFR and SDR-D components due to the large distance from the substrate source (1 μm). Taking into account the short refresh times due to short DTs, it becomes

DOI: 10.1021/am508052k
ACS Appl. Mater. Interfaces 2015, 7, 3289−3297

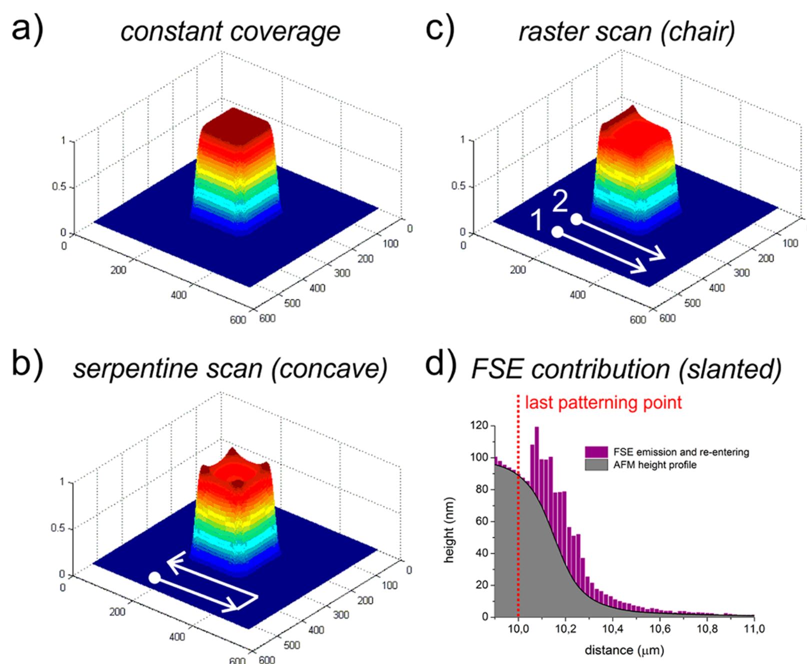

Figure 4. (a) Continuum model calculations of a raster/serpentine scanning strategy imposing a constant surface coverage of precursor adsorbates over time and position: a flat surface is obtained for both patterning strategies. Subsequently, surface diffusion was enabled together with raster (c) and serpentine strategy (b) revealing the chairlike and concave shapes, respectively, as experimentally observed (see Figure 3). (d) Monte Carlo simulations of electron trajectories (5 keV primary electrons) for real deposit shape (AFM profile in gray) and material (typical PtC_5 composition). The purple bars indicate exiting and re-entering FSE contributions (entailing SE-IIIs), as suggested for the slanted morphologies (arbitrary intensity scale). The far-reaching proximity deposition is then expected to increase the base level on which subsequent deposition along the slow patterning axis takes place leading to the ascending morphologies shown in Figure 3c for the slanted shape.

evident that the edge point E has a higher coverage and consequently a higher volume growth rate due to the stronger SDR-S component compared to central SDR-D contributions. This situation becomes even more dominant at corner points C (Figure 3f), as there are two different SDR-S directions that contribute compared to a single directional supply at point E. Cumulatively, this explains the concave shape shown in the representative 3D AFM inset in Figure 3b. To further support these assumptions, the continuum model has been used to simulate the results.[32,33] First, constant precursor coverage over time and position has been assumed during patterning leading to flat surfaces, as shown in Figure 4a. Then, dynamic depletion and surface diffusion were enabled, which lead to concave shapes for the shortest DTs, as representatively shown in Figure 4b, in agreement with experimental findings. Increasing DTs during the experiments (right-hand shift in Figure 2) lead to increased refresh times and improve the local replenishment situation for each patterning point resulting in flat surfaces.

In contrast, when using short DTs but higher beam currents (upward direction in Figure 2) the volumetric growth rates also increase. The higher deposits have then to be considered as morphological barrier which complicates the diffusion via substrate related SDR-S paths (average diffusion lengths have been estimated to be <25 nm via simulations in Winkler et al.[17] in agreement with previous work by Alkemade et al.[34,35]). Consequently, the SDR-S component decreases at increasing deposit heights and deposit related SDR-D contributions dominate which finally lead to the tunnel shapes as discussed later. Therefore, it can be concluded that the evolving concave shape is a consequence of short refresh times and site specific precursor gradients due to the different replenishment components (SDR-S at edges/corners versus SDR-D for central areas). Experiments (short DTs, low beam currents) with deposit heights above the average diffusion lengths[17] still show the concave shape, which is attributed to the fact that once the concave shape evolved during early growth, it is mimicked for further growth. By that, the experimentally observed concave height morphology can be understood as a direct visualization of lateral precursor gradients at such patterning conditions. This demonstrates that for the highest shape retention the classically used concept of the growth regime has to be expanded to account for the lateral distribution as subtle gradients impact the final morphology.

Next, the slanted morphology at highest DTs and beam currents is considered (red area in Figure 2). As shown by Winkler et al.[17] such patterning conditions lead to strong local depletion and an excess number of electrons (molecule limited regime). Also, it has to be considered that the pixel growth rate is high leading to deposit heights above the average diffusion lengths.[17] Consequently, the growth front is predominantly replenished by the gas flux and SDR-D related downward diffusion leading to lower growth efficiencies compared to situations where SDR-S components are strongly contributing.[17] Based on quantitative AFM data, Monte Carlo electron scattering simulations have been conducted to investigate the surface flux of forward scattered electrons (FSE). Figure 4d shows the AFM height profile (gray) with emitted and re-entering FSEs as purple overlay together with the last patterning point indicated by the dashed vertical line. On one hand, these FSE are expected to directly contribute to the dissociation process, on other hand they trigger a cascade of secondary electrons (defines as SE-III) which are assumed to be the predominant dissociation species due to their relatively higher dissociation cross-section.[36−38] As discussed in detail by

DOI: 10.1021/am508052k
ACS Appl. Mater. Interfaces 2015, 7, 3289−3297

Schmied et al.[24] these FSE contributions not only leads to a broadening of the deposit slope but also to a FSE related proximity deposition since re-entering FSEs impact substrate areas where all replenishment components (GFR, SDR-S) provide comparable high precursor coverage. Hence, as shown by the scheme in Figure 3g, FSE/SE-III contributions (purple shades) lead to deposit growth outside the scanning pattern. Subsequent patterning rows then start on higher base levels which ultimately lead to the ascending deposit heights along the slow patterning direction as schematically shown in Figure 3g (brown box). Further evidence comes from final cross sections (solid red line in Figure 3c), which show higher structures on the front end also recognizable in the representative 3D AFM inset. This explanation is further consistent with the fact that this effect should only be dominant for a high number of (unconsumed) FSEs which require high beam currents and long DTs in agreement with the parameter map in Figure 2 (see also Supplement 3, Supporting Information). The main point of this section is the finding that lateral precursor gradients can result in excessive deposition at deposit slope via electron emission (FSE/SE-III) and entailed re-entry which leads to unwanted proximity deposition.

Finally, the patterning dependent morphologies need to be discussed which evolve for low-to-medium DTs and medium-to-high beam currents (blue region in Figure 2). First, the raster scan is considered which leads to a chair like morphology as shown in Figure 1a. It is well-known that the local depletion increases with DT on a single pixel.[1] This, in turn, induces a concentration gradient in the beam proximity, which initiates surface diffusion toward the exposed patterning pixel. As demonstrated by Plank et al.[26] the radius of this concentration gradient can reach 100 nm for deposition parameters according to the blue range in Figure 2. This implies that subsequent patterning points start at slightly depleted areas, which reduce the volume growth rate. Expanding this concept along a single scan line, the growth rate continuously decays until it reaches a nonzero steady-state situation governed by GFR and SDR-D components. If the line scan is long enough, (indicated by arrows in Figure 1a) the starting point of consecutive lines are not affected by proximity related depletion as it is fully replenished during the line scan. Again, this chairlike morphology directly reflects the transient behavior of the precursor coverage during each line scan where it is initially high at the beginning of the line and decays to a steady state value. To investigate this assumption via calculations, we again used the continuum model. Figure 4c shows the result in which the chair like feature on the left-hand side is clearly evident (see patterning directions at the bottom). The decay length, however, should be a function of the DT (and current) because longer beam pulses should establish steady state conditions during the first patterning points. This has been verified by additional experiments together with its dependence on the gas flux direction (Supplement 2, Supporting Information) which, together with the calculations, support the explanation for chair like surface shapes.

When changing the patterning strategy from raster to serpentine at same parameters, the morphology changes into tunnel shapes, as shown in Figure 1b. Figure 3d gives the associated cross-sectional profiles along the slow and fast patterning direction revealing the downward bent characteristics only for the fast scan axis (compare to the 3D AFM inset and the arrows). To explain this behavior, we must consider the dynamically changing SDR-S: due to the high beam currents, the deposit heights in the range of 100 nm exceed the average diffusion lengths which minimize SDR-S as replenishment components.[17] This implies that the volume growth rate at the line ends (path from point C to D in Figure 3h) decays, as experimentally observed. In contrast, the SDR-D still delivers precursor molecules as the replenishment of every deposit plateau after every loop as the GFR stays constant. Additionally, we condsider the different replenishment situation for subsequently patterned points E and F in Figure 3h: while point E is strongly depleted due to the quasi-stationary beam movement at the reversal point (D → E), point F has more time to be replenished by GFR and SDR-D components, further increasing the central volume growth rates. Both effects together lead to lower surface coverage at the reversal points (indicated by the yellow bars), leading to downward bent side walls parallel to slow patterning axis as experimentally observed (blue line and 3D AFM image in Figure 3d). When reducing the beam current at short DTs, the tunnels are shaped into concave morphologies as expected. This can be explained by the reduced deposits heights that enable SDR-S components to contribute, which first balances the tunnel shapes and then dominates the situation toward concave shapes, as experimentally observed.

The most important finding from this section is the concept that growth regimes necessarily has to be expanded to include evolving lateral gradients. This not only has strong impact on the surface morphology as discussed above, but it is also expected to have implications on the lateral chemistry and functionality as it is strongly connected to local growth regimes.[39,40] From a practical point of view, we can state that the most beneficial patterning strategy seems to be the serpentine approach which, within the right parameter range, provides extremely flat surfaces, however, with rounded edges. The latter aspect is discussed in the following section, including a compensation strategy based on the fundamental understanding derived above.

3.2. Edge Effect Correction in Flat Shape Exposure Conditions. As outlined in the previous section, flat shapes are obtained by achieving laterally homogeneous precursor coverage due to a local equilibrium between depletion and GFR, SDR-D, and SDR-S. Consequently, we can refer to the knowledge of classical resist-based e-beam lithography[41,42] to address any shape deviations, especially to improve the sharpness of round edges due to proximity effects. As discussed in detail by Schmied et al.,[24] the side walls of a FEBID deposit show a symmetrically increasing/decreasing slope around the edge patterning points as schematically indicated in Figure 5b,c. Careful correlation revealed the lateral expansion of the upper edge rounding toward a constant height in good agreement with the backscatter electrons (BSE) radius of about 100 nm in typical PtC_5 deposits.[8,24] Similar to the FSE discussion, it has to be noted that we assume BSE-related secondary electrons type II (SE-II) as the predominant dissociation species and BSE only as predominant trigger-electrons, although a certain contribution via direct BSE dissociation is also assumed. To explain the rounded top edge, we consider different patterning points, as shown by the scheme in Figure 5a. The growth rate for a central point is given by (1) direct exposure at this point and (2) by BSE/SE-II contributions from surrounding areas according to the BSE radius within the deposit. However, the growth rate of edge points consists only from its direct exposure and BSE/SE-II support from the inner areas meaning ~38% decay of BSE/SE-II contributions. The situation is even

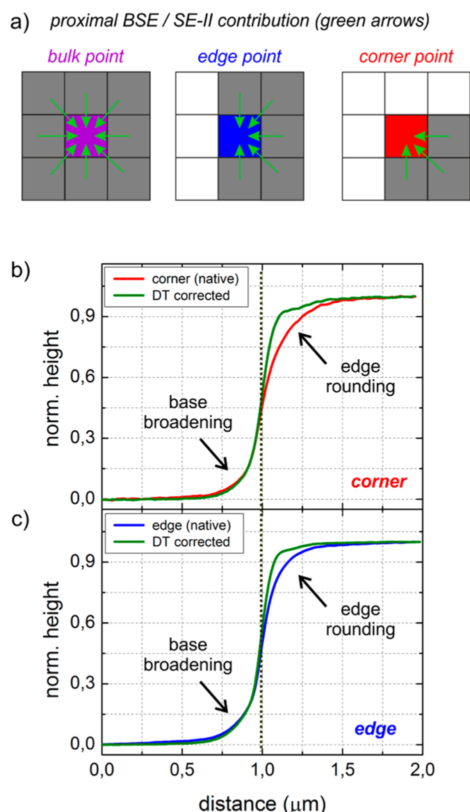

Figure 5. Illustration of edge-sharpness improvement within flat shape exposure conditions. (a) Schematic top view showing the proximity effect due to BSE/SE-II contributions from surrounding deposit areas for (left) bulk, (center) edge, and (right) corner points, which illustrate that missing neighbors lead to reduced volume growth rates at edge and corner patterning points. The real edge profiles (AFM cross sections) are shown in (b, red line) corner points and (c, blue line) edge points; (b and c, green curves) improvements in edge sharpness can be achieved by applying additional dwell time for patterning points close to the edges (within the BSE radius in PtC_5). However, the base broadening effects are a convolution of substrate related BSE/SE-II and deposit related FSE contributions, which cannot be compensated by the given strategy.[8,24]

worse for corner points in which ∼63% of the BSE/SE-II contribution gets lost (details are in Supplement 4, Supporting Information) compared to central patterning points. Figure 5b,c show AFM height cross sections across a corner and an edge by red and blue curves, respectively. As can be seen, the edge rounding for corners is highest as expected due to the above-mentioned explanation. However, this lack of dissociating electrons at edges and corners can be corrected by dynamic DT adaption. The result of such a compensation strategy is also shown in Figure 5b and considerably minimizes the edge sharpness and supports the model above. The base broadening, however, is a complex process between substrate related BSE/SE-II and FSE/SE-III,[8,24] which cannot be compensated by the DT approach. Note that independent of the position or compensation, the outer tails are always similar. Hence, the introduced compensation allows sharpening of upper edges and corners but cannot be used for reducing the base broadening. The latter can only be reduced by highest primary energies as shown in detail by Schmied et al.[24] Please note, despite the strong improvement based on simple calculations (Supplement 4, Supporting Information) we consider a simulation based compensation approach as most promising as it can account for different situations such varying deposit footprints or smaller heights where the vertical expansion of the interaction volume can change the situation. Such simulation and experimental compensation strategies with electron beam parameter adaptations and gas flux vector contributions will be elaborated in a future work.

4. CONCLUSION

In conclusion, we have demonstrated how the surface morphology changes as a function of lateral precursor gradients, induced by varying dwell times and beam currents. We could classify the shapes in four different types: (1) flat, (2) concave, (3) slanted, and (4) patterning dependent. The latter can be further categorized into different shapes such as trenches, chairlike, and tunnel-shapes for spiral, raster, and serpentine scanning, respectively. The serpentine patterning strategy turned out to be most symmetric and predictable in terms of generating flat-top surface morphologies. Although the flat regime provides sufficiently homogeneous surface properties, the edges and corners are always found to be rounded which, together with previous studies, is suggested to originate from backscattered electrons of the deposit. However, we successfully demonstrated an edge-correction approach, which considerably enhances edge and corner sharpness. Together with previous studies, we can summarize some major effects that disrupt ideal surfaces: (1) gas flux effects, avoidable;[17] (2) surface curvature, avoidable (this study); (3) edge rounding, compensable (this study); and (4) base broadening, minimizable.[7,21,24] The main aspect of this study, however, is the fact that lateral precursor gradients are responsible for the observed deviations from ideally flat surfaces. Also, despite the fact that lowest beam currents and shortest dwell times have often been considered ideal, as it promotes the electron limited regime, the study demonstrated that lateral precursor gradients have strong implications and can lead to nonideal results. Therefore, the well-established concept of the growth regime has to be expanded to include possible subtle lateral gradients to exploit the full potential toward high fidelity shapes for real FEBID applications.

5. METHODOLOGY

All FEBID deposits were fabricated with a NOVA 200 dual beam system (FEI, The Netherlands) using MeCpPt(IV)Me_3 precursor in combination with a standard FEI gas injection system (GIS) having inner and outer diameters of 500 and 830 μm, respectively. The GIS was tilted by 52° with respect to the sample surface and placed at a vertical distance of 180 ± 10 μm with the long GIS main axis arranged in a lateral distance of 200 ± 10 μm with respect to the deposition area as described in detail in [17]. Si samples with an area of 10 × 10 mm and with 3 nm SiO_2 (see reference 16) were used and prepared in a laminar flow box for experiments. After immediate transfer of the samples to the dual beam microscope chamber, a background pressure of at least 9×10^{-6} mbar was established before any experiment was conducted.

After beam focusing in the eucentric height (5 mm), the stage was moved to the deposition area (blanked e-beam) and then rested for at least 15 min to minimize mechanically induced stage drift. The precursor was preheated to 45 °C for at least 30 min prior to any experiments and opened for at least 3 min prior to any deposition to provide equilibrium surface coverages. All experiments in this study have been performed at 5 keV primary energies and a pixel distance (point pitch) of 13 nm. The electron beam movement was controlled via stream files, generated with Matlab (release 2010b, MathWorks, U.S.) and double checked on errors in the point sequence. After successful deposition the structures were characterized via Atomic

force microscopy (AFM) performed with a Dimension 3100 microscope (Bruker AXS, Billerica, MA) operated with a Nanoscope IVa controller and equipped with a XYZ Hybrid scan head using Olympus OMCL TS-160/TS-240 cantilever in tapping mode. AFM tip convolution plays a negligible role at upper edges/corners due to comparable large curvatures (>20 nm in XY; < 10 nm in Z) compared to the AFM tip radii of about 5 nm. At deposit side walls, tip convolution only plays a role for deposits above 100 nm thickness, leading to slight overestimation of deposit base widths. However, as morphological effects on the deposit surface were the main focus of the study, the latter influences are of minor relevance. Analyses were performed using NanoScope Analysis software (v1.4, Bruker AXS, Billerica, MA) and Gwyddion (v2.37). A detailed description of the continuum model calculations and finite difference simulation is given in reference 17.

■ ASSOCIATED CONTENT

Ⓢ Supporting Information

Morphological features obtained by using spiral patterning strategies; independency of chairlike and slanted morphologies on the directed gas flux; details of dwell time correction at edges and corners to minimize the top edge rounding effect; and deposit morphology evolution for raster and spiral patterning in dependency on dwell times and beam currents. This material is available free of charge via the Internet at http://pubs.acs.org.

■ AUTHOR INFORMATION

Corresponding Author

*E-mail: harald.plank@felmi-zfe.at. Tel: +43 316 873 8821.

Notes

The authors declare no competing financial interest.

■ ACKNOWLEDGMENTS

R.W. and H.P. gratefully acknowledge the valuable support provided by Prof. Dr. Ferdinand Hofer, DI Roland Schmied, DI Barbara Geier, DI Angelina Orthacker, DI Thomas Ganner, Ulrich Haselmann, Georg Arnold, and Martina Dienstleder. R.W. and H.P. also acknowledge financial support by the COST action CELINA (No. CM1301) and the EUROSTARS project TRIPLE-S (No. E! 8213). P.D.R. and J.D.F. acknowledge that their contributions were supported by the Center for Nanophase Materials Sciences, which is sponsored at Oak Ridge National Laboratory by the Scientific User Facilities Division, Office of Basic Energy Sciences, U.S. Department of Energy.

■ REFERENCES

(1) Utke, I.; Russell, P. E. *Nanofabrication Using Focused Ion and Electron Beams: Principles and Applications.*; Oxford University Press: New York, 2012.

(2) Van Dorp, W. F.; Hagen, C. W. A Critical Literature Review of Focused Electron Beam Induced Deposition. *J. Appl. Phys.* **2008**, *104*, 081301.

(3) Botman, a; Mulders, J. J. L.; Hagen, C. W. Creating Pure Nanostructures from Electron-Beam-Induced Deposition Using Purification Techniques: A Technology Perspective. *Nanotechnology* **2009**, *20*, 372001.

(4) Van Dorp, W. F.; Hansen, T. W.; Wagner, J. B.; De Hosson, J. T. M. The Role of Electron-Stimulated Desorption in Focused Electron Beam Induced Deposition. *Beilstein J. Nanotechnol.* **2013**, *4*, 474−480.

(5) Randolph, S. J.; Fowlkes, J. D.; Rack, P. D. Focused, Nanoscale Electron-Beam-Induced Deposition and Etching. *Crit. Rev. Solid State Mater. Sci.* **2006**, *31*, 55−89.

(6) Utke, I.; Hoffmann, P.; Melngailis, J. Gas-Assisted Focused Electron Beam and Ion Beam Processing and Fabrication. *J. Vac. Sci. Technol., B: Microelectron. Nanometer Struct.—Process., Meas., Phenom.* **2008**, *26*, 1197.

(7) Hari, S.; Hagen, C. W.; Verduin, T.; Kruit, P. Size and Shape Control of Sub-20 Nm Patterns Fabricated Using Focused Electron Beam-Induced Processing. *J. Micro/Nanolithogr., MEMS, MOEMS* **2014**, *13*, 033002.

(8) Arnold, G.; Timilsina, R.; Fowlkes, J. D.; Orthacker, A.; Kothleitner, G.; Rack, P. D.; Plank, H. Fundamental Resolution Limits during Electron Induced Direct Write Synthesis. *ACS Appl. Mater. Interfaces* **2014**, *6*, 7380−7387.

(9) Mehendale, S.; Mulders, J. J. L.; Trompenaars, P. H. F. A New Sequential EBID Process for the Creation of Pure Pt Structures from MeCpPtMe3. *Nanotechnology* **2013**, *24*, 145303.

(10) Gavagnin, M.; Wanzenboeck, H. D.; Belić, D.; Bertagnolli, E. Synthesis of Individually Tuned Nanomagnets for Nanomagnet Logic by Direct Write Focused Electron Beam Induced Deposition. *ACS Nano* **2013**, *7*, 777−784.

(11) Gabureac, M.; Bernau, L.; Utke, I.; Boero, G. Granular Co−C Nano-Hall Sensors by Focused-Beam-Induced Deposition. *Nanotechnology* **2010**, *21*, 115503.

(12) Huth, M.; Porrati, F.; Schwalb, C.; Winhold, M.; Sachser, R.; Dukic, M.; Adams, J.; Fantner, G. Focused Electron Beam Induced Deposition: A Perspective. *Beilstein J. Nanotechnol.* **2012**, *3*, 597−619.

(13) Gabureac, M. S.; Bernau, L.; Boero, G.; Utke, I. Single Superparamagnetic Bead Detection and Direct Tracing of Bead Position Using Novel Nanocomposite Nano-Hall Sensors. *IEEE Trans. Nanotechnol.* **2013**, *12*, 668−673.

(14) Kolb, F.; Schmoltner, K.; Huth, M.; Hohenau, A.; Krenn, J.; Klug, A.; List, E. J. W.; Plank, H. Variable Tunneling Barriers in FEBID Based PtC Metal-Matrix Nanocomposites as a Transducing Element for Humidity Sensing. *Nanotechnology* **2013**, *24*, 305501.

(15) Plank, H.; Noh, J. H.; Fowlkes, J. D.; Lester, K.; Lewis, B. B.; Rack, P. D. Electron-Beam-Assisted Oxygen Purification at Low Temperatures for Electron-Beam-Induced Pt Deposits: Towards Pure and High-Fidelity Nanostructures. *ACS Appl. Mater. Interfaces* **2014**, *6*, 1018−1024.

(16) Geier, B.; Gspan, C.; Winkler, R.; Schmied, R.; Fowlkes, J. D.; Fitzek, H.; Rauch, S.; Rattenberger, J.; Rack, P. D.; Plank, H. Rapid and Highly Compact Purification for Focused Electron Beam Induced Deposits: A Low Temperature Approach Using Electron Stimulated H_2O Reactions. *J. Phys. Chem. C* **2014**, *118*, 14009−14016.

(17) Winkler, R.; Fowlkes, J.; Szkudlarek, A.; Utke, I.; Rack, P. D.; Plank, H. The Nanoscale Implications of a Molecular Gas Beam during Electron Beam Induced Deposition. *ACS Appl. Mater. Interfaces* **2014**, *6*, 2987−2995.

(18) Sachser, R.; Reith, H.; Huzel, D.; Winhold, M.; Huth, M. Catalytic Purification of Directly Written Nanostructured Pt Microelectrodes. *ACS Appl. Mater. Interfaces* **2014**, *6*, 15868−15874.

(19) Stanford, M. G.; Lewis, B. B.; Noh, J. H.; Fowlkes, J. D.; Roberts, N. A.; Plank, H.; Rack, P. D. Purification of Nanoscale Electron-Beam-Induced Platinum Deposits via a Pulsed Laser-Induced Oxidation Reaction. *ACS Appl. Mater. Interfaces* **2014**, *6*, 21256−21263.

(20) Begun, E.; Dobrovolskiy, O.; Sachser, R.; Gspan, C.; Plank, H.; Huth, M. Post-Growth Purification of Co Nanostructures Prepared by Focused Electron Beam Induced Deposition. *Nanotechnology***2015**, in print.

(21) Van Oven, J. C.; Berwald, F.; Berggren, K. K.; Kruit, P.; Hagen, C. W. Electron-Beam-Induced Deposition of 3-Nm-Half-Pitch Patterns on Bulk Si. *J. Vac. Sci. Technol., B: Microelectron. Nanometer Struct.—Process., Meas., Phenom.* **2011**, *29*, 06F305.

(22) Van Dorp, W. F.; van Someren, B.; Hagen, C. W.; Kruit, P.; Crozier, P. A. Approaching the Resolution Limit of Nanometer-Scale Electron Beam-Induced Deposition. *Nano Lett.* **2005**, *5*, 1303−1307.

(23) Van Dorp, W. F.; Hagen, C. W.; Crozier, P. A.; Kruit, P. Growth Behavior near the Ultimate Resolution of Nanometer-Scale Focused

Electron Beam-Induced Deposition. *Nanotechnology* **2008**, *19*, 225305−225309.
(24) Schmied, R.; Fowlkes, J. D.; Winkler, R.; Rack, P. D.; Plank, H. Fundamental Edge Broadening Effects during Focused Electron Beam Induced Nanosynthesis*Beilstein J. Nanotechnol.***2015**, accepted.
(25) Utke, I.; Friedli, V.; Purrucker, M.; Michler, J. Resolution in Focused Electron- and Ion-Beam Induced Processing. *J. Vac. Sci. Technol., B: Microelectron. Nanometer Struct.—Process., Meas., Phenom.* **2007**, *25*, 2219−2223.
(26) Plank, H.; Smith, D. A.; Haber, T.; Rack, P. D.; Hofer, F. Fundamental Proximity Effects in Focused Electron Beam Induced Deposition. *ACS Nano* **2012**, *6*, 286−294.
(27) Bret, T.; Utke, I.; Hoffmann, P.; Abourida, M.; Doppelt, P. Electron Range Effects in Focused Electron Beam Induced Deposition of 3D Nanostructures. *Microelectron. Eng.* **2006**, *83*, 1482−1486.
(28) Lassiter, M. G.; Rack, P. D. Nanoscale Electron Beam Induced Etching: A Continuum Model That Correlates the Etch Profile to the Experimental Parameters. *Nanotechnology* **2008**, *19*, 455306−455314.
(29) Smith, D. A.; Fowlkes, J. D.; Rack, P. D. Understanding the Kinetics and Nanoscale Morphology of Electron-Beam-Induced Deposition via a Three-Dimensional Monte Carlo Simulation: The Effects of the Precursor Molecule and the Deposited Material. *Small J.* **2008**, *4*, 1382−1389.
(30) van Dorp, W. F.; Lazar, S.; Hagen, C. W.; Kruit, P. Solutions to a Proximity Effect in High Resolution Electron Beam Induced Deposition. *J. Vac. Sci. Technol., B: Microelectron. Nanometer Struct.—Process., Meas., Phenom.* **2007**, *25*, 1603.
(31) Friedli, V.; Utke, I. Optimized Molecule Supply from Nozzle-Based Gas Injection Systems for Focused Electron- and Ion-Beam Induced Deposition and Etching: Simulation and Experiment. *J. Phys. D. Appl. Phys.* **2009**, *42*, 125305.
(32) Szkudlarek, A.; Gabureac, M.; Utke, I. Determination of the Surface Diffusion Coefficient and the Residence Time of Adsorbates via Local Focused Electron Beam Induced Chemical Vapour Deposition. *J. Nanosci. Nanotechnol.* **2011**, *11*, 8074−8078.
(33) Utke, I.; Friedli, V.; Purrucker, M.; Michler, J. Resolution in Focused Electron- and Ion-Beam Induced Processing. *J. Vac. Sci. Technol., B: Microelectron. Nanometer Struct.—Process., Meas., Phenom.* **2007**, *25*, 2219−2223.
(34) Chen, P.; van Veldhoven, E.; Sanford, C. A.; Salemink, H. W. M.; Maas, D. J.; Smith, D. A.; Rack, P. D.; Alkemade, P. F. A. Nanopillar Growth by Focused Helium Ion-Beam-Induced Deposition. *Nanotechnology* **2010**, *21*, 455302.
(35) Alkemade, P. F. A.; Miro, H.; van Veldhoven, E.; Maas, D. J.; Smith, D. A.; Rack, P. D. Pulsed Helium Ion Beam Induced Deposition: A Means to High Growth Rates. *J. Vac. Sci. Technol., B: Microelectron. Nanometer Struct.—Process., Meas., Phenom.* **2011**, *29*, 06FG05.
(36) Van Dorp, W. F.; Wnuk, J. D.; Gorham, J. M.; Fairbrother, D. H.; Madey, T. E.; Hagen, C. W. Electron Induced Dissociation of Trimethyl(methylcyclopentadienyl) Platinum (IV): Total Cross Section as a Function of Incident Electron Energy. *J. Appl. Phys.* **2009**, *106*, 074903.
(37) Wnuk, J. D.; Gorham, J. M.; Rosenberg, S. G.; van Dorp, W. F.; Madey, T. E.; Hagen, C. W.; Fairbrother, D. H. Electron Induced Surface Reactions of the Organometallic Precursor Trimethyl-(methylcyclopentadienyl)platinum(IV). *J. Phys. Chem. C* **2009**, *113*, 2487−2496.
(38) Spencer, J. A.; Rosenberg, S. G.; Barclay, M.; Wu, Y.-C.; McElwee-White, L.; Fairbrother, D. H. Understanding the Electron-Stimulated Surface Reactions of Organometallic Complexes to Enable Design of Precursors for Electron Beam-Induced Deposition. *Appl. Phys. A: Mater. Sci. Process.* **2014**, *117*, 1631−1644.
(39) Winkler, R.; Geier, B.; Plank, H. Spatial Chemistry Evolution during Focused Electron Beam-Induced Deposition: Origins and Workarounds. *Appl. Phys. A: Mater. Sci. Process.* **2014**, *117*, 1675−1688.
(40) Plank, H.; Haber, T.; Gspan, C.; Kothleitner, G.; Hofer, F. Chemical Tuning of PtC Nanostructures Fabricated via Focused Electron Beam Induced Deposition. *Nanotechnology* **2013**, *24*, 175305.
(41) Okazaki, S. High Resolution Optical Lithography or High Throughput Electron Beam Lithography: The Technical Struggle from the Micro to the Nano-Fabrication Evolution. *Microelectron. Eng.* **2015**, *133*, 23−35.
(42) Demers, H.; Poirier-Demers, N.; Couture, A. R.; Joly, D.; Guilmain, M.; De Jonge, N.; Drouin, D. Three-Dimensional Electron Microscopy Simulation with the CASINO Monte Carlo Software. *Scanning* **2011**, *33*, 135−146.

Supplements

Towards Ultraflat Surface Morphologies During Focused Electron Beam Induced Nanosynthesis: Disruption Origins and Compensation

R. Winkler [1], A. Szkudlarek [2,3], J.D. Fowlkes [4], P.D. Rack [4,5] , I. Utke [2] and H. Plank [1,6,]*

[1] Graz Centre for Electron Microscopy, Steyrergasse 17, 8010 Graz, AUSTRIA

[2] EMPA, Swiss Federal Laboratories for Materials Science and Technology, Laboratory for Mechanics of Materials and Nanostructures, Feuerwerkerstrasse 39, 3602 Thun, SWITZERLAND

[3] AGH University of Science and Technology, Academic Centre for Materials and Nanotechnology al. A. Mickiewicza 30, 30-059 Krakow, POLAND

[4] Center for Nanophase Materials Sciences, Oak Ridge National Laboratory, Oak Ridge, Tennessee 37831, USA

[5] Department of Materials Science and Engineering, University of Tennessee, Knoxville, Tennessee 37996, USA

[6] Institute for Electron Microscopy and Nanoanalysis, Graz University of Technology, 8010 Graz, AUSTRIA

* corresponding author: E-mail: harald.plank@felmi-zfe.at , Tel: +43 316 873 8821

Supplement 1: Spiral-In and Spiral-Out Patterning

In contrast to chair (raster scanning) or tunnel like shapes (serpentine scanning), spiral-in and spiral-out strategies exhibit ridge and trench features at diagonals and central areas as shown in Figure S 1. As these strategies are very sensitive to parameter variation which can disrupt the surface even more than can be seen in Figure S 1,[17] these strategies are entirely inappropriate when aiming for flattest surface morphologies.

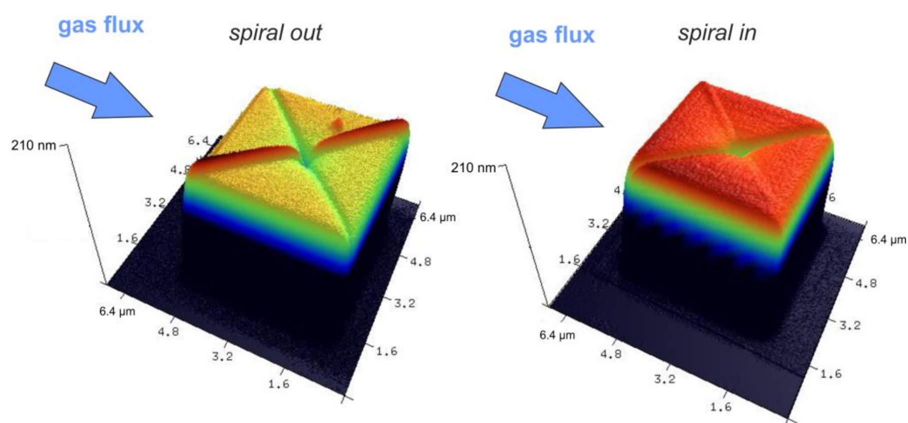

Figure S 1: 3D-AFM image of spiral-out (left) and spiral-in (right) deposits fabricated at 5 keV, 1600 pA, 1 µs dwell time, 13 nm point pitch with 1000 loops identical to the chair- and tunnel-like deposits in Figure 1 . The gas flux directions during the experiments are indicated by the blue arrows.

Supplement 2: Chair-Like Shape: Rotation and Dwell Time Variation

First, the directional gas flux was excluded as influencing factor concerning the highest features at each single line starting point. For that, the pattern was systematically rotated as indicated together with the gas flux by the schemes in Figure S 2. The blue and red curves correspond to AFM height cross sections along the individual scan line and in perpendicular orientation, respectively. Note, that all cross sections have been taken across the deposit center.

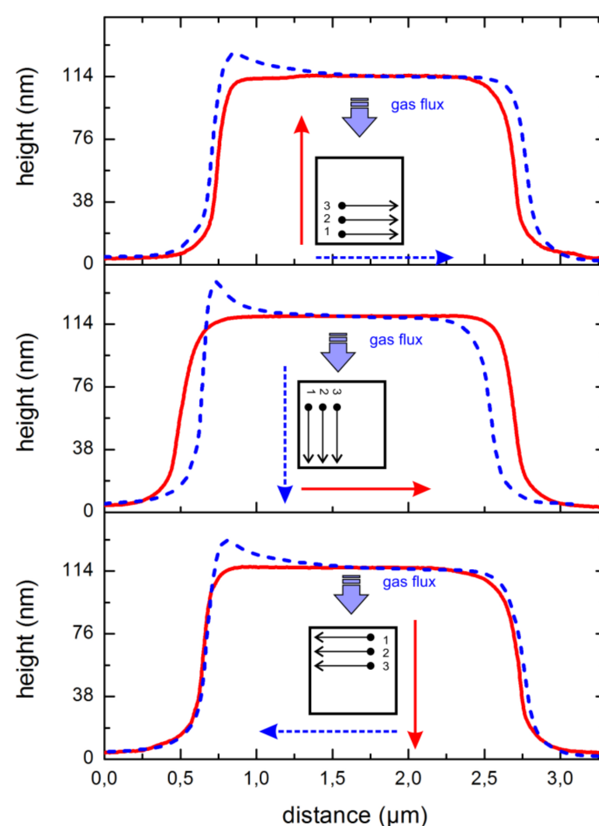

Figure S 2: AFM height cross section profiles for three different raster scan patterning directions (5 keV, 1600 pA, 13 nm PoP, 1 µs DT and 1000 loops), demonstrating that the formation of the chair is independent on the gas flux direction.

Supplement 3: Exclusion of Directional Gas Flux Influences on the Slanted Morphology

As the morphology slant is observed, we had to exclude the directional gas flux as originating or contributing factor. Therefore, we repeated the experiments with rotated pattern orientation. In Figure S 3 the according 2D AFM plots can be seen in which we denote the fast and slow patterning axis with FPA and SPA, respectively, following the notation in Figure 3e. As can be seen in Figure S 3 all orientations show the slant along the slow patterning axis independently on the relative gas flux which fully excludes gas related influences. By that, the given explanation via FSE / SE-III contributions is fully consistent. Please note, the resulting height differences between the four rotations are explained by the shadowing effect.[17]

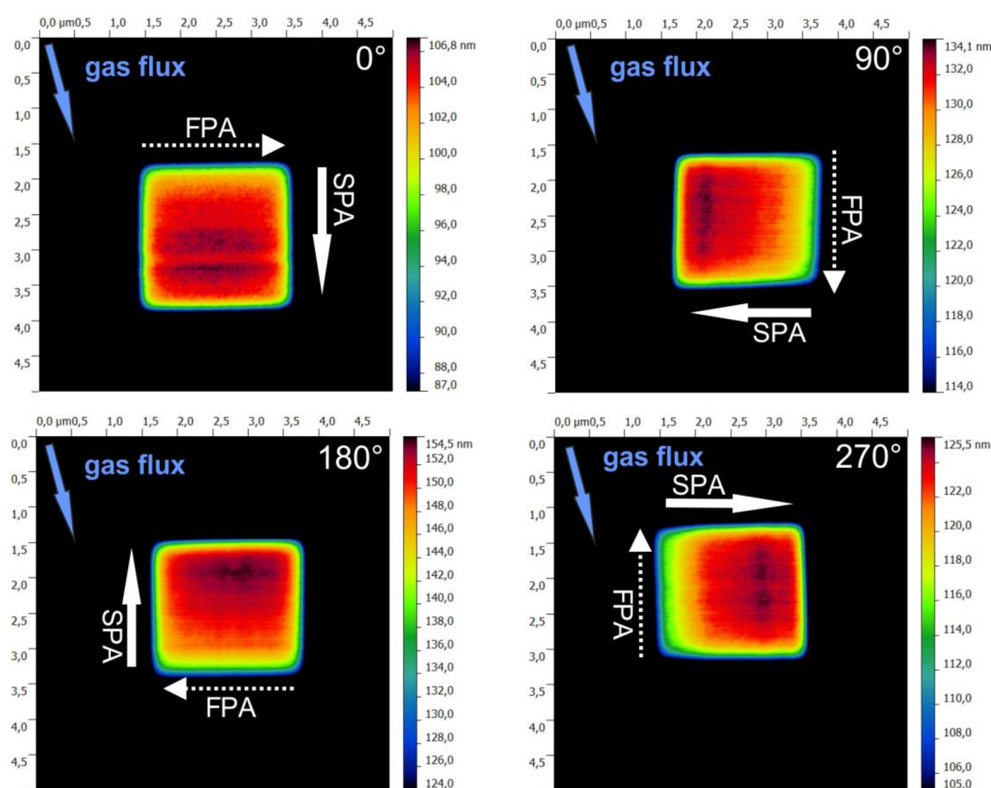

Figure S 3: 2D AFM height images where the color scale is adjusted to visualize the top 20 nm of the deposits fabricated at 5 keV, 1600 pA, 1000 µs dwell time, 13 nm point pitch in a single pass pattern via serpentines strategies. According to Figure 3e we defined the fast and slow patterning axis and indicated the respective directions in each image. The four different cases represent the systematic pattern rotation together with the gas flux direction (blue). As can be seen all deposits show the slant along the slow patterning axes which fully excludes the gas flux as decisive element for the ascending morphology. By that the FSE / SE-III approach is fully consistent.

Supplement 4: Edge Compensation

As input parameter for an appropriate edge / corner compensation, the relevant BSE radii and its lateral distribution have to be accessed. For that, Monte Carlo simulations (CASINO, V 3.2.0.4)[42] have been used where a scanning e-beam with 5 keV primary energy was scanned across the edge of PtC_5 deposit on Si-SiO_2 (3 nm). Please note again, we consider the BSE distribution just as trigger for SE-II species which are assumed to predominantly dissociate the precursor molecules. Based on the found BSE radius of approximately 100 nm, we can identify the lateral compensation radius of about 7 pixels. To get a rough estimation on the amount of correction we assumed 8, 5, and 3 nearest neighbours for central, edge and corner pixel points according to the schemes in Figure 5a. This leads to a multiplicative DT correction factor of 8/3 for corner and 8/5 for edge pixel points. Going towards the pad center, we assumed a linear decrease in seven steps from 8/5 to 1 for edges and from 8/3 to 1 for corners, respectively. Please note, this calculations can only be an approximation as the actually edge rounding effect differs within the flat-shape parameter range. This approximation has then been implemented in a stream file which led to the results shown in Figure 5b and Figure 5c. As a cross check, we have also overcompensated the edges and corners by doubled correction factors (8/5 → 16/5 and 8/3 → 16/3). As summarized in Figure S 4, the first assumptions already provide strong improvements while the overcompensation successfully confirmed the intended approach. Nevertheless, we consider a computer aided compensation approach as necessary which is currently under development.

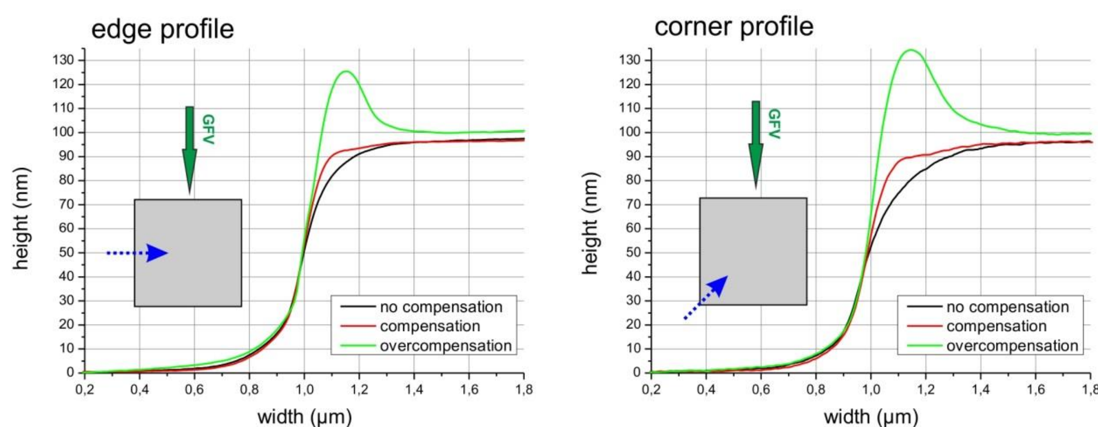

Figure S 4: AFM cross sectional profiles for uncompensated (black), compensated (red) and overcompensated (green) patterning parameters for edges (left) and corners (right) together with the gas flux direction (GFV). The dotted blue arrows indicate the position of the AFM cross sections.

Supplement 5: Parameter Variation for Raster and Spiral Strategies

As shown in the main manuscript, the influence of the patterning strategy gets particularly obvious for high beam currents and low dwell times (Figure 2, blue). Following the proposed interpretation by a decrease of the beam current (Figure 2, yellow) the concave shape – as shown for the serpentine – should also appear for raster and spiral scans. This has experimentally verified as shown in Figure S 5: increasing dwell times (top row) lead first to flat and then to slanted morphologies as predicted. When reducing the current (bottom) row, the morphology transforms into the concave shapes with a mixed morphology in between. The underlying mechanisms follow the explanations in the main text. In contrast, for spirals the shadowing effect dominates, leading to a segmented disrupted morphology explained in details in [17].

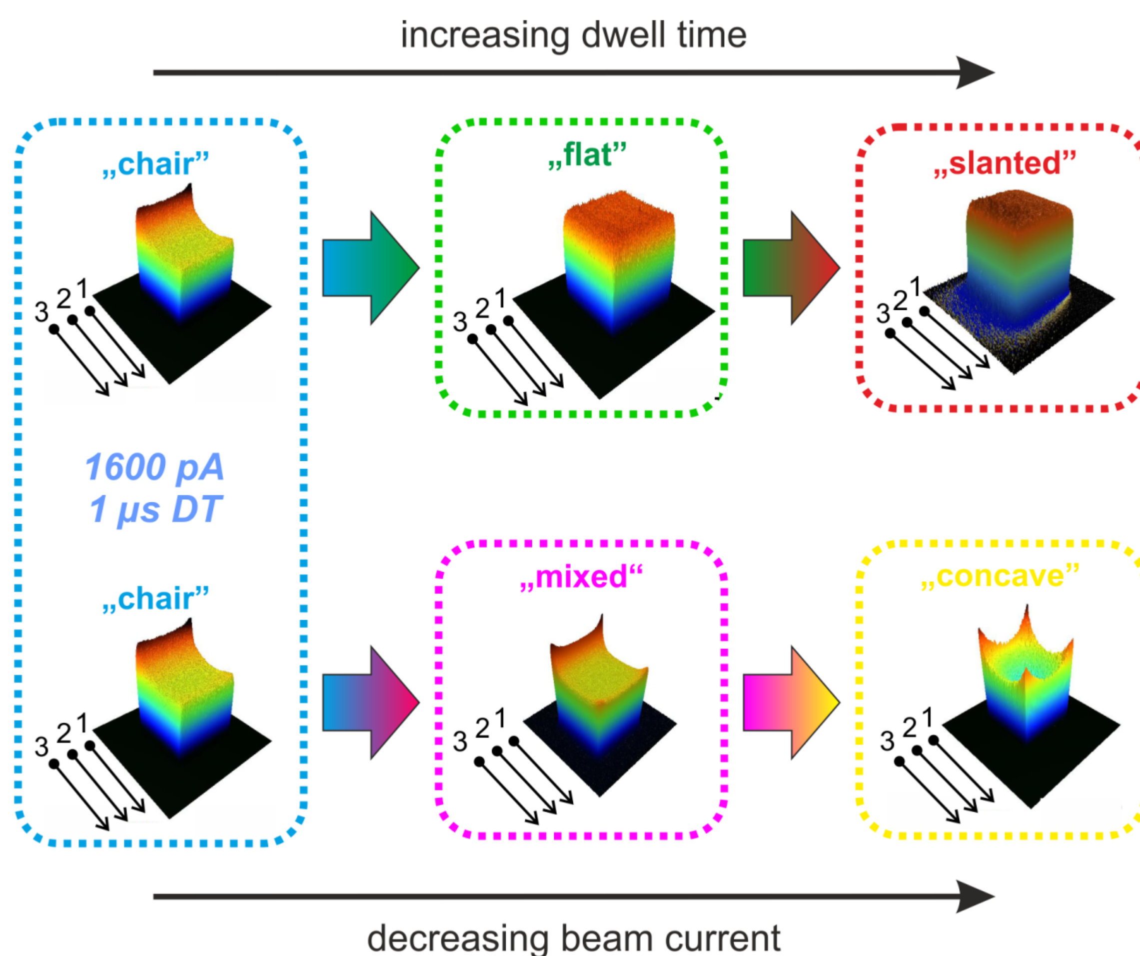

Figure S 5: 3D-AFM height images of deposits fabricated via raster scans, demonstrating the morphological transition for dwell times increasing from 1 µs to 1000 µs (top row for constant beam current of 1600 pA) and beam currents from 1600 pA to 25 pA (bottom row for constant dwell time of 1 µs). All structures have been fabricated at 5 keV, 13 nm PoP and adapted frame loops to keep the total exposure time constant.

References

(1) Utke, I.; Russell, P. E. *Nanofabrication Using Focused Ion and Electron Beams: Principles and Applications.*; Oxford University Press: New York, 2012.

(2) Van Dorp, W. F.; Hagen, C. W. A Critical Literature Review of Focused Electron Beam Induced Deposition. *J. Appl. Phys.* **2008**, *104*, 081301.

(3) Botman, a; Mulders, J. J. L.; Hagen, C. W. Creating Pure Nanostructures from Electron-Beam-Induced Deposition Using Purification Techniques: A Technology Perspective. *Nanotechnology* **2009**, *20*, 372001.

(4) Van Dorp, W. F.; Hansen, T. W.; Wagner, J. B.; De Hosson, J. T. M. The Role of Electron-Stimulated Desorption in Focused Electron Beam Induced Deposition. *Beilstein J. Nanotechnol.* **2013**, *4*, 474–480.

(5) Randolph, S. J.; Fowlkes, J. D.; Rack, P. D. Focused, Nanoscale Electron-Beam-Induced Deposition and Etching. *Crit. Rev. Solid State Mater. Sci.* **2006**, *31*, 55–89.

(6) Utke, I.; Hoffmann, P.; Melngailis, J. Gas-Assisted Focused Electron Beam and Ion Beam Processing and Fabrication. *J. Vac. Sci. Technol. B Microelectron. Nanom. Struct.* **2008**, *26*, 1197.

(7) Hari, S.; Hagen, C. W.; Verduin, T.; Kruit, P. Size and Shape Control of Sub-20 Nm Patterns Fabricated Using Focused Electron Beam-Induced Processing. *J. Micro/Nanolithography, MEMS, MOEMS* **2014**, *13*, 033002.

(8) Arnold, G.; Timilsina, R.; Fowlkes, J. D.; Orthacker, A.; Kothleitner, G.; Rack, P. D.; Plank, H. Fundamental Resolution Limits during Electron Induced Direct Write Synthesis. *ACS Appl. Mater. Interfaces* **2014**, *6*, 7380–7387.

(9) Mehendale, S.; Mulders, J. J. L.; Trompenaars, P. H. F. A New Sequential EBID Process for the Creation of Pure Pt Structures from MeCpPtMe3. *Nanotechnology* **2013**, *24*, 145303.

(10) Gavagnin, M.; Wanzenboeck, H. D.; Belić, D.; Bertagnolli, E. Synthesis of Individually Tuned Nanomagnets for Nanomagnet Logic by Direct Write Focused Electron Beam Induced Deposition. *ACS Nano* **2013**, *7*, 777–784.

(11) Gabureac, M.; Bernau, L.; Utke, I.; Boero, G. Granular Co-C Nano-Hall Sensors by Focused-Beam-Induced Deposition. *Nanotechnology* **2010**, *21*, 115503.

(12) Huth, M.; Porrati, F.; Schwalb, C.; Winhold, M.; Sachser, R.; Dukic, M.; Adams, J.; Fantner, G. Focused Electron Beam Induced Deposition: A Perspective. *Beilstein J. Nanotechnol.* **2012**, *3*, 597–619.

(13) Gabureac, M. S.; Bernau, L.; Boero, G.; Utke, I. Single Superparamagnetic Bead Detection and Direct Tracing of Bead Position Using Novel Nanocomposite Nano-Hall Sensors. *IEEE Trans. Nanotechnol.* **2013**, *12*, 668–673.

(14) Kolb, F.; Schmoltner, K.; Huth, M.; Hohenau, A.; Krenn, J.; Klug, A.; List, E. J. W.; Plank, H. Variable Tunneling Barriers in FEBID Based PtC Metal-Matrix Nanocomposites as a Transducing Element for Humidity Sensing. *Nanotechnology* **2013**, *24*, 305501.

(15) Plank, H.; Noh, J. H.; Fowlkes, J. D.; Lester, K.; Lewis, B. B.; Rack, P. D. Electron-Beam-Assisted Oxygen Purification at Low Temperatures for Electron-Beam-Induced Pt Deposits: Towards Pure and High-Fidelity Nanostructures. *ACS Appl. Mater. Interfaces* **2014**, *6*, 1018–1024.

(16) Geier, B.; Gspan, C.; Winkler, R.; Schmied, R.; Fowlkes, J. D.; Fitzek, H.; Rauch, S.; Rattenberger, J.; Rack, P. D.; Plank, H. Rapid and Highly Compact Purification for Focused Electron Beam Induced Deposits: A Low Temperature Approach Using Electron Stimulated H2O Reactions. *J. Phys. Chem. C* **2014**, *118*, 14009–14016.

(17) Winkler, R.; Fowlkes, J.; Szkudlarek, A.; Utke, I.; Rack, P. D.; Plank, H. The Nanoscale Implications of a Molecular Gas Beam during Electron Beam Induced Deposition. *ACS Appl. Mater. Interfaces* **2014**, *6*, 2987–2995.

(18) Sachser, R.; Reith, H.; Huzel, D.; Winhold, M.; Huth, M. Catalytic Purification of Directly Written Nanostructured Pt Microelectrodes. *ACS Appl. Mater. Interfaces* **2014**, *6*, 15868–15874.

(19) Stanford, M. G.; Lewis, B. B.; Noh, J. H.; Fowlkes, J. D.; Roberts, N. A.; Plank, H.; Rack, P. D. Purification of Nanoscale Electron-Beam-Induced Platinum Deposits via a Pulsed Laser-Induced Oxidation Reaction. *ACS Appl. Mater. Interfaces* **2014**, *6*, 21256–21263.

(20) Begun, E.; Dobrovolskiy, O.; Sachser, R.; Gspan, C.; Plank, H.; Huth, M. Post-Growth Purification of Co Nanostructures Prepared by Focused Electron Beam Induced Deposition. *Nanotechnology* **2015**, in print.

(21) Van Oven, J. C.; Berwald, F.; Berggren, K. K.; Kruit, P.; Hagen, C. W. Electron-Beam-Induced Deposition of 3-Nm-Half-Pitch Patterns on Bulk Si. *J. Vac. Sci. Technol. B Microelectron. Nanom. Struct.* **2011**, *29*, 06F305.

(22) Van Dorp, W. F.; van Someren, B.; Hagen, C. W.; Kruit, P.; Crozier, P. A. Approaching the Resolution Limit of Nanometer-Scale Electron Beam-Induced Deposition. *Nano Lett.* **2005**, *5*, 1303–1307.

(23) Van Dorp, W. F.; Hagen, C. W.; Crozier, P. A.; Kruit, P. Growth Behavior near the Ultimate Resolution of Nanometer-Scale Focused Electron Beam-Induced Deposition. *Nanotechnology* **2008**, *19*, 225305–225309.

(24) Schmied, R.; Fowlkes, J. D.; Winkler, R.; Rack, P. D.; Plank, H. Fundamental Edge Broadening Effects during Focused Electron Beam Induced Nanosynthesis. *Beilstein J. Nanotechnol.* **2014**, in review.

(25) Utke, I.; Friedli, V.; Purrucker, M.; Michler, J. Resolution in Focused Electron- and Ion-Beam Induced Processing. *J. Vac. Sci. Technol. B Microelectron. Nanom. Struct.* **2007**, *25*, 2219–2223.

(26) Plank, H.; Smith, D. A.; Haber, T.; Rack, P. D.; Hofer, F. Fundamental Proximity Effects in Focused Electron Beam Induced Deposition. *ACS Nano* **2012**, *6*, 286–294.

(27) Bret, T.; Utke, I.; Hoffmann, P.; Abourida, M.; Doppelt, P. Electron Range Effects in Focused Electron Beam Induced Deposition of 3D Nanostructures. *Microelectron. Eng.* **2006**, *83*, 1482–1486.

(28) Lassiter, M. G.; Rack, P. D. Nanoscale Electron Beam Induced Etching: A Continuum Model That Correlates the Etch Profile to the Experimental Parameters. *Nanotechnology* **2008**, *19*, 455306–455314.

(29) Smith, D. A.; Fowlkes, J. D.; Rack, P. D. Understanding the Kinetics and Nanoscale Morphology of Electron-Beam-Induced Deposition via a Three- Dimensional Monte Carlo Simulation: The Effects of the Precursor Molecule and the Deposited Material. *Small J.* **2008**, *4*, 1382–1389.

(30) Van Dorp, W. F.; Lazar, S.; Hagen, C. W.; Kruit, P. Solutions to a Proximity Effect in High Resolution Electron Beam Induced Deposition. *J. Vac. Sci. Technol. B Microelectron. Nanom. Struct.* **2007**, *25*, 1603.

(31) Friedli, V.; Utke, I. Optimized Molecule Supply from Nozzle-Based Gas Injection Systems for Focused Electron- and Ion-Beam Induced Deposition and Etching: Simulation and Experiment. *J. Phys. D. Appl. Phys.* **2009**, *42*, 125305.

(32) Szkudlarek, A.; Gabureac, M.; Utke, I. Determination of the Surface Diffusion Coefficient and the Residence Time of Adsorbates via Local Focused Electron Beam Induced Chemical Vapour Deposition. *J. Nanosci. Nanotechnol.* **2011**, *11*, 8074–8078.

(33) Utke, I.; Friedli, V.; Purrucker, M.; Michler, J. Resolution in Focused Electron- and Ion-Beam Induced Processing. *J. Vac. Sci. Technol. B* **2007**, *25*, 2219–2223.

(34) Chen, P.; van Veldhoven, E.; Sanford, C. A.; Salemink, H. W. M.; Maas, D. J.; Smith, D. A.; Rack, P. D.; Alkemade, P. F. A. Nanopillar Growth by Focused Helium Ion-Beam-Induced Deposition. *Nanotechnology* **2010**, *21*, 455302.

(35) Alkemade, P. F. A.; Miro, H.; van Veldhoven, E.; Maas, D. J.; Smith, D. A.; Rack, P. D. Pulsed Helium Ion Beam Induced Deposition: A Means to High Growth Rates. *J. Vac. Sci. Technol. B Microelectron. Nanom. Struct.* **2011**, *29*, 06FG05.

(36) Van Dorp, W. F.; Wnuk, J. D.; Gorham, J. M.; Fairbrother, D. H.; Madey, T. E.; Hagen, C. W. Electron Induced Dissociation of Trimethyl (methylcyclopentadienyl) Platinum (IV): Total Cross Section as a Function of Incident Electron Energy. *J. Appl. Phys.* **2009**, *106*, 074903.

(37) Wnuk, J. D.; Gorham, J. M.; Rosenberg, S. G.; van Dorp, W. F.; Madey, T. E.; Hagen, C. W.; Fairbrother, D. H. Electron Induced Surface Reactions of the Organometallic

Precursor Trimethyl(methylcyclopentadienyl)platinum(IV). *J. Phys. Chem. C* **2009**, *113*, 2487–2496.

(38) Spencer, J. A.; Rosenberg, S. G.; Barclay, M.; Wu, Y.-C.; McElwee-White, L.; Howard Fairbrother, D. Understanding the Electron-Stimulated Surface Reactions of Organometallic Complexes to Enable Design of Precursors for Electron Beam-Induced Deposition. *Appl. Phys. A* **2014**, *117*, 1631–1644.

(39) Winkler, R.; Geier, B.; Plank, H. Spatial Chemistry Evolution during Focused Electron Beam-Induced Deposition: Origins and Workarounds. *Appl. Phys. A* **2014**, *117*, 1675–1688.

(40) Plank, H.; Haber, T.; Gspan, C.; Kothleitner, G.; Hofer, F. Chemical Tuning of PtC Nanostructures Fabricated via Focused Electron Beam Induced Deposition. *Nanotechnology* **2013**, *24*, 175305.

(41) Okazaki, S. High Resolution Optical Lithography or High Throughput Electron Beam Lithography: The Technical Struggle from the Micro to the Nano-Fabrication Evolution. *Microelectron. Eng.* **2015**, *133*, 23–35.

(42) Demers, H.; Poirier-Demers, N.; Couture, A. R.; Joly, D.; Guilmain, M.; De Jonge, N.; Drouin, D. Three-Dimensional Electron Microscopy Simulation with the CASINO Monte Carlo Software. *Scanning* **2011**, *33*, 135–146.

6.4 Appendix 4 - Publication 4

Publication 4

High-Fidelity 3D-Nanoprinting Using a Focused Electron Beam: Growth Characteristics.

Winkler, R.; Lewis, B. B.; Fowlkes, J. D.; Rack, P. D.; Plank, H.

ACS Nano **2017**, *in review*.

High-Fidelity 3D-Nanoprinting via Focused Electron Beams: Growth Fundamentals

R. Winkler [1], B.B. Lewis [2,3], J.D. Fowlkes [2,3,†], P.D. Rack [2,3] and H. Plank [1,4]*

[1] Graz Centre for Electron Microscopy, Steyrergasse 17, 8010 Graz, AUSTRIA
[2] Department of Materials Science and Engineering, University of Tennessee, Knoxville, Tennessee 37996, USA
[3] Center for Nanophase Materials Sciences, Oak Ridge National Laboratory, Oak Ridge, Tennessee 37831, USA
[4] Institute of Electron Microscopy and Nanoanalysis, Graz University of Technology, 8010 Graz, AUSTRIA

* corresponding author: E-mail: harald.plank@felmi-zfe.at
† co-corresponding author: E-mail: fo2@ornl.gov

1 Abstract

While 3D-printing is currently experiencing significant growth and having a significant impact on science and technology, the expansion into the nano-world is still a highly challenging task. Among the increasing number of approaches, focused electron beam induced deposition (FEBID) was recently demonstrated to be a viable candidate towards a generic direct-write fabrication technology with spatial nanometer accuracy for complex shaped 3D nano-architectures. In this comprehensive study, we explore the FEBID parameter space and demonstrate desirable and undesirable implications towards precise, predictable, and reproducible 3D nanofabrication. We identify the optimum parameter windows for stable operation but also provide fundamental insights in the growth dynamics to understand and in turn adapt the process towards the most robust direct-write fabrication regime for freestanding 3D nanoarchitectures.

Keywords: 3D nanoprinting, direct write, additive manufacturing, focused electron beam induced deposition, nanofabrication

2 Introduction

In recent years, 3D-printing has emerged as an important technology due to its unique flexibility in design and fabrication of complex objects. While this direct-write approach of macroscopic objects has already taken the step forward from a prototyping tool to an accessible commercial platform, 3D-printing on the nanoscale is still very challenging. The interest towards smaller structures is driven by the general miniaturization trend on one hand, but also by the access to completely new physical effects at smaller dimensions. With proper fabrication methods on such a small length scale numerous applications in the field of microelectronics, photonics, metamaterials, M(N)EMS, plasmonics, nanomagnetics or microfluidics are possible. The assembly of micrometer feature sizes and slightly below are possible with several approaches. For example, 2-photon stereolithography[1] enables well-defined and highly complex architectures with outstanding optical or mechanical properties[2]. However, common to any lithographic technique this process is a two-step process. There are only a few direct-write approaches[3] that are able to print freestanding 3D-structures in the sub-micrometer regime: electroplating techniques, laser induced sintering / photo-reduction or particle beam induced deposition. The latter class provides unique flexibility in printing of complex 3D-structures[4,5] together with excellent spatial resolution on almost any substrate morphology and surface morphology[6]. Focused particle beam induced deposition utilizes either **i**ons (F**I**BID) or **e**lectrons (F**E**BID) which chemically dissociates physisorbed precursor molecules, whereas non-volatile decomposition products remain on the surface forming the intended deposit. While FIBID[7–10] has faster growth rates, the application of electrons eliminates unwanted sputtering, ion implantation or significant substrate heating. Furthermore, FEBID allows the fabrication of free-standing features in the sub-50 nm regime while it is complicated to go below 150 nm using traditional liquid Ga^+ FIBID[9]. While promising in theory, FEBID had the long-standing problem of chemical impurities, which reduce or even entirely mask the intended functionalities. Among many different approaches to purify FEBID materials during[11] or after fabrication[12–14], *in situ* laser assisted FEBID[15] and a post synthesis electron stimulated purification in water vapor has turned out to be applicable for 3D nanostructures[4]. By that, the intended functionalities such as electric[15] or optical[4] were successfully demonstrated and paved the way for the expansion into the third dimension. Although several examples of freestanding 3D structures were shown in FEBID´s early years[16–23], 3D FEBID nanoprinting has recently experienced a renaissance[4,5,15,24,25] due to both, the improved fundamental understanding of FEBID processes but also due to the improved technological possibilities of state-of-the-art instrumentation. A turning point was recently achieved by Fowlkes et al. who demonstrated the predictable fabrication of highly complex, free-standing 3D nano-architectures by simulations and complementary experiments[5]. Slightly after, 3D synthesis and material purification were combined by Winkler et al. who demonstrated the fabrication of freestanding 3D plasmonic structures[4]. Very recently, Keller et al. realized nano-magnetic spin-ice architectures using 3D-FEBID[26]. Additionally, the mechanical properties of FEBID and atomic layer deposition coated nanoarchitectures have been recently studied[27]. These achievements in various fields collectively demonstrate the high potential of FEBID as generic 3D nano-printing technology. However, FEBID is known to be a very complex process due to the high number of involved and largely interdependent variables involving electron-precursor-solid interactions. Based on this motivation, this contribution comprehensively evaluates and discusses the implication of numerous process parameters during FEBID based 3D-nanoprinting. The main outcome is a deeper understanding of the underlying mechanisms, which lead to several overarching guidelines for precise, predictable, and reproducible 3D nanofabrication using focused electron beams.

3 Results

Deposition of freestanding structural elements via FEBID is achieved by utilizing comparably slow patterning speeds in the range between 10 nm.s^{-1} and 100 nm.s^{-1} for different precursor and at typical beam conditions discussed below. Although simple in principle, predictable and reproducible fabrication is challenging due to the complex interplay between the manifold and interdependent FEBID parameters, where the ideal range lies in a relatively small process window. While large and complex multi-branch structures are possible as recently demonstrated by several work groups[4,5,15,26,27], we focus here on the controlled FEBID fabrication of single branch elements, which are the fundamental building blocks for complex 3D nano-architectures. We classify the process parameters into three main categories as schematically shown in Figure 1: ***1)*** beam parameters, ***2)*** gas parameters and ***3)*** patterning parameters. Please note, that even more factors than listed in the main manuscript can have an impact. While some of these factors are mentioned in the main text at appropriate places (with related sections in the Supplementary Information (**SI**)), some others are of minor relevance in typical setups and / or are beyond the scope of this study (e.g. chemical composition and surface energies of the substrate etc.). Most of the main parameters are self-sufficiently investigated in the result section, followed by a more detailed analysis about their implications and consequences in the discussion section. As it becomes clear below, we logically combine our discussion of point pitches and dwell times into the patterning velocity.

3.1 Beam Parameters

As primary electron energies and, in particular beam currents, are critical parameters for 3D FEBID, we first focus on these parameters. Secondly, we study the implications of the beam focus and the convergence angle including brief discussions concerning the astigmatism and the beam shift at appropriate positions.

3.1.1 Primary Electron Energies and Beam Currents

For the majority of this study a test structure called "diving board" is used as shown by a tilted SEM image in Figure 2:a. The structure consists of a vertical *pedestal*, fabricated by a stationary beam, followed by a laterally grown *segment* using different sets of point pitches (**PoP**) and dwell times (**DT**), meaning the pixel to pixel distance and the pulse duration, respectively. While the pedestal minimizes substrate related influences as discussed later, the lateral segment branch is of essential importance as its inclination angle gives information about wanted and unwanted effects. For that, we define the inclination angle ζ as 0° for a fully horizontal branch giving angles larger than zero for upwards oriented branches as indicated. Figure 2:b directly compares 15 segment arrays fabricated at different primary electron energies and beam currents as indicated. While the primary energies between 5 keV and 30 keV can be precisely selected, the related lowest possible beam currents are determined by fixed aperture sizes in our instrumentation leading to beam currents specified in the SEM images top right. Each array consists of 12 individual diving boards with DTs ranging from 3 ms – 50 ms as indicated in Figure 2:c together with the fabrication sequence (exact DTs are specified in the caption). As the PoP was held constant at 1 nm (explanation will be given later), the segments within each array represents a different patterning velocity **PV** (validation of this approach is also given later). A detailed look on Figure 2: b reveals two unwanted morphological issues namely **1)** side branching and **2)** co-deposition. Direct comparison of all arrays shows that unwanted side branching[19] is prominent for higher beam currents highlighted in b for the 10 keV / 130 pA array by the red circle. The effect of co-deposition at

the underlying substrate (see yellow circle for the 10 keV / 33 pA array), however, not only decreases for smaller beam currents but also for increasing electron energies (compare central column upwards). Apart from these qualitative observations, Figure 3 summarizes the segment angles as a function of the applied DTs (lower abscissa) and the corresponding patterning velocity (upper abscissa) for a fixed PoP of 1 nm. As mentioned, the beam currents are not identical due to machine limitations, which prevents a direct comparison of different energies in this graph. A complete set of data including higher beam currents and lower primary electron energies is given in SI 1. Normalizing the vertical volume growth rate (**zVGR**) to the applied beam currents reveals the expected gradual decrease in efficiency for increasing primary electron energies by a factor of 47 rel. % between 5 keV and 30 keV (see SI 1). The dashed lines in Figure 3a indicate constant zVGRs according to the relation $zVGR = PV \cdot \tan(\alpha)$, with patterning velocity PV and segment angle ζ. As is evident, the experimental data deviate from these curves, which clearly indicates non-constant growth rates for different DTs at constant primary electron energies and beam currents. This is indicative of mass transport limited growth as discussed later in detail. Nevertheless, Figure 3 demonstrates that the DT variation can be used to control the segment angles at constant PoPs, which is the basis for predictable 3D nanofabrication via FEBID. As is evident from the beam parameter sweep in Figure 2: a, most defined structures with eliminated co-branching and minimized co-deposits are obtained at low beam currents and high primary electron energies. Furthermore, high PVs around 100 nm.s^{-1} are possible for these setting, resulting in short process times which minimizes possible drift influences. Based on these results, further experiments in this study were done at 30 keV and 21 pA unless not otherwise stated.

3.1.2 Beam Focus

To achieve predictable and reproducible 3D nano-architectures, the beam focus is critical. Here, we demonstrate the consequences of small defocus settings on the segment angles α. For that, we started with the in-focus fabrication of appropriate pedestals followed by the segment fabrication using three different PVs of 91 nm.s^{-1}, 143 nm.s^{-1} and 333 nm.s^{-1} , leading to segment angles of 54°, 42° and 10°, respectively. Next, we introduced small beam blurs before the segment fabrication using the same PVs. The upper panel of Figure 4 acts as control experiment and shows the structure diameter variation as a function of the blurred primary beam for 91 nm.s^{-1}, which reveals an almost linear behaviour as expected[28]. The lower panel summarizes the implications of a defocused, blurred beam on the final segment angles for different PVs. Note, the highest acceptable blur before no 3D segment can be fabricated is represented by the last data points in the graph for each PV. As evident from the inset in Figure 4, this critical blur strongly decays with increasing PVs (e.g. 2 nm for 333 nm. s^{-1}), which illustrates the strong demand for a careful focus setting to achieve both, predictable and reproducible 3D nanofabrication. In the context of beam quality, we also want to emphasise the importance of astigmatism settings, which might lead to distorted branch widths in the XY plane. Finally, we want to comment on using the electronic beam shift, as our experience suggests that the focus conditions change as a function of the lateral beam deflection. Specifically, when in-focus conditions are established at the extremum of the X or Y beam shift (for focusing apart of the area of interest), no reliable 3D architectures could be fabricated when the beam was centred again and vice-versa. Hence, we only used the centred e-beam position (zero beam shift) for 3D nano-fabrication in all our experiments.

3.1.3 Convergence Angle

As described in the previous section, the focus quality is of high importance for 3D nano-fabrication. One possibility to find ideal in-focus conditions in a simple way is to increase the electron beam convergence angle. This can be done by either varying the working distance of the microscope or by changing the microscope operation for some instruments (e.g. called immersion mode in our instrumentation). The latter has the additional advantage of slightly smaller focal spot sizes as it is primarily intended for high-resolution imaging. As changing the working distance is much more complicated in dual beam microscopes (as it means to leave the eucentric height), we here chose immersion mode to demonstrate the consequences of an increased convergence angle. Two identical diving board arrays were fabricated (as described in Figure 2:) at 18 keV and 39 pA, which are the highest possible primary electron energy and the lowest beam current in immersion mode at the eucentric height (4.9 mm working distance) for our instrument, respectively. As reference data, we used the same parameters in standard operation mode, which differs by their convergence semi-angles being 1.45 ° and 4.35 ° for immersion mode, respectively. Figure 5 shows a direct comparison of the resulting segment angles for two consecutive experiments each (labelled as 1 and 2 in the legend). The insets are tilted SEM images of the first experiments for low and high convergence angles (indicated top right) showing diving boards fabricated at 3 ms, 15 ms, 27 ms, and 39 ms (top down). The first observation is the slightly reduced branch thicknesses by about 20 % in immersion mode (right SEM image), which corresponds to segment widths of (54±2) nm and (46±2) nm, measured at identical segment angles. This effect is mainly attributed to the slightly smaller electron beam diameter. Another observation is the minimization of the co-deposit underneath the segments for the high convergence angles. We attribute this effect again to the higher angle, leading to a broader impact area of transmitted electrons and by that a less distinct co-deposition feature. As evident in the main panel of Figure 5, segment angles reveal a widely similar behaviour with a slight offset to higher angles for medium and high DTs. For very low DTs, however, a faster drop in segment angle is observed as well as an inability to fabricate branches with very high patterning velocity. Although most likely instrument specific we want to mention another observation concerning the reproducibility. As mentioned above, Figure 5 shows two consecutive experiments for both operation modes. While the curves for the standard mode lies practically over each other (bright and dark blue), the immersion mode curves reveal clear deviations (bright and dark red). Considering that the arrays were fabricated less than 10 minutes without any beam changes, this approach is less reliable for our instrumentation and should be pre-tested on other systems as well. In summary, higher convergence angles provide ***1)*** slightly smaller branch features (~ 20 %), ***2)*** reduced co-deposit and ***3)*** simplifies in-focus conditions during initial setup (see previous section). Conversely, there are the disadvantages of ***1)*** more complicated fabrication of almost horizontal structures and ***2)*** a limited applicability for the predictable fabrication of very high 3D nano-architectures as in-focus conditions decay more severely with height. Finally, we also want to mention ***3)*** the unstable character in our immersion mode, ***4)*** the working-distance determined limitation of the highest possible primary electron energies and ***5)*** the application of high magnetic fields in close proximity to the surface in high-resolution immersion mode in our instrument, which can interact for instance with magnetic materials. As the disadvantages dominate, the application of higher convergence angles does not appear to be favourable for 3D nano-printing unless smallest 3D structures possible are targeted.

3.2 Patterning Parameter

While simple, planar shapes can be fabricated with the integrated patterning software packages on most microscopes, a more sophisticated approach is required to control the electron beam movement

for the fabrication of complex 3D-nanostructures. For this study, FEBID exposure files (also called stream-files) are used, which consist of a sequential list of X / Y coordinates together with the associated DTs (further parameters such as beam blanking, defocus and other may be possible depending on the instrument used). Although more complex in generation, it opens up the indispensably required freedom for arbitrary 3D geometries. An excellent software for transforming a CAD-design into such a coordinate file is the software package 3BID, developed by Fowlkes et al.[25]. In the following we demonstrate the influences of the patterning parameters point pitch (**PoP**) and dwell times (**DT**), which together dictates the patterning velocity (**PV**). Finally we discuss the patterning engine accuracy for completeness. Please note, in this study we mainly consider the diving board architecture which relies on continous exposure sequence. For complex structures, however, an intermittend patterning strategy, so-called 3D interlacing is not only optional but adventageous to provide stable and precise 3D nanoarchitectures. However, this important aspect is not adressed in this article as we focus on the tilted base elements of any 3D architecture as a foundation for complex 3D nano-printing. For more details on 3D interlacing we refer the reader to our recent studies[4,25].

3.2.1 Point Pitch and Dwell Times

FEBID is typically done in a discrete pulsed fashion defined by the pulse duration (dwell time - DT) and the patterning pixel distance (point pitch - PoP) which results in an effective patterning velocity (PV). While a stationary exposure results in vertical pillars, a lateral beam motion allows the fabrication of inclined side branches, so-called segments. We first demonstrate the interdependency of the PoP and DT which effectively results in segment angles as a function of patterning velocity. Figure 6 shows the segment angles as a function of the PoP (0.1 nm – 20 nm) for different PVs (50 $nm.s^{-1}$ – 125 $nm.s^{-1}$). To maintain constant PV, the DT was systematically increased for increasing PoP. As is demonstrated in Figure 6, the segment angles remain constant for a PoP range between 0.1 nm and 2 nm, followed by a decrease for PoPs where the electron beam effectively “skips off” the previous deposition and / or too little material is deposited by the beam periphery. The essential finding of these data is that for a given PV, the PoP can be varied by more than one order of magnitude without any significant consequences on the segment angle. This insensitivity allows to fix the PoP at an appropriate value (1 nm throughout this study) and then use only the DTs for a precise control over segment angles as shown in Figure 3. This approach also allows the introduction of the patterning velocity PV by the ratio $^{PoP}/_{DT}$. While Figure 3 graphically summarizes the results for 5 keV – 30 keV at lowest possible currents and a fixed PoP of 1 nm, SI 2 provides an expanded table for PVs to achieve different segment angles as a function of primary electron energies and beam current as a practical starting point for 3D nano-fabrication.

3.2.2 Patterning Direction

As initially demonstrated by Bret et al., the patterning direction relative to the gas flux direction can play a significant role[29]. As elaborated via simulations by Fowlkes et al.[5], this effect depends on the local depletion degree (e.g. induced by high currents or long dwell times), which, in turn implies that the precursor surface coverage should be kept as high as possible to minimize any spatial growth rate variations during 3D FEBID. This requires first a proper arrangement of the gas injection system (**GIS**). In brief, the GIS has to be aligned close to the substrate surface (100 µm our current setup) and radial distance relative to the point of fabrication (150 µm in our case). Furthermore, the long GIS axis should be aligned in such way that it intersects with the area of deposition to prevent any lateral gradients[29–32]. Using this idealized setup, we performed a rotated series of diving boards at identical parameters

summarized in the polar plot in Figure 7 where the green arrows indicate the segment patterning direction relative to the main gas flux vector (**GFV**) indicated by the top arrow. There is a very small variation of segment angles of less than 2°, which indicates a very homogenous spatial gas situation. To investigate the spatial homogeneity of the gas field, similar rotation arrays have been fabricated for higher beam currents (44 pA instead of 21 pA) at the same primary electron energies (30 keV), however, with lower segment angles around 5° to provoke influences/instabilities of possible gas field gradients. The results are practically identical ($\Delta\zeta < 2°$), which indicates that the spatial gas situation is still sufficient for stronger local depletion due to the higher beam currents (details can be found in SI 3). For completeness, we want to mention that geometrical shadowing can nevertheless appear for large and complex structures, which would require more sophisticated GIS setups as discussed in literature[29]. Furthermore we want to point out, that changing the precursor material (experiments shown here for $MeCpPt^{IV}Me_3$) naturally leads to a different gas coverage situation which might enable a prominent influence of patterning direction.

3.2.3 Refresh Time

For diving board fabrication, a continuous sequence of patterning points is used, which typically leads to gradual precursor depletion at the growing front unless true electron limited regime conditions are established[33,34]. While the latter is challenging to achieve even for optimized GIS arrangements and primary beam parameters, the introduction of additional refresh times in between two consecutive pattering points can further help to improve the gas coverage situation. In this section we demonstrate the influence of an additional refresh times (**RT**) on the segment angles. From an experimental point of view, it is complicated to extract the exact gas replenishment situation on top of pedestals due to their small dimensions and the narrow gas replenishment channel from the substrate to the new point of deposition. Hence, we used the segments without the pedestals (see SEM side view image in Figure 8) in combination with idealized GIS arrangements and primary beam conditions as discussed above (30 keV, 21 pA). The main panel in Figure 8 shows the relative height increase (left ordinate) together with the segment angle (right ordinate) for a constant PV of 100 $nm.s^{-1}$ as a function of the specific refresh times (**SRT**) which is the refresh time per nm of lateral growth. The latter was introduced as for a given PV, there exists an infinite number of PoP – DT duplets. To clarify this situation, we consider two duplets using PoPs of 0.1 nm and 1 nm with a constant PV of 100 $nm.s^{-1}$. When introducing a RT of e.g. 10 ms it follows, that after 100 nm lateral fabrication, the branch experiences 10.000 ms and 1.000 ms total additional refresh times for the small and the large PoP, respectively. Hence, we normalized the refresh times to the unit patterning length by $^{RT}/_{PoP}$ further called specific refresh time. By that, we not only decouple the RT from the used PoP-DT duplet values but also from total branch lengths to obtain a general value. The different symbols in Figure 8 represents different PoPs with adapted DTs to achieve the constant PV of 100 $nm.s^{-1}$ (see legend). The results reveal two main features: ***1)*** independent of the used PoPs, the data show a general trend, which further confirms the applicability of the combined quantity PV; and ***2)*** there is an initial plateau up to about 10 ms/nm, followed by an increase for higher SRT values. The plateau suggests widely homogenous segment heights and angles ($\Delta h_{REL} < 5\%$ and $\Delta\zeta < 2°$) which is attributed to the complicated surface replenishment along the narrow pathways as discussed in the related section later. The main results of this graph, however, is the wide independency on the used PoP-DT duplets for constant PVs and, importantly, the weak dependency of segment angles on short additional RTs, which increases the predictability and shape homogeneity during 3D FEBID.

3.3 Gas Parameter

In FEBID, the "precursor working regime" is one the most central element as it ultimately dictates the resolution and proximity effects and the deposit chemistry[35–38]. The local working regime, which describes the ratio of available precursor molecules and electrons (primary, backscattered, forward scattered and secondary electrons), depends on the above discussed primary electron beam parameters, the patterning procedures but also on the GIS alignment and the precursor type. While the GIS aspect has already been discussed in the context of patterning directions above, we here focus on the precursor temperature due to its implications on the total flux and surface residence time and finally we discuss a small variety of different precursor types.

3.3.1 Precursor Temperature

Besides an optimized GIS alignment, local precursor coverage can also be increased by a higher precursor flux leading to improved working regime conditions. This can be achieved by adjustable gas valves, the introduction of inert co-flow gases or by changing the temperature of the precursor crucible. While the two former measures depend on the technical setup, the latter can be easily done on virtually all gas injection systems. However, it should be kept in mind, that the temperature not only changes the total flux but also thermodynamic precursor properties such as sticking coefficients, residence times and average diffusion lengths[33,34]. Although convoluted, we here demonstrate the temperature related implications on the 3D growth for Pt based precursor. Figure 9a-d shows tilted SEM images of three PtC_x diving boards fabricated with identical setups (30 keV, 21 pA, PV = 160 $nm.s^{-1}$) but at different precursor temperatures of 45°C (a), 35°C (b) and 30°C (c), with the first being the suggested default temperature for this precursor. Decreasing precursor temperatures leads to lower growth rates, reflected in both shorter pedestals and lower segment angles. Note, although the segment diameter looks thinner for the lowest precursor temperatures (Figure 9c), a direct comparison with a horizontal segment at highest temperatures and adapted PVs of 350 $nm.s^{-1}$ (Figure 9d) reveals similar values of (29±2) nm (33±2) nm for 30 °C and 45 °C, respectively. Thus, we can therefore conclude that lowering the precursor temperature leads to slightly smaller branch dimensions, however, with the disadvantage of lower volume growth rates. Hence, a standard temperature of 45°C was used for all other experiments in this study. More experiments on segment growth at different precursor temperatures and argon co-flow can be found in Lewis et al.[15].

3.3.2 Precursor Type

To date, numerous FEBID precursors have been introduced and are still a subject of intensive research and development[14,39,40]. Based on partly very different physical, chemical and thermodynamic properties such as dissociation cross section[41,42], sticking coefficients[43], residence times[44,45] and the resulting diffusion lengths on the substrate[44], the local working regime and by that the spatial growth rates can strongly vary, resulting in very different 3D growth characteristics. In this study, the main focus was on the well-studied platinum precursor $MeCpPt^{IV}Me_3$ but compared with the Au, W, and SiO_x based precursors $Me_2Au(acac)$, $W(CO)_6$) and tetraethylorthosilicate (TEOS), respectively. Figure 9e compares SEM images of diving board architectures with segment angles around 45° for the various precursors with the required patterning velocities listed. Compared to the standard Pt precursor, TEOS appears to deposit approximately 1.2 times more efficient while W and Au are found to be 4.5 times slower. Please note, that although TEOS generates electrically insulating materials, 3D geometries are complicated due to local charging[22]. For magnetic materials Keller et al. recently demonstrated the successful fabrication of CoFe based 3D nano-trees[26] together with previous literature on free-standing

Cu and Co structures[29,46,47]. In essence, 3D FEBID is expected to be possible with many different precursor materials, showing same general trends as discussed here for the organometallic precursor $MeCpPt^{IV}Me_3$. However, different growth parameters and regimes will necessarily need to be calibrated.

3.4 Other Influences

While previous sections focused on parameter settings and their implications on final 3D growth, there are further effects, which partly rely on technical limitations. Although they might not appear for some instruments, we want to comment on those, which have turned out to be of relevance during this study. First, an incubation time is required before 3D FEBID is started (at least 15 minutes in this study) to allow for the mechanical stabilization of the sample stage. Considering the small PoP values in the nanometer range and below and the relatively long patterning times, it is obvious that even slow sample drift can lead to distortions or collapse of 3D architectures (see SI 4)[4,15]. Second, a steady state of precursor gas coverage is indispensable for high-fidelity 3D nanofabrication. This includes both, sufficient pre-heating times of the precursor crucible as well as sufficient times between GIS valve opening and deposition start. Together with the previously mentioned sample stage stabilization we routinely use 30 minutes preheating times, 15 minutes stage stabilization and 5 minutes GIS opening times before any 3D nanofabrication. Following these practical rules, the reproducibility in consecutive epxeriments on the same but also on different systems lies in the lower percentage range which is indispensable for 3D nano-fabrication and predicatable 3D nano-printing (see SI 4). Finally, we want to mention patterning engine related limitations with respect to the addressable pixel numbers. In brief, we have found that even for a situation where 1 addressable single pixel point is equal to 1 patterning point (1 nm distance in this study), the 3D architectures are identical (see SI 5). Although slight pixel inaccuracies are very likely for such 1-to-1 situations, we attribute this finding to the widely insensitivity of the PoP settings as discussed above. This aspect is of particular relevance if very large 3D architectures are targeted, where the highest number of available pixels are required.

4 Discussion

During the last decade, the fundamental understanding of the FEBID process has significantly increased[14,33,43,48,49]. The central element in this respect is the local balance between available precursor molecules and potentially dissociating electron species, summarized in the term “working regime”. In principle, the situation can be divided into two extremes. On the one hand, there are always enough precursor molecules available and the number of electrons limit the growth, which is then called electron-limited regime (**ELR**). The other extreme is strong excess of electrons where the number of available molecule limit the growth, called molecule-limited or mass transport limited regime (**MLR**). In between ELR and MLR, there is a transition area where the diffusion is involved, called diffusion-enhanced regime (**DER**). While ELR conditions are highly desirable for stable FEBID processing (planar, bulky 3D, free-standing, 3D, or high-resolution fabrication), such regimes are challenging to establish in typical setups[50]. Using these regime terms for considerations of individual influences we start the discussion with GIS related details, then focus on the primary beam conditions and finally include the patterning related aspects. By that, the following discussion acts as strategy guide towards predictable and reproducible 3D nanofabrication complemented by fundamental insights in growth dynamics based on the above shown results.

4.1 Technical Setup

On the route towards the most favourable ELR conditions, the GIS setup is crucial in general[30,31,51] but in particular for freestanding 3D nano-architectures as studied in this work. The essential message here is that the GIS should be ***1)*** as close as possible to the fabrication region in XYZ; ***2)*** carefully aligned concerning the long GIS axis with respect to the fabrication point; and ***3)*** installed at high angles to maximize the local precursor flux. In combination with the energy dependent lowest possible beam currents in our instrumentation (see legend in Figure 3), we found a minimal influence of differently oriented 3D branch directions as summarized in Figure 7. This setup is furthermore found to provide sufficient precursor flux even for doubled beam currents as summarized in SI 3). Please note, further increased beam currents and / or the dwell times will eventually change the local regime conditions towards MLR situations where directional effects might occur due to geometrical shadowing and / or by insufficiently replenished growth fronts, leading to distorted or collapsed growth[5,29,30]. Concerning the precursor type, we demonstrate the suitability for 3D nanofabrication for the prominent Pt precursor as well as for SiO_x, Au and W based precursor in this work as well as in previous studies, respectively[4,5,15]. Concerning the precursor temperature (Pt precursor) we have found that lower temperatures provides minor improvements on the achievable branch dimensions ((29±2) nm instead of (33±2) nm) but a clearly reduced volume growth rate as summarized in Figure 9. We attribute the latter effect mainly to the reduced precursor flux as the expected increase in residence times[44,52] should increase the volume growth rate which, however, is not observed. While the increase of the precursor temperature leads to higher fluxes[28] excessive heating might lead to problems due to the risk of temperature-induced decomposition together with reduced residence times and therefore is not suggested.

4.2 Beam Setup

As one have better control over the number of electrons than the dynamically changing number of precursor molecules, ELR conditions provide higher precision concerning the 3D fabrication. Such conditions are established when the local precursor coverage at new deposition areas are kept sufficiently high compared to the potentially dissociating electrons. This, in turn, implies that local precursor consumption needs to be low while the precursor replenishment rates are relatively high. The former is achieved for low beam currents and / or sufficiently low beam pulses while the latter benefits from ideal GIS setups and by the introduction of additional refresh times in between two consecutive beam pulses. As a starting point we compare the effects for increasing beam currents in Figure 2:b. The lowest possible values (left column) provide highest shape fidelity. For higher beam currents, one can first observe more pronounced co-deposits underneath the individual segments (representatively indicated by the yellow circle for 10 keV). This originates from an increasing number of transmitted electrons, which are not scattered significantly in the upper segment as studied in detailed by Fowlkes et al.[5] . As the current increases, the growth of additional side branches (see red circle) occurs which clearly reflects an shift in the working regime in the topmost segment. This is accompanied by a stagnation of the segment angle (equivalent to the zVGR) for higher currents at same DTs as the available number of precursor molecules determine the achievable segment angle while the exceeding electrons transmit the structures and lead to new co-segments underneath (see SI 1). Beside this clear indication that lowest beam currents are most appropriate for 3D nanofabrication, the vertical growth rate dependency on the DT for different primary electron energies provide a deeper insight into the dynamic growth. The dashed lines in Figure 3 indicate constant vertical growth rates zVGR following the relation $zVGR = PV \cdot \tan(\zeta)$ with patterning velocity *PV*

segment angle ζ. The comparison with the experimental results for e.g. 15 keV (green pentagons), however, reveal that the curve does not entirely follow a constant zVGR. To investigate that behaviour in more detail, Figure 10 shows the variation of the vertical growth rate zVGR as a function of the applied DTs for different primary electron energies and currents (see top legend). As evident, for lowest beam currents all curves reveal an initial increase followed by a decrease, which becomes more pronounced for higher primary electron energies. Please note, the absolute values cannot be directly compared due to the different beam currents used in these experiments. A normalization, however, confirms the expected result of highest efficiencies for lowest primary electron energies due to more appropriate dissociation cross section for primary, back-scattered and forward-scattered electrons and higher secondary electron yield (see SI 1). We start the discussion for 30 keV / 21 pA (black diamonds) which reveal the most pronounced peak around 15 ms DT. To understand the initial increase in zVGR keep in mind that increasing dwell times lead to higher segment angles as shown by the three SEM insets at selected DTs. Consequently, the electron beam has an increasing path through the segment, which generates more secondary electrons[53] and by that lead to increasing dissociation events, which explains the initially rising tendency. Surprisingly, this increase is not continuous for 30 keV / 21 pA but peaks at an angle around 57° achieved at 15 ms. The following zVGR decay for further increased DTs is attributed to a DER shift due to precursor depletion, which cannot be entirely replenished via direct gas flux adsorption and short-range surface diffusion from areas close to the new growth front[32,37]. To test this hypothesis, Figure 10b shows the specific zVGR (nm.(s.pA)$^{-1}$) as a function of the DTs for 30 keV but different beam currents. The peak position shifts to lower DTs (equivalent to segment angles of 55°, 50° and 42°) together with decreasing specific zVGR (equivalent to efficiencies) for increasing beam currents (see legend). This observation is consistent with the hypothesis presented above that higher beam currents lead to stronger local depletion for the same DT (reduced efficiencies) with the consequence that the DER shift emerges already at lower DTs (peak shift). Following this hypothesis, we now focus on lowest primary electron energies of 5 keV at 5 pA shown by the blue squares in Figure 10a. We again observe the initial zVGR rise attributed to the increased dissociation cross section and higher SE generation by the increased pathway for increasing segment angles. However, for 5 keV we observe a saturation behaviour for higher DTs instead of a clear decay for 30 keV (compare to black diamonds). To explain this missing regime shift, we need to consider two details. First, the saturation angle for 5 keV is around 50° at about 30 ms DT (compare to Figure 3) leading to a path length of around 105 nm which is in the range of the interaction volume depth in PtC_5[54] for 5 keV electrons. This means that SE generation starts to saturate around this value in agreement with the zVGR curve. Second, the 5 keV experiments were performed at very low beam current of 5 pA where local depletion is minimal and by that reduced the demands on the replenishment. This assumption is valid when considering the absolute zVGR values for 30 keV (black diamonds) and 5 keV (blue squares) in Figure 10a. In other words, the 5 keV / 5 pA experiment only reveals the zVGR increase as a consequence of the increased SE generation due to higher segment angles while the working regime is still closer in the electron limited range. Once, the beam current is increased from 5 pA to 25 pA, as shown by the dashed blue line in Figure 10a, an only decreasing behaviour is found due to the very high efficiencies at 5 keV. This curve reveals the typical growth rate vs. dwell time dependency which further supports the assumption of the decay being the regime shift from ELR → DER. For primary electron energies in between 30 keV and 5 keV, the zVGR decay for higher DTs gradually changes to a plateau, which is the consequence of the decreasing beam currents specified in the legend. By that, we can conclude that the 5 keV / 5 pA indeed establish working regime very close to or maybe even in the electron limited regime while the 30 keV / 21 pA situation shows a clear shift into DER conditions as a consequence of the higher beam current. Interestingly, all curves with a distinct peak and the 10 keV / 7.5 pA experiment seem to approach similar zVGR levels between 50 nm.s^{-1} and 60 nm.s^{-1}. This might reflect

the highest possible coverage situation for such free-standing diving boards and implies that as long experimental conditions yield vertical growth rates below this value, ELR conditions (or close to) are established while values above induce a DER shift. Next, we want to comment on the reduced co-deposit formation for increasing primary electron energies as evident in Figure 2:b. At first glance, this seems to be in conflict with the above mentioned argument as 30 keV experiments are done with the 4-fold beam current compared to the 5 keV case which clearly reveal a co-deposit. To explain this feature, one has to keep in mind that transmitted electrons enter the Si substrate and then have very different BSE (and thus SE II) radii around 8 µm and 0.3 µm for 30 keV and 5 keV, respectively[35,38]. Hence, the areal density of BSE and more importantly the related SE-II re-emission is much lower for high primary energies, therefore, leading to largely distributed and extremely thin co-deposits, which are barely visible via SEM. The final detail to discuss is the electron beam convergence semi-angle, which can be changed by system dependent technical options or by variation of the working distance. As summarized in Figure 5, higher convergence angles result in slightly smaller branch diameters due to inherently smaller beam diameter. In our systems we have achieved a branch diameter reduction from (54±2) nm to (46±2) nm for convergence angles of 1.45 mrad and 4.35 mrad, respectively. At the same time, the focusing procedures are simplified which is of relevance for critical parameter settings as discussed below. The downside of this approach is the reduced depth of focus, which might limit the high-resolution fabrication of very tall structures. To provide numbers for our system, the beam diameter increases by 10 nm in a height of 3.4 µm and 1.1 µm for 1.45 mrad and 4.35 mrad, respectively, which clearly limits the maximum height of the aimed 3D architecture. Also, we want to comment that the timely focus stability in our system was strongly reduced in the high-convergence, immersion mode as shown in Figure 5. To conclude this section, we can state that the application of lowest possible beam currents is the key for the most stable regime conditions. The choice of primary electron energies finally remains on technical possibilities but should include the aspects of efficiency (low keV are beneficial) unwanted co-deposits underneath freestanding 3D branches and beam diameter size (high keV are preferable). Also, a purpose and technically dependent quantity is the convergence angle which provides slightly smaller 3D branches and simplified focusing procedures, however, at the expense of the depth of focus which could limit the achievable heights of 3D architectures. Finally, we want to emphasize the importance of the focus quality during 3D FEBID as summarized in Figure 4. As evident, the introduction of a defocus (equivalent to non-focused conditions in initial setups) leads to a systematic decay of the segments angles, which is the consequence of less growth volume in the z-direction. The critical blur where no stable growth is achieved (last points in each curve) when incremental deposited volumes are too small to provide constant lateral growth. While slow patterning velocities are less sensitive for slightly defocused situations, high patterning velocities are extremely sensitive to defocus as shown by the inset in the main panel of Figure 4. In summary, these results clearly demonstrate the importance of careful beam focusing which otherwise could lead to different segment angles and higher branch thicknesses, both unwanted side effects on the route to predictable and reproducible 3D nano-architectures via FEBID.

4.3 Patterning Setup

In the final step, we focus on the patterning parameters and their implications on the final 3D nano-architectures. The main parameters are the pixel distance PoP and the pulse duration DT, which often cannot be set independently due to their interdependence[32,33,37,49]. For ideal technical setups including the application of very low beam currents, however, the PoP reveals very little cross-influence on different DTs unless it is set in the proper range. Figure 6 summarizes this widely independent behaviour for a PoP range from 0.1 nm to about 2 nm at constant patterning velocities, achieved by

proper DT adaption. Once the used PoP comes into the range of the total beam diameter, the beam tails gets increasingly responsible for the formation of new incremental volumes which, by nature of the beam profile, leads to less deposited volume, therefore leading to decreasing segment angles noted in the shaded yellow. Although this data reveal, that the PoP can also be used for segment angle control the useful range is comparable small before no stable 3D structure can be grown. Hence, it is much more reliable to fix the PoP (1 nm in our study) and use only the DT as appropriate parameter for variation of the segment angles as summarized in Figure 3. By that, both parameters can be combined into the simpler patterning velocity PV via $^{PoP}/_{DT}$. Please note, as evident for PVs of 50 nm.s^{-1}, even downwards growing structures were achieved (~ -5°) which was also observed in FIBID before[9]. The observation of the insensitive character of the PoP in certain ranges is attributed to the ideal GIS alignment in combination with low beam currents, which stabilizes the working regime by minimizing the local depletion for each single pulse, simplifying the replenishment requirements for constant growth. Increasing the beam current naturally leads to a narrowing of the independent PoP range, which again complicates the situation. Another way to improve the gas coverage, and by that shift the working regime toward ELR, is the introduction of additional refresh times in between two subsequent patterning points. Figure 8 summarizes the relative height variation (proportional to the segment angle, shown at the right ordinate) in dependency on the specific refresh times SRT. As mentioned in the respective result section the introduction of the SRT was needed to account for the infinite number of PoP-DT duplets for a given patterning velocity PV. By that, the RT was decoupled from PoP and DT and from the total length of the segment. As evident in Figure 8, there is one general trend independent of the applied PoP-DT duplets, which starts with a plateau followed by a continuous increase of vertical heights (and segment angles at the right ordinate). At first glance, the weak dependency for small SRT up to about 10 ms.nm^{-1} is slightly unexpected compared to previous literature where an immediate rise is often observed[33,49]. To explain this situation we have to consider the replenishment situation on such small structures. First, replenishment of new growth fronts via substrate related diffusion has to happen along a very narrow pathway. Taking into account the random motion of precursor molecules together with the comparable short diffusion range[37] it becomes obvious that proper replenishment from the substrate cannot take place immediately. The initial plateau in Figure 8 is therefore attributed to the more complicated replenishment boundary conditions described above. For sufficient SRTs, however, the situation gets improved as the coverage gradient gradually moves upward to the new point of deposition, then exploiting the expected improvement. The second replenishment mechanism is short range surface diffusion by molecules which are adsorbed from the gas phase in close proximity (~ diffusion range) to the new growth front. This, however, is a constant factor, which is assumed to be mainly responsible for the replenishment of new growth fronts. The essential part of these findings, however, is the fact that additional refresh times, introduced by e.g. 3D interlacing, do not affect the growth as long as the SRT is sufficiently small. Please note the threshold value around 10 ms.nm^{-1} found in this experimental series is not generally valid but a consequence of the used primary beam and gas parameter. Considering our approach of performing these experiments without a pedestal the presented results represent the best situation possible due to the large substrate around the segment. Consequently, the threshold value is expected to shift to even higher values on segments fabricated on pedestals or other segments. Therefore, in the context of highly predictable 3D nano-architectures the surface area of underlying architectures – acting as replenishment channels - has to be linked to the growth rates and finally be considered in the 3D design which will be subject of a future study. The next detail to be discussed is the patterning direction defined by the branch growth direction with respect to the gas flux vector GFV. As already discussed in the section technical setup, a proper GIS alignment can minimize spatial effects, which might occur from geometrical shadowing[37] and inherent spatial gas flux gradients[32,55]. As summarized

in Figure 7, a rotational segment angle precision better than 2° is achieved for 30 keV / 21 pA diving board architectures with an average angle of 45° using the same patterning parameters for all directions. In additional experiments, we confirmed the same accuracy ± 2° for even doubled beam currents and provocative horizontal segments angles of 4° in average (see SI 3). On the one hand, these results confirm that the chosen GIS setup reveal a very homogeneous gas flux distribution with constant gas coverage to provide spatially predictable and reproducible 3D nano-architectures. On the other hand, these results might be surprising as we have argued in the previous section that 30 keV / 21 pA does not establish ELR conditions, which are expected to be the key for spatial homogeneous 3D growth. However, here it is very important to emphasize that the same parameters were used for all experimental rotation series. This implies similar conditions, which are not necessarily in the electron limited regime. In other words, even if ELR conditions are not fully established, the spatial growth is constant based on a spatially and temporal homogenous gas coverage. Finally, we want to comment on the patterning strategy itself. The diving board architecture in this study used a consecutive sequence of patterning points. This approach was chosen for two different reasons. First, the single segments can be considered as the base element for any other 3D architecture in a modular way. And second, it represents the most unfavourable strategy due to a continuous growth front, which is very sensitive on parametric variations. While ideal for the purpose of this studies, more complex, multi-branched 3D nano-architectures require a 3D interlacing patterning as we recently demonstrated[4,5]. In slight detail, 3D interlacing provides higher spatial accuracies by means of the target XYZ position in 3D space to generate complex but connected 3D nano-architectures. For that, multiple branches are grown parallel instead of fully finished sequentially. This approach also minimizes possible drift problems via mechanical influences and / or substrate charging and minimizes anisotropic proximity effects (e.g. structure thickening and bending[56]).

4.4 Strategy Guide

Based on the previous discussion we here want to provide a short summary guide including practical aspects. Beside the technical, beam and patterning setup the user has to calibrate the system. First, an experimental series of diving boards with varying PoPs at constant PVs is recommended for lowest possible beam currents at either very high or very low primary electron energies depending on the relevance of possible co-deposits underneath the segments (start values can be found in the SI). After *identification and fixation of the ideal PoP* (see Figure 6), a diving board series with different patterning velocities PV (e.g. DT) should follow (see Figure 2:) to *determine the segment angles vs. the patterning velocity PV* as shown in Figure 3. This also allows the recalculation of the vertical growth rates zVGR to identify the established working regime as summarized in Figure 10, which could lead to different beam settings. Once these data are available, the design of the intended 3D architecture can start with the central segment-angle vs. PV chart. While a bit more challenging in the direct fabrication of appropriate stream files, the software package 3BID by Fowlkes et al.[25] allows comfortable design, once the calibration curves are available. Finally, we want to refer to the section "*Other Influences*" which summarizes a few more observations, which, however, might be technically induced and therefore not evident on all systems.

5 Conclusion

In this comprehensive study, we evaluated the impact of numerous influencing factors during direct-write fabrication of freestanding 3D nano-architectures using Focused Electron Beam Induced Deposition (FEBID). While some of them are of major importance (gas injection system alignment, primary electron energy, beam current, patterning velocity, refresh time, and beam focus), others reveal more subtle implications on the final outcome (convergence angle, precursor temperature). Although complex in their mutual relationships the effects can mostly be traced back to the working regime, which describes the balance between locally available precursor molecules and potentially dissociating electron species. In this context we not only explain details in 3D growth but also derive certain rules to be followed on the route towards precise, predictable and reproducible 3D nanofabrication via FEBID. The full potential of this work is exploited in combination with the appropriate software package 3BID[25], which allows convenient design of even complex, multi-branch 3D structures. In combination, both aspects the detailed understanding and the comfortable realization leverage FEBID from a more scientifically oriented technology into a true 3D nanoprinter. With that we paved the way in 3D-nanofabrication from a trial-and-error approach to a reliable generic 3D technology, relevant for novel concepts in diverse research and development fields such as nano-optics, magnetics, nano-mechanics or NEMS in general.

6 Methods

Focused electron beam induced deposition experiments were conducted on two Dual Beam Microscopes (FEI Company, the Netherlands): Nova 200 (Austria) and Nova 600 (US). In both, FEI standard gas injection systems were used to introduce the precursor $MeCpPt^{(IV)}Me_3$ (CAS: 94442−22−5). $Me_2Au(acac)$ (acetylacetonate-dimethyl-gold(III), CAS: 14951−50−9) and Tetraethyl orthosilicate (TEOS, CAS: 78−10−4) precursor was used only on the Nova 200, tungsten hexacarbonyl ($W(CO)_6$, CAS: 14040-11-0) was installed on the Nova 600. The precursor were heated to 45° (Pt) ,30°C (Au), and 55°C (W) at least 30 minutes before any deposition. The TEOS precursor was heated to 28°C with water co-flow during deposition. Scan rotation was applied for all experiments in such way, that the gas flux vector was perpendicular to the patterning direction of the segments. As substrate a 1 × 1 cm² silicon wafer with a 3 nm thick oxide layer was used[12]. Patterning was performed via suitable FEBID exposure files, which were generated by a self-written C++ program. A 16-bit and a 12-bit patterning engine was used for the Nova 200 and the Nova 600, respectively. The fabrication order of diving boards within an array was arranged in a “towards the nozzle” fashion to reduce possible shadowing effects[37]. SEM images in 52° stage tilt were taken with low dose conditions to avoid unwanted structure bending. The primary electron energy / beam current experiments shown in Figure 2 were performed in one shot, including careful beam alignments for each energy / current setting. Error bars for angle and thickness / heights measurements are estimated to ± 2° and ± 20 nm, respectively. For refresh time experiments a fast beam blanker was used at the Nova 200 (FEI Company, The Netherlands).

7 Acknowledgements

RW and HP gratefully acknowledge the valuable support provided from Prof. Dr. Ferdinand Hofer. The same authors also acknowledge financial support by the COST action CELINA (Nr. CM1301), EUROSTARS project TRIPLE- S (Nr. E! 8213), the bmvit exchange program and FFG – Production of the Future project SENTINEL (Nr. 850652). A portion of this research was conducted at the Center for Nanophase Materials Sciences, which is a DOE Office of Science User Facility.

8 Figures

Figure 1

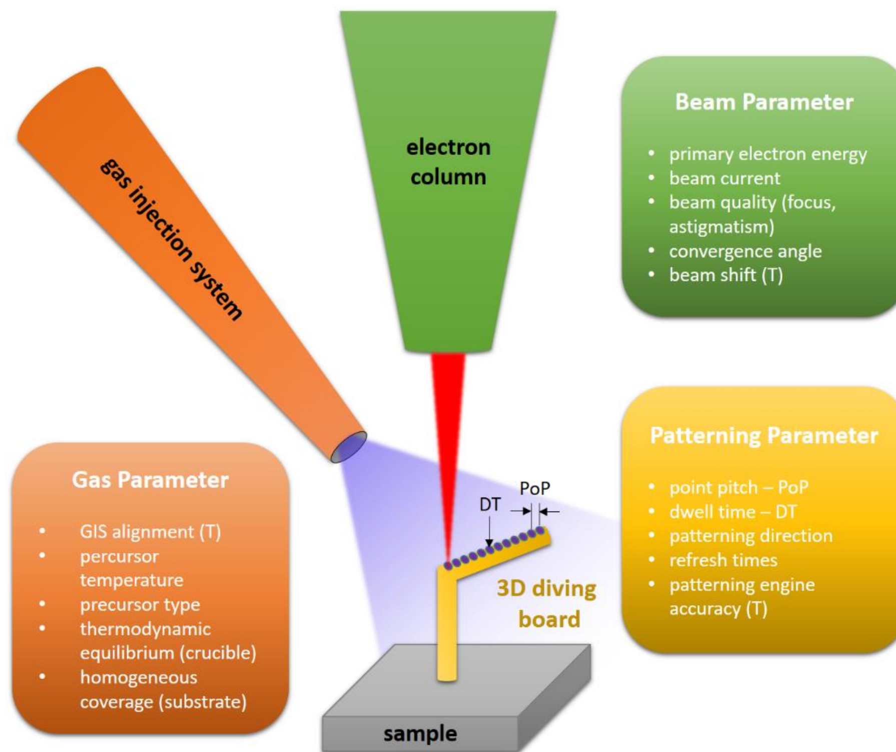

Figure 1: Overview of the most important parameters during 3D-FEBID addressed in this article following a classification into three categories while the suffix (T) indicates technically related influences. Beside the electron column, the beam, the gas injection system and the sample, the scheme also shows the here used 3D diving board geometry consisting of a vertical pedestal followed by differently angled lateral segments. The patterning points are indicated, together with their main parameters dwell time (DT) and point pitch (PoP).

Figure 2

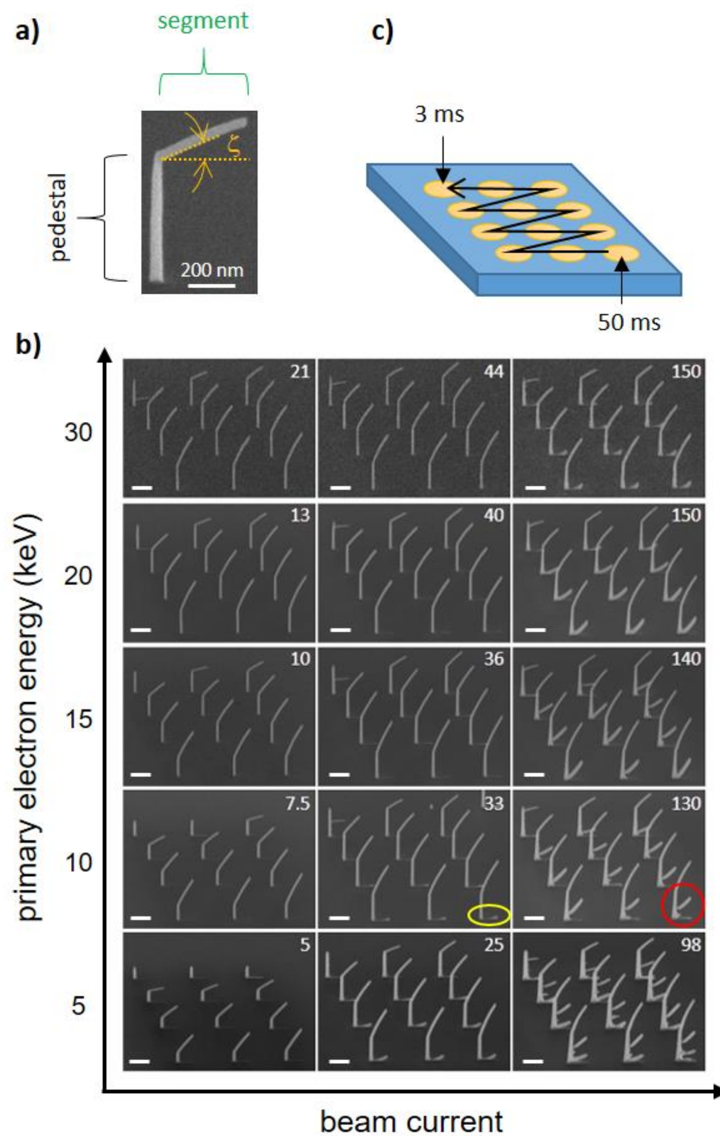

Figure 2: Diving board arrays as a function of various beam parameters fabricated from the MeCpPtMe$_3$ precursor. (a) SEM side view image of a diving board architecture. The element of interest is the segment, which is defined by the resulting angle with respect to the horizontal orientation as indicated. (b) Tilted SEM images of 15 diving board arrays (scale bars are 400 nm) fabricated at different primary electron energies (ordinate) and the three lowest beam currents possible in our instrumentation (as indicated in pA in each SEM image top right). Each array was fabricated using a fixed point pitch of 1 nm, while dwell times were decreased from 50 ms to 3 ms (50, 43, 39, 35, …, 3 ms) according to the scheme in (c). Co-branching and co-deposition are indicated in the 10 keV experiments by red and yellow circles, respectively.

Figure 3

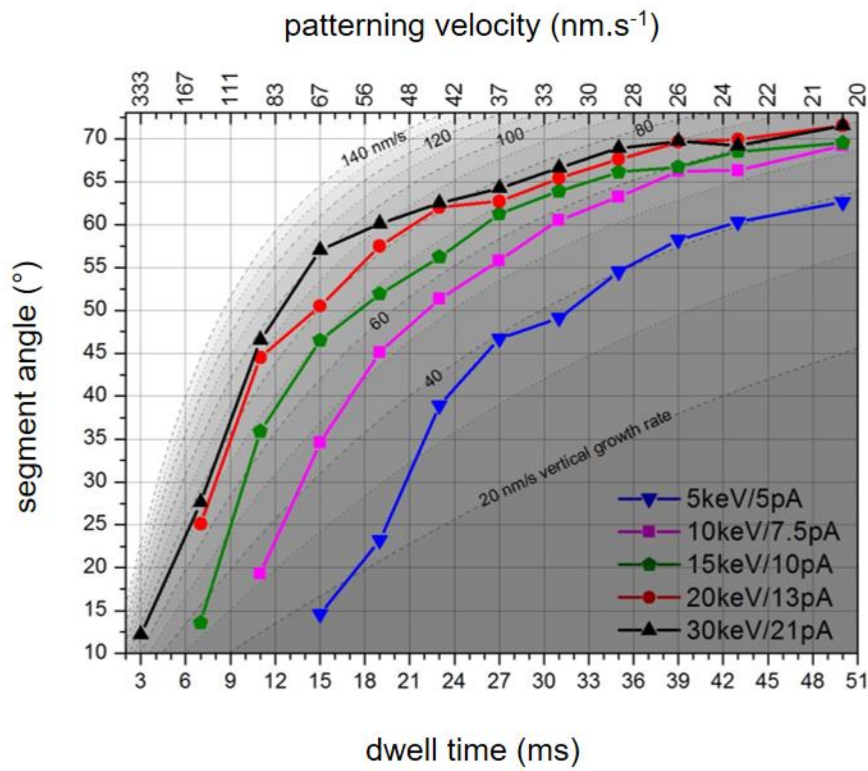

Figure 3: Dwell time based control of segment angles. The graph summarizes the segment angles as a function of the applied dwell times for different primary electron energies and lowest possible beam current in our instrumentation (constant PoP of 1 nm). The dwell time variation is equivalent to a patterning velocity as shown on the top abscissa. The dashed lines represents constant vertical growth rates at different values recalculated from segment angles and dwell times (see main text). Please note that the curves are not directly comparable due to different beam currents used.

Figure 4

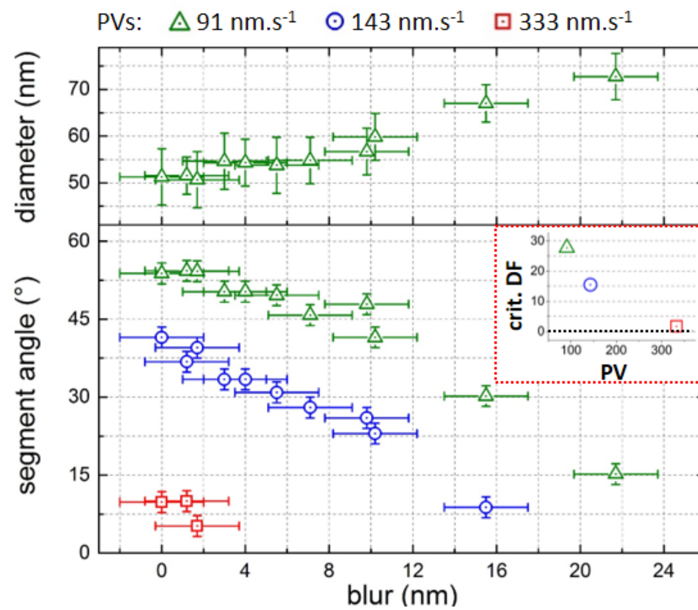

Figure 4: Influence of focus quality on segment angles. The upper panel gives the segment width as a function of the beam blur induced by a defocus for a PV of 91 nm.s^{-1}. The main panel summarizes the segment angle variation as a function of beam blur for different PVs (see legend on top). The inset gives the critical defocus values vs. the patterning velocity where the last stable diving board could be fabricated.

Figure 5

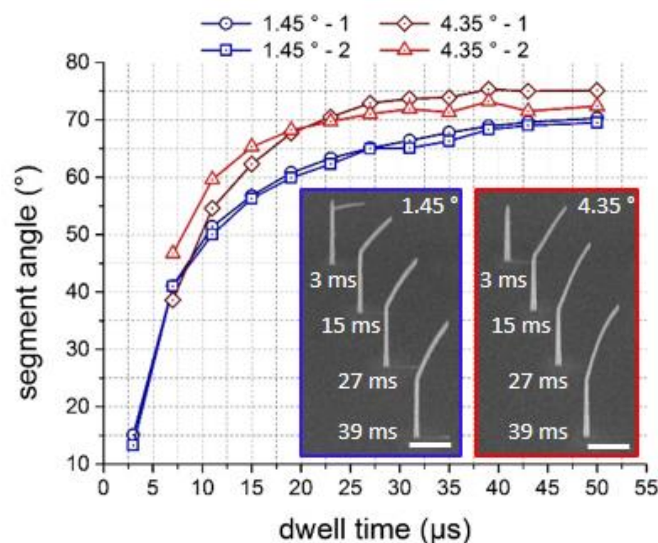

Figure 5: The implications of the electron convergence semi-angle on final segment angles. The main panel shows two consecutive experiments (light and dark colors, respectively) following the approach in Figure 2: using convergence semi-angles of 1.45 ° (blue) and 4.35 ° (red) at the same working distances (~ 4.9 mm) for 18 keV and 39 pA. While generally similar, the high convergence angle leads to slightly higher segment angles together with a faster drop at very low DT. The inset gives two tilted SEM images of diving board arrays at low and high convergence angles (see indicated top right) for selected DTs (see indication). While the branches are slightly thinner (~ 20 rel.%, see main text), the reproducibility is slightly reduced. Scale bars are 500 nm.

Figure 6

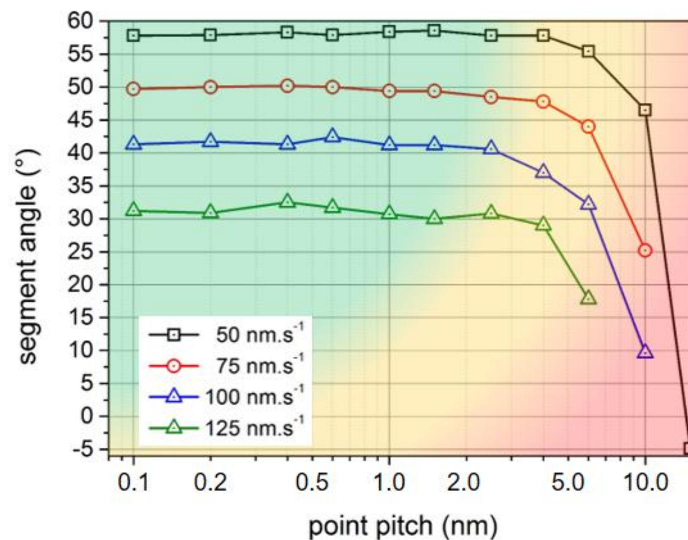

Figure 6: Influence of the point pitch (PoP) on segment angles for constant patterning velocities, realized by according dwell time adaption. As evident, the point pitch is found to be widely independently for a range between 0.1 nm and 2 nm for all PVs. At higher point pitches the segment angle decreases and eventually becomes unstable as the beam radius approaches the PoP.

Figure 7

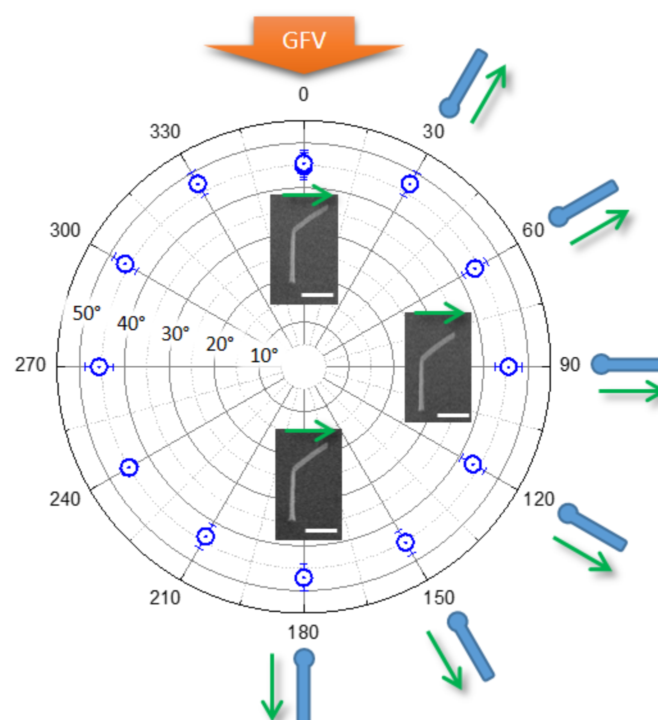

Figure 7: Segment angle as a function of the patterning direction in relation to a fixed gas flux vector (GFV) performed at 30 keV / 21 pA with an average angle of ~ 45 °. The indications at the right show the patterning direction (green arrows) starting from the pedestals (circular regions) together with tilted SEM images as insets for rotation angles of 0°, 90° and 180°. Individual segment angles deviate by less than ± 2° within the full rotation, which reveals a homogeneous spatial gas field for the chosen setup (see main text).

Figure 8

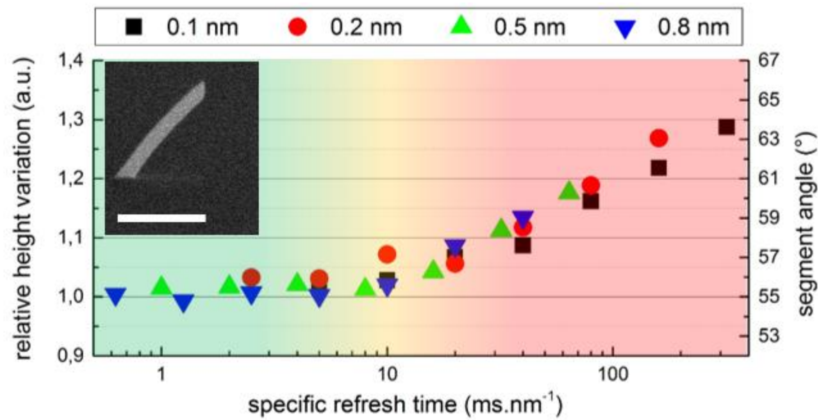

Figure 8: Implication of additional refresh times on relative height increase (left ordinate) and absolute segment angles (right ordinate). The experiments used a segment growth directly at the substrate (see SEM side view image, scale bar is 400 nm) to emulate the best replenishment situation (see discussion in the main text). While all experiments have been done at 30 keV / 21 pA and a constant patterning velocity (PV) of 100 nm.s^{-1} (excluding refresh times), the different symbols relate to different point pitches (PoP) with adapted dwell times to establish the constant PV. The specific refresh time is the refresh time per unit patterning length, which decouples this value from different PoP values and branch lengths. Beside the PoP independent general trend, there is an initial plateau up to about 10 ms.nm^{-1}, which indicates insignificant replenishment on short time scales due to the narrow replenishment pathway as discussed in the main text.

Figure 9

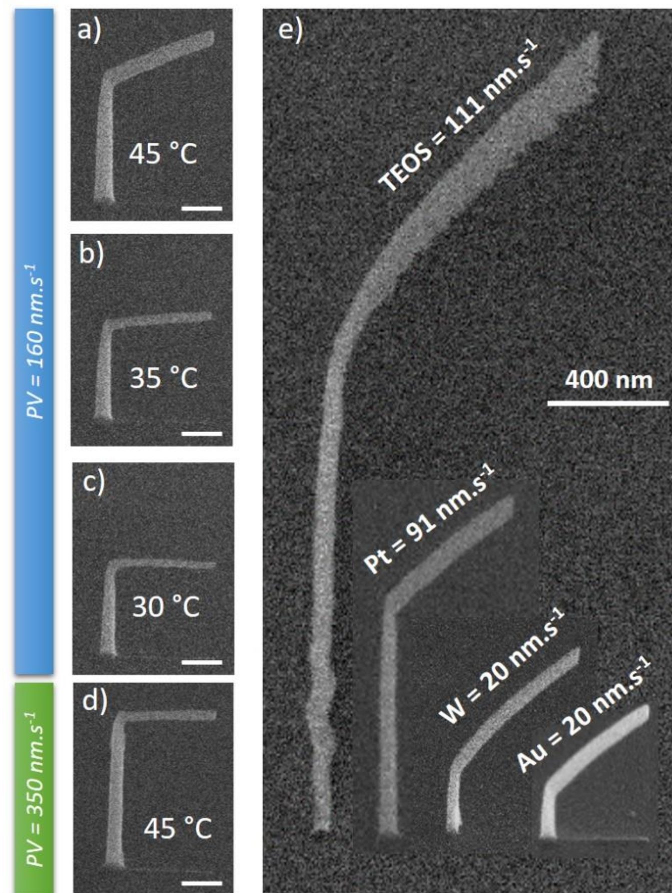

Figure 9: Effects of precursor temperature (a – d) and precursor type (e) during diving board fabrication at 30 keV / 21 pA. The tilted SEM images from (a) to (c) shows diving boards (scale bars are 200 nm), fabricated from a Pt precursor at fixed patterning velocities of 160 nm.s^{-1} for precursor temperatures of 45 °C, 35 °C and 30 °C, respectively. (d) gives a diving board, fabricated at the standard temperature of 45 °C, however, with an adapted PV of 350 nm.s^{-1} for direct comparison of segment thicknesses at almost horizontal branches. As evident, lowering the precursor temperature lead to slightly thinner branch heights, however, with the downside of lower volume growth rates reflected in both, shorter pedestals and smaller segment angles. (e) demonstrates the applicability of SiO_x (TEOS), Pt ($MeCpPt^{IV}Me_3$), W ($W(CO)_6$) and Au ($Me_2Au(acac)$) precursor for 3D nano-printing using the diving board architecture at 30 keV / 21 pA. Please note, the image is an in-scale comparison of four individual images for direct comparison, also containing the individual related patterning velocities for similar segment angles around 45°, which, in turn allows one to estimate the deposition efficiencies.

Figure 10

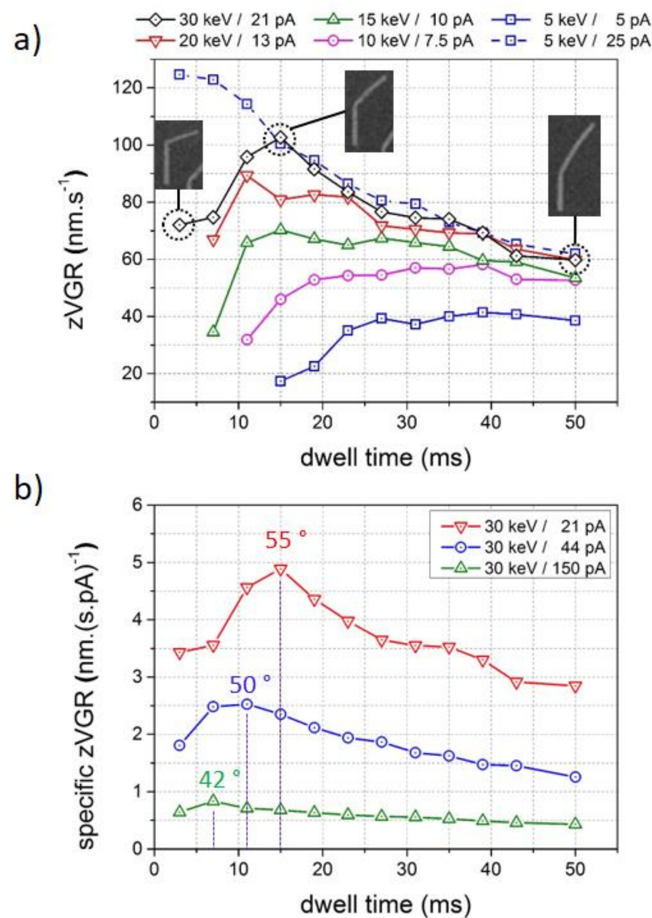

Figure 10: Vertical growth rates zVGR as a function of pixel dwell times at a point pitch of 1 nm. a) shows the dynamic behaviour for different primary electron energies and lowest possible beam currents (see top legend) with the exception of the 5 keV / 25 pA experiments shown by the dashed line. The SEM insets give tilted SEM images of diving boards at selected dwell times for the 30 keV / 21 pA experiment as indicated by the circles. A detailed discussion is given in the main text. b) shows the specific zVGR (equivalent to an efficiency) for the 30 keV situation, however, for increasing beam currents according to the legend. As evident, the peak gradually shifts to lower dwell times and segment angles (as specified), which indicates an earlier emerging regime shift for higher beam currents (see main text).

9 Table of Contents Graphics

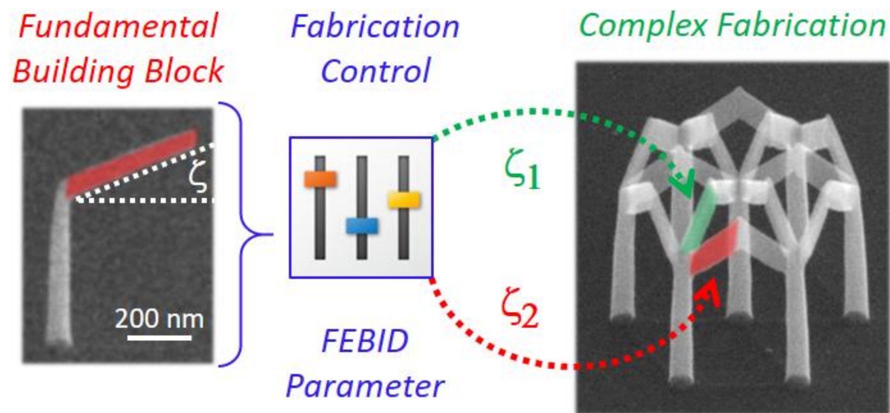

Exploring the parameter space during 3D nanoprinting via focused electron beam induced deposition (FEBID) to enable predictable and reproducible fabrication of differently angled fundamental building blocks which then can be combined into complex, high-fidelity 3D nano-architectures.

10 References

(1) Hohmann, J. K.; Renner, M.; Waller, E. H.; von Freymann, G. Three-Dimensional M-Printing: An Enabling Technology. *Adv. Opt. Mater.* **2015**, *3*, 1488–1507.

(2) Montemayor, L.; Chernow, V.; Greer, J. R. Materials by Design : Using Architecture in Material Design to Reach New Property Spaces. **2015**, 1122–1129.

(3) Hirt, L.; Reiser, A.; Spolenak, R.; Zambelli, T. Additive Manufacturing of Metal Structures at the Micrometer Scale. *Adv. Mater.* **2017**, *201604211*, 1–30.

(4) Winkler, R.; Schmidt, F.-P.; Haselmann, U.; Fowlkes, J. D.; Lewis, B. B.; Kothleitner, G.; Rack, P. D.; Plank, H. Direct-Write 3D Nanoprinting of Plasmonic Structures. *ACS Appl. Mater. Interfaces* **2017**, *9*, 8233–8240.

(5) Fowlkes, J. D.; Winkler, R.; Lewis, B. B.; Stanford, M. G.; Plank, H.; Rack, P. D. Simulation-Guided 3D Nanomanufacturing via Focused Electron Beam Induced Deposition. *ACS Nano* **2016**, *10*, 6163–6172.

(6) Peinado, P.; Sangiao, S.; Teresa, J. M. De. Focused Electron and Ion Beam Induced Deposition on Flexible and Transparent Polycarbonate Substrates. *ACS Nano* **2015**, *9*, 6139–6146.

(7) Kometanitakayuki, R.; Kondokazuhiro, H.; Kaitojun-ichi, Y. H.; Kometani, R. Performance of Nanomanipulator Fabricated on Glass Capillary by Focused-Ion-Beam Chemical Vapor Deposition Performance of Nanomanipulator Fabricated on Glass Capillary by Focused-Ion-Beam Chemical Vapor Deposition. **2005**, *298*, 1–5.

(8) Igaki, J.; Kometani, R.; Nakamatsu, K.; Kanda, K.; Haruyama, Y.; Ochiai, Y.; Fujita, J.; Kaito, T.; Matsui, S. Three-Dimensional Rotor Fabrication by Focused-Ion-Beam. **2006**, *83*, 1221–1224.

(9) Guo, D.; Kometani, R.; Warisawa, S.; Ishihara, S. Three-Dimensional Nanostructure Fabrication by Controlling Downward Growth on Focused-Ion-Beam Chemical Vapor Deposition. *Jpn. J. Appl. Phys.* **2012**, *51*.

(10) Guo, D.; Kometani, R.; Warisawa, S.; Ishihara, S. Growth of Ultra-Long Free-Space-Nanowire by the Real-Time Feedback Control of the Scanning Speed on Focused-Ion-Beam Chemical Vapor Deposition. *J. Vac. Sci. Technol. B Microelectron. Nanom. Struct.* **2013**, *31*, 61601.

(11) Shawrav, M. M.; Taus, P.; Wanzenboeck, H. D.; Schinnerl, M.; Stöger-Pollach, M.; Schwarz, S.; Steiger-Thirsfeld, A.; Bertagnolli, E. Highly Conductive and Pure Gold Nanostructures Grown by Electron Beam Induced Deposition. *Sci. Rep.* **2016**, *6*, 34003.

(12) Geier, B.; Gspan, C.; Winkler, R.; Schmied, R.; Fowlkes, J. D.; Fitzek, H.; Rauch, S.; Rattenberger, J.; Rack, P. D.; Plank, H. Rapid and Highly Compact Purification for Focused Electron Beam Induced Deposits: A Low Temperature Approach Using Electron Stimulated H2O Reactions. *J. Phys. Chem. C* **2014**, *118*, 14009–14016.

(13) Plank, H.; Noh, J. H.; Fowlkes, J. D.; Lester, K.; Lewis, B. B. B.; Rack, P. D. Electron-Beam-Assisted Oxygen Purification at Low Temperatures for Electron-Beam-Induced Pt Deposits: Towards Pure and High-Fidelity Nanostructures. *ACS Appl. Mater. Interfaces* **2014**, *6*, 1018–1024.

(14) Botman, A.; Mulders, J. J. L.; Hagen, C. W. Creating Pure Nanostructures from Electron-Beam-Induced Deposition Using Purification Techniques: A Technology Perspective. *Nanotechnology* **2009**, *20*, 372001.

(15) Lewis, B. B.; Winkler, R.; Sang, X.; Pudasaini, P. R.; Stanford, M. G.; Plank, H.; Unocic, R. R.; Fowlkes, J. D.; Rack, P. D. 3D Nanoprinting via Laser-Assisted Electron Beam Induced Deposition: Growth Kinetics, Enhanced Purity, and Electrical Resistivity. *Beilstein J. Nanotechnol.* **2017**, *8*, 801–812.

(16) Koops, H. W. P. Constructive Three-Dimensional Lithography with Electron-Beam Induced Deposition for Quantum Effect Devices. *J. Vac. Sci. Technol. B Microelectron. Nanom. Struct.* **1993**, *11*, 2386.

(17) Koops, H. W. P.; Kaya, A.; Weber, M. Fabrication and Characterization of Platinum Nanocrystalline Material Grown by Electron-beam Induced Deposition. *J. Vac. Sci. Technol. B Microelectron. Nanom. Struct. Process. Meas. Phenom.* **1995**, *13*, 2400–2403.

(18) Fujita, J.; Ishida, M.; Ichihashi, T.; Ochiai, Y.; Kaito, T.; Matsui, S. Carbon Nanopillar Laterally Grown with Electron Beam-Induced Chemical Vapor Deposition. *J. Vac. Sci. Technol. B* **2003**, *21*, 2990–2993.

(19) Mølhave, K.; Madsen, D. N.; Dohn, S.; Bøggild, P. Constructing, Connecting and Soldering Nanostructures by Environmental Electron Beam Deposition. *Nanotechnology* **2004**, *15*, 1047–1053.

(20) Bret, T.; Utke, I.; Gaillard, C.; Hoffmann, P. Periodic Structure Formation by Focused Electron-Beam-Induced Deposition. *J. Vac. Sci. Technol. B* **2004**, *22*, 2504–2510.

(21) Takeguchi, M.; Shimojo, M.; Furuya, K. Fabrication of Magnetic Nanostructures Using Electron Beam Induced Chemical Vapour Deposition. *Nanotechnology* **2005**, *16*, 1321–1325.

(22) Gazzadi, G. C.; Frabboni, S.; Menozzi, C. Suspended Nanostructures Grown by Electron Beam-Induced Deposition of Pt and TEOS Precursors. *Nanotechnology* **2007**, *18*, 445709–7.

(23) Kretz, J.; Rudolph, M.; Weber, M.; Koops, H. W. P. Three-Dimensional Structurization by Additive Lithography, Analysis of Deposits Using TEM and EDX, and Application to Field-Emitter Tips. *Microelectron. Eng.* **1994**, *23*, 477–481.

(24) Esposito, M.; Tasco, V.; Cuscuná, M.; Todisco, F.; Benedetti, A.; Tarantini, I.; Giorgi, M. De; Sanvitto, D.; Passaseo, A. Nanoscale 3D Chiral Plasmonic Helices with Circular Dichroism at Visible Frequencies. *ACS Photonics* **2015**, *2*, 105–114.

(25) Fowlkes, J. D.; Winkler, R.; Lewis, B. B.; Fernández-Pacheco, A.; Skoric, L.; Sanz Hernandez, D.; Stanford, M.; Mutunga, E.; Rack, P. D.; Plank, H. High-Fidelity 3D-Nanoprinting Using a Focused Electron Beam: Computer-Aided Design (CAD). *ACS Nano* **2017**, *submitted*.

(26) Keller, L.; Mamoori, M. K. I. Al; Pieper, J.; Stockem, I.; Schr, C.; Barth, S.; Winkler, R.; Plank, H.; Pohlit, M.; Jens, M.; *et al.* Direct-Write of Free-Form 3D Nanostructures with Controlled Magnetic Frustration. *Nat. Commun.* **2017**, *in review*.

(27) Lewis, B. B.; Mound, B. A.; Srijanto, B.; Fowlkes, J. D.; Pharr, G. M.; Rack, P. D. Growth and Nanomechanical Characterization of Nanoscale 3D Architectures Grown via Focused Electron Beam Induced Deposition. *Nanoscale* **2017**, submitted.

(28) Plank, H.; Gspan, C.; Dienstleder, M.; Kothleitner, G.; Hofer, F. The Influence of Beam Defocus on Volume Growth Rates for Electron Beam Induced Platinum Deposition. *Nanotechnology* **2008**, *19*, 485302.

(29) Bret, T.; Utke, I.; Hoffmann, P. Influence of the Beam Scan Direction during Focused Electron Beam Induced Deposition of 3D Nanostructures. *Microelectron. Eng.* **2005**, *78–79*, 307–313.

(30) Winkler, R.; Fowlkes, J.; Szkudlarek, A.; Utke, I.; Rack, P. D.; Plank, H. The Nanoscale Implications of a Molecular Gas Beam during Electron Beam Induced Deposition. *ACS Appl. Mater. Interfaces* **2014**, *6*, 2987–2995.

(31) Friedli, V.; Utke, I. Optimized Molecule Supply from Nozzle-Based Gas Injection Systems for Focused Electron- and Ion-Beam Induced Deposition and Etching: Simulation and Experiment. *J. Phys. D. Appl. Phys.* **2009**, *42*, 125305–125311.

(32) Winkler, R.; Szkudlarek, A.; Fowlkes, J. D.; Rack, P. D.; Utke, I.; Plank, H. Toward Ultraflat Surface Morphologies During Focused Electron Beam Induced Nanosynthesis: Disruption

Origins and Compensation. *ACS Appl. Mater. Interfaces* **2015**, *7*, 3289–3297.

(33) Utke, I.; Russell, P. E. *Nanofabrication Using Focused Ion and Electron Beams: Principles and Applications.*; Oxford University Press: New York, 2012.

(34) Szkudlarek, A.; Szmyt, W.; Kapusta, C.; Utke, I. Lateral Resolution in Focused Electron Beam-Induced Deposition: Scaling Laws for Pulsed and Static Exposure. *Appl. Phys. A* **2014**, *117*, 1715–1726.

(35) Schmied, R.; Fowlkes, J. D.; Winkler, R.; Rack, P. D.; Plank, H. Fundamental Edge Broadening Effects during Focused Electron Beam Induced Nanosynthesis. *Beilstein J. Nanotechnol.* **2015**, *6*, 462–471.

(36) Winkler, R.; Geier, B.; Plank, H. Spatial Chemistry Evolution during Focused Electron Beam-Induced Deposition: Origins and Workarounds. *Appl. Phys. A Mater. Sci. Process.* **2014**, *117*, 1675–1688.

(37) Winkler, R.; Fowlkes, J.; Szkudlarek, A.; Utke, I.; Rack, P. D.; Plank, H. The Nanoscale Implications of a Molecular Gas Beam during Electron Beam Induced Deposition. *ACS Appl. Mater. Interfaces* **2014**, *6*, 2987–2995.

(38) Arnold, G.; Timilsina, R.; Fowlkes, J. D.; Orthacker, A.; Kothleitner, G.; Rack, P. D.; Plank, H. Fundamental Resolution Limits during Electron Induced Direct Write Synthesis. *ACS Appl. Mater. Interfaces* **2014**, *6*, 7380–7387.

(39) Porrati, F.; Sachser, R.; Gazzadi, G. C.; Frabboni, S.; Huth, M. Fabrication of FeSi and Fe3Si Compounds by Electron Beam Induced Mixing of [Fe/Si]2 and [Fe3/Si]2 Multilayers Grown by Focused Electron Beam Induced Deposition. *J. Appl. Phys.* **2016**, *119*, 234306.

(40) de Teresa, J. M.; Fernández-Pacheco, A.; Córdoba, R.; Serrano-Ramón, L.; Sangiao, M.; Ibarra, M. R. Review of Magnetic Nanostructures Grown by Focused Electron Beam Induced Deposition (FEBID). *J. Phys. D. Appl. Phys.* **2016**, *49*, 243003.

(41) van Dorp, W. F. The Role of Electron Scattering in Electron-Induced Surface Chemistry. *Phys. Chem. Chem. Phys.* **2012**, *14*, 16753.

(42) Thorman, R. M.; Ragesh Kumar, T. P.; Howard Fairbrother, D.; Ingólfsson, O. The Role of Low-Energy Electrons in Focused Electron Beam Induced Deposition: Four Case Studies of Representative Precursors. *Beilstein J. Nanotechnol.* **2015**, *6*, 1904–1926.

(43) Van Dorp, W. F.; Hagen, C. W. A Critical Literature Review of Focused Electron Beam Induced Deposition. *J. Appl. Phys.* **2008**, *104*, 81301–81342.

(44) Szkudlarek, A.; Gabureac, M.; Utke, I. Determination of the Surface Diffusion Coefficient and the Residence Time of Adsorbates via Local Focused Electron Beam Induced Chemical Vapour Deposition. *J. Nanosci. Nanotechnol.* **2011**, *11*, 8074–8078.

(45) Fowlkes, J. D.; Geier, B.; Lewis, B. B.; Rack, P. D.; Stanford, M. G.; Winkler, R.; Plank, H. Electron Nanoprobe Induced Oxidation: A Simulation of Direct-Write Purification. *Phys. Chem. Chem. Phys.* **2015**, *17*, 18294–18304.

(46) Fernández-Pacheco, A.; Serrano-Ramón, L.; Michalik, J. M.; Ibarra, M. R.; De Teresa, J. M.; O'Brien, L.; Petit, D.; Lee, J.; Cowburn, R. P. Three Dimensional Magnetic Nanowires Grown by Focused Electron-Beam Induced Deposition. *Sci. Rep.* **2013**, *3*, 1492–1495.

(47) Gazzadi, G. C.; Frabboni, S. Structural Transitions in Electron Beam Deposited Co-Carbonyl Suspended Nanowires at High Electrical Current Densities. *Beilstein J. Nanotechnol.* **2015**, *6*, 1298–1305.

(48) Toth, M.; Lobo, C.; Friedli, V.; Szkudlarek, A.; Utke, I. Continuum Models of Focused Electron Beam Induced Processing. *Beilstein J. Nanotechnol.* **2015**, *6*, 1518–1540.

(49) Utke, I.; Hoffmann, P.; Melngailis, J. Gas-Assisted Focused Electron Beam and Ion Beam

Processing and Fabrication. *J. Vac. Sci. Technol. B Microelectron. Nanom. Struct.* **2008**, *26*, 1197.

(50) Utke, I.; Hoffmann, P.; Melngailis, J. Gas-Assisted Focused Electron Beam and Ion Beam Processing and Fabrication. *J. Vac. Sci. Technol. B Microelectron. Nanom. Struct.* **2008**, *26*, 1197–1276.

(51) Kohlmann, K. T.; Thiemann, M.; Brünger, W. H. E-Beam Induced X-Ray Mask Repair with Optimized Gas Nozzle Geometry. *Microelectron. Eng.* **1991**, *13*, 279–282.

(52) Friedli, V.; Santschi, C.; Michler, J.; Hoffmann, P.; Utke, I. Mass Sensor for in Situ Monitoring of Focused Ion and Electron Beam Induced Processes. *Appl. Phys. Lett.* **2007**, *90*, 53106.

(53) van Dorp, W. F.; Lazar, S.; Hagen, C. W.; Kruit, P. Solutions to a Proximity Effect in High Resolution Electron Beam Induced Deposition. *J. Vac. Sci. Technol. B* **2007**, *25*, 1603–1608.

(54) Drouin, D.; Couture, A. R.; Joly, D.; Tastet, X.; Aimez, V.; Gauvin, R. CASINO V2.42 - A Fast and Easy-to-Use Modeling Tool for Scanning Electron Microscopy and Microanalysis Users. *Scanning* **2007**, *29*, 92–101.

(55) Friedli, V.; Utke, I. Optimized Molecule Supply from Nozzle-Based Gas Injection Systems for Focused Electron- and Ion-Beam Induced Deposition and Etching: Simulation and Experiment. *J. Phys. D. Appl. Phys.* **2009**, *42*, 125305.

(56) Burbridge, D. J.; Gordeev, N. Proximity Effects in Free-Standing EBID Structures. *Nanotechnology* **2009**, *20*, 285308.

Supporting Information

High-Fidelity 3D-Nanoprinting via Focused Electron Beams: Growth Fundamentals

R. Winkler [1], B.B. Lewis [2,3], J.D. Fowlkes [2,3,†], P.D. Rack [2,3] and H. Plank [1,4]*

[1] Graz Centre for Electron Microscopy, Steyrergasse 17, 8010 Graz, AUSTRIA

[2] Department of Materials Science and Engineering, University of Tennessee, Knoxville, Tennessee 37996, USA

[3] Center for Nanophase Materials Sciences, Oak Ridge National Laboratory, Oak Ridge, Tennessee 37831, USA

[4] Institute of Electron Microscopy and Nanoanalysis, Graz University of Technology, 8010 Graz, AUSTRIA

* corresponding author: E-mail: harald.plank@felmi-zfe.at

† co-corresponding author: E-mail: fo2@ornl.gov

Supplement 1: Efficiencies and Full Segment Angle Dataset

As evident from Figure 3 in the main manuscript, there is an increasing vertical volume growth rate (**zVGR**) found for increasing primary electron energies (**PEE**) at same dwell times (**DTs**). This seems to be in contradiction on first sight as the dissociation cross section should be higher for lower PEEs[1] However, to explain this observation, the relevant beam currents have to be taken into account as well which range from 5 pA at 5 keV up to 21 pA at 30 keV (see legend in Figure 3). Therefore, the Figure S 1 shows the specific zVGR by normalizing the relevant values to the used beam currents. As evident, these data then show the expected trend of a decreasing efficiency for increasing PEEs (the error bars are the standard deviation after averaging all relevant data points). For completeness, we want to mention again, that setting identical beam currents is not possible in our instrumentation.

Also, Figure 3 in the main manuscript summarize only the data for lowest possible beam currents as shown in the left column in Figure 2b. For completeness, we here display the segment angles for all beam currents and PEEs mentioned in the main manuscript (Figure S 2) and complement these data by same experiments at 2 keV and 1 keV in Figure S 3.

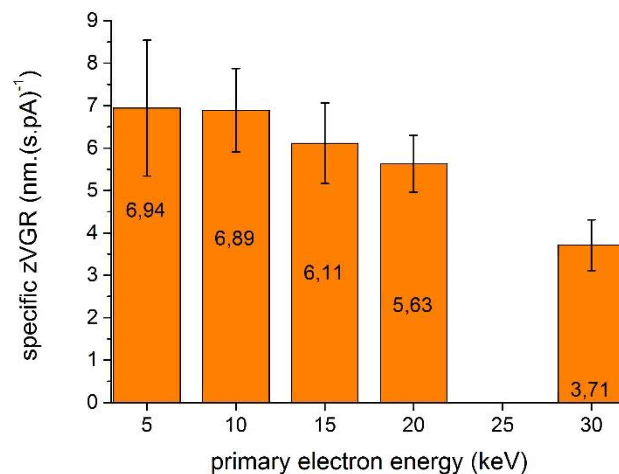

Figure S 1: vertical growth rates normalized to the used beam currents (specific zVGR) vs. primary electron energy (PEE) during segment fabrication. The tendency reveal the expected behaviour of decaying specific growth rates (equivalent to efficiencies) for increasing PEEs.

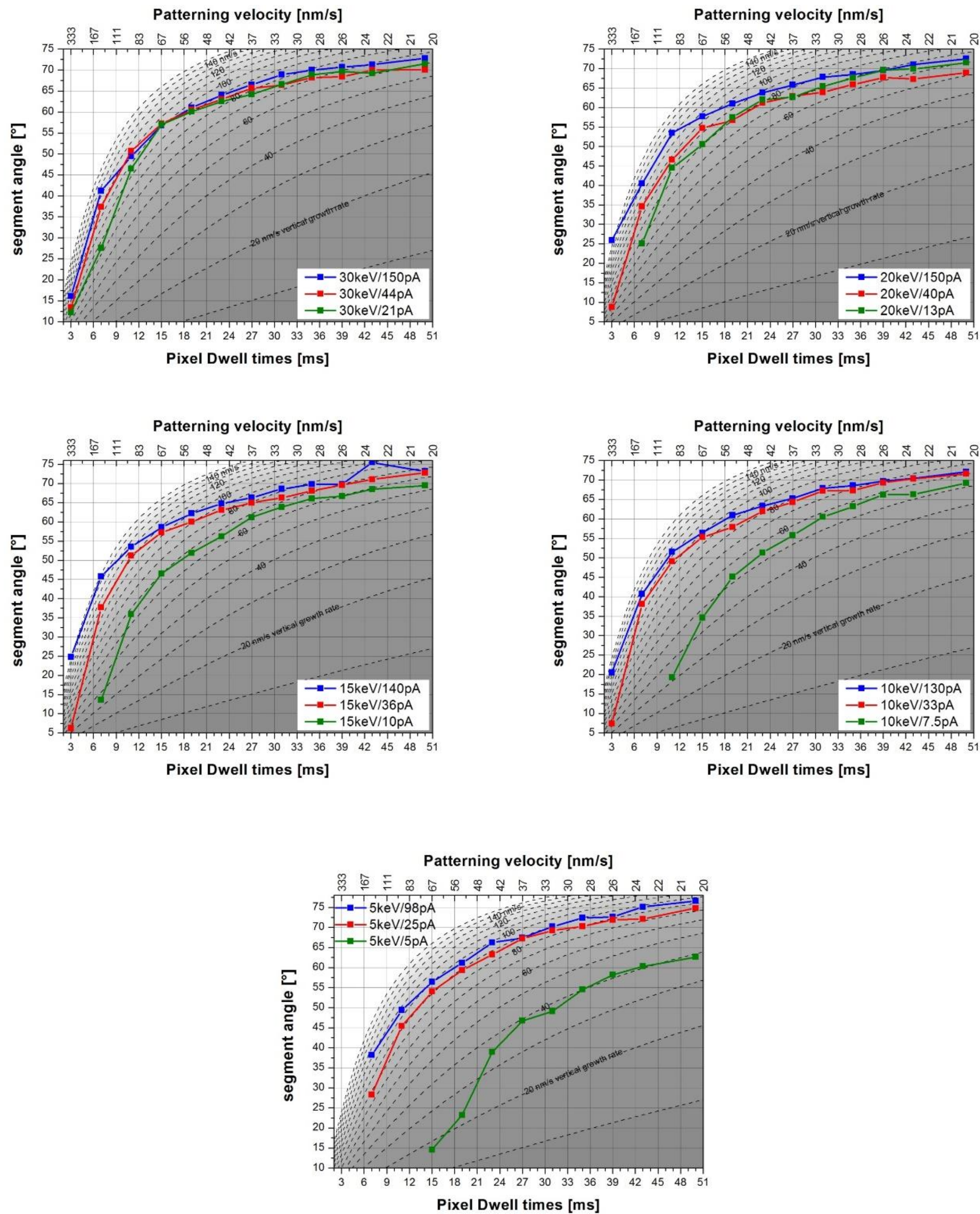

Figure S 2: Segment angles as a function of the applied dwell times for different primary electron energies and the three lowest possible beam currents in our instrumentation using constant point pitches of 1 nm. As in the main manuscript, the according patterning velocities are shown on the top abscissa. The dashed lines represents constant vertical growth rates at different values recalculated from segment angles and dwell times (see main manuscript).

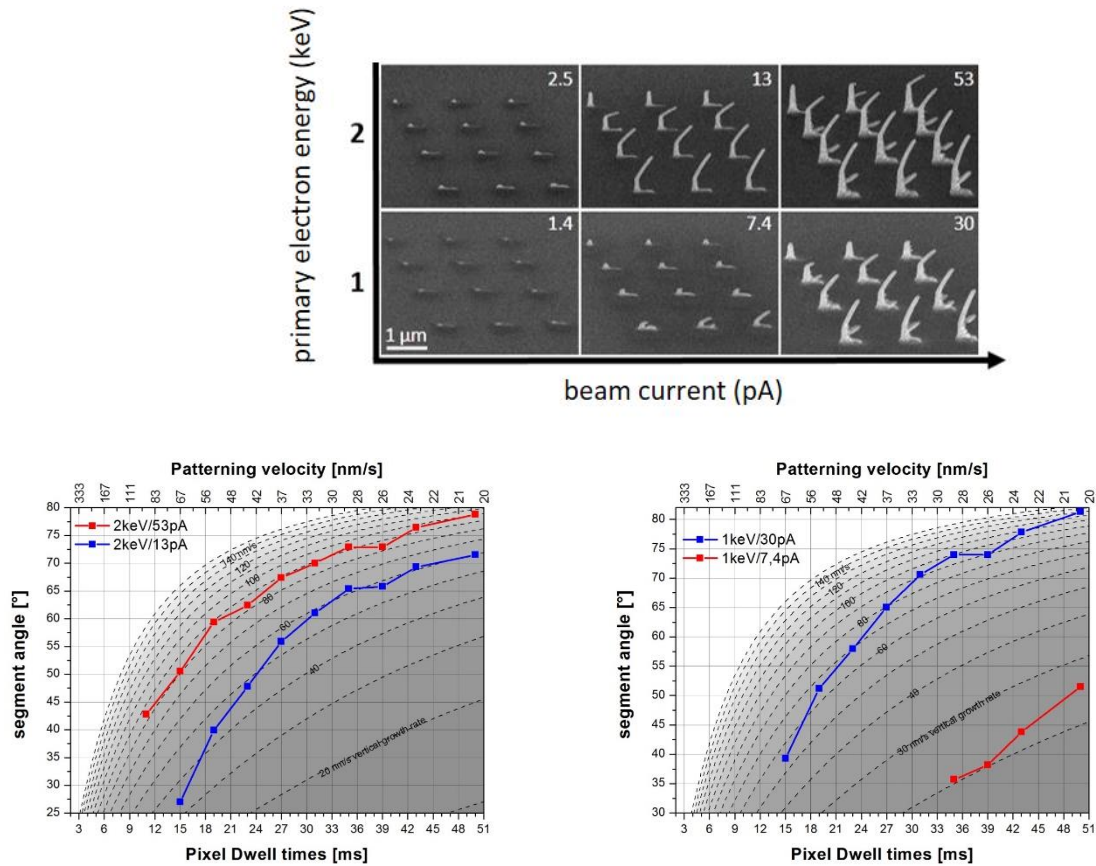

Figure S 3: Expanded experiments of segment angle fabrication for 2 keV and 1 keV. The upper image gives tilted SEM images of the diving board arrays following the fabrication approach shown in Figure 2c. The lower panels summarize the segment angles as a function of the applied dwell times for 2 keV (left) and 1 keV (right) at the three lowest possible beam currents in our instrumentation using constant point pitches of 1 nm. As in the main manuscript and in Figure S 2, the according patterning velocities are shown on the top abscissa. The dashed lines represents constant vertical growth rates at different values recalculated from segment angles and dwell times (see main manuscript).

Supplement 2: Start Values for Segment Angles

Table S 1: Starting values for required patterning velocities to achieve segment angles of nominal 60°, 45°, 30°, and 15° for different primary electron energies and beam currents using a fixed point pitch of 1 nm in our instrumentations (NOVA 200 and NOVA 600 by FEI Company, The Netherlands). Please note, that these values might lead to slightly different segment angles, depending on the used GIS arrangement, different precursors ($MeCpPt^{IV}Me_3$ used here) and other technical differences. Hence, this table is intended to act as starting point for proper 3D nanoprinting.

Primary Electron Energy (keV)	Beam Current (pA)	Pattern Velocities for Segment Angles (nm/s)			
		60°	**45°**	**30°**	**15°**
1	*7.4*	--	23	--	--
	30	41	59	--	--
2	*13*	33	46	63	--
	53	51	82	--	--
5	*5*	23	38	48	67
	25	51	91	133	--
	98	56	91	--	--
10	*7.5*	32	52	72	--
	33	48	105	167	205
	130	56	118	204	--
15	*10*	38	69	100	138
	36	53	110	168	240
	140	60	145	250	--
20	*13*	48	91	125	--
	40	45	100	167	250
	150	56	125	250	--
30	*21*	52	93	132	270
	44	54	108	172	294
	150	56	113	191	--

Supplement 3: Rotational Experiments at Higher Currents and Alternative Architecture

As shown in Figure 7 of the main manuscript, the segment angles reveal very small variation in dependency on the patterning direction with respect to the gas flux vector (GFV). While those experiments have been done at lowest beam currents, we also conducted similar experiments with higher beam currents. The main intention here was to reveal any radial dependencies, which in turn, would indicate that the spatial gas flux homogeneous enough for lowest but maybe not sufficient any more for slightly higher currents which increase the depletion during each single pulse (see also discussion and Figure 10 in the main manuscript). Figure S 4 summarizes the result of such rotation experiments using 30 keV and 44 pA which is a double beam current compared to the data in figure 7 of the main manuscript. To further provoke the appearance of any inhomogeneities, we chose DTs leading to very low segment angles around 4° as shown by the left SEM image and the red circles in the polar plot. As evident, the precision is found in the same region of ± 2°. In an additional step, we used closed arch structures as shown by the right SEM image. Here, it is important to note, that the growth of both branches was not sequentially by continuous branch formation but parallel using the 3D-interlacing approach. As evident in the polar plot by the blue triangles, the average angles are around 6° with a variation of ± 2° in agreement with all other experiments. This not only demonstrates the high predicatability and reproducibility but also indicates that the used GIS setup provides a sufficiently high and spatially homogeneous gas flux field as indispensably needed for high-fidelity fabrication of 3D nanoarchitectures via FEBID.

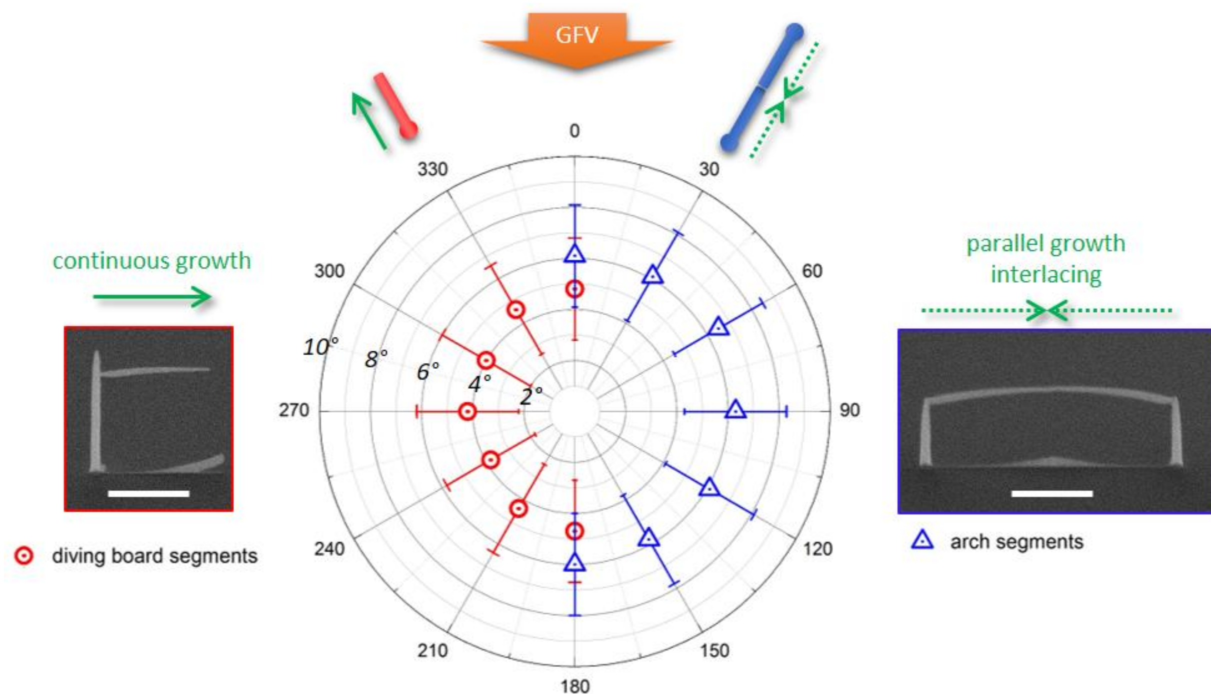

Figure S 4: Segment angles as a function of the patterning direction for a fixed gas flux vector (GFV) performed at 30 keV / 44 pA and constant point pitches of 1 nm. Two different 3D architectures have been used. First, the classical diving board architecture (left SEM image) using the continuous growth procedure as indicated by the green arrow on top. DTs have been adapted to achieve low angle segments of averagely 4°. Second, we fabricated closed arch structures with average segment angles around 6° as shown by the right SEM image using an interlaced fabrication strategy which is equivalent to a parallel growth from the pedestals to the central connection point (indicated by the dotted arrows). For both experiments, we have observed an excellent precision of less than ± 2° within the full rotation, which reveals a homogeneous spatial gas field for the chosen setup (see main manuscript) and a widely independence on the patterning direction.

Supplement 4: Mechanical Drift Issues and Reproducibility

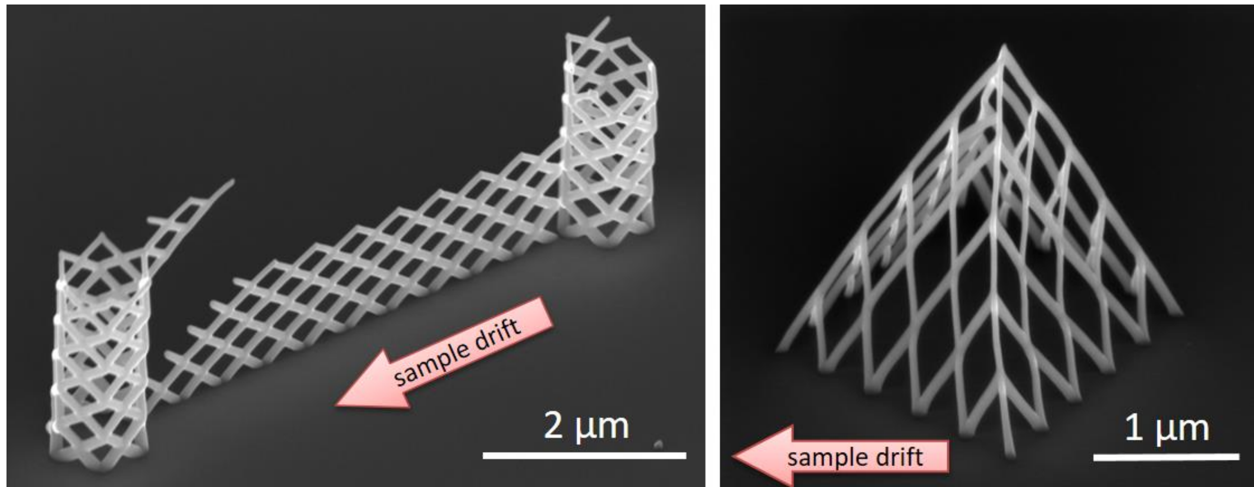

Figure S 5: Technically induced sample drift issues during 3D FEBID. In these provocative experiments (left: two towers connected by a fence; right: Pt-C pyramide), sample drift after stage movement lead to distortion effects. The underlying reason is non-equilibrium of the mechanical stage which can entirely prevent precise nanofabrication. The required stabilization time naturally depends on the used system and was set to 15 minutes for our instrumentation to reach equibrilated conditions.

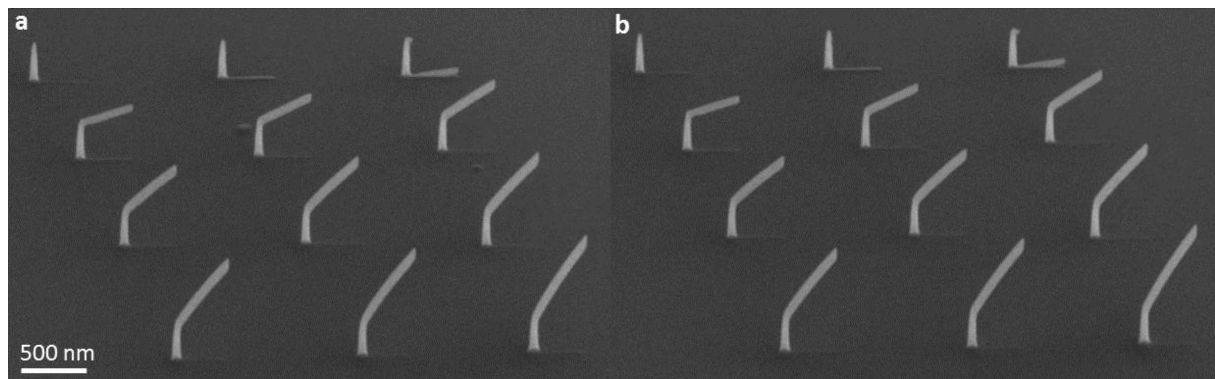

Figure S 6: The redroducibility in 3D FEBID is very high after providing the system sufficient times to mechanically equilibrate (see Figure S 5) and establish a homogeneous precursor coverage by the introduction of wating times as described in the main manuscript.

Supplement 5: Patterning Engine Accuracy

A technical aspect to consider is the accuracy of the patterning engine in terms of addressing discrete beam displacement steps. Figure S 7 shows 7 segments fabricated with identical fabrication parameters (30 keV / 21 pA, 5 ms DT and 1 nm PoP) but different pixel resolution. In more detail, 1 px means that two consecutive pixels are separated by 1 nm (1-to-1 situation), which can be adjusted by the used magnification of the microscope as the number of addressable pixels is always constant. In contrast, 7px means that 1 nm separation requires a jump of 7 px which is higher in the intrinsic addressability. Despite the highly sensitive segment setup (almost horizontal branches) no differences in the resulting shape was observed. This finding is of highly practical importance as the used magnification can be neglected as additional parameter. Especially for patterning engines with low bit depths this finding is good news as large-scaled 3D structures can be fabricated with same precision as with high bit depth patterning engines. As mentioned in the main text of the manuscript this insensitivity can be explained by the widely invariant character of the PoP (see Figure 6) which therefore tolerates a certain degree of positioning inaccuracies for the critical 1-to-1 situation.

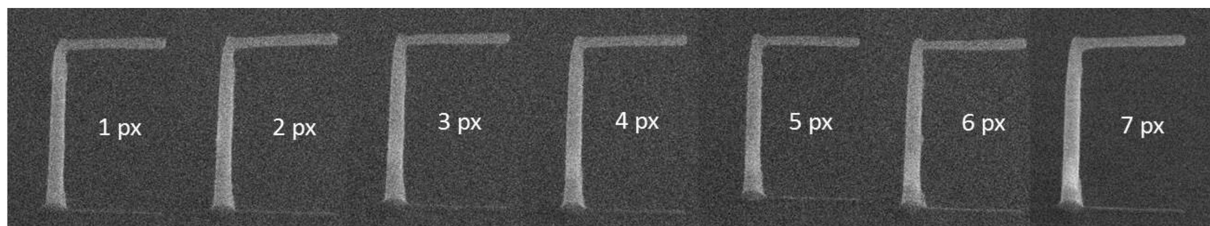

Figure S 7: Testing pattern engine accuracy with identical segments at different magnifications. For all segments a point pitch of 1 nm and a dwell time of 5 ms were used to fabricate a horizontal branch of 400 nm length at 30 keV / 21 pA. The microscope magnification was adapted in such way that 1 nm correspond to 1 pixel (1 px), 2 pixels (2 px), …, 7 pixels (7 px) in the FEBID exposure file. These finding reveals that for 3D fabrication at low beam currents the patterning engine resolution is of minor relevance.

References

(1) Utke, I.; Russell, P. E. *Nanofabrication Using Focused Ion and Electron Beams: Principles and Applications.*; Oxford University Press: New York, 2012.

6.5 APPENDIX 5 - PUBLICATION 5

Publication 5

Simulation-Guided 3D Nanomanufacturing via Focused Electron Beam Induced Deposition.

Fowlkes, J. D.; Winkler, R.; Lewis, B. B.; Stanford, M. G.; Plank, H.; Rack, P. D.

ACS Nano **2016**, *10* (6), 6163–6172.

ACSNANO www.acsnano.org

ARTICLE

Simulation-Guided 3D Nanomanufacturing *via* Focused Electron Beam Induced Deposition

Jason D. Fowlkes,*[†,‡] Robert Winkler,[§] Brett B. Lewis,[‡] Michael G. Stanford,[‡] Harald Plank,*[§,∥] and Philip D. Rack[†,‡]

[†]Nanofabrication Research Laboratory, Center for Nanophase Materials Sciences, Oak Ridge National Laboratory, Oak Ridge, Tennessee 37831, United States

[‡]Materials Science and Engineering Department, The University of Tennessee, Knoxville, Tennessee 37996, United States

[§]Graz Centre for Electron Microscopy, Steyrergasse 17, 8010 Graz, Austria

[∥]Institute for Electron Microscopy and Nanoanalysis, Graz University of Technology, Steyrergasse 17, 8010 Graz, Austria

Supporting Information

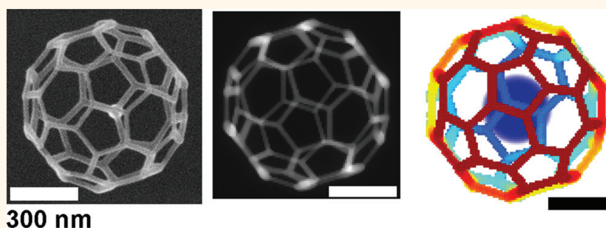

ABSTRACT: Focused electron beam induced deposition (FEBID) is one of the few techniques that enables direct-write synthesis of free-standing 3D nanostructures. While the fabrication of simple architectures such as vertical or curving nanowires has been achieved by simple trial and error, processing complex 3D structures is not tractable with this approach. In part, this is due to the dynamic interplay between electron−solid interactions and the transient spatial distribution of absorbed precursor molecules on the solid surface. Here, we demonstrate the ability to controllably deposit 3D lattice structures at the micro/nanoscale, which have received recent interest owing to superior mechanical and optical properties. A hybrid Monte Carlo−continuum simulation is briefly overviewed, and subsequently FEBID experiments and simulations are directly compared. Finally, a 3D computer-aided design (CAD) program is introduced, which generates the beam parameters necessary for FEBID by both simulation and experiment. Using this approach, we demonstrate the fabrication of various 3D lattice structures using Pt-, Au-, and W-based precursors.

KEYWORDS: *3D nanoprinting, direct-write, focused electron beam induced deposition, nanofabrication*

Resist-free, direct-write additive manufacturing techniques ideally allow for the fabrication of functional micro- and nanostructures on practically any given surface including where classical resist-based techniques cannot be used. In particular, focused electron beam induced deposition (FEBID) is attracting increasing attention owing to sub-10 nm[1,2] resolution, while being one of the few techniques that allow truly three-dimensional (3D) fabrication. FEBID uses a nanoscale focused electron beam to dissociate adsorbed precursor molecules. A condensed deposit forms as a result of dissociation at the beam−precursor intersection. Appropriate sequential beam scanning in the substrate plane (x−y) can generate out-of-plane deposition (z), forming a 3D deposit. Thus, FEBID has the potential to be a versatile 3D additive nanomanufacturing technique.

Nanohelix metamaterial arrays have recently been deposited over tens of micrometers by FEBID, representing the current state-of-the-art in nanoscale 3D direct-write.[3] Also, 3D FEBID has recently been demonstrated using a nanoelectrospray liquid precursor injection method.[4] In the previous two decades arches,[5,6] angled segments,[7] helices,[8,9] optically active pillar arrays,[10] square frame antennas,[11] and electron optics[12] have been demonstrated. Matsui demonstrated solid object, layer-by-layer deposition of complex 3D replicas using the Ga^+ ion beam as well as helices[13] and angled segments.[14] Moving forward, more complex 3D objects relevant to nanoscale prototyping will be required. Thus, design by simulation is required to both predict the ideal scanning pattern and tackle complex 3D designs in order to avoid time-consuming trial and error approaches typically used.

In the past, we have reported a Monte Carlo simulation[15,16] coupled with an atomic level handling of the precursor−solid interaction for the purpose of understanding FEBID-related phenomena at the nanoscale, but this method can be intractable for simulating relatively large scale features. For example, each precursor molecule was handled as a discrete particle that executed a random-walk motion to emulate the diffusion of the virtual molecule on the deposit surface,[17] a computationally expensive process. Conversely, we[18] and others[19−21] have also

Received: March 27, 2016
Accepted: June 10, 2016
Published: June 10, 2016

ACS Publications © 2016 American Chemical Society

DOI: 10.1021/acsnano.6b02108
ACS Nano 2016, 10, 6163−6172

created pseudo-2D continuum simulations applicable for larger length scales for the purpose of computationally extracting material parameters as well as for understanding basic scanning-induced growth regimes.[22,23] The 2D simulation,[24] however, is a more suitable approach for depositing simple structures within the limit of small and finite surface curvature and is incapable of treating truly 3D structures. Recent developments in continuum modeling[20] have made it possible to elucidate critical precursor−solid parameters[25] using fully 3D simulations. Here, we report a full 3D simulation that bridges the spatial length scale between approximately 10 nm and 1 μm and is capable of replicating complex lattices/meshes deposited by experimental FEBID.

We overview the elements incorporated into a hybrid Monte Carlo−continuum simulation[26] while referencing previously reported details. After the brief simulation overview, we focus on the comparison between experiments and simulations. The FEBID simulation is calibrated based on careful experiments and implementing materials parameters available in the literature. A major aspect of this work is the successful convergence of experiments and simulations. Following this convergence, a CAD program was created for the purpose of designing complex 3D geometries as input for both FEBID simulations and experiments. The CAD program output is a data set that includes beam spatial coordinates and beam dwell times necessary to generate the prescribed 3D object. Robustness was tested by executing 3D FEBID on two different dual-beam machines. 3D objects (ring, frame, cube, and icosahedron geometries, all in mesh form) predicted by simulation were replicated across both microscopes with a nanoscale level of resolution.

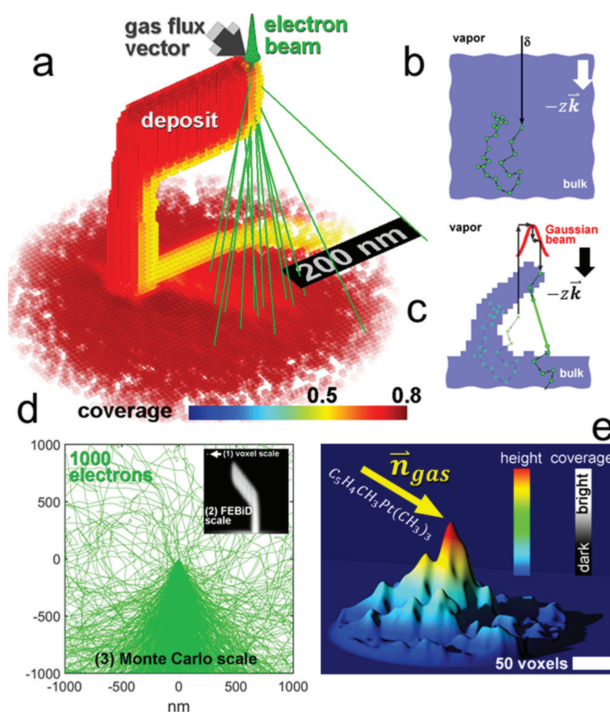

Figure 1. (a) 3D FEBID (focused electron beam induced deposition) simulation results for the "segment" geometry. The beam energy was 30 keV, the beam current was 21 pA, and the FWHM of the electron beam was 4 nm. The colormap reflects the precursor molecule coverage for the case of a partially directed gas beam (20 mTorr, indicated as gas flux vector) and a purely diffuse component (10 mTorr). Precursor coverage is relatively lower in the shadow cast by the segment-terminated pillar because the directed gas flux is blocked. More details are provided in the S1. (b) Monte Carlo simulation of an electron trajectory immersed in an infinite 3D solid using a point source beam (δ). (c) The electron trajectory in (b) is adapted to the 3D deposit geometry for FEBID. Adaption includes accounting for the real Gaussian beam shape as well as transport through a vacuum in which no scattering occurs. (d) Multi-length scale nature of the simulation. (1) The image pixel size reflects the simulation voxel size of 8 nm, (2) a simulated deposit (white), and (3) primary electron trajectories (green) for the geometry described in (c) for the beam energy of 30 keV. The scale on the graph applies also to the image. (e) Simulation illustrating the precursor coverage for a precursor flux with directed and diffuse components on a surface with an arbitrary morphology. The "mountain range" morphology highlights the expected shadowing pattern for a purely directed precursor flux.

SIMULATION DESCRIPTION

The results of a FEBID simulation are shown in Figure 1a. Details related to the 3D rendition are provided in S1. First, a vertical nanopillar was deposited using a stationary beam dwell of 2.4 s. This nanopillar served as a support for the subsequent deposition of a suspended segment. The segment was grown by translating the virtual electron beam (FWHM = 4 nm), parallel to the substrate plane, using a digital step length of 0.2 nm and an exposure time of 2.4 ms. The geometry presented in Figure 1a serves as a model structure to describe the simulation details in the following simulation overview.

OVERVIEW

The hybrid Monte Carlo−continuum simulation consists of two distinct parts: a Monte Carlo simulation that calculates the electron−solid interaction (Figure 1b) and an FEBID simulation of precursor surface adsorption, transport, and deposition. The FEBID simulation consists of two main subroutines.

In the first subroutine, electron trajectories, derived in the Monte Carlo simulation, are adapted to the shape of the evolving 3D deposit (Figure 1c). Electron trajectory adaption is the first step toward generating an emitted secondary electron distribution and an effective secondary electron current density over the surface of the 3D deposit. This subroutine is executed each time the electron beam is displaced to the next position on the 3D deposit surface, *i.e.*, at the beginning of each unique dwell time (τ_d).

In the second subroutine, the coupled rate equations describing precursor adsorption, desorption, surface diffusion, dissociation, and deposition are solved. In particular, the rate equation describing deposition includes the emitted secondary electron current density profile derived from the adapted Monte Carlo subroutine. The second subroutine is executed repeatedly during each dwell time, with a time step ($\Delta t \ll \tau_D$), in order to simulate time-dependent changes in precursor coverage and electron beam induced dissociation dynamically during the continuous electron irradiation.

MONTE CARLO SIMULATION

The Monte Carlo algorithm, which is executed first, generates a series of unique electron trajectories in an infinite 3D domain that is larger than the beam impact region (BIR) so as to fully encapsulate the electron trajectory (Figure 1b). The domain has the material properties (atomic number, atomic weight, and density) characteristic of the deposit material. Each electron starts at an embedded virtual beam position of (x_i,y_i,z_i), parallel

DOI: 10.1021/acsnano.6b02108
ACS Nano 2016, 10, 6163−6172

to the $-z$ direction and with an initial energy of E_o. Elastic (Rutherford cross-section) and inelastic (continuous slowing down approximation) scattering processes[27] occur as the electron propagates through the solid until the electron reaches a cutoff energy of 100 eV, where the Monte Carlo routine stops (see S2 for the justification). Each electron scattering event is characterized by (1) the (x,y,z) coordinates and (2) the inelastic electron energy loss (and subsequently the primary electron energy). This information is saved to a file for use in the FEBID simulation.

FEBID SIMULATION

Subroutine #1: Electron Trajectory Adaption. Electron trajectories originally calculated in the extended solid are adapted to construct the beam interaction volume and its convolution with the 3D deposit. Electron trajectory adaption to the deposit includes accounting for the real Gaussian beam shape, electron transport through a vacuum upon escape from the deposit surface, in which no scattering occurs, and primary electron re-entry into the deposit as described in detail in S3. The 3D deposit is contained within a domain of cubic voxels. Each voxel has a unique material identifier; "B" indicating bulk/deposit, "V" vacuum/vapor phase, and "S" a surface voxel. Each electron trajectory is adapted to the 3D deposit by first shifting the initial coordinate (x_i,y_i,z_i) of the sampled trajectory to the beam-deposit surface impact point (Figure 1c). An additional displacement is executed to reconstruct the Gaussian shape of the focused electron probe (Figure 1c). The current model does not include the effect of beam defocus in the z-coordinate, which, for the small structures demonstrated, is appropriate. Subsequently, each additional (x,y,z) coordinate defining the scattering path is referenced to the voxel that it intersects. A statistically significant (S4) number of primary electron trajectories are used and scaled to generate the required total electron dose per dwell time.

Inelastic electron energy loss (dE/ds) (see Methods) occurs if an electron passes through a "B" voxel. A fraction of the energy loss (f) leads to secondary electron generation according to

$$n_{SE} = \frac{f}{\varepsilon}\frac{dE}{ds}\Delta s \tag{1}$$

where n_{SE} is the number of secondary electrons (SE) created, ε is the energy required to create a secondary electron, and Δs is the path length of the electron trajectory that intersects the specific "B" voxel. Data for f is unavailable for the deposited material composition PtC_5, so f was arbitrarily set to equal to 1 and $\varepsilon = 73$ eV was calculated from atomic values available for Pt ($\varepsilon = 30$ eV) and C ($\varepsilon = 80$ eV), using atomic averaging from Lin *et al.*[28] Conveniently, these values recovered the experimentally measured SE yield of 0.1, which provided an additional calibration between simulations and experiments. Liberated secondary electrons are emitted in an isotropic geometry from an origin located along the primary electron scattering trajectory. Random spherical point picking is used to generate each SE trajectory, where the radius of the sphere is equal to the secondary electron mean free path. The number of secondary electrons that traverse each surface voxel "S" is accumulated, then stored, as input for integration with the continuum rate equations. The result is a three-dimensional secondary electron surface emission profile, constructed using

$$i_{SE}(x, y, z) = \frac{\sum n_{SE}}{\left(\frac{n_{PE}q}{i_b}\right)(\Delta z^2)} \tag{2}$$

where $n_{PE}q/i_b$ is the time for n_{PE} electrons to impact the deposit for the primary electron beam current setting of i_b, q is the charge per electron, and Δz^2 is the surface area per surface voxel (S5) face yielding the electron flux term $i_{SE}(x,y,z)$.

Finally, in the event that an electron passes through a vacuum voxel "V", the electron trajectory is extended along its current trajectory until the electron either reenters the solid or exits the simulation domain. In the former case, the remaining coordinates defining the total scattering path are also shifted by the translation in the vacuum and the electron trajectory continues scattering in the solid (Figure 1c). In the latter case, the current trajectory is terminated.

The various length scales of the simulation are shown in Figure 1d. A single voxel ($\Delta z = 8$ nm edge length) in the simulation domain is shown as (1) in the inset, the inset boundaries define a typical continuum simulation domain size (720 nm) inset (2), while the main Figure 1d window shows a cross-section through the buried beam impact point in the Monte Carlo simulation for 30 keV point electron source.

Subroutine #2: Rate Equation Solver. The time-dependent precursor surface concentration at each surface voxel in the simulation is described by

$$\frac{\partial C(x, y, z)}{\partial t} = D\nabla^2 C(x, y, z) + \delta\Phi(x, y, z) \times\left[1 - \frac{C(x, y, z)}{s_p}\right] - \frac{C(x, y, z)}{\tau} - \sigma C(x, y, z)\, i_{SE}(x, y, z) \tag{3}$$

where the terms appearing on the right-hand side, moving from left to right, treat precursor surface diffusion, adsorption, desorption, and the electron beam induced dissociation, respectively. The precursor surface impingement flux $\Phi(x,y,z)$ is treated as space-dependent (Figure 1e) because past experiments have revealed that the precursor flux has both diffuse and directed contributions,[24] an effect observed previously by Bret *et al.*[29] and Friedli *et al.*[30] The directed component of the precursor flux is space-dependent and depends critically on the orientation of the surface normal vector with respect to the so-called gas flux vector (GFV) of the precursor beam emerging from the gas injection system. The gas flux vector is the propagation vector of the directed portion of the precursor "beam". S6 provides details on how the directed gas flux is calculated. The diffuse gas flux is assumed to be constant over the entire simulation domain containing the deposit. Importantly, the surface flux calculation requires knowledge of the surface normal, and the method used to approximate the surface normal is provided in S6.

SIMULATION PARAMETERS

PtC_5 deposits were grown using the $MeCpPt^{IV}Me_3$ precursor using an electron beam acceleration voltage (E_o) of 30 keV, a beam current (i_b) of 21 pA, and a local, total precursor pressure (P_T) of 30 mTorr. A stationary electron beam dwell was used to determine the electron yields from the surface; the secondary electron yield per incident primary electron (δ_{SE}) was 0.1 for a flat, semi-infinite PtC_5 substrate. The equilibrium precursor surface coverage (θ_o) for the flat PtC_5 surface for our gas injection system was calculated to be 0.73 when the precursor nozzle was oriented at 38° with respect to the substrate normal vector and the precursor capillary tube. Parameters necessary for this calculation were (1) the precursor sticking probability

DOI: 10.1021/acsnano.6b02108
ACS Nano 2016, 10, 6163−6172

(unknown, assumed $\delta = 1$), (2) the surface diffusion coefficient 0.4 $\mu m^2/s$ of $MeCpPt^{IV}Me_3$[31] and (3) the mean surface residence time (τ) of 100 μs for the $MeCpPt^{IV}Me_3$ molecule adsorbed on PtC_5.[26] Regarding the parameter (τ), an experimentally derived value of ~29 μs is reported in the literature,[32] yet we have found that by increasing the parameter to 100 μs a better fit to our experiments is achieved.[26] Additional information regarding the experiments is provided in the Methods section.

The model applied in the simulation assumes that only secondary electrons contribute to electron impact dissociation.[33] Forward scattered electrons (FSE) and backscattered electrons (BSE) influence precursor dissociation indirectly, through the SEs that they generate as they exit/reenter the deposit or substrate. The SE-driven precursor dissociation is well known to be the highest probability pathway for dissociation.[34] A mean dissociation cross-section ($\sigma = 0.013$ nm^2) was determined by integrating the energy-dependent cross-section, reported in ref 35 over the SE emission range 0−50 eV weighted to the number of SEs emitted per unit energy.[24] The Methods also contains a complete table of parameters used in the simulation.

A floating parameter for this simulation was introduced to fit the remaining difference between experiments and simulations. This parameter is defined as the variable χ, and the best fit value was $\chi = 2.1$ (see S7 for effect of χ and τ_d). This parameter was multiplied by σ in order to increase the FEBID growth rate for the simulations. The contributions of primary, backscattered, and forward scattered electrons to FEBID are ignored as well as low-energy electron attachment reactions, which could account for some fraction of χ.

RESULTS AND DISCUSSION

Simulation Accuracy and Information Recovery. The predecessor to this simulation was a 2D hybrid Monte Carlo and continuum simulation reported in ref 24. The simulation includes (1) the implications of the precursor beam or GFV and (2) beam scanning but excludes (1) a treatment of precursor diffusion in 3D and assumes (2) growth exclusively in the vertical dimension, normal to the original substrate surface. On one hand, the 2D simulation predicted well the effects of beam scanning strategies on nanoscale pseudo-2D deposit geometries, but the approach is limited to evolving deposits with negligible surface curvature. As such, the simulation is incapable of predicting the evolution of complex 3D features. A series of test experiments are now presented, which were contrived for the purpose of reproducing pseudo-2D simulated results reported previously and to help validate the 3D simulation.

Simulations of Pseudo-2D FEBID. FEBID is used frequently to deposit thin square/rectangular prisms, which serve as electrical contacts, defect repair films, *etc.* The thin square prism is achieved by a simple raster scanning approach even when a directed precursor beam is used.[24] However, unwanted surface artifacts evolve for more complex scanning strategies. An outward spiral scanning tactic is shown in Figure 2a. This pattern leads to the deposition of peculiar surface features in part because the beam trajectory switches abruptly between trajectories toward, away from, and perpendicular to the GFV.[24] The GFV orientation with respect to the shot pattern and projected on the $x-y$ plane is provided Figure 2a. The GFV is oriented at 38° with respect to the substrate surface normal for the experiments and simulations reported here. The colored 2D AFM height image map in Figure 2a shows the experimental results of such a scanning strategy.

A nanoscale surface morphology evolves with four distinct terraces for the spiral-out patterning. An acceleration voltage of 5 keV and a beam current of 400 pA were used to deposit the pattern.[24] The characteristic size of the beam was FWHM = 27.1 nm with a pixel point pitch of 13 nm and a 1 ms beam dwell per pixel point. A purely directional beam producing a local precursor pressure of 15 mTorr at the growth surface reproduced experimental results using the pseudo-2D simulation.[24] The 3D simulation reported here reproduced the pseudo-2D simulation results reported previously with a slight adjustment in some parameters (S8).

The terraced surface morphology of the thin square prism was recovered using the 3D simulation (Figure 2b). The 3 × 3 vertical voxel slice illustrates the fractional deposit occupancy near the surface of the deposit. One goal of the current 3D simulation is to make multi-length-scale simulations more tractable. Numerical stability is maintained during the finite difference part of the subroutine if $\Delta tD/\Delta z^2 < 0.125$ is satisfied. It was determined that Δz could be increased up to a length of 8 nm without sacrificing the desired nanoscale resolution. Moreover, the voxel size of 8 nm was found to yield an execution speed comparable with the 2D simulation while slightly sacrificing lateral resolution, as evident in the 3D plot in Figure 2b. Conveniently, accounting for partial voxel filling in the simulation and the voxel surface normal routine (S6) effectively reveals growth features at subvoxel resolution. In the case of the square prism, the deposit growth front proceeds predominantly in the vertical direction (z) over all (x,y) space. Thus, the summation of voxel occupancy in the z-dimension estimates well subvoxel details as shown in Figure 2c. The 1 × 3 voxel array is the summation of voxel occupancy in the 3 × 3 slice in Figure 2b. The simulation reveals important details such as the trenches between the terraces, which were also observed in experiments but not revealed by the previous pseudo-2D simulation. The maximum height of the simulated prism (57 nm) matched experiments (62 nm) as well as the ratio of ledge heights (min/max simulation = 0.65, experiment 0.68) (S9). Figure 2d shows an AFM image of the complementary thin film prism deposited experimentally.

Advanced 3D Simulations. Experiments revealed that the most resolved 3D structures are produced at the highest possible primary energy (30 keV) for conventional field-emission SEMs, and a relatively low current (21 pA) as reported previously.[36,37] Figure 3 shows an SEM image of an array of angled segments, supported by vertical pillars, deposited with a variable dwell time (3−50 ms) for $\Lambda = 1$ nm. The "segment" geometry is a critical basic element required to create any 3D object with a mesh or lattice structure.[13,14,38] The insets representatively show complementary segments deposited from the Au- and W-containing organometallic precursors dimethylgold acetylacetonate[39] and tungsten hexacarbonyl, respectively, demonstrating the applicability of the 3D growth conditions to multiple precursor molecules. As lateral beam size scales inversely with PE energy and in proportion to the PE current, the experimental conditions used favored a small probe to achieve high resolution. However, the SE yield is relatively low at 30 keV, making dissociation and subsequent deposition less efficient. Ancillary deposition is therefore reduced outside the BIR.

Control of the segment angle of the growing deposit (ζ, Figure 4a) is critical for the 3D direct-write process. Specifically, the capability to grow segments spanning from

DOI: 10.1021/acsnano.6b02108
ACS Nano 2016, 10, 6163−6172

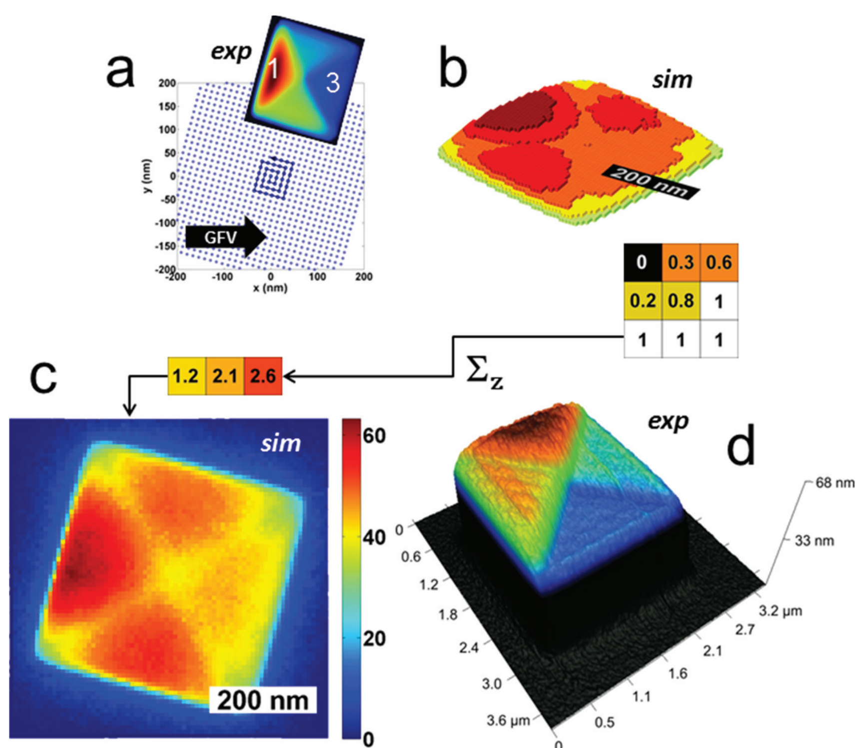

Figure 2. (a) Spatial map in the x−y plane of primary electron beam shots for a spiral-out scanning strategy.[24] The projection of the gas flux vector in the x−y plane is shown. An AFM image shows the experimental result for this scanning strategy (E_o = 5 keV, i_b = 400 pA, r_b = 27.1 nm, Λ = 13 nm, α = 15°, β = 52°). α and β defined in Table I, Methods. The edge length of the prism is 2 μm. Ledge #1 is 62 nm high, while ledge #3 is 42 nm high. (b) The complementary simulation of filled voxels yields a similar morphology. However, the voxel size of 8 nm impairs the resolution. The bottom of (b) represents a 3 × 3 vertical slice through the prism, revealing partially filled surface voxels where the fraction and colormap indicate the volume fraction of the deposit. (c) Subvoxel resolution is estimated/recovered by executing a summation operation of total deposition in the z-direction, the direction of the FEBID growth front for this geometry. Above (c) is the summation of the 3 × 3 voxel array in the vertical/z-dimension. (d) High-resolution 3D AFM image of the complementary, experimentally derived thin film prism.

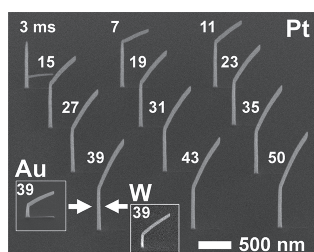

Figure 3. Experimental study of segment angle (ζ°) *vs* beam dwell time for PtC_5 deposited from the MeCp(Pt^{IV})Me_3 precursor. After an initial constant pillar growth, the beam is scanned with a pixel point pitch (Λ) fixed at 1 nm, and the scan length was 400 nm. The beam dwell time (τ_d) is superimposed over the SEM image for each segment in units of milliseconds. The bottom left insets shows AuC_x and WC_x segments, derived from the precursors dimethylgold acetylacetonate and tungsten hexacarbonyl, for a dwell time of 39 ms (Λ = 1 nm).

horizontal (ζ = 0°) to vertical (ζ = 90°) is necessary to construct all possible segment orientations for 3D objects. The segment geometry was explored here to (1) quantify the experimentally assessable direct-write angle range and to (2) test the accuracy of the simulation. The segment morphology is deposited by a two-step direct-write sequence. An initial, stationary beam produces a vertical pillar morphology where the height is controlled by the total dwell time with a nearly linear dependence, which suggests a steady-state FEBID condition. Next, the beam is laterally displaced at constant velocity with a fixed pixel point pitch to produce the segment component. The scan speed controls the segment angle, as has been observed previously.[8] The vertical pillar served as a reproducible platform for segment growth, as standard substrate proximity effects are minimized for the suspended segments, particularly when using the highest primary beam energy. The stage current signal collected during EBID is sensitive to patterning changes such as the pillar to segment transition.[40] S10 provides a complementary EBID simulation for the previously reported "tip on suspended rod"[40] geometry, demonstrating the successful emulation of the stage current signal.

A simulated segment is shown in Figure 4a in cross-section through the length of the segment. A top-down view of the segment is provided in the inset shown at the top. The segment width (w = 24 nm), nanopillar diameter (d = 56 nm), segment angle (ζ = 42°), and thickness (t = 80 nm) all agreed well with experimental results of segment width (w = 26 nm), nanopillar diameter (d = 53 nm), segment angle (ζ = 47°), and thickness (t = 73 nm). The experimental values were determined from an image measurement where the image pixel size was 2.4 nm. The pixel point pitch during the segment growth was 1 nm with a constant pixel dwell time of 11 ms.

Simulations also predicted the effect of beam dwell time on the segment angle (Figure 4b). Lastly, experiments revealed that the angle of the GFV with respect to beam displacement

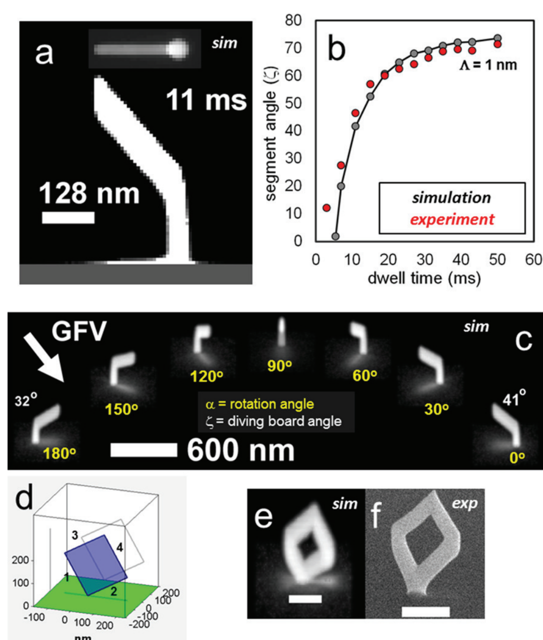

Figure 4. (a) Simulated segment grown at 30 keV and 21 pA with a dwell time per pixel of 11 ms and 1 nm pixel point pitch. The 3D object was grown in two steps: a static dwell of 1.75 s to generate the vertical pedestal followed by a line scan in the $x-y$ plane to create a segment characterized by a beam speed of 9.1×10^{-2} nm/ms. The inset shows a top-down image of the segment. The pixel size in the image is 8 nm and equal to the simulation voxel size. (b) Simulated (gray) and experimental results (red) for the segment angle (in degrees) as a function of beam dwell time. (c) Consistent with experiments, simulations revealed that the segment angle variation with respect to segment growth direction relative to the gas flux vector (α) was negligible. (d) FEBID design for a tilted square frame with segments labeled. Projections of the frame on the $x-y$, $y-z$, and $x-z$ planes are shown in gray for 3D clarity. The temporal distribution of beam dwell positions is shown in the movie file in S12. A movie of the FEBID growth is provided in S13, and a virtual SEM image of the simulated result is provided in (e) (see S14 for virtual SEM method). The snapshot in (e) was taken at an angle of 52° with respect to the virtual substrate normal and was stretched by a factor of 1/sin(52°) in the vertical direction to mimic (f) the tilted experimental SEM image. The scale bars in (e) and (f) are 200 nm.

vector (α), where GFV_{xy} indicates the GFV projected onto the substrate plane, had a negligible effect on the segment angle, as confirmed by simulations shown in the image collage provided in Figure 4c. For reference, α is arbitrarily defined as 0° when the beam displacement vector was antiparallel with the GFV_{xy} and 180° when parallel with the GFV_{xy}.[24] A previous study[29] has demonstrated a strong dependence on the GFV and beam scanning direction during 3D EBID. In S11, complementary 3D EBID simulations are presented that support the authors' claim that surface coverage variations dictate the final morphology for complex and highly oriented 3D surfaces.

The results presented in Figure 4b served as a turning point for the evolution of the simulation. Previously, physical experiments were used to calibrate the 3D simulation; however, once the simulation was verified/calibrated using the results presented in Figure 4b, CAD files were generated for the desired 3D structure and exported to the simulator, which tested the growth conditions, which were finally verified experimentally.

Direct-Write, Computer-Aided Design (CAD). 3D objects for direct-write design were first defined by vectors spanning object edges. The models are defined as 3D mesh structures with linear segments connecting object vertices. The CAD program determines each segment angle and linearly interpolates the requisite segment angle for the simulated data points in Figure 4b to generate a stream file of x, y, and τ_d coordinates for each pixel. 3D object construction requires segment connectivity to form meshes/frame elements. FEBID experiments were conducted to test the robustness and predictability of simulated designs for assembling connecting segments. A vertical and tilted frame was simulated at 30 keV, 21 pA, where the lower edge of the square (segment 2 in Figure 4d) was raised at 30° with respect to the underlying substrate. The simulated result is shown in a virtual SEM image (Figure 4e) where the substrate has been tilted at an angle of 52°. The image has been stretched in Figure 4e along the vertical coordinate by a factor of 1/sin(52°) in order to emulate the real image acquisition conditions for the complementary experiment shown in Figure 4f.

The distribution of beam shots required to deposit the square frame was divided into four phases. This distribution is described below, while a movie of the shot distribution in provided in S12. In general, to construct multiple edge geometries, two approaches are possible: (1) serial growth of entire segments or parallel growth of multiple segments. For the square geometry in Figure 4d–f for instance one can grow segments 1 and 2 in parallel or in series followed by a series or parallel growth of segments 3 and 4. A subtle advantage is realized by doing parallel edge growth associated with (1) the slight accumulation of precursor that occurs at each growth front when the other edge(s) are being exposed and (2) the symmetric proximal deposition that each segment realizes relative to asymmetric proximal deposition when the exposure is executed in series. Initially, in phase 1, the *beam alternated*, per shot, between the growth of segments 1 and 2. It is important to note that segments 2 and 3 required a per-shot dwell time of 1.98 ms, while segments 1 and 4 required a dwell time of 3.73 ms due to the different segment angles. The pixel point pitch was constant at 0.2 nm for all phases of exposure. As a result, during the first phase, segment 1 completes before segment 2. A second phase then ensues where the growth of segment 2 is completed. Upon completion, segments 3 and 4 are then exposed in the same alternating fashion. Segment 4 finishes first, leading to the fourth and last phase of growth, where segment 3 grows to the point of frame closure. Simulation results closely replicated the experiment as highlighted in Figures 4e,f. Thus, the methodology was tested further by attempting the deposition of a 3D object (Figure 5a) which required the assembly of multiple frames and the final convergence to a single vertical point for high-fidelity reproduction.

A 3D cube CAD file was generated, grown by experiment (Figure 5a) and simulated (Figures 5b,c) successfully, on the first attempt. The cube was oriented in the design phase such that all segment angles were equal. A short pedestal was initially deposited using a static dwell of 0.75 s in order to provide a take-off point for the cube edge growth. Multiple phases of parallel growth ensued, which are evident in the movie provided in S15. This particular geometry requires a high density of pixel dwells (10 000) packed in a relatively small area (cube edge = 250 nm), leading to proximal deposition, or staining, on the underlying substrate. Strategies to minimize this proximity effect will be described in our near future work.

DOI: 10.1021/acsnano.6b02108
ACS Nano 2016, 10, 6163–6172

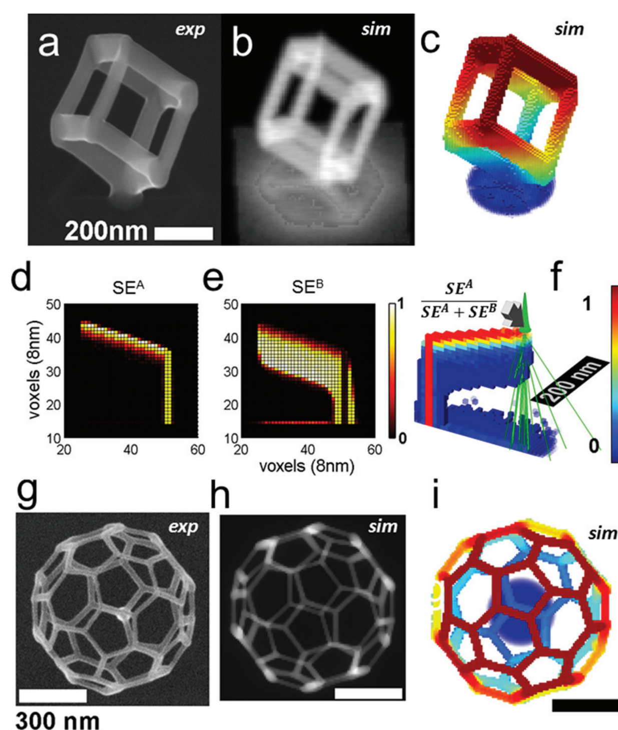

Figure 5. (a) SEM image of FEBID growth of a cubic frame. The segment length was 200 nm, and the cubic frame was rotated vertically by 54.7°. The rotation made all segment angles equal at 35.3°, requiring a dwell time (τ_d) of 11.0 ms at a pixel point pitch (Λ) of 1 nm. 2008 individual pixel dwells were required to write the cubic mesh. (b) Virtual SEM image of the simulation results that mimics the experiment in (a). (c) Simulation results rendered in the form of deposit surface voxels where the colormap is normalized to the vertical *z*-coordinate (see S15 for FEBID movie). (d) Segment slice, deposited using τ_d = 2.4 ms and Λ = 0.2 nm, showing the history of the deposited voxels based on SEs generated from the first scattering step of an electron (SE^A). (e) On the other hand secondary electrons generated beyond the first scattering event (SE^Bs) dominate the segment thickness due to transmitted primary electrons. Also, the substrate staining is caused mostly by SE^Bs with little contribution from SE^As. (f) Slice though the full 3D segment morphology where half the structure has been removed to reveal the interior. The colormap in this case reveals the fraction of SE^A and SE^B (where $SE^B = 1 - SE^A$) contribution on the same plot. (g) 3D truncated icosahedron deposited by FEBID with a characteristic edge dimension of 200 nm. The SEM image was acquired at 0° tilt in the top-down configuration. The truncated icosahedron design with a bottom hexagon was rotated 15° off the substrate plane on one of the hexagon vertices. The comparable simulated results are shown in (h) and (i).

Two candidates may be responsible for deposition on the supporting substrate: (1) electrons that "miss" the leading edge of the segment and strike the underlying substrate and (2) primary electrons that transmit through the deposit and re-enter the substrate. The relative contributions can be distinguished using the simulation by correlating the scattering step number with each deposition event. The consequent secondary electrons liberated during the first scattering step of the primary electron impact are denoted as SE^A, and secondary electrons generated by a scattering step >1 are denoted as SE^B.

The fraction of deposition stimulated by SE^A (first scattering step) *versus* SE^B (scattering step >1) was tracked for each deposit voxel. Figure 5d shows a slice through a segment grown using a dwell time of 1.6 ms and Λ = 0.2 nm, where the colormap reveals the normalized fraction of deposition generated by SE^As. The data are revealing; very little contribution arises from SE^A-induced deposition at the substrate surface. Conversely, Figure 5e shows that the substrate nanowire is deposited mainly by SE^Bs originating from the transmitted beam. Finally, Figure 5f shows the same information in a slightly different fashion, which provides insight into both modes of growth on a single figure. The 3D "B" voxel-based image has been sliced down the middle to reveal the history. Red portions of the colormap are driven mostly by SE^A-induced deposition, while blue areas are induced by SE^Bs. Also demonstrated by Figure 5d−f is the relative contribution of the segment growth; the figures illustrate that the segment thickness is dominated by growth induced by the exiting beam where the growth front is in the downward direction.

A 3D truncated icosahedron mesh was deposited (Figure 5g) and served as a model structure to test a more complex geometry. This geometry required 10 vertical levels of exposure forming 20 hexagons and 12 pentagons in the final mesh. Correct segment intersection at the last vertices deposited, during the last exposure level (Figure 5h,i), served as a qualitative test of segment angle precision.

CONCLUSIONS

Focused electron beam induced deposition is capable of the direct-write nanofabrication of complex free-standing 3D nanostructures. Understanding the dynamic interplay of the scanning electron beam and the adsorbed precursor molecules is critical to accelerating the state of the art of FEBID as a 3D nanoprinting tool. To this end, we have developed a fully 3D hybrid Monte Carlo−continuum simulation to predict the growth of 3D objects *via* FEBID. Excellent agreement between experiments and simulations was realized. A CAD program that generates complex 3D structures and translates the necessary *x*−*y* coordinates and electron beam dwell times was also developed. The tractable simulation speed made it possible to test and optimize the pattern sequences to better guide our experimental capabilities for the growth of complex 3D deposits. For the case of the 3D truncated icosahedron demonstrated here, most of the critical electron−solid, precursor−solid, and electron−precursor interactions critical to growth take place on the surface of the deposit itself, with very little influence from the supporting substrate.

The most significant assumptions made in the simulation are as follows. The energy dependence of the total electron impact dissociation cross-section of the precursor $\sigma(E)$ is neglected in favor of a single value σ_m estimated using the mean energy of the secondary electron energy distribution.[24] Further, the effect of secondary electron refraction at the deposit interface is ignored when SEs intersect the deposit/vacuum interface. These features were included in previous, atom-level simulations[16] and are necessary to accurately predict sub-10 nm surface features. Also, the directed component of the precursor beam is a highly idealized model because zero beam divergence is assumed. This simplification could lead to poor FEBID emulation for the case of complex geometries, which exhibit complex shadowing patterns during growth. Nonetheless, these features can be adapted into the current simulation yet were intentionally omitted in favor of simulation speed. The agreement between experiments and simulations at the mesoscopic scale validate their exclusion in the results presented

DOI: 10.1021/acsnano.6b02108
ACS Nano 2016, 10, 6163−6172

here. In addition, supplements S10 and S11 provide complementary simulations of mesoscale artifacts reported previously.[29,40,41] In the future, translation of the simulation algorithm onto a high-performance computing platform will make it possible to include these features without the sacrifice of simulation process time.

METHODS/EXPERIMENTAL

Monte Carlo Simulation. The electron–solid interactions were emulated using a Monte Carlo electron scattering simulation reported previously[26] where a single scattering methodology was used. Elastic scattering was treated using the screened Rutherford cross-section.[27] The inelastic energy loss was treated using the continuous energy loss approximation implementing the Joy and Luo modified Bethe expression:[27]

$$\frac{dE}{dS} = -7.85 \times 10^{4}\frac{\rho \times Z}{AW \times E}\ln\left(\frac{1.166(E + 0.85J)}{J}\right)\left[\frac{keV}{cm}\right] \quad (4)$$

where Z is the atomic number, AW is the atomic weight, E is the electron energy, and J is the mean ionization potential.[27]

Continuum Simulation. An explicit forward time marching, centered space difference method was used to solve the 3D parabolic diffusion equation for the case of $MeCpPt^{IV}Me_3$ diffusion on the PtC_5 surface. Emulating surface diffusion in all three Cartesian dimensions required using both first and second nearest neighbor surface voxels in the centered difference approximation.[42] The improved Euler method (Huen's method) was used to approximate the ordinary differential equation describing the time-dependent surface coverage (adsorption and desorption) of $MeCpPt^{IV}Me_3$. Due to the coupling between diffusion and adsorption/desorption (*via* eq 3), these numerical methods had to be executed concurrently on the same time step. Numerical stability required that the time step be determined by the finite differencing method, which was $\Delta t \approx 10\ \mu s$. As an example of simulation timing, eq 3 was solved consecutively, 1289 times per 11 ms beam dwell, while the Monte Carlo sampling, described previously, was recalculated at the beginning of each beam dwell, or every 11 ms.

Experimental Section. Two different dual-beam microscopes were used for FEBID experiments: a Nova 200 and a Nova 600 (FEI Company, The Netherlands) in Austria and the US, respectively. While the $MeCpPt^{IV}Me_3$ precursor was used on both machines, $Me_2Au(acac)$ precursor was used only on the Nova 200 and $W(CO)_6$ only on the Nova 600. All experiments were performed on always new Si substrates with a 5 nm SiO_2 top layer[43] that were prepared in a laminar flow box (Austria) and clean room conditions (US) and immediately transferred to the microscopes. No special substrate cleaning procedures were used. Prior to any deposition experiment, the precursor reservoirs were preheated to 45 °C (Pt), 30 °C (Au), and 55 °C (W) for at least 30 min. To provide equilibrium between adsorption and desorption on the sample surfaces, the gas injection system (GIS) valves were opened for at least 3 min before the patterning processes. Chamber pressures were 6×10^{-6} and 1×10^{-6} mbar before and 2×10^{-5} and 1.5×10^{-5} mbar after valve opening in Austria and the US, respectively. The working distance during deposition for experiments performed in Austria was 5 mm according to the eucentric height, while deposition in the US was performed with a working distance of 6 mm due to the location of the GIS nozzles. S16 summarizes in table form further experimental details including the GIS nozzle positions and angles for the different microscopes

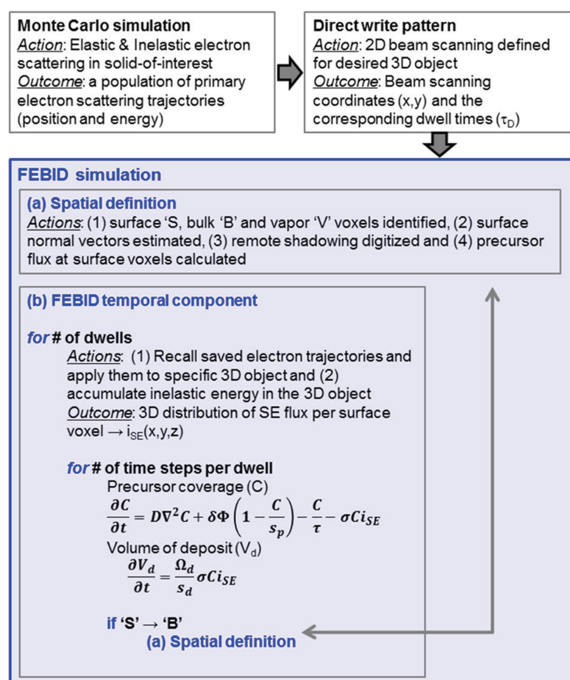

Figure 6. Hybrid Monte Carlo–continuum 3D focused electron beam induced deposition simulation execution flow diagram.

Table 1. Variables Critical to the Simulation Including Materials Properties, Electron Beam Settings, and Precursor Properties

Symbol	Description	Value	Unit
E_o	*Primary electron beam energy*	30	keV
i_b	*Primary electron beam current*	21	pA
FWHM	*Focused electron beam size*	4	nm
τ_d	*Electron beam dwell time per pixel*	3-50	ms
Λ	*Pixel point pitch*	0.2,1	nm
v	*Electron beam speed*	0.02-0.2	nm/s
D	*Diffusion coefficient of $MeCpPt^{IV}Me_3$*	0.4	$\mu m^2/s$
P	*Total pressure at deposit surface*	30	mTorr
P_{beam}	*Specular component of total pressure*	20	mTorr
P_b	*Diffuse component of total pressure*	10	mTorr
τ	*Mean surface residence time of $MeCpPt^{IV}Me_3$ on PtC_5*	100	μs
δ	*Sticking probability of $MeCpPt^{IV}Me_3$ on PtC_5*	1	
σ	*Mean, total dissociation cross-section for $MeCpPt^{IV}Me_3$*	0.013	nm^2
ε	*Energy required to create a secondary electron in PtC_5*	73	eV
f_{SE}	*Fraction of inelastic energy for secondary electron creation*	1	
λ	*Mean free path of a secondary electron in PtC_5*	2.5	nm
s_p	*Surface site density for $MeCpPt^{IV}Me_3$ adsorption*	2.8	$sites/nm^2$
s_d	*Surface density of PtC_5*	4.8	$molecules/nm^2$
χ	*Residual fitting parameter for the FEBID simulation*	2.1	
α	*Angle between beam scanning vector and gas flux vector project on the substrate*	0-180	degrees
β	*Angle between substrate surface and gas nozzle axis*	52	degrees
ζ	*Segment angle with respect to the substrate plane*	0-90	degrees

DOI: 10.1021/acsnano.6b02108
ACS Nano 2016, 10, 6163–6172

and precursors. Electron beam optimization was carefully done on a predeposited dot followed by beam blanking and stage moves toward real deposition areas in close proximity. To prevent any further mechanical drift, a waiting period of about 10 min was introduced before deposition. Patterning was performed using stream files, which allow precise process control. Subsequent electron imaging was done at low dose and in 52° stage tilt position after a waiting period of more than 30 min to enable desorption of precursor molecules.

Atomic force microscopy was performed using a Dimension 3100 AFM (Bruker Nano) with a Nanoscope IVa controller and a XYZ Hydrid scan head in tapping mode using Olympus OMCL TS-240 AFM tips. Details on the fabrication process of the spiral out pad in Figure 2d are given in ref 24.

Figure 6 provides an abbreviated flow diagram for the 3D FEBID simulation. Lastly, a complete table of simulation parameters is provided in Table 1.

ASSOCIATED CONTENT

Supporting Information

The Supporting Information is available free of charge on the ACS Publications website at DOI: 10.1021/acsnano.6b02108.

(S1) Three-dimensional rendering of deposits and movie, (S2) cutoff energy used in the Monte Carlo electron scattering simulation, (S3) Monte Carlo electron trajectory mapping to 3D deposits, (S4) electron interaction volume creation, (S5) surface area of surface voxels, (S6) deposit surface normal estimation and surface orientation dependent surface flux, (S7) 3D FEBID simulation calibration factor, (S8) FEBID parameters, (S9) comparison of 3D FEBID simulation results with a previous 2D FEBID simulation, (S10) 3D FEBID simulations of published work I: sample current monitor, (S11) 3D FEBID simulations of published work II: low-angle segments (PDF)

(S12) Movie of the beam dwell pattern for a 3D vertical square frame, (S13) movie of 3D FEBID simulation results for vertical square frame, (S14) virtual SEM images of 3D FEBID simulation results, (S15) movies of 3D FEBID simulation of a vertical, vertex standing cube and a virtual SEM rotation around the deposited cube, (S16) various experimental FEBID conditions (ZIP)

AUTHOR INFORMATION

Corresponding Author

*E-mail (J. D. Fowlkes): fo2@ornl.gov.
*E-mail (H. Plank): harald.plank@felmi-zfe.at.

Notes

The authors declare no competing financial interest.

ACKNOWLEDGMENTS

J.D.F. and P.D.R. acknowledge the creation of the model and simulation conducted at the Center for Nanophase Materials Sciences, which is a DOE Office of Science User Facility. R.W. and H.P. gratefully acknowledge the valuable support provided by Prof. Dr. Ferdinand Hofer. R.W. and H.P. also acknowledge financial support by the COST action CELINA (No. CM1301), EUROSTARS project TRIPLE-S (No. E! 8213), and the bmvit exchange program. M.G.S. acknowledges support from the National Defense Science and Engineering Graduate Fellowship funded through the AFOSR. B.B.L. acknowledges support *via* the University of Tennessee Chancellor's Fellowship program.

REFERENCES

(1) van Dorp, W. F. Sub-10 nm Writing: Focused Electron Beam-Induced Deposition in Perspective. *Appl. Phys. A: Mater. Sci. Process.* **2014**, *117*, 1615−1622.

(2) van Dorp, W. F.; Zhang, X. Y.; Feringa, B. L.; Hansen, T. W.; Wagner, J. B.; Hosson, J. T. M. Molecule-by-Molecule Writing Using a Focused Electron Beam. *ACS Nano* **2012**, *6*, 10076−10081.

(3) Esposito, M.; Tasco, V.; Cuscuna, M.; Todisco, F.; Benedetti, A.; Tarantini, I.; De Giorgi, M.; Sanvitto, D.; Passaseo, A. Nanoscale 3D Chiral Plasmonic Helices with Circular Dichroism at Visible Frequencies. *ACS Photonics* **2015**, *2*, 105−114.

(4) Fisher, J. S.; Kottke, P. A.; Kim, S.; Federov, A. G. Rapid Electron Beam Writing of Topologically Complex 3D Nanostructures using Liquid Phase Precursor. *Nano Lett.* **2015**, *15*, 8385−8391.

(5) Kretz, J.; Rudolph, M.; Weber, M.; Koops, H. W. P. 3-Dimensional Structurization by Additive Lithography, Analysis of Deposits using TEM and EDX, and Application to Field-Emitter Tips. *Microelectron. Eng.* **1994**, *23*, 477−481.

(6) Koops, H. W. P.; Kaya, A.; Weber, M. Fabrication and Characterization of Platinum Nanocrystalline Material grown by Electron-Beam Induced Deposition. *J. Vac. Sci. Technol., B: Microelectron. Process. Phenom.* **1995**, *13*, 2400−2403.

(7) Gazzadi, G. C.; Frabboni, S.; Menozzi, C. Suspended Nanostructures grown by Electron Beam-Induced Deposition of Pt and TEOS Precursors. *Nanotechnology* **2007**, *18*, 445709.

(8) Molhave, K.; Madsen, D. N.; Dohn, S.; Boggild, P. Constructing, Connecting and Soldering Nanostructures by Environmental Electron Beam Deposition. *Nanotechnology* **2004**, *15*, 1047−1053.

(9) Hoflich, K.; Yang, R. B.; Berger, A.; Leuchs, G.; Christiansen, S. The Direct Writing of Plasmonic Gold Nanostructures by Electron-Beam-Induced Deposition. *Adv. Mater.* **2011**, *23*, 2657−2661.

(10) Koops, H. W. P.; Hoinkis, O. E.; Honsberg, M. E. W.; Schmidt, R.; Blum, R.; Bottger, G.; Kuligk, A.; Liguda, C.; Eich, M. Two-Dimensional Photonic Crystals produced by Additive Nanolithography with Electron Beam-Induced Deposition act as Filters in the Infrared. *Microelectron. Eng.* **2001**, *57−8*, 995−1001.

(11) Utke, I. *Nanofabrication Using Focused Ion and Electron Beams, Principles and Applications*; Oxford University Press, 2012.

(12) Floreani, F.; Koops, H. W.; Elsasser, W. Operation of High Power Field Emitters Fabricated with Electron Beam Deposition and Concept of a Miniaturised Free Electron Laser. *Microelectron. Eng.* **2001**, *57−58*, 1009−1016.

(13) Matsui, S.; Kaito, T.; Fujita, J.; Komuro, M.; Kanda, K.; Haruyama, Y. Three-Dimensional Nanostructure Fabrication by Focused-Ion-Beam Chemical Vapor Deposition. *J. Vac. Sci. Technol., B: Microelectron. Process. Phenom.* **2000**, *18*, 3181−3184.

(14) Matsui, S. Focused-Ion-Beam Deposition for 3-D Nanostructure Fabrication. *Nucl. Instrum. Methods Phys. Res., Sect. B* **2007**, *257*, 758−764.

(15) Smith, D. A.; Fowlkes, J. D.; Rack, P. D. A Nanoscale Three-Dimensional Monte Carlo Simulation of Electron-Beam-Induced Deposition with Gas Dynamics. *Nanotechnology* **2007**, *18*, 265308.

(16) Plank, H.; Smith, D. A.; Haber, T.; Rack, P. D.; Hofer, F. Fundamental Proximity Effects in Focused Electron Beam Induced Deposition. *ACS Nano* **2012**, *6*, 286−294.

(17) Smith, D. A.; Fowlkes, J. D.; Rack, P. D. Simulating the effects of surface diffusion on electron beam induced deposition *via* a three-dimensional Monte Carlo simulation. *Nanotechnology* **2008**, *19*, 415704.

(18) Fowlkes, J. D.; Rack, P. D. Fundamental Electron-Precursor-Solid Interactions Derived from Time-Dependent Electron-Beam-Induced Deposition Simulations and Experiments. *ACS Nano* **2010**, *4*, 1619−1629.

(19) Rykaczewski, K.; White, W. B.; Fedorov, A. G. Analysis of Electron Beam Induced Deposition (EBID) of Residual Hydrocarbons in Electron Microscopy. *J. Appl. Phys.* **2007**, *101*, 054307.

(20) Toth, M.; Lobo, C.; Friedli, V.; Szkudlarek, A.; Utke, I. Continuum Models of Focused Electron Beam Induced Processing. *Beilstein J. Nanotechnol.* **2015**, *6*, 1518−1540.

DOI: 10.1021/acsnano.6b02108
ACS Nano 2016, 10, 6163−6172

(21) Lobo, C. J.; Toth, M.; Wagner, R.; Thiel, B. L.; Lysaght, M. High Resolution Radially Symmetric Nanostructures from Simultaneous Electron Beam Induced Etching and Deposition. *Nanotechnology* **2008**, *19*, 025303.
(22) Winkler, R.; Geier, B.; Plank, H. Spatial Chemistry Evolution during Focused Electron Beam-Induced Deposition: Origins and Workarounds. *Appl. Phys. A: Mater. Sci. Process.* **2014**, *117*, 1675–1688.
(23) Winkler, R.; Szkudlarek, A.; Fowlkes, J. D.; Rack, P. D.; Utke, I.; Plank, H. Toward Ultraflat Surface Morphologies During Focused Electron Beam Induced Nanosynthesis: Disruption Origins and Compensation. *ACS Appl. Mater. Interfaces* **2015**, *7*, 3289–3297.
(24) Winkler, R.; Fowlkes, J.; Szkudlarek, A.; Utke, I.; Rack, P. D.; Plank, H. The Nanoscale Implications of a Molecular Gas Beam during Electron Beam Induced Deposition. *ACS Appl. Mater. Interfaces* **2014**, *6*, 2987–2995.
(25) Cullen, J.; Bahm, A.; Lobo, C. J.; Ford, M. J.; Toth, M. Localized Probing of Gas Molecule Adsorption Energies and Desorption Attempt Frequencies. *J. Phys. Chem. C* **2015**, *119*, 15948–15953.
(26) Fowlkes, J. D.; Geier, B.; Lewis, B. B.; Rack, P. D.; Stanford, M. G.; Winkler, R.; Plank, H. Electron Nanoprobe Induced Oxidation: a Simulation of Direct-Write Purification. *Phys. Chem. Chem. Phys.* **2015**, *17*, 18294–18304.
(27) Joy, D. C. An Introduction to Monte-Carlo Simulations. *Scanning Microscopy* **1991**, *5*, 329–337.
(28) Lin, Y.; Joy, D. C. A New Examination of Secondary Electron Yield Data. *Surf. Interface Anal.* **2005**, *37*, 895–900.
(29) Bret, T.; Utke, I.; Hoffmann, P. Influence of the Beam Scan Direction during Focused Electron Beam Induced Deposition of 3D Nanostructures. *Microelectron. Eng.* **2005**, *78–79*, 307–313.
(30) Friedli, V.; Utke, I. Optimized Molecule Supply from Nozzle-based Gas Injection Systems for Focused Electron- and Ion-Beam Induced Deposition and Etching: Simulation and Experiment. *J. Phys. D: Appl. Phys.* **2009**, *42*, 125305.
(31) Cullen, J.; Lobo, C. J.; Ford, M. J.; Toth, M. Electron-Beam-Induced Deposition as a Technique for Analysis of Precursor Molecule Diffusion Barriers and Prefactors. *ACS Appl. Mater. Interfaces* **2015**, *7*, 21408–21415.
(32) Friedli, V.; Santschi, C.; Michler, J.; Hoffmann, P.; Utke, I. Mass Sensor for *in situ* Monitoring of Focused Ion and Electron Beam Induced Processes. *Appl. Phys. Lett.* **2007**, *90*, 053106.
(33) Silvis-Cividjian, N.; Hagen, C. W.; Leunissen, L. H. A.; Kruit, P. The Role of Secondary Electrons in Electron-Beam-Induced-Deposition Spatial Resolution. *Microelectron. Eng.* **2002**, *61–62*, 693–699.
(34) Utke, I.; Hoffmann, P.; Melngailis, J. Gas-Assisted Focused Electron Beam and Ion Beam Processing and Fabrication. *J. Vac. Sci. Technol. B* **2008**, *26*, 1197–1276.
(35) van Dorp, W. F. The Role of Electron Scattering in Electron-Induced Surface Chemistry. *Phys. Chem. Chem. Phys.* **2012**, *14*, 16753–16759.
(36) Schmied, R.; Froch, J. E.; Orthacker, A.; Hobisch, J.; Trimmel, G.; Plank, H. A Combined Approach to Predict Spatial Temperature Evolution and its Consequences during FIB Processing of Soft Matter. *Phys. Chem. Chem. Phys.* **2014**, *16*, 6153–6158.
(37) Arnold, G.; Timilsina, R.; Fowlkes, J.; Orthacker, A.; Kothleitner, G.; Rack, P. D.; Plank, H. Fundamental Resolution Limits during Electron-Induced Direct-Write Synthesis. *ACS Appl. Mater. Interfaces* **2014**, *6*, 7380–7387.
(38) Kometani, R.; Warisawa, S.; Ishihara, S. The 3D Nanostructure Growth Evaluations by the Real-Time Current Monitoring on Focused-Ion-Beam Chemical Vapor Deposition. *Microelectron. Eng.* **2010**, *87*, 1044–1048.
(39) Botman, A.; Mulders, J. J. L.; Weemaes, R.; Mentink, S. Purification of Platinum and Gold Structures after Electron-Beam-Induced Deposition. *Nanotechnology* **2006**, *17*, 3779–3785.
(40) Bret, T.; Utke, I.; Hoffmann, P.; Abourida, M.; Doppelt, P. Electron Range Effects in Focused Electron Beam Induced Deposition of 3D Nanostructures. *Microelectron. Eng.* **2006**, *83*, 1482–1486.
(41) Bret, T.; Utke, I.; Gaillard, C.; Hoffmann, P. Periodic Structure Formation by Focused Electron-Beam-Induced Deposition. *J. Vac. Sci. Technol., B: Microelectron. Process. Phenom.* **2004**, *22*, 2504–2510.
(42) Hamilton, B.; Bilbao, S. Hexagonal vs. Rectilinear Grids for Explicit Finite Difference Schemes for the Two-Dimensional Wave equation. *J. Acoust. Soc. Am.* **2013**, *133*, 015120.
(43) Geier, B.; Gspan, C.; Winkler, R.; Schmied, R.; Fowlkes, J. D.; Fitzek, H.; Rauch, S.; Rattenberger, J.; Rack, P. D.; Plank, H. Rapid and Highly Compact Purification for Focused Electron Beam Induced Deposits: A Low Temperature Approach Using Electron Stimulated H_2O Reactions. *J. Phys. Chem. C* **2014**, *118*, 14009–14016.

DOI: 10.1021/acsnano.6b02108
ACS Nano 2016, 10, 6163–6172

Simulation Guided 3D Nanomanufacturing *via* Focused Electron Beam Induced Deposition

Jason D. Fowlkes[a,b], Robert Winkler[c], Brett B. Lewis[b], Michael G. Stanford[b] Harald Plank[c,d] and Philip D. Rack[a,b]

[a] Nanofabrication Research Laboratory, Center for Nanophase Materials Sciences, Oak Ridge National Laboratory, Oak Ridge, Tennessee 37831, United States
[b] Materials Science and Engineering Department, The University of Tennessee, Knoxville, Tennessee 37996, United States
[c] Graz Centre for Electron Microscopy, Steyrergasse 17, 8010 Graz, Austria.
[d] Institute for Electron Microscopy and Nanoanalysis, Graz University of Technology, Steyrergasse 17, 8010 Graz, Austria

Supplement 1

3D rendering

Surface voxels are rendered as shaded cubes in the 3D object images. Precursor coverage at each surface voxel is indicated by color. The precursor coverage is normalized to the maximum coverage. As a result, shadowing effects linked to the directed component of the impinging precursor flux are observed. The gas flux vector (grey) shows the directed component of the precursor flux. The gas flux vector is aimed at the beam impact region. Directly above the beam impact point the Gaussian nature of the beam is indicated by a green patch object. The z-component indicates the relative intensity of the beam, in its own z-coordinate system, while the FWHM of the beam profile accurately reflects the beam shape in the coordinate system of the deposit. The substrate lies in the x–y plane and the out–of–plane coordinate is z. Information to render the deposit is saved following each dwell time in the beam pattern.

Surface voxels lying in the substrate plane also exhibit transparency. Beyond the boundary, surface voxels are not rendered to (1) save rendering time and (2) provide contrast with the white background for the upper portions of the 3D object.

During each dwell, a defined number of electron trajectories are sampled to provide a visualization of the interaction of individual electron trajectories with the deposit. These are shown as the green trajectories. The surface voxels are given a slight transparency value within a small sphere (r=25 nm) centered at the beam impact point so that the partial penetration of the primary beam may be observed.

S1_FEBID_Segment.wmv

Supplement 2

While the cutoff energy of 100 eV is above the energy necessary to create a secondary electron (ε= 73 eV), the primary electron position at the end of its trajectory is typically very deep in the solid (~2.2 μm) for the an electron acceleration voltage of 30,000 eV as shown in the figure S2.1;

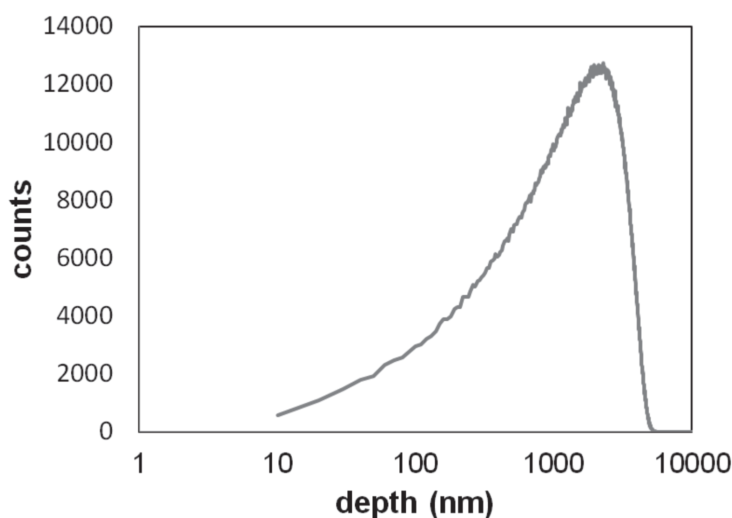

Figure S2.1 A histogram of the depth at which the primary electron energy (30 keV) decays to the cutoff value of (100 eV) in the PtC_5 solid. The histogram was constructed using five million electron trajectories. It was assumed that the electron is reabsorbed by the solid at 100 eV. A semi–infinite bulk substrate was used consisting of flat PtC_5 where the vacuum interface was located at (depth = 0 nm) and the bulk extended into the region for (depth > 0). (depth < 0) was the vacuum phase. The bin size of the histogram is 10 nm.

Thus, secondary electrons created at the end of primary trajectories contributed negligibly to the surface emitted SE distribution because of the small inelastic mean free path of the SE (λ = 2.5 nm). In addition, the total number of secondary electrons created between the incident energy and the cutoff energy for a single primary electron is;

$$\frac{(30{,}000-100)eV}{73.1\frac{eV}{SE}}=\frac{29{,}900eV}{73.1\frac{eV}{SE}}=409.0\ SE$$

while only;

$$\frac{100eV}{73.1\frac{eV}{SE}}=1.37\ SE$$

would be generated if the cutoff energy were extended to 0 eV from 100 eV. This is only 0.3% of the total number of secondary electrons generated per primary electron.

Supplement 3

The following slides may also be viewed in the file, “Supplement 3 (electron trajectory mapping.pdf”.

Supplement 3

Schematic description of the electron trajectory mapping translated from the Monte Carlo simulation to the continuum solver

Each primary electron trajectory is launched from a position that is *buried* within an *infinite solid* (figure S3.1). The solid has the properties of the material to be deposited, e.g., atomic number, atomic weight and density. Moreover, each trajectory is initiated from a common starting position (green data point indicated with white border) and with a propagation vector directed along the -z direction. An elastic scattering event is indicated by each green data point. A large population (tens-of-thousands) of individual trajectories are generated although only a single trajectory is shown here for demonstration. Later, these trajectories are randomly called during execution of the continuum simulation in order to construct the 3D electron-solid interaction profile, for each unique beam impact position. As the following slides will demonstrate, the use of the infinite solid approach in the Monte Carlo simulation makes it possible to map the 3D electron-solid interaction profile *for a 3D object of any shape*. An example object is shown in (figure S3.2) with the center of the beam impact region (BIR) indicated by the light red line. The real beam shape is best described by a Gaussian profile (red curve) where (I) is the beam current and (x) is one of three Cartesian coordinates.

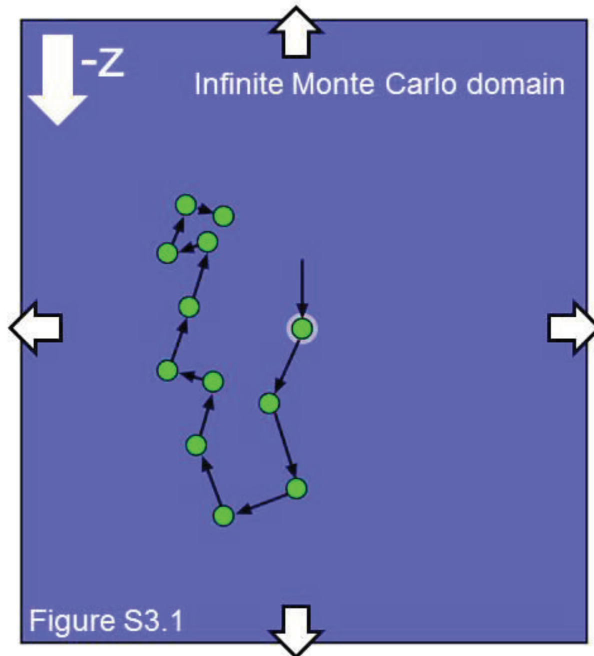

Figure S3.1

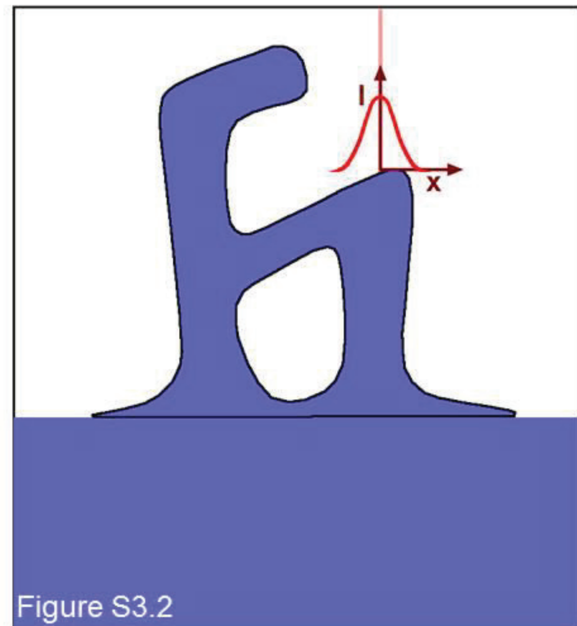

Figure S3.2

The algorithm for the construction of the 3D electron-solid interaction profile is triggered in response to a primary electron beam displacement. A primary electron trajectory is randomly selected. The trajectory is translated to the centerline of the beam impact region (large, yellow arrow, figure S3.3).

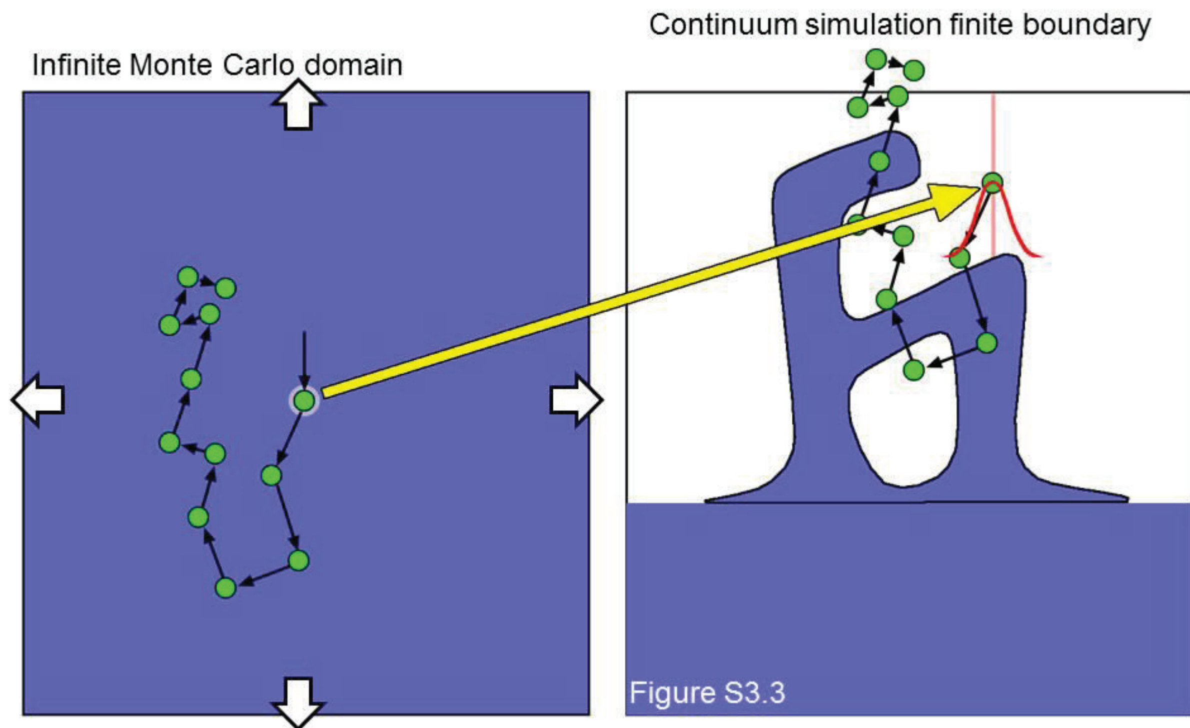

Figure S3.3

Next, random number sampling weighted to the Gaussian distribution, is used to determine a refined primary electron impact point (yellow arrows in figure S3.4). The surface position of the 3D deposit at the beam impact (x,y) region is aligned in the z-coordinate with the first elastic scattering event of the trajectory. The previous position of the trajectory, taken from the last viewgraph, is shown in transparency for reference.

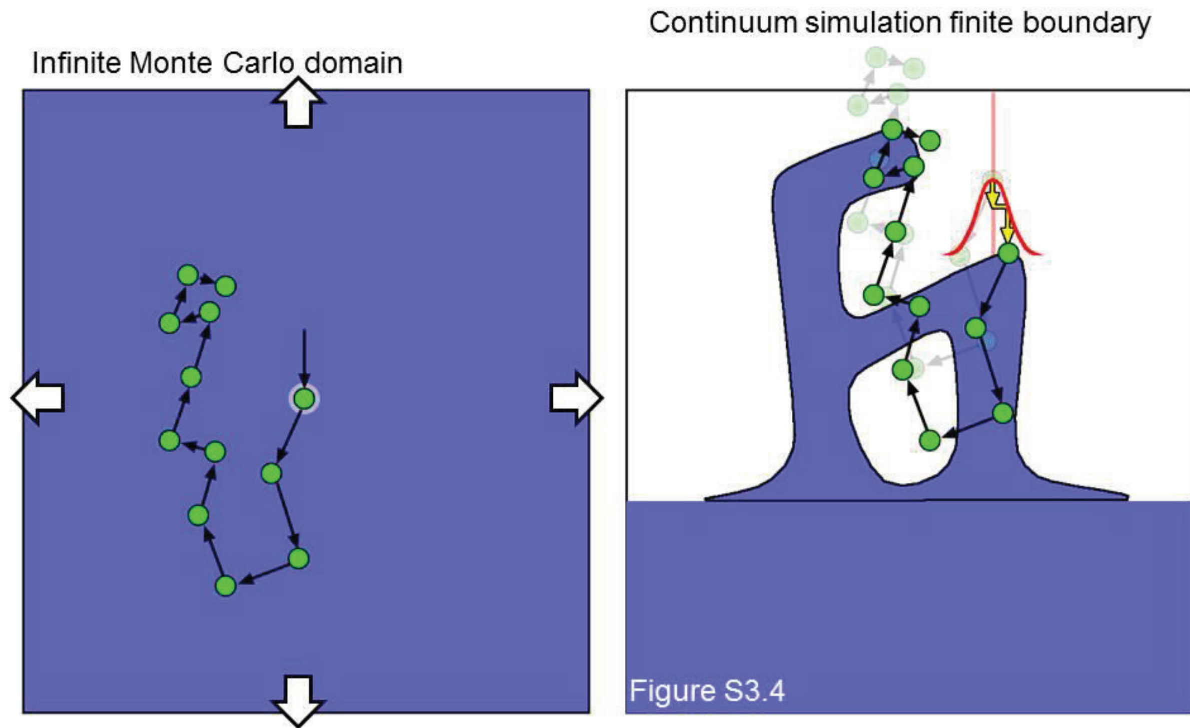

Figure S3.4

The next step is the adaption of the trajectory (figure S3.5) to the 3D deposit by (1) accounting for vacant space, e.g., translation through the vapor phase or (2) escape from the continuum simulation boundary. This process is shown on the following viewgraph figure S3.6.

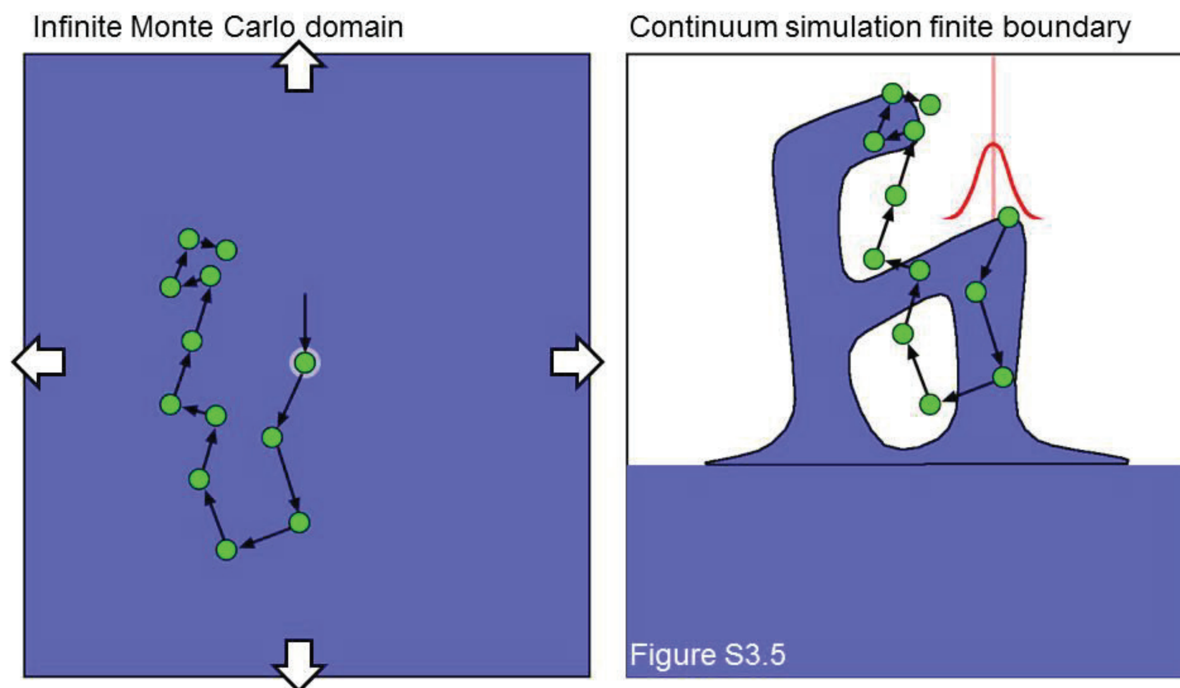

Figure S3.5

Event (#1) (figure S3.6) indicates a pure translation across a region of vapor phase space while event (#2) represents both an escape from the dense solid and intersection with the continuum simulation boundary. Intersection with the simulation boundary terminates the tracking of the trajectory. This completes adaption of the trajectory to the deposit.

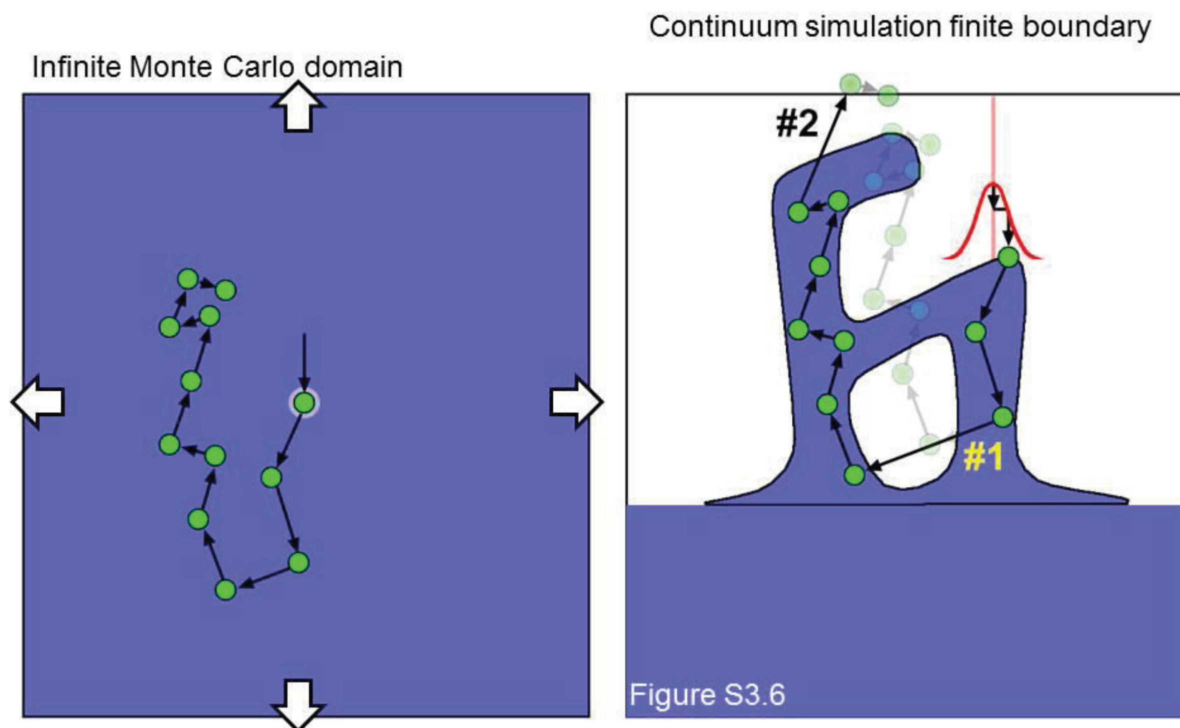

Figure S3.6

Here is shown the trajectory before (*left*) and after (figure S3.7) adaption.

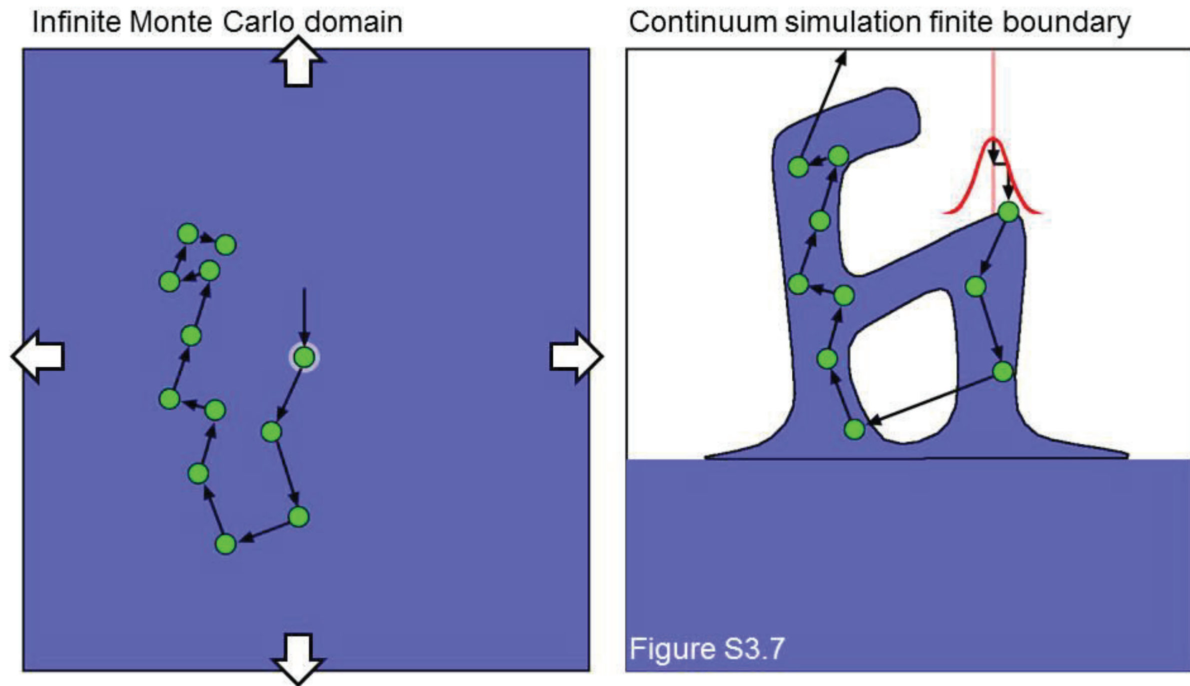

Secondary electron creation from the adapted trajectory follows as the next step. Each linear segment of the primary electron trajectory connects the (n^{th}) and ($n+1^{th}$) elastic scattering events. These segments are divided into sub-voxel size increments (figure S3.8) in order to allocate inelastic energy deposition into the solid. The continuous slowing down approximation predicts the rate of energy loss for each segment (dE/ds). Inelastic energy is distributed to each green data point according to $\Delta E = (dE/ds)\Delta s$ where (Δs) is the distance between the green data points. This inelastic energy is converted into a quantity of secondary electrons by dividing (ΔE) by the energy required to create a secondary electron (ε). The emission of secondary electrons is described on the next viewgraph, figure S3.9.

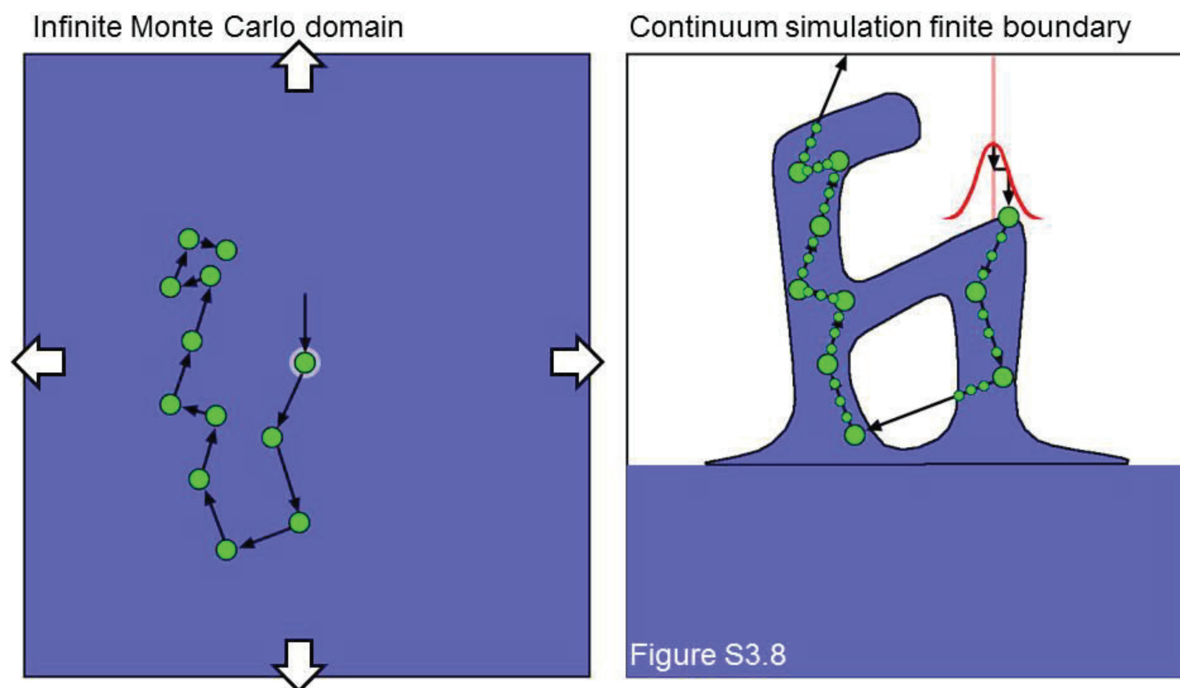

Figure S3.8

Secondary electrons (SE) are emitted in an isotropic manner from each green data point along the primary electron trajectory. The radius of emission is equal to the mean free path of the secondary electron (λ) which is an input parameter for the simulation. Random point picking from a spherical surface is used to determine the trajectory of the (SE). The hot color map below (figure S3.9) indicates qualitatively the SE emission profile for the primary electron trajectory. The highest probability of finding an SE is indicated by red shaded regions in the color map while yellow shaded regions indicate a lower probability of a finding an SE.

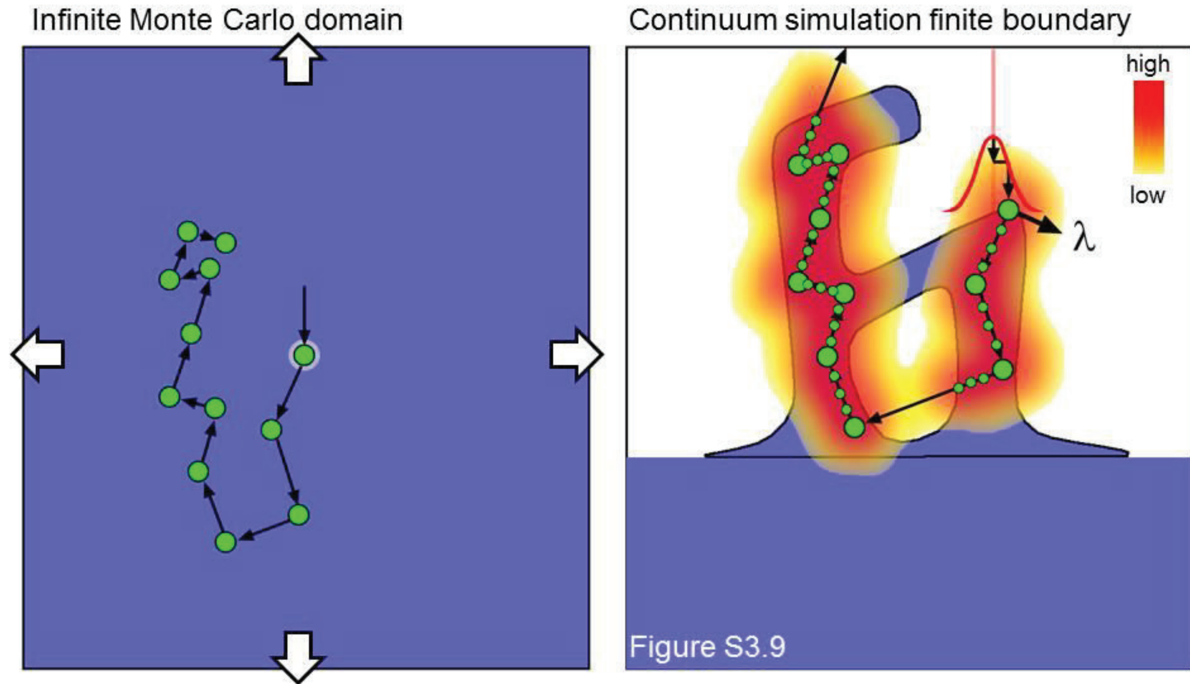

Figure S3.9

The continuum simulation domain consists of a 3D Cartesian domain of voxels. The surface voxels that surround the deposit (mesh network in figure S3.10) represent the voxels where the differential equation describing precursor surface coverage, precursor electron impact dissociation and surface diffusion will be calculated. Each SE emitted is tested to determine intersection events with the surface voxel population. In the event that an intersection is detected, the SE is associated with that surface voxel. SE accumulation is repeated for each sub–division per trajectory, and for all trajectories, leading to the construction of a 3D SE emission profile. *The SE emission profile serves as a multiplication factor in the electron dissociation term in the continuum simulation (equation 3, main text) and serves as the link between the Monte Carlo simulation and the continuum simulation.*

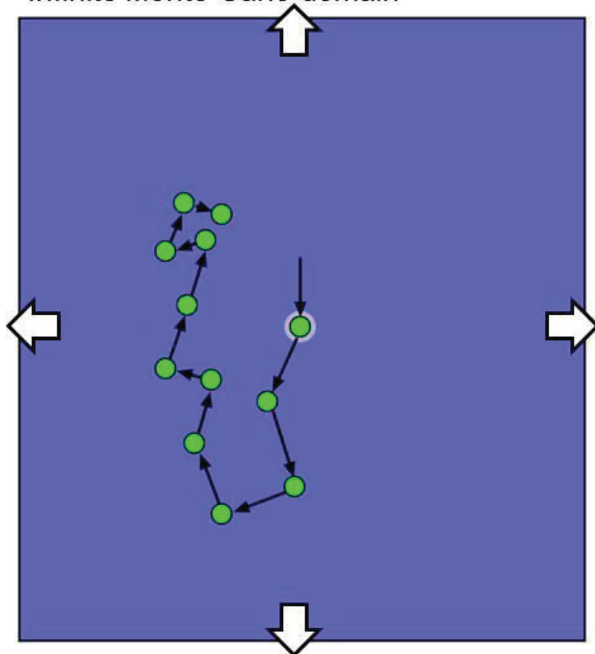

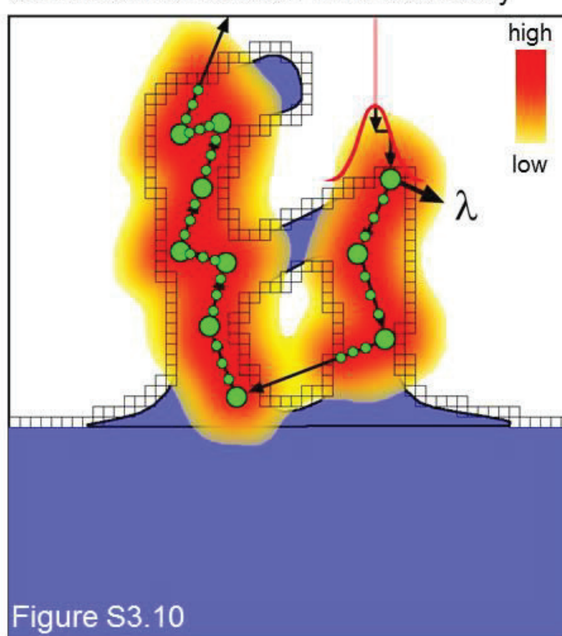

Figure S3.10

The SE surface density populating the surface voxel matrix is shown in figure S3.11 for the current beam position (light red line).

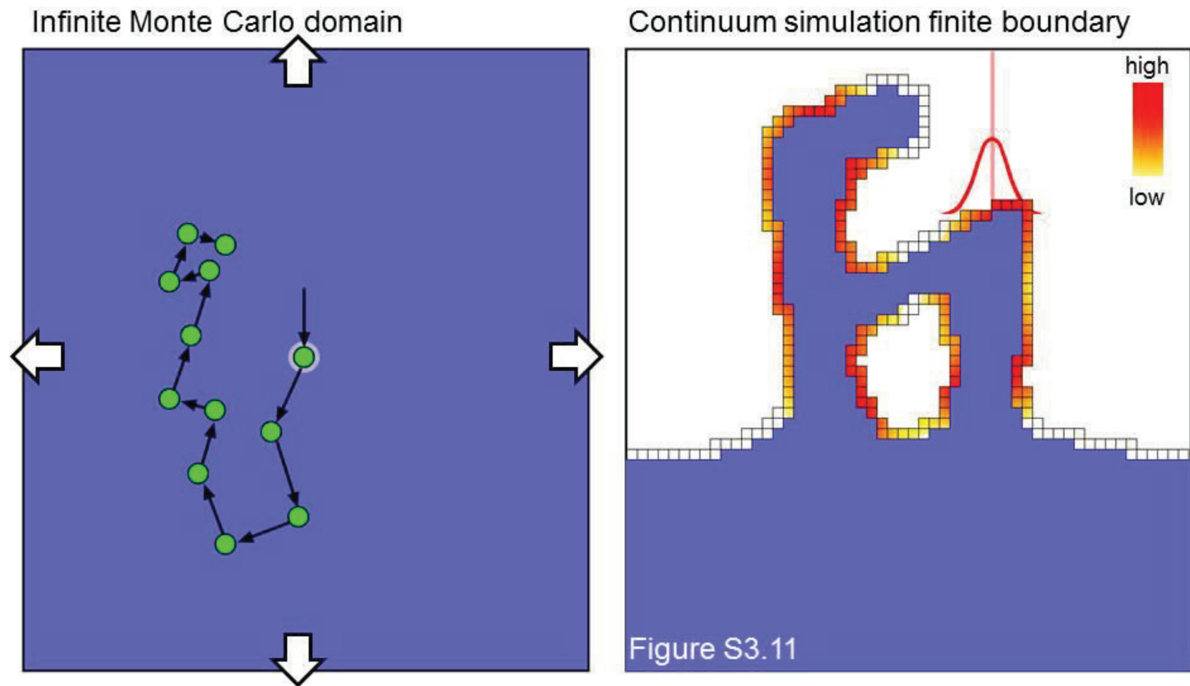

Figure S3.11

Supplement 4

The number of sampled electron trajectories per dwell (N_d) was set to be much less than the actual number derived from the beam current (i_b) and dwell time (τ_d);

$$N_d << \frac{i_b \tau_d}{q} \quad [1]$$

in order to accelerate simulation process time. This was possible because the electron spatial distribution could be approximated by a small number of electrons, for the voxel size of the 8 nm used, and the distribution simply multiplied by a scaling factor to represent the total current. The artifact of this procedure is the introduction of noise in the deposited energy profile spanning the beam interaction volume. This effect can best be seen in the spatial distribution of the primary beam impact as shown in figure S4.1(a). The radial electron spatial distribution profiles for different scaling factors are demonstrated where the yellow curve simulates, for example, 315,000 electrons and the other curves are smaller sample sizes which are 4, 40, and 40,000 times fewer electrons and normalized by the scaling factor. Clearly if the sample size is too small, the graph becomes too noisy. However, this effect is damped due to the relatively large (8 nm) voxel size used in the simulation. Figures S4.1(b–e) illustrate the effective spot size relative to a single voxel where the color map is a base 10 logarithm of the electron histogram is shown in the (x–y) plane over the beam impact region. The bin size in these examples is 0.5 nm. The voxel size (8 nm) of the simulation has been overlaid with the center of the beam impact region for comparison. Lastly, simulated FEBID results are shown in figure S4.2(a–c) using the complementary beam profiles presented in figure S4.1(b–d).

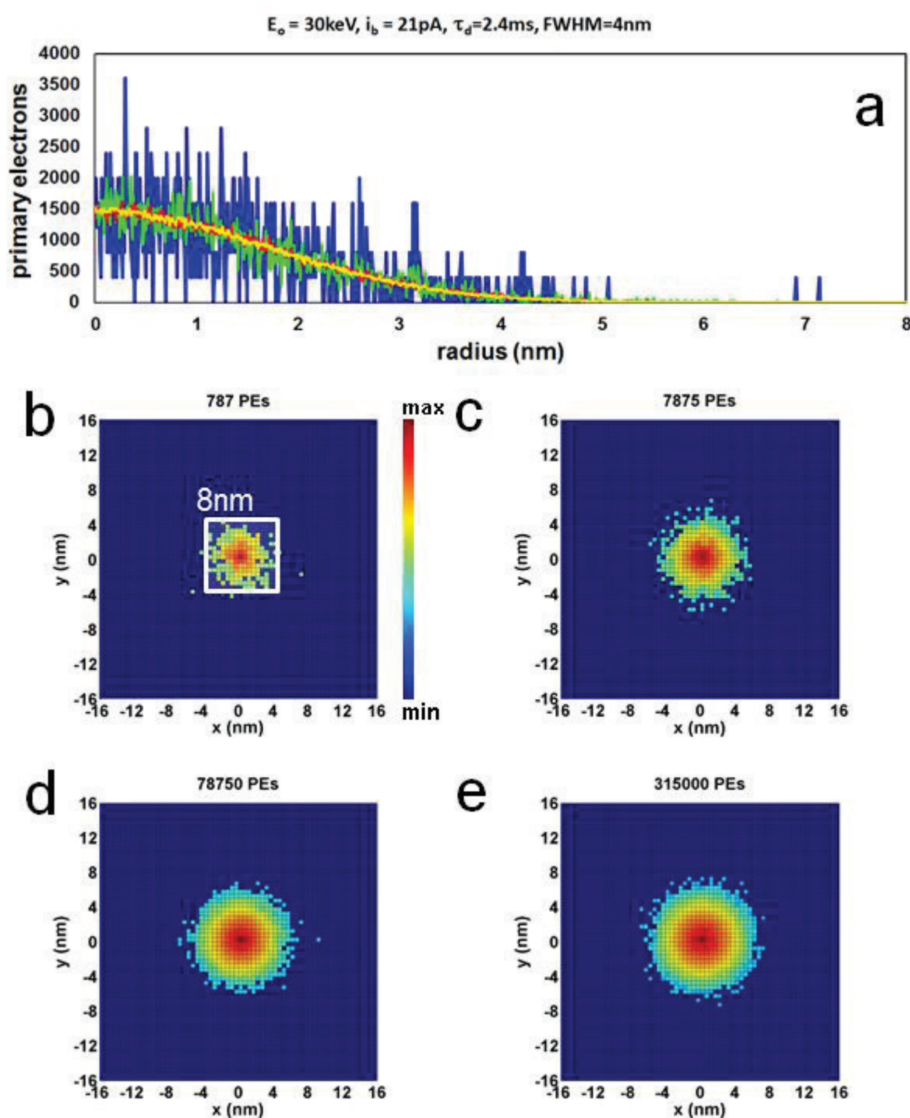

Figure S4.1 The radial Gaussian beam profile estimated for the case of a beam with a characteristic width of FWHM = 4 nm, a current of 21 pA and beam dwell time of 2.4 ms. This current and dwell time setting amounts to 315,000 incident electrons. The beam profile can be approximated by using only 0.25% (blue), 2.5% (green), 25% (red) and 100% (yellow) of the actual 315,000 electrons to construct the profile. Renormalization of each profile yields an integrated number of electrons for each profile of 315,000.

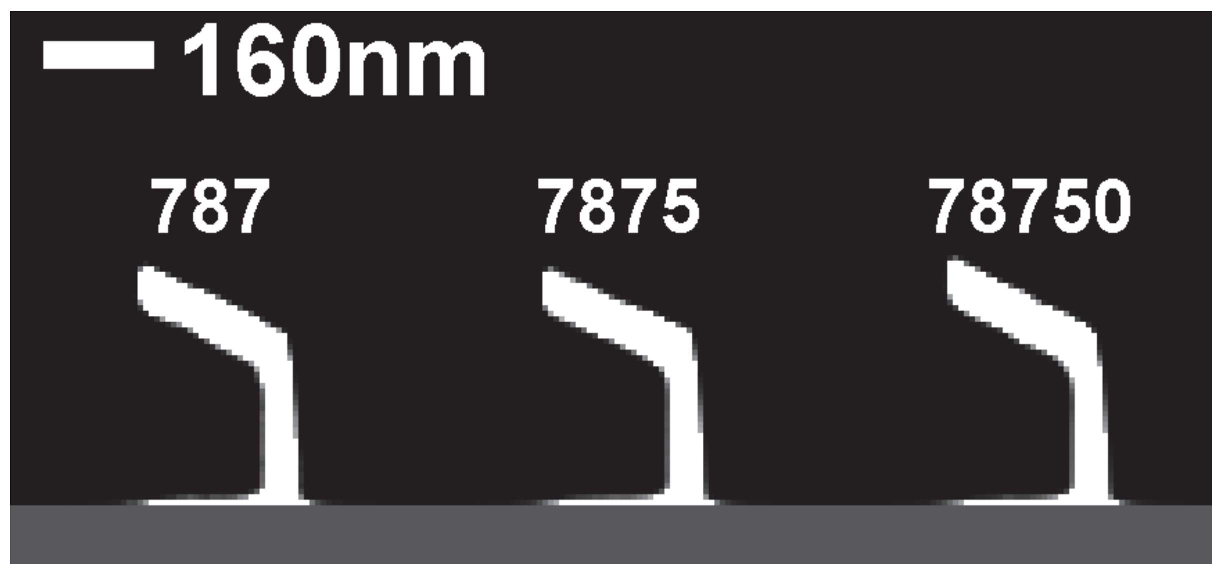

Figure S4.2 A FEBID segment constructed using a 2.4 ms dwell time per pixel. Number of electrons (superimposed) as few as 787 could be used to construct the beam profile without impacting simulation results, *e.g.*, the segment angle is roughly the same for each of the three complementary shown.

Supplement 5

There exist 9 unique surface voxel configurations, relative to the six, 1st nearest neighbor voxels, in a 3D cubic lattice[1]. Five configurations dominate the surface area for a growing segment; classes 2–6 as provided by Mullikin and Verbeek[2]. The average surface area per voxel based on unbiased random plane orientations, assuming that each surface voxel type is equally probable in the segment geometry, yields an average, empty surface area $2.2\Delta z^2$ per voxel. Surface voxels fill dynamically as deposition ensues from an empty surface area of $2.2\Delta z^2$ to zero surface area. Thus, a further estimate of the average surface area taken over the filling process is simply $2.2\Delta z^2/2$, or $1.1\Delta z^2$ which we assume is simply Δz^2.

Supplement 6

Precursor Beam Influence & Surface Normal Estimation

A projected beam of precursor molecules introduces a directed component in the precursor flux which depends on the angle of incidence of the beam with respect to the surface normal for a given surface voxel 'S'. The surface normal vector is thus estimated for each surface voxel contained inside the simulation domain as described below. Ultimately, the surface normal vector is used to calculate the number of impinging precursor molecules per surface voxel.

The calculation for the estimation of the surface normal vector uses the volume fraction of deposited solid contained within a 3x3x3 'cubic block' of voxels. The central voxel in this cubic block contains the surface voxel–of–interest (VOI) for calculation of the surface normal vector. The voxel edge length is Δz = 8 nm. Thus, each cubic block has a 24 nm total edge length. Figure S6(a) shows a vertical slice of a representative cubic block which passes through the central surface voxel. In the following summary of the calculation, the 2D slice is used for clarity of demonstration, relative to a true 3D depiction.

The surface normal is calculated in part using the volume fraction (D) of deposit contained within each surface voxel contained in the cubic block. 'D' can be expressed as;

$$D(\mathrm{x,y,z}) = \frac{V(x,y,z)}{\Delta z^3} \quad [1]$$

where V(x,y,z) is the total volume of deposit currently in the voxel, Δz^3 is the voxel volume. Thus, surface voxel occupancy has a possible range of;

$$0 \leq D(x,y,z) < 1 \quad [2]$$

Conversion of a 'D' voxel into a bulk voxel 'B' occurs when D = 1 and indicates complete filling. Any time that this condition is satisfied during the simulation, a sub–routine is triggered which updates the 'S', 'B' and 'V' status of the neighbor voxels. Voxels residing in the vapor phase are indicated by 'V'.

Deposition accumulates in surface voxels

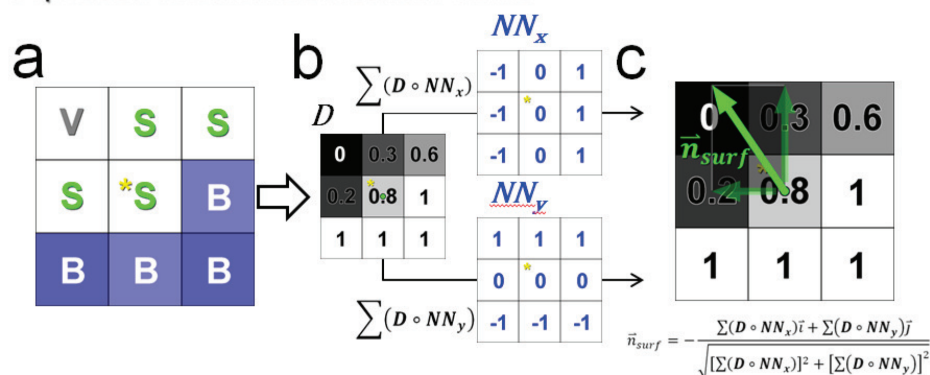

Specular precursor flux depends on the local surface normal

d

$$\Phi_T = \Phi_b + \Phi_{beam} \frac{\vec{n}_{surf} \cdot (-\vec{n}_{gas})}{|\vec{n}_{surf}||\vec{n}_{gas}|}$$

Figure S6 (a) A slice through a cubic block (3x3x3) of voxels. 'V' indicates a vapor phase voxel, 'S' a surface voxel and 'B' a bulk voxel. The surface normal calculation, for the element of surface contained in the voxel labeled 'S*', requires the volume fraction of deposit 'D' contained within each 'S' voxel in the (3x3x3) cubic block. (*In this figure, a 2D representation of a 3D calculation is shown for clarity*) (b) A slice though the cubic block in (a) showing complementary example values for 'D'. Elementwise multiplication of the cubic block 'D' with the nearest–neighbor block in each of the three Cartesian coordinates makes it possible to estimate the surface normal vector according the equation shown in (c). (d) Ultimately, the precursor molecular flux (Φ) arriving at the voxel 'S*' is the superposition of a diffuse component (Φ_b), which is independent of the surface normal vector, and a directed component (Φ_{beam}) which requires the estimated surface normal vector ($\mathbf{n}_{surf}$).

The summation of the elementwise multiplication of 'D' with a nearest neighbor array, *i.e.*, NN_x, NN_y and NN_z shown in figure S6(b), for each Cartesian dimension yields an estimate of the surface normal (figure S6(b)) at the VOI. The unit surface normal is recovered according to the equation provided in figure S6(c) which is shown as the green vector – the z and x components are also shown in partial transparency.

The total precursor pressure per voxel is divided into both a directed component (P_{beam}) based on the gas flux vector, and a diffuse (referred to a background P_b) component;

$$P_T(x,y,z) = P_b + Shad(x,y,z) \cdot P_{beam} \cdot cos(\beta(x,y,z)) \quad [3]$$

Shad(x,y,z) is a logic variable (0/1) that accounts for any shadowing that occurs from the FEBID deposit which can obstruct the line-of-sight of the precursor to the VOI. cos(β) takes into account the local orientation of the surface normal with respect to the gas impingement vector. The simulation requires input of P_T and, P_b and/or P_{beam}. Importantly, P_{beam} is the maximum of

the directed component of pressure. The purely diffuse partial pressure (P_b) is a constant at all surface voxels in the simulation domain. The diffuse precursor flux is derived from the local pressure (P) according to;

$$\Phi = \frac{P}{\sqrt{MW \cdot T}} \quad [4]$$

where MW is the molecular weight of the precursor and T the precursor temperature. The total precursor flux impinging on the VOI is then;

$$\Phi_T(x,y,z) = \Phi_b + Shad(x,y,z) \cdot \Phi_{beam} \cdot cos(\beta(x,y,z)) \quad [5]$$

The directed component is treated as a function of the dot product between the surface normal ($\mathbf{n}_{\mathbf{surf}}$) at 'S*' and the (negative) of the gas propagation vector ($\mathbf{n}_{\mathbf{gas}}$). An arbitrary surface is generated in order to demonstrate how the directed component of the precursor flux is treated. The diffuse component was set to equal zero in case shown in figure 2(e) example. The colormap represents the surface height while the brightness of each pixel indicates the number of molecules impinging at the surface. The equation provided as figure S6(d) is valid from β = 0–90° where β is the angle between $\mathbf{n}_{\mathbf{surf}}$ and $-\mathbf{n}_{\mathbf{gas}}$;

$$-(\vec{n}_{gas}) \cdot \vec{n}_{surf} = |\vec{n}_{gas}||\vec{n}_{surf}| \cos(\beta) \quad [6]$$

The directed component of pressure is 0 for β > 90 which we refer to as 'local' shadowing where the geometric cross–section for precursor impingement at that surface element is 0. A projection, ray casting scheme is implemented to determine 'remote shadowing' where precursor impingement is 0 due to a remote obstacle casting a shadow at the surface VOI.

Supplement 7

The remaining calibration factor (χ) required scaling FEBID by 2.1 to achieve convergence between experiment and simulation. Even more recently, the pre–exponential variable and activation energy describing $MeCpPt^{IV}Me_3$ physisorption have been determined and yield τ~5 ms for our RT growth conditions[3]. Precursor surface coverage increases with increasing (τ) leading to more dissociation according to the term $\sigma \cdot C \cdot i_{SE}$ in equation 3 main text. It was shown that a lower value of the scaling factor (χ) could be used (χ=1.5) in order to reproduce the experimental derived segment angle curve provided in figure 4(b) main text with very little change in segment object morphology, a further step towards convergence.

Supplement 8

In our previous paper we reported a diffusion coefficient of 0.65 $\mu m^2/s$ for $MeCpPt^{IV}Me_3$ diffusion on a PtC_x surface[4]. Recently, a more refined value of 0.4 $\mu m^2/s$ has been published[5]. The updated value was used here. Also in [6], we used a total precursor pressure of 15 mTorr. In reality, this is a somewhat floating parameter due to the fact that (1) the sticking probability of $MeCpPt^{IV}Me_3$ on PtC_x is unknown (we assume δ=1 here) and (2) the multiplication of the precursor pressure with the sticking probability ($\delta * P_T$) dictates in the precursor surface accumulation term in the rate models making is difficult to isolate either value. Lastly, the surface density of the deposit has been updated from 9.6 PtC_5 molecules/nm^2 to 4.8 PtC_5 molecules/nm^2 which is more accurate estimate of deposit surface density based on the deposit density of 4.5 g/cm^3.

Supplement 9

PtC_5 thin film prisms (width=500 nm) were simulated as a function of the specular to diffuse pressure ratio. The purpose of the simulation set was to determine the ratio that simultaneously reproduced (1) the maximum height of the prism and (2) the ratio of minimum ledge height to the maximum ledge height derived from experiments.

The lateral extent of the beam exposure in the (x–y) plane was 500 nm x 500 nm for simulations while it was 2000 nm x 2000 nm for real experiments. The total $MeCpPt^{IV}Me_3$ pressure was fixed at 30 mTorr while the specular/diffuse (*in units of mTorr/mTorr*) components varied over the range 30/0, 25/5, 20/10, 15/15, 10/20 5/25. The beam acceleration voltage was 5 keV, the primary beam current was 400 pA and the beam size was FWHM=27 nm. The spiral–out beam scanning strategy, shown in figure 2(a), main text, was used where the pattern rotation angle (α) was 15°.

Simulation results are presented as height histograms in figure S9(a) along with the experimental results (black histogram). The collection of histograms have been shifted along the y–axis for both clarity and comparison purposes. The experimental value for ratio representing the minimum ledge height to maximum ledge height was 0.68 for the experiment and is superimposed on the histogram. Also, the experimental histogram has been extended down the figure as a shaded flow in order to compare the results with simulations. The actual AFM tapping mode height image is shown in figure S9(b) with the ledge of minimum height '3' and the ledge of maximum height labelled '1'.

The simulation at 20 mTorr specular pressure and 10 mTorr diffuse pressure (blue curve) best represented the experimental result (while also later describing results at 30 keV for the 3D segment based objects) in terms of the ledge surface morphology, ledge height ratio (=0.65) and only slightly under represented the maximum height by 5 nm. Complementary, simulated morphologies are shown in figure S9(c) where the color border around the images matches the histogram in figure S9(a). At higher diffuse pressures, the maximum height better reflected experiments but at the expense of the ledge morphology which became more uniform across the prism (*see red and orange histogram complementary images in figure S9(c)*).

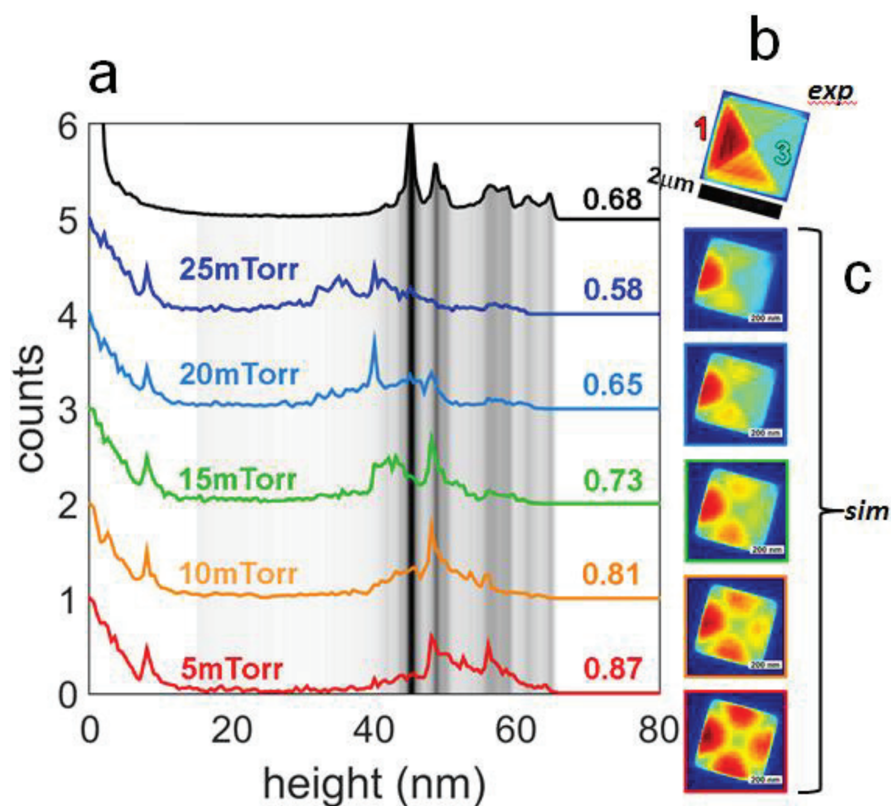

Figure S9 (a) Height histograms for thin film prisms prepared by FEBID using the spiral–out scanning strategy. Each individual histogram has been shifted in the counts coordinate to avoid overlap and provide visual clarity. The black histogram was derived from atomic force microscopy data (b). The value of 0.68 associated with the black histogram is the height ratio calculated by (b) dividing the mean height of the lowest ledge (3) on the thin film prism surface by the mean height of the highest ledge (1). The remaining simulations are complementary simulations of the experiment where the ratio of diffuse–to–directed pressure was varied, at constant total pressure, in order to the replicate the experimental ledge height ratio. The directed pressure of 20 mTorr and background pressure of 10 mTorr best reproduced the results.

Supplement 10

The ability to collect the sample current signal from the focused electron beam induced deposition (FEBID) simulation was tested in response to a reviewer request. The test consisted of simulating FEBID for a published morphology, a so–called “tip on suspended rod” structure, which included a sample current trace acquired during the growth of the structure (figure S10(a)). The published information can be found in,[7] “Electron range effects in focused electron beam induced deposition of 3D nanostructures”, *Microelectronic Engineering* **83**, 1482-1486 (2006) on page 1485 in figure 4. The “tip on suspended rod” was grown in *experiments* using an acceleration voltage of 25 keV, a beam current of 500 pA and a beam width of $4\sigma \sim 132$nm using the precursor hexafluoro-acetylacetonato-copper(I)-vinyltrimethylsilane. In the EBID *simulation (figure S10(b))*, an acceleration voltage of 30 keV, a beam current of 21 pA and a beam width of FWHM = 5nm using the precursor MeCp(Pt^{IV})CpMe$_3$. The precursor MeCp(Pt^{IV})CpMe$_3$ was used in place of (hfac)CuVTMS because fewer parameters are currently available for the hfac(Cu)VTMS precursor. Moreover, a smaller version of the “tip on suspended rod” morphology was simulated in order in reduce the total simulation process time.

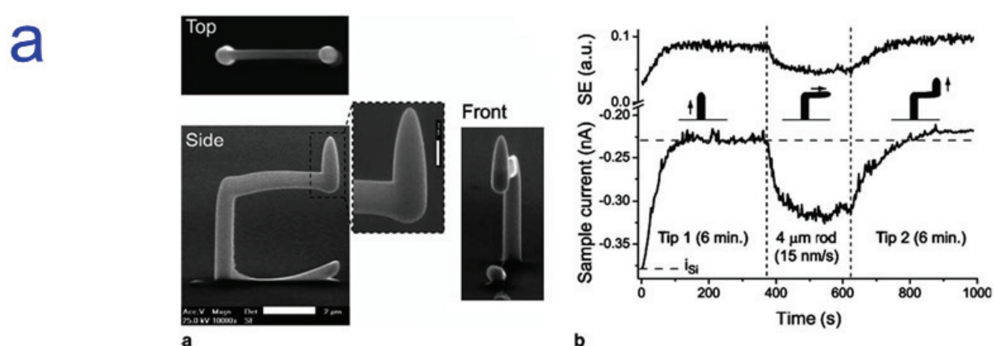

Reproduced with permission from, Bret, T.; I. Utke; Hoffmann, P.; Abourida, M.; Doppelt, P.; “Electron range effects in focused electron beam induced deposition of 3D nanostructures”, *Microelectronic Engineering* **2006**, 83, 1482-1486. This image appeared as figure 4.

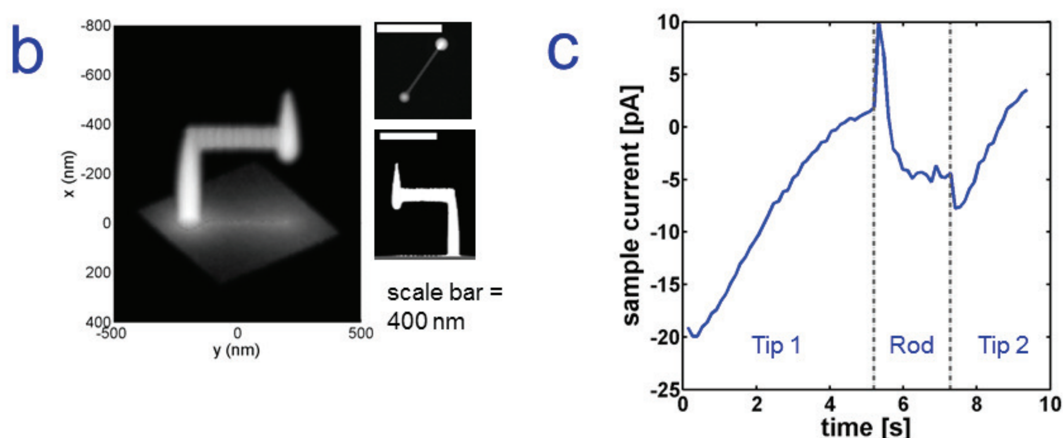

Figure S10 (a) The “tip on suspended rod” structure grown using an acceleration voltage of 25 keV, a primary electron beam current of 500 pA and the precursor hexafluoro-acetylacetonato-

copper(I)-vinyltrimethylsilane[7]. (b) A 3D FEBID simulation of the “tip on suspended rod” structure using an acceleration voltage of 30 keV, a primary electron beam current of 21 pA and the precursor $MeCp(Pt^{IV})CpMe_3$. (c) The stage sample current acquired during the 3D FEBID simulation. Compare with the stage current collected experimentally in (b).

The acceleration voltage, in part, determines the sample current signal because the penetration depth of the primary electrons is very large (tens of micrometers at 25-30 keV) relative to the tip and rod dimensions (see S2). In addition, although the deposits consist of different metals, (1) carbon contamination contributes significantly to the composition (~55 at%C for the Cu experiment and ~83 at%C for the Pt simulation) making the relative material parameters such as atomic number, molecular weight and density, which dictate beam penetration, comparable.

The secondary electrons that are liberated from the deposit when the primary beam intersects the surface contribute significantly to the sample current signal, along with primary electrons that penetrate and dissolve in the solid. Primary electrons can also be scattered at very high angles away from the deposit due to large angle elastic scattering although this is relatively low probability event relative to the other current affecting factors.

The stage current signal can be collected periodically during FEBID and provides a reliable method to track changes in the deposit morphology, indirectly, without the use of secondary electron imaging. The current signal is described by;

$$i_s = i_b - \delta_I i_b - \eta i_b - \delta_{II} \eta i_b \quad [1]$$

where (i_s) is the sample current, (i_b) is the incident primary beam current, (δ_I) is the secondary electron number 1 yield, (δ_{II}) is the secondary electron number 2 yield and (η) is the backscattered electron yield. The total secondary electron yield (δ_T) is given by;

$$\delta_T = \delta_I + \delta_{II} \eta \quad [2]$$

The continuum simulation domain boundary is typically 1-2μm in edge length along the x, y and z dimensions. This has the effect of discounting the terms (ηi_b) and ($\delta_{II} \eta i_b$) because the backscattered electrons fall outside the simulation region. However, due to the deep beam penetration at 25 and 30 keV, described above, these terms contribute relatively little compared with (i_b) and (δ_I). Thus, the sample current derived from the simulation (figure S10(c)) resembled closely the experimental curve. Specifically, the sample current shape during the growth of the (1) tip, (2) rod and (3) tip geometries was the same for both experiments and simulations. The only noticeable differences are the spikes observed in the simulated sample current at the tip/rod and rod/tip boundaries. This observed difference is attributed to the difference in the beam pixel point pitch (Λ) to beam diameter (FWHM) ratio between experiments (Λ/FWHM = 0.48nm/55nm = 0.009) and simulation ($\Lambda/2r_b$ = 1nm/4nm = 0.25). For example, when the beam displacement begins after the growth of the first tip the beam makes a relatively large displacement relative to the tip diameter striking the highly tapered apex causing a large ejection of secondary electrons to the large surface area exposed to the beam.

EBID Simulation growth conditions

An acceleration voltage of 30keV and a beam current of 21pA used to simulate the FEBID of the "tip on suspended rod". The beam radius was 4nm, the beam dwell time per pixel was 5.2ms and the pixel point pitch during the rod growth was 1nm. A total of 1000 stationary beam dwells were used to grow the first tip. Next, the rod was deposited with 400 beam dwells at a beam speed of (v = 192 nm/s). The final tip was deposited also using 400 beam dwells. The total pressure was 30mTorr $MeCp(Pt^{IV})CpMe_3$.

Supplement 11

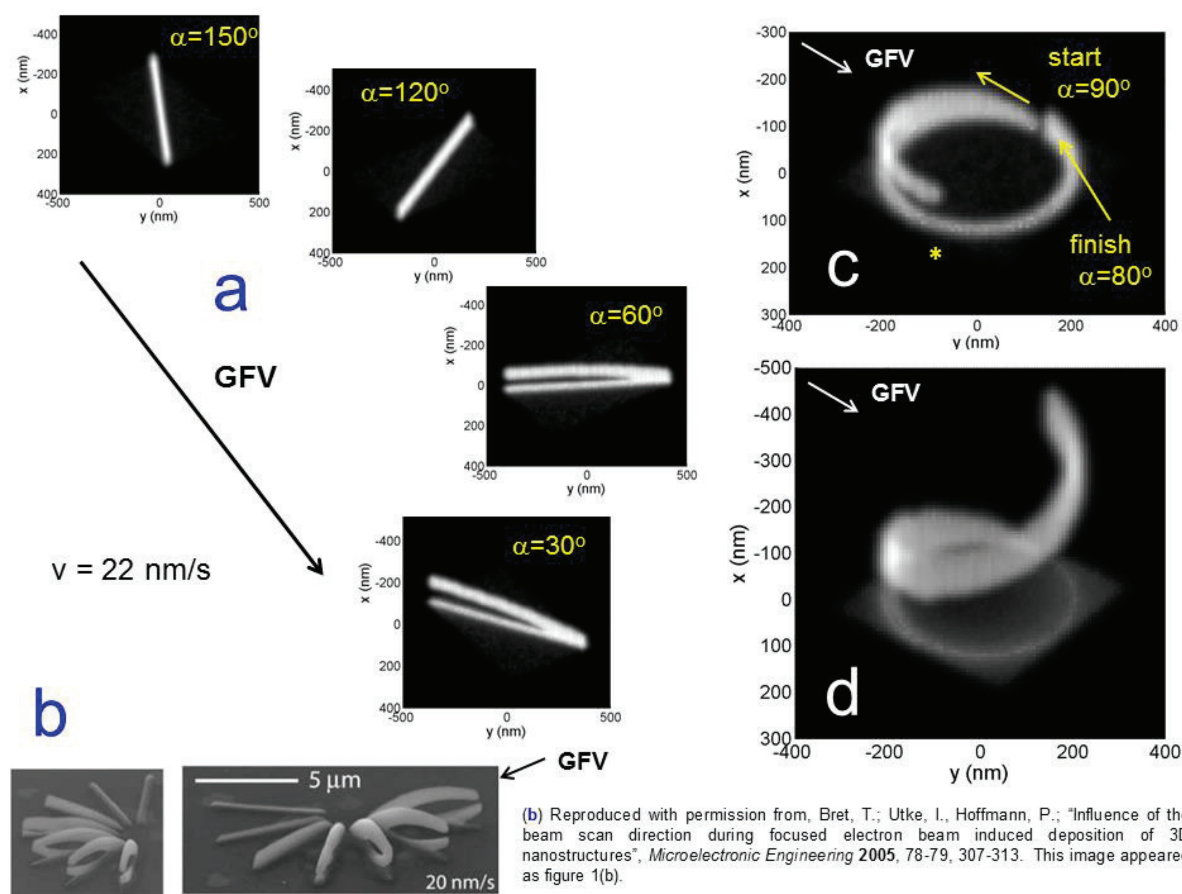

Figure 11 (a) Virtual SEM images (tilt = 52°) of four different 3D FEBID MeCp(Pt^{IV})$CpMe_3$ simulations with a variable electron beam scanning directions. Each scan was an 800 nm line scan with a pixel point pitch of 0.53 nm and a constant electron beam velocity of 22 nm/s. (b) (hfac)CuVTMS experiments reported in[8]. The direction of the gas flux vector (GFV) during the experiments is superimposed for reference. (c) A virtual SEM image (tilt = 38°) of a circular beam scanning pattern. The radius of the pattern was 200 nm. The precursor flux was 66% directed and 33% diffuse during the simulation for a total pressure of 1.3 mTorr MeCp(Pt^{IV})$CpMe_3$. (d) The results of a complementary simulation to (c) where the directed component of the precursor flux is 0% and the diffuse component is 100%, again for a total pressure of 1.3 mTorr.

In the article[8], Bret *et al.*, "Influence of the beam scan direction during focused electron beam induced deposition of 3D nanostructures", *Microelectronic Engineering* 78-79, 307-313 (2005), the direction of gas nozzle was shown to strongly influence the vertical growth rate depending on the scanning during FEBID, more so than was observed during the simulations and experiments reported in this article. However, the strong GFV dependence was observed in

simulations when the beam speed, electron dose and precursor surface coverage were adjusted to match the experiments reported[8].

The simulations reported here have implemented a primary beam current of 21 pA and a beam size of FWHM = 4nm. Conversely, a beam current of 500 pA and a beam diameter of 55 nm was used in[8]. A smaller total segment size was simulated in order in reduce the total simulation process time. Therefore, the simulated current density is;

$$e_d^-|_{sim} = \frac{i_b}{\pi \cdot HWHM^2} = \frac{21[pA]}{\pi(2[nm])^2} = 1.7 \left[\frac{pA}{nm^2}\right]$$

A representative experimental current density reported in[8] was;

$$e_d^-|_{exp} = \frac{i_b}{\pi \cdot HWHM^2} = \frac{500[pA]}{\pi(27[nm])^2} = 0.2 \left[\frac{pA}{nm^2}\right]$$

In order to have an equivalent current density between experiments and simulations, a new simulation beam size was calculated using the reported electron current density 0.2 pA/nm^2 yet keeping constant the primary beam current at 21 pA;

$$HWHM = \sqrt{\frac{i_b}{\pi e_d^-|_{exp}}} = 5.5\ [nm]$$

The beam dwell time per pixel used in the experiments (τ_d = 24ms) was also used in the simulation to achieve a common primary electron dose;

$$\frac{i_b \tau_d}{\pi \cdot HWHM^2} = \frac{21[pA] \cdot 24x10^{-3}[s]}{\pi(5.5[nm])^2} = 5.3x10^{-3} \left[\frac{pC}{nm^2}\right]$$

In order to further close the gap between the experiments and simulations, the equilibrium coverage of (hfac)CuVTMS reported in[8], of ~10^{-1} (hfac)CuVTMS molecules/nm^2, was adapted to the simulation by forcing the equilibrium precursor coverage of $Me(Pt^{IV})CpMe_3$ to this value by changing the total pressure which is an input parameter to the simulation (*a direct comparison between the two cases was not possible as the total electron impact dissociation cross section for hexafluoro-acetylacetonato-copper(I)-vinyltrimethylsilane is unknown*). Based on the reported value of 0.1 molecules/nm^2, the precursor site density of 2.8 $Me(Pt^{IV})CpMe_3$ sites/nm^2 yields a fractional surface coverage (θ) of ~0.03, or 3% coverage. However, initial simulations revealed that the segment geometry does not lift-off of the substrate surface vertically as observed in experiments (*discussed below*). In order to achieve substrate lift-off, the total pressure was raised from ~0.4 mTorr to P_T = 1.3 mTorr (*where the directed component (P_{beam}) of 0.875 mTorr and a background pressure (P_b) of 0.417 mTorr*) yielding 10% surface coverage of $Me(Pt^{IV})CpMe_3$. Complementary experimental and simulated results were achieved under these conditions.

3D EBID simulation growth conditions

An acceleration voltage of 30keV and a beam current of 21pA used to simulate the FEBID of the low angle segment features. The beam radius was 5.5nm, the beam dwell time per pixel was 24ms and the pixel point pitch during the rod growth was 0.53nm. The total length of the segments grown was 800nm. The beam velocity was v = 0.53 nm / 0.024 s = 22 nm/s.

Figure S11(a) shows the results of four FEBID simulations where the beam scanning direction was changed relative to the gas flux vector (GFV). The superimposed angle-based values provided in figure S11(a) represent the orientation of the beam scanning direction with respect to the GFV. For example, a value of 180° indicates the beam is scanning away from the GFV, parallel to the projection of the GFV in the substrate plane. Conversely, a value of 0° indicates anti-parallel scanning where the beam is moving toward the GFV. This is the most favorable condition for vertical growth. This angle is referred to as the rotation angle (α) in the main text.

Similarities between experiments and simulations

Several similarities were found between the published (hfac)CuVTMS experiments and the $Me(Pt^{IV})CpMe_3$ simulations. The comparison is made for a common beam speed; (v = 22nm/s simulations, figure S11(a)) and (v = 20 nm/s experiments, figure S11(b)). A strong dependence of the vertical growth rate on the GFV orientation was observed in both cases: nanowires are grown only on the surface in the range of $\alpha = 90^o$-180° while self-suspended segments are grown for $\alpha = 0^o$-90°. The GFV vector in figure S11(b) indicates $\alpha = 0^o$, or the direction of anti-parallel scanning for the experiments. In the case of segment growth, an underlying nanowire is produced underneath the segment for both cases. EBID simulations also revealed that the nanowire height increased with a decrease in (α) as seen clearly in the experiments (figure S11(b) In figure S11(a) the nanowire labelled ($\alpha = 150^o$) was 55 nm thick while the nanowire at ($\alpha = 120^o$) was 70 nm thick.

Ultimately, the reduction in surface coverage from 74% to 10% was required to reproduce the GFV-beam scanning dependence for a comparable current and linear dose rates between experiments and simulations. Nonetheless, because not all parameters are known for the (hfac)CuVTMS precursor the presented simulation results are circumstantial.

Differences between experiments and simulations

Experiments performed by Bret *et al*.[8] revealed an underlying, secondary nanowire forms during FEBID and can lift-off of the substrate surface while the initial, suspended segment is still growing above (20nm/s panel in figure S11(b)). This was not observed in simulations. In simulations it was found that the height of the underlying nanowire was relatively smaller and would only lift-off the substrate in cases where the beam velocity exceeded the lateral growth velocity of the segment causing the beam to fall off the segment starting the growth of a new nanowire. The observed difference in the underlying nanowire growth could be due to the fact that kinetic growth conditions are not quite equivalent between the new cases. This discrepancy will be investigated further in the future.

A circular scanning pattern makes it possible to investigate the GFV influence dynamically because the patterning orientation is continuously changing in a controlled and predictable fashion. Figure S11(c) shows a virtual SEM image of a 3D FEBID simulation where a circular scanning pattern was used. Beam scanning initiated at (α = 0°) indicated as the "starting" position in the virtual SEM image. This is the preferred orientation for lift-off. Vertical growth continues but continuously decreases as the beam turns continuously away from the gas nozzle. Eventually the beam velocity exceeds the lateral segment growth rate and the beam falls off of the segment. FEBID begins anew on the substrate surface and a new nanowire begins to thicken. FEBID was executed for $\Delta\alpha$ = 350°.

An additional simulation was executed to determine the influence of the directed nature of the GFV. The simulation shown in figure S11(c) was repeated using the same total pressure of precursor (P_T = 1.3mTorr) but with a zero directed component of precursor (totally diffuse gas flux). Every voxel in the domain experienced the same molecular flux regardless of the orientation of the deposit surface. A complete, single turn helix can be deposited under these modified conditions figure S11(d) and provides a direct measure of the influence of the GFV, in this case its absence.

Supplement 12

S12_BeamDwellPattern.wmv

Supplement 13

In this example, the surface voxels ‘S’ are rendered with a colormap that is linked to the x-direction. All other settings are the same as described in **SI1**.

S13_Frame3DFEBID.wmv

Supplement 14

Virtual SEM images are generated by projecting the 3D object on a virtual, flat rectangular screen. The screen position is characterized by an azimuthal, rotation and distance coordinate. The collection of information of the 'screen' empirically mimics real secondary electron collection at a very high positive collection bias such that all secondary electrons are captured. For example, in a real detector a certain fraction of SEs emitted, from the surface, with an unfavorable trajectory for collection may be reoriented at relatively high bias and collected, even if they are emitted from region lying in the shadow of the detector. The virtual screen had a pixel size equal to that of the simulation domain =8 nm. The 'intensity' contributed by a surface voxel to the screen was set equal to the fraction of deposit residing there. The position on the screen of the 'counts' was determined by projecting a vector from the deposit, to the screen, with an orientation parallel to the surface normal of the screen which is directed at typically the center–of–mass of the deposit. Even surface sites lying in the shadow of the detector, cast by the detector, were considered as collected mimicking the high bias condition mentioned above. The 'signal' was integrated without a possibility of saturation in counts and stored in the array SE_{img}. Image processing led to the final image intensity described by;

$$SE_{img}(x_s, y_s) = \sqrt[3]{\int_t D_{img} \nabla^2 SE_{img}(x_s, y_s) dt + \frac{SE_{img}(x_s, y_s)}{N_c}}$$

which, again, is a purely empirical expression. Coordinates in the reference frame of the screen are x_s and y_s where $x_s(x,y,z)$ and $y_s(x,y,z)$. Qualitatively, the expression can be understood as follows. The 1st term describes an image diffusion operation executed in the image plane to smoothen out frequencies imposed on the image by the voxel nature of the deposit. The 2nd term averages the raw signal based on the number of counts which makes it possible to dampen the image contrast. Lastly, the 3rd root makes it possible to image both the 3D object as well as the faint amount of substrate deposition due to the beam proximity effect.

S14_Frame3DFEBID_vSEM.wmv

Supplement 15

The cube edge length for these FEBID cube structures was 200 nm while the images shown in Figures 5 a-b, in the main text, were grown with an cube edge length of 250 nm.

S15_Cube3DFEBID.wmv

S15_Cube3DFEBID_vSEM.wmv

Supplement 16

Experiment / machine	Precursor	GIS angle to substrate	Vertical GIS distance to substrate	Lateral GIS position to beam center (X/Y)
Pads/Nova 200	$MeCpPt^{IV}Me_3$	52°	180±20 µm	200±10 µm / 40±10 µm
3D / Nova 600	$MeCpPt^{IV}Me_3$	52°	100±20 µm	0±10 µm / 150±10 µm
3D / Nova 200	$MeCpPt^{IV}Me_3$	38°	470±20 µm	30±10 µm / 170±10 µm
3D / Nova 200	$Me_2Au(acac)$	52°	380 ±20 µm	40±10 µm / 130±10 µm
3D/ Nova 600	$W(CO)_6$	38°	100±20 µm	0±10 µm / 150±10 µm

References (Supplement)

1. Windreich, G.; Kiryati, N.; Lohmann, G. Voxel-based Surface Area Estimation: from Theory to Practice. *Pattern Recogn.* **2003**, 36, 2531-2541.

2. Mullikin, J. C.; Verbeek, P. W. Surface Area Estimation of Digitized Plane. *Bioimaging* **1993**, 1, 6-16.

3. Cullen, J.; Bahm, A.; Lobo, C. J.; Ford, M. J.; Toth, M. Localized Probing of Gas Molecule Adsorption Energies and Desorption Attempt Frequencies. *J. Phys. Chem. C* **2015**, 119, 15948-15953.

4. Winkler, R.; Fowlkes, J.; Szkudlarek, A.; Utke, I.; Rack, P. D.; Plank, H. The Nanoscale Implications of a Molecular Gas Beam during Electron Beam Induced Deposition. *ACS Appl. Mater. Interfaces* **2014**, 6, 2987-2995.

5. Cullen, J.; Lobo, C. J.; Ford, M. J.; Toth, M. Electron-Beam-Induced Deposition as a Technique for Analysis of Precursor Molecule Diffusion Barriers and Prefactors. *ACS Appl. Mater. Interfaces* **2015**, 7, 21408-21415.

6. Winkler, R.; Geier, B.; Plank, H. Spatial chemistry evolution during focused electron beam-induced deposition: origins and workarounds. *Appl. Phys. A: Mater. Sci. Process.* **2014**, 117, 1675-1688.

7. Bret, T.; Utke, I.; Hoffmann, P.; Abourida, M.; Doppelt, P. Electron Range Effects in Focused Electron Beam Induced Deposition of 3D Nanostructures. *Microelectron. Eng.* **2006**, 83, 1482-1486.

8. Bret, T.; Utke, I.; Hoffmann, P. Influence of the Beam Scan Direction during Focused Electron Beam Induced Deposition of 3D Nanostructures. *Microelectron. Eng.* **2005**, 78-79, 307-313.

6.6 APPENDIX 6 - PUBLICATION 6

Publication 6

Direct-Write 3D Nanoprinting of Plasmonic Structures.

Winkler, R.; Schmidt, F.-P.; Haselmann, U.; Fowlkes, J. D.; Lewis, B. B.; Kothleitner, G.; Rack, P. D.; Plank, H.

ACS Appl. Mater. Interfaces **2017**, *9* (9), 8233–8240.

ACS APPLIED MATERIALS & INTERFACES

March 8, 2017
Volume 9
Number 9
pubs.acs.org/acsami

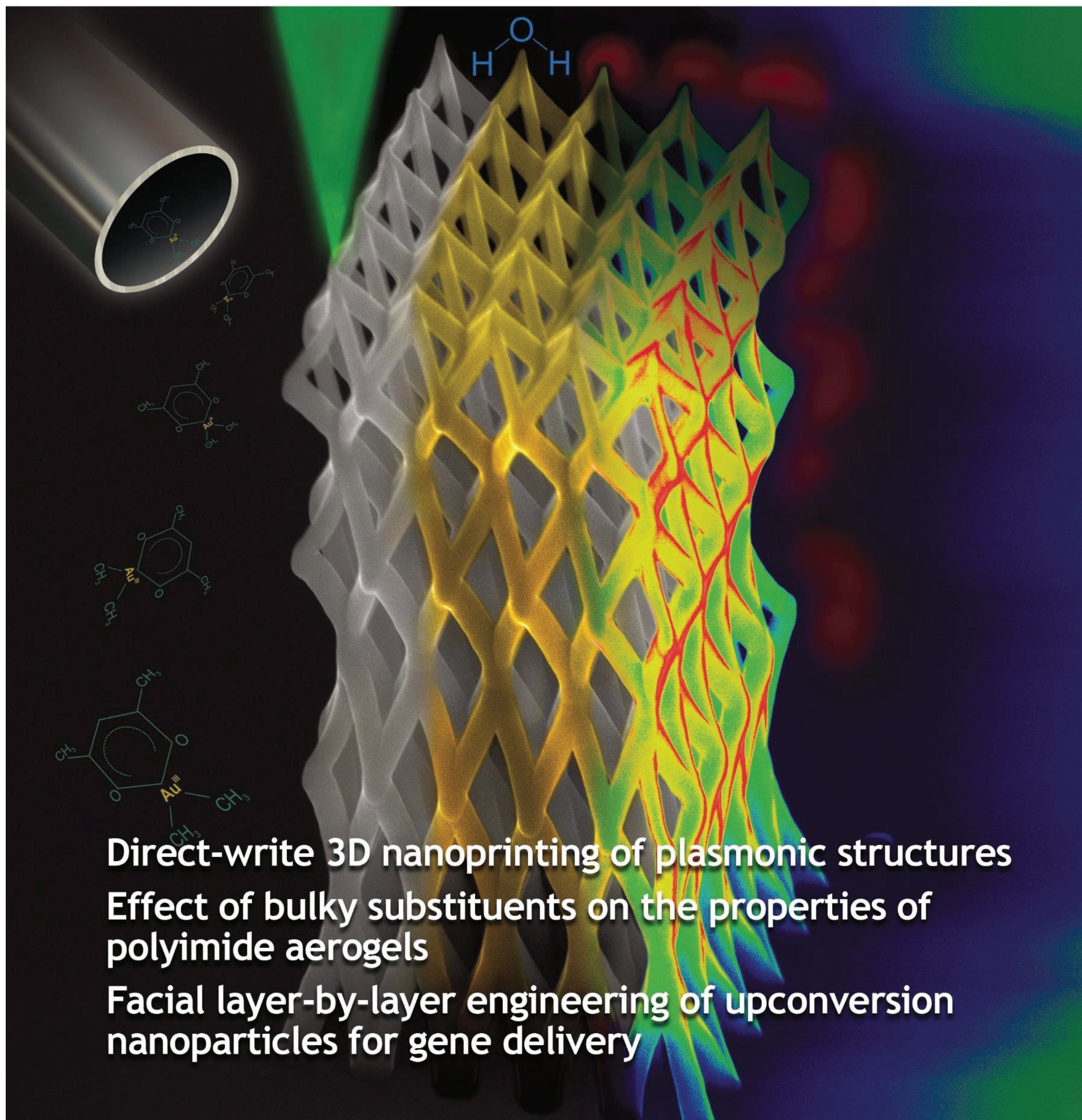

ACS Publications
Most Trusted. Most Cited. Most Read.

www.acs.org

ACS APPLIED MATERIALS & INTERFACES
Research Article
www.acsami.org

Direct-Write 3D Nanoprinting of Plasmonic Structures

Robert Winkler,[†] Franz-Philipp Schmidt,[†,‡] Ulrich Haselmann,[†] Jason D. Fowlkes,[§,⊥] Brett B. Lewis,[§,⊥] Gerald Kothleitner,[†,¶] Philip D. Rack,[*,§,⊥] and Harald Plank[*,†,¶]

[†]Graz Centre for Electron Microscopy, Steyrergasse 17, 8010 Graz, Austria
[‡]Institute of Physics, Karl-Franzens-University, Universitätsplatz 5, 8010 Graz, Austria
[§]Center for Nanophase Materials Sciences, Oak Ridge National Laboratory, Oak Ridge, Tennessee 37831, United States
[⊥]Department of Materials Science and Engineering, University of Tennessee, Knoxville, Tennessee 37996, United States
[¶]Institute of Electron Microscopy and Nanoanalysis, Graz University of Technology, 8010 Graz, Austria

Supporting Information

ABSTRACT: During the past decade, significant progress has been made in the field of resonant optics ranging from fundamental aspects to concrete applications. While several techniques have been introduced for the fabrication of highly defined metallic nanostructures, the synthesis of complex, free-standing three-dimensional (3D) structures is still an intriguing, but so far intractable, challenge. In this study, we demonstrate a 3D direct-write synthesis approach that addresses this challenge. Specifically, we succeeded in the direct-write fabrication of 3D nanoarchitectures via electron-stimulated reactions, which are applicable on virtually any material and surface morphology. By that, complex 3D nanostructures composed of highly compact, pure gold can be fabricated, which reveal strong plasmonic activity and pave the way for a new generation of 3D nanoplasmonic architectures that can be printed on-demand.

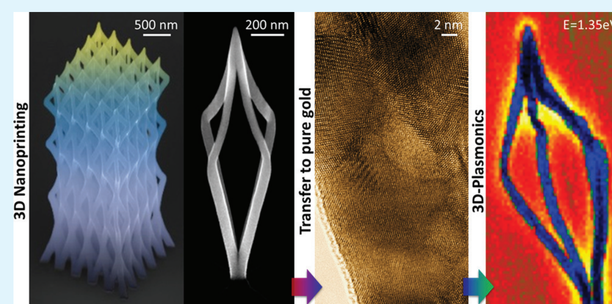

KEYWORDS: *focused electron beam induced deposition, 3D nanoprinting, plasmonics, gold, purification, nanofabrication, surface plasmon resonance, nanostructures*

INTRODUCTION

Surface plasmons in metallic nanostructures are known to have unique properties as they enable light concentration into the deep subwavelength regime. They are thus of high interest for new types of photonic devices[1] such as novel light sources,[2] sensor devices,[3,4] for improvements in data storage technology,[5] and in photovoltaics.[6] A high flexibility for the design of the metallic nanostructures is therefore in high demand. Several factors affect the plasmonic activity, namely: (1) the shape and size of the metallic nanostructure, (2) the quality of the metal in terms of its purity and crystallinity, and (3) accurate positioning on the area of interest. Different approaches have been used so far, but it is very challenging to meet all these requirements. On one hand, wet chemical synthesis enables the production of single crystalline nanoparticles with well-defined shape and high metallic purity.[7,8] However, accurate positioning on the substrate, particularly an arrangement of multiple nanoparticles with tunable, well-defined relative distances, is not possible. On the other hand, electron beam lithography (EBL) overcomes this positioning problem but is limited to quasi two-dimensional (2D) structures and flat surfaces. While these challenges are daunting, focused electron beam induced deposition (FEBID) has the potential to meet these stringent requirements as it is a maskless, direct-write bottom-up synthesis method for the fabrication of 1D, 2D, and 3D architectures with spatial nanometer resolution[9−12] on virtually any substrate material and surface morphology.[13] FEBID uses gaseous precursors, injected in electron beam microscopes, which dynamically physisorb, diffuse, and desorb to establish an equilibrium surface coverage. The focused electron beam decomposes the precursor molecules, which leads to a highly localized functional deposit whose size, shape, and position can be precisely controlled on the lower nanometer scale. In the past, FEBID has been used to rapidly prototype passive and active applications[14−18] and has already found its way into commercial applications for lithography mask repair[19,20] or stress−strain sensing for atomic force microscopy cantilevers.[21,22] However, FEBID deposits notoriously contain very high carbon content of 90 at. % and more for some precursors after fabrication, which compromise the intended functionality.[23] Although a few examples of pure materials after fabrication have been demonstrated,[23−26] most efforts were put on in situ or postgrowth purification processes such as fabrication on hot substrates,[25,27] coflow with reactive gases,[28]

Received: October 14, 2016
Accepted: November 23, 2016
Published: November 23, 2016

ACS Publications © 2016 American Chemical Society

DOI: 10.1021/acsami.6b13062
ACS Appl. Mater. Interfaces 2017, 9, 8233−8240

synchronized laser assisted FEBID,[29,30] and other in situ/ex-situ processes.[21,23,31−37] An essential step forward was achieved by Geier et-al who introduced the first postgrowth purification approach for platinum based FEBID materials leading to pure and highly compact metallic nanostructures without morphological disruption.[38] In this study, we successfully expand their basic purification concept to a gold-based FEBID precursor and, more importantly, to complex free-standing 3D architectures, a much more challenging task than with simple planar or bulky 3D structures. This chemical postgrowth transfer into highly compact, pure gold is then combined with one of FEBID's unique attributes by means of direct-write 3D fabrication. In the past, this capability was mostly restricted to free-standing nanopillars for detailed insight in fundamental processes.[24,39−41] While Fowlkes, et al. recently succeeded in mimicking experimental 3D fabrication via simulations,[42] we here move an essential step further and demonstrate FEBID-based fabrication of complex and highly precise 3D nanoarchitectures, which meets the high demands for advanced plasmonic applications after the successful chemical transformation into pure gold. The roadmap of this study is graphically summarized in Figure 1. First, we report on our recent breakthrough progress toward real 3D nanoprinting of complex, freestanding 3D-nanoarchitectures (Figure 1a−e) by using advanced patterning strategies. Next, we demonstrate the chemical material transfer of carbon containing FEBID deposits into highly compact pure Au nanostructures (Figure 1f−h). Then we confirm the plasmonic response of planar FEBID based Au structures, which reproduce the response of reference Au disks prepared via classical electron beam lithography[43] (Figure 1i−l). This not only fulfills the long lasting promise of FEBID as fabrication tool for plasmonic nanostrutures, but also paves the way for FEBID based 3D plasmonics. Hence, in the last step, we adapt the purification process for the carbon removal in 3D nanostructures and successfully demonstrate the plasmonic activity of free-standing 3D Au nanoarchitectures (Figure 1m−o) whose fabrication is extremely challenging or even impossible with alternative techniques. By that, the proposed approach opens the possibility of entirely new capabilities for the on-demand fabrication of 3D architectures for resonant optics on virtually any surface.

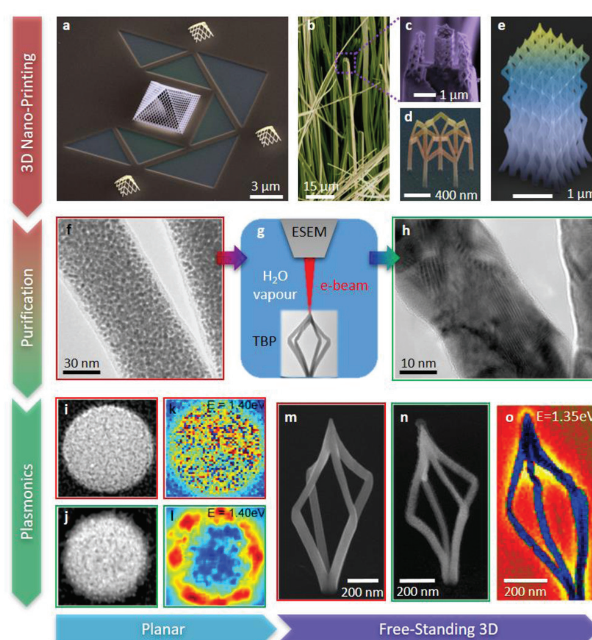

Figure 1. Route toward 3D plasmonic Au structures. (a−e) FEBID's 3D nanoprinting capabilities via SEM images: (a) replica of the glass pyramid of the Louvre with nanobranch diameters of ∼50 nm; (b, c) FEBIDs direct-write capabilities of complex 3D nanostructures on highly exposed, nonflat areas (mineralic nanowires); (d, e) on-demand fabrication of free-standing nanoarchitectures, which are extremely challenging or even impossible with alternative techniques on that scale. (f−h) The approach toward purely metallic 3D objects imaged via bright-field TEM, while as-deposited FEBID materials reveal the typical nanogranular composition of metal grains (dark spots) embedded in a carbon matrix (f), the latter is entirely removed by e-beam exposure in water vapor environments (g) leading to highly compact, crystalline gold structures (h). This paves the way toward planar plasmonics in a first step, illustrated in panels i−l: the application of the purification process (g) transforms as-deposited Au−C disks (i, HAADF image of a 400 nm wide disk) into pure Au materials (j) switching from no plasmonic response (k, STEM EEL map at 1.4 eV taken from (i) to a strong plasmonics activity (l). After the plasmonic suitability of FEBID based materials is confirmed in principle, the process is transferred to free-standing 3D tetragonal-bipyramids (TBP, see also inset in panel g): after initial 3D nanoprinting of TBPs (m, tilted SEM image), the structures are purified with the same approach (g) leading to compact 3D Au structures (n, tilted SEM image), further investigated via STEM EELS measurements, which reveal strong plasmonic activity for FEBID based true 3D nanoarchitectures (o, STEM EEL map at 1.35 eV). Note the surface contamination after purification (n) is a SEM-only feature and absent if directly using TEM.

3D NANOPRINTING

In the past decade, FEBID has made significant, yet incremental progress toward synthesis of freestanding nanostructures.[44,45] Together with a deeper understanding of the dynamic surface processes concerning precursor molecule adsorption, diffusion, and desorption and its relation to the process parameters,[46−49] we recently succeeded in the identification of a widely stable process window where the intended 3D nanostructures becomes very predictable, which prevents exhaustive trial-and-error approaches mostly used in the past.[42] In previous experiments, we determined that high primary electron beam energies (30 keV), low beam currents (21 pA) in combination with pixel distances (point pitch, PoP) in the (sub)nanometer range and pulse durations (dwell times, DT) on a millisecond scale are ideal for 3D synthesis. While general control over tilt angles of free-standing 3D structures is achieved by careful variation of PoPs and DTs, the patterning point sequence is the essential element for predictable and reproducible 3D fabrication. Although the primary beam parameters lead to minimized local precursor depletion during a beam pulse,[9,50,51] continuous growth mode for individual branches lead to varying growth rates dependent on the height making the result unpredictable. Figure 2, panel a shows a top view and a tilted SEM image after a fabrication attempt for a tetragonal-bipyramid (TBP, as depicted in Figure 1g) using a continuous growth mode. As schematically given on top, this strategy tries to grow each single branch individually (see number and arrows). One reason for the structural collaps is attributed to increasing local depletion leading to strongly reduced growth followed by new growth events at the substrate. To prevent such a situation, patterning has been changed to an interlaced patterning sequence as schematically depicted on top of Figure 2, panel b. This strategy jumps between different branches (see

DOI: 10.1021/acsami.6b13062
ACS Appl. Mater. Interfaces 2017, 9, 8233−8240

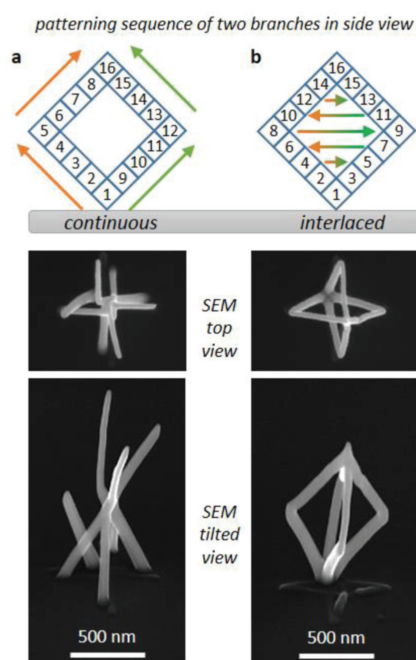

Figure 2. Application of advanced patterning strategies to achieve predictable and reproducible 3D nanoarchitectures. (a) In a continuous growth strategy, each single branch is grown individually as outlined in the top scheme (see numbers and arrows). The results are entirely collapsed structures as evident by top- and side-view SEM images. To get stable 3D growth as shown in the SEM images in panel b, an interlaced patterning sequence is introduced, which grows all four branches almost simultaneously by systematic patterning jumps, as indicated on top of panel b for a two branch structure in a side view (see also arrows). Note, both structures used same number of patterning points, DTs, PoPs, and total fabrication times as only the patterning sequence has been changed, which demonstrates the high importance for the fabrication of more complex structures as shown in Figure 1, panels a−e.

numbers and arrows) by essentially introducing sufficient refresh times in between two consecutive beam pulses at the same branch. This establishes a replenished growth front prior to the next beam pulse, which leads to a stable growth mode as can be seen by the TBP in Figure 2, panel a (both attempts used the same DTs and PoPs without any additional pause times). At the same time, this strategy mitigates proximity effects that produce spatial distortions[39,52] and drift issues (further details can be found in Supporting Information 1). Following this interlace approach, even complex 3D nanostructures, as representatively shown in Figure 1, panels a−e, can be fabricated in a predictable, reliable, reproducible fashion (see also Supporting Information 1). These examples demonstrate FEBID's high flexibility concerning the fabrication of 3D nanoarchitectures, which exploit their full potential together with applicability on virtually any surface material and morphology (more examples can be found in Supporting Information 2). To demonstrate FEBID based 3D plasmonics in this study, tetragonal-bipyramid geometries consisting of four individual branches that converge in the vertical dimension into a single apex have been chosen (see Figures 1g,n, and 2b). The intentions of this geometry are the expected enhanced plasmonic resonances at branch areas and in particular at the tip[53] with typical end radii of ∼10 nm. However, for strong plasmonic resonance, the critical issue of carbon impurities in the 3D gold deposits had to be solved first as discussed in the following.

■ MATERIAL PURITY FOR PLASMONICS

Although a variety of precursor materials are available for FEBID,[23] most of them lead to a nano-granular composition consisting of metallic nanograins (2-5 nm) (see Figure 1f) embedded in a carbon matrix with partly enormous C contents depending on the used organometallic precursor (e.g., the Au precursor used here contains about 95 at. % carbon[23]). This long-lasting drawback reduces or even entirely masks the intended magnetic, electric, or plasmonic functionality. Here we successfully solved the impurity problem with a postgrowth purification approach for the $Me_2Au(acac)$ (acetylacetonate-dimethyl-gold(III) precursor to obtain pure gold materials as a central gateway for plasmonic applications. Specifically, the as-deposited Au−C FEBID structures are exposed to a scanning e-beam in a 10 Pa H_2O ambient in an environmental scanning electron microscope[38] (ESEM) (Figure 1g). A comprehensive characterization of such treated Au−C deposits using atomic force microscopy (AFM), scanning electron microscopy (SEM) based energy dispersive X-ray spectroscopy (EDXS), and transmission electron microscopy (TEM) based electron energy loss spectroscopy (EELS) not only revealed the entire removal of carbon, but also the pore/crack free morphology after purification, which is essential for plasmonic application (see Supporting Information 3). To evaluate the latter aspect, we fabricated two sets of 60 nm thick Au−C FEBID disks with diameters ranging from 250−400 nm, all deposited on 15 nm thick Si_3N_4 membranes for subsequent EELS characterization. One set was used for as-deposited characterization, while the second disk set was purified via the above-described approach. In addition, a third set of Au reference disks with same diameters and thickness was prepared using electron beam lithography (EBL)[54] to evaluate the behavior of FEBID based Au disks as described in the following.

■ 2D PLASMONICS

To study the plasmonic behavior of planar FEBID Au disks, TEM-based nanocharacterization has been performed as it provides energy dependent response information with laterally resolved information on the lower nanoscale. Figure 3 shows scanning transmission electron microscopy (STEM) based high-angle annular dark field (HAADF) survey images (left column in Figure 2a) together with EELS measurements of the laterally resolved plasmonic response of FEBID based as-deposited Au−C (top row) and fully purified Au (central row) in comparison with EBL based Au reference disks.[55−58] As evident, as-deposited Au−C disks (top row) do not produce a plasmonic response at any electron loss energy (A → D). However, fully purified Au FEBID disks (central row) clearly reveal surface plasmon resonances. A direct comparison of the EEL signal originating from the disk center of as-deposited and fully purified FEBID disks (see indication in column D in Figure 3a) is given in Figure 3, panel b. Note, the central plasmon activity indicates the presence of the so-called breathing mode,[43] which is characteristic for such geometries. By comparing the purified FEBID disks (central row) with the Au EBL reference disks (bottom row), a very similar qualitative behavior is observed.[43,59] By starting at low energies, the expected dipole (A), quadrupole (B), and hexapole (C) resonances are clearly observed.[55−58] In addition, the breathing

DOI: 10.1021/acsami.6b13062
ACS Appl. Mater. Interfaces 2017, 9, 8233−8240

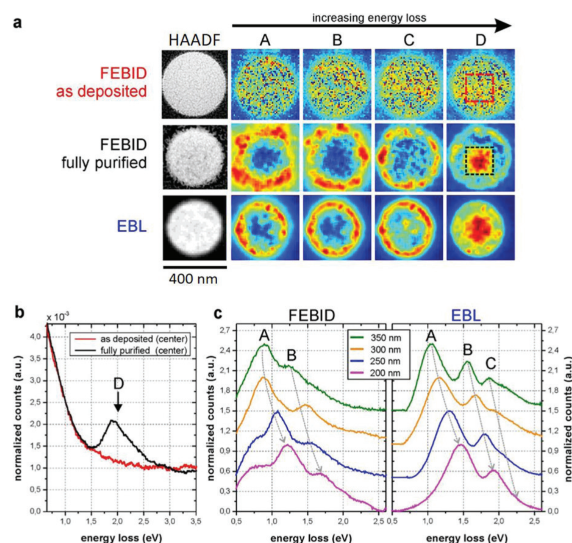

Figure 3. EEL maps and spectra of FEBID and EBL disks. (a) HAADF survey images (left column) together with corresponding EEL maps at increasing electron loss energies (columns A−D) for as-deposited gold disk (thickness 60 nm, diameter 400 nm, top row), fully purified disk (height/diameter decrease to 30 nm/350 nm, central row), and EBL gold disks (same dimensions as for purified disk, bottom row). (b) Direct comparison of EEL spectra acquired at the center of as-deposited and fully purified FEBID disks (see panel a, column D). (c) EEL spectra acquired along the disk circumference of fully purified FEBID and EBL disks for different disk diameters.

mode (D) is observed for both fabrication methods. As expected, distinct peak shifts to higher energies were observed with decreasing disk size as shown in the EEL spectra in Figure 3, panel c for pure FEBID disks (left) and Au EBL reference disks (right). Here EEL spectra originating from the edge region along the disk circumference are displayed. While the dipole (A) and quadrupole mode (B) are well resolved in both sets of spectra, the hexapole mode (C) is only visible in the EBL reference data set for the larger disk diameters. The corresponding EEL map (C) at an energy of 1.6 eV in Figure 3, panel a (center row), however, clearly shows a ring shaped distribution similar to the hexapolar EEL map of the EBL reference (bottom row), which confirms the formation of the hexapole mode in fully purified FEBID disks as expected. The main differences between FEBID and EBL disks are two-fold. First, slightly less pronounced plasmonic peaks are observed for the fully purified FEBID disks (Figure 3c, left curves). The reduction in peak sharpness and intensity originates from the slightly rougher edges for purified FEBID disks as evident in the HAADF image in Figure 3, panel a. As this is equivalent to a superposition of slightly different diameters within one structure, the peaks in the EEL spectra are broader and less intense. The second deviation between EBL and FEBID disks is a general peak shift to lower energies for purified structures. We attribute this effect not only to the smaller nanograin sizes for FEBID based materials as reported in literature before,[60] but also to very small nanovoids possibly formed during fabrication or purification. Despite these slight deviations, these results clearly demonstrate that fully purified FEBID based Au disks exhibit the critical characteristics required for plasmonic applications. Besides the fact that we here fulfilled the long lasting promise of FEBID concerning the on-demand fabrication of plasmonically active Au nanostructures, this achievement paves the way for the expansion to free-standing 3D arachitectures as first ever demonstrated in the following.

■ 3D PLASMONICS

First, free-standing TBPs have been synthesized via FEBID's 3D-nanoprinting capabilities as shown by TEM and SEM images in Figures 1, panels g and n, 2, panel b, and 4, panel a.

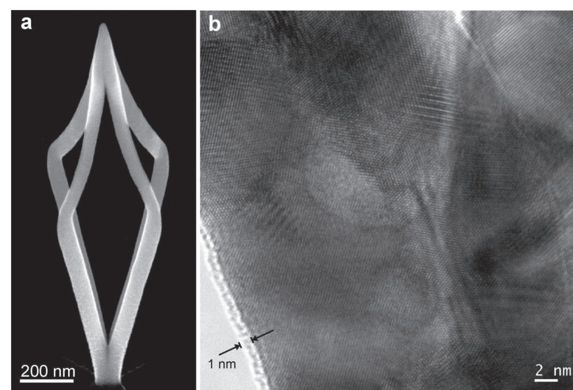

Figure 4. Purification of free-standing gold-nanostructures. (a) Purified tetragonal-bipyramid geometry. (b) High-resolution TEM image of a fully purified 3D-FEBID structure exposing highly compact and crystalline gold branches with diameters below 25 nm and surface contamination layers of less than 1 nm.

These 3D Au−C TBPs were then transferred into pure gold via the electron-stimulated H_2O purification process described earlier. Although free-standing 3D purification requires higher electron doses as well as reduced dwell times and lower purification rates to prevent structural collapsing (see Supporting Information 4), this approach is capable of yielding intact 3D TBP geometries as shown Figure 4, panel a. High-resolution TEM (Figure 4b) confirms the highly compact inner structure, reveals branch diameters of approximately 25 nm, and indicates minimal surface contamination after the purification process of less than 1 nm. In preparation for plasmonic characterization via STEM-EELS, pure gold TBP structures were fabricated on copper TEM grids with a 300 nm thick insulating SiO_X[23] spacer layer (see Supporting Information 1) to prevent electrical contact between TBPs and the substrate. As summarized in Figure 5, fully purified Au TBPs reveal strong plasmonic activity, while no plasmonic response was observed for as-deposited Au−C TBPs. Specifically, Figure 5, panel a gives a HAADF survey image of a fully purified 3D TBP structure together with correlated and deconvolved EEL maps at different electron loss energies in Figure 5, panels b−d, which confirm the surface plasmon resonances (see also Supporting Video). The first noteworthy detail is the symmetric appearance of plasmon modes across the TBP structure, which exhibits the precision of initial FEBID fabrication and the minimally disrupting purification procedure with respect to the local dimensions (see Supporting Information 4). As intended by the TBP design, highest plasmonic activity was found at the branching areas and the tip region due to superpositioned oscillations from the involved branches (see Figure 5 and Supporting Video). This becomes also evident in Figure 6, which shows two unprocessed raw EEL spectra taken from two different regions-of-interest at a free-standing double-branch structure as evident from the survey image (inset top right).

DOI: 10.1021/acsami.6b13062
ACS Appl. Mater. Interfaces 2017, 9, 8233−8240

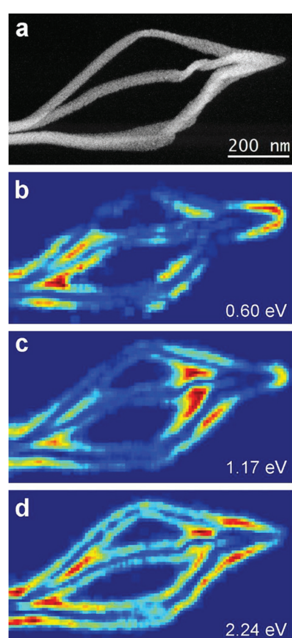

Figure 5. Plasmonic response of FEBID based 3D Au nanostructures. HAADF survey image (a) together with EEL maps revealing the plasmonic activities at different electron loss energies (see indications in b-d and also see Supporting Video). Noteworthy are the widely symmetric appearances, which reveal the high precision after initial fabrication and also the minimally invasive character of the material purification.

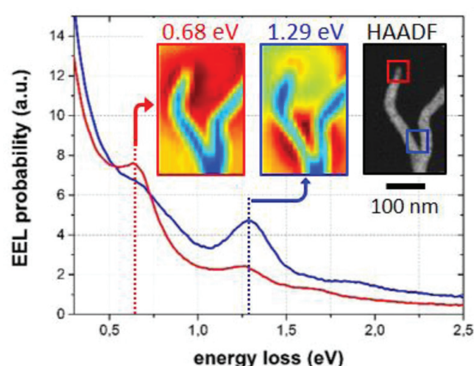

Figure 6. Unprocessed EEL spectra on a fully purified 3D Au structure taken from the tip region (red) and the branched area (blue) as indicated in the HAADF survey image top right. While the clear appearance of plasmon peaks in uncorrected spectra indicates the high material quality, the EEL maps insets give laterally resolved information at energy losses of 0.68 and 1.29 eV, which confirm the highly localized plasmonic acitivites.

The corresponding EEL maps were taken from 0.68 and 1.29 eV (see dashed lines at the red and blue curve, respectively), which again reveal the highly localized plasmonic activity. Particularly noteworthy is the fact that even the here shown as-acquired raw data clearly reveal the plasmon peaks further indicate the high material quality after purification (Figure 6). Together with FEBID's high flexibility in overall and local 3D design (see Figure 1, panels a–e and Supporting Information 2), the here proposed 3D nanoprinting approach might open up entirely new possibilities for fundamental science in the field of optical resonance beyond current limitations.

CONCLUSION

The application of free-standing, 3D, plasmonically active architectures with spatial nanometer resolution strongly relies on proper synthesis methods. Although different approaches have been used to generate plasmonic nanostructures, they are restricted to precisely placed quasi planar features in the case of lithographically methods or complex geometries with no ability to control their placement in the case of wet chemical processing. Here we successfully demonstrated an innovative direct-write, bottom-up synthesis approach, which allows the on-demand fabrication of complex, free-standing 3D nano-structures composed of pure gold for plasmonic applications. The latter can range from device oriented integration on practically any surface toward fundamentally oriented studies concerning 3D plasmonics, which, for example, in combination with 3D TEM tomography, might enable entirely new physical insights. Beyond plasmonics, FEBID based 3D nanoprinting can be considered as a generic approach for nanoscale 3D fabrication with the potential to push the limits of nanoscale optical, mechanical, magnetic, and even multifunctional 3D metamaterials beyond current limitations.

METHODS

Fabrication General. FEBID was performed on a NOVA 200 dual beam instrument (FEI, The Netherlands) equipped with five FEI gas injection systems (GIS). Silicon dioxide was deposited from Tetraethyl orthosilicate (TEOS, CAS: 78–10–4), inserted via a nozzle at 52° with relation to the substrate and a vertical distance of 120 μm. For Au–C deposition, the precursor material $Me_2Au(acac)$ (acetylaceto-nate- dimethyl-gold(III), CAS: 14951–50–9), and for Pt–C deposits $MeCpPt(IV)Me_3$ (CAS: 94442–22–5), was used with similar spatial arrangement. Au- and Pt-based precursors were heated to 30 and 45 °C, respectively, for at least 30 min prior to any deposition. The long axes of the GIS nozzles were aligned in such way that they coincided with the beam center. The nozzle angles with relation to the surface were 52° for Au and 38° for the Pt-GIS. For a symmetrical gas replenishment situation, scan rotation was applied in such way that scan direction was perpendicular to the nozzle main axes. Beam focusing was carefully done at high magnification by deposition of small pillars (5 s) in close proximity to the region of interest until pillar diameters below 40 and 50 nm for Au and Pt, respectively, were achieved in top view. Prior to any deposition, the stage was not moved for at least 15 min, and gas flux was turned on for at least 5 min before any fabrication step. In general, electron exposure of the region of interest was reduced to a minimum to prevent contamination. Base pressure of the dual beam chamber was 3×10^{-6} mbar, while the background pressure increased to 6×10^{-6} mbar and 1×10^{-5} mbar for Au- and Pt-based precursor, respectively. For preliminary purification tests, FEBID structures were deposited on carefully precleaned 1×1 cm^2 silicon wafer with a 3 nm SiO_2 top layer.

Fabrication of Au Pads and Disks. The 2×2 μm^2 Au–C pads with heights ranging from 60–150 nm were deposited with 5 keV, 1600 pA, 100 μs dwell time, 13 nm point pitch using serpentine scanning with the slow scan axis directing toward the GIS (these pads were used for purification studies as discussed in Supporting Information 3). Au disks for plasmonics were fabricated with 30 keV, 150 pA, 5 ms dwell time, and 5 nm point pitch using serpentine strategies with the slow scan axis directed to the GIS. All disks were directly fabricated on plasma precleaned TEM grids with 15 nm thick Si_3N_4 membranes (Ted Pella; Prod-Nr: 21569–10). Gold reference nanodisks were prepared by EBL in a RAITH e-line system using a poly(methylmetacrylate) resist on a 15 nm thick Si_3N_4 membrane and a standard gold evaporation and lift-off procedure.[54]

Tetragonal-Bipyramids Fabrication. A copper TEM grid with a rectangle hole was cut into half and clamped flat on a specimen holder. For a better visibility in the ESEM and correlation of the fabricated structures at the TEM, slits in a distance of about 20 μm were initially

DOI: 10.1021/acsami.6b13062
ACS Appl. Mater. Interfaces 2017, 9, 8233–8240

milled with the focused ion beam using 30 kV, 20 nA, and 52° stage tilt. The grid was then mounted upright in a SEM stab and both edges chamfered for 12° (30 kV, 5 nA, stage tilt 40°) to remove any material that might cast a shadow during TEM investigations. Next, silicon dioxide squares (1.5 × 1.5 μm^2, 300 nm in height) were deposited from tetraethyl orthosilicate (TEOS) precursor in combination with H_2O water at primary energy of 5 kV and a beam current of 6.3 nA. Finally, small markers were cut (30 kV, 500 pA), which indicated the location of the pads to ensure visibility in ESEM mode. TBP fabrication was done at 30 keV, 21 pA, and a PoP of 0.5 nm using the parameters and patterning strategies specified in Supporting Information 1.

Purification. Purification was done in a QUANTA 200 ESEM (FEI, The Netherlands) right after fabrication. The beam current was determined with a Faraday cup in high-vacuum mode, and purification was performed in ESEM-mode at a water vapor pressure of 10 Pa stabilized for at least 30 min prior to purification without e-beam exposure. Au−C pads were purified with primary energy of 5 keV, a beam current of 1.9 nA, a point pitch of 6 nm, and a dwell time of 1 μs. Disks for plasmonic investigations were purified of 5 keV, 0.5 nA, and a DT of 1 μs at a PoP of 6 nm. Total electron doses of 28 C/cm^2 were applied for all pads and disks. The 3D purification was done at with 5 keV, 1.2 nA, a DT of 1 μs, and a PoP of 4 nm. Electron doses varied from 5−200 C/cm^2.

Characterization. AFM characterization was done with a FastScan Bio AFM microscope in tapping mode and soft repulsive conditions using AFM tips with spring constants of 4 N/m (Bruker AXS, CA, USA). Postprocessing was done with Bruker Nanoscope software. EDXS was performed with a Si(Li)-detector (XL-30 EDXS system; EDAX; USA) in a QUANTA 200 ESEM (FEI, The Netherlands). For C/Au ratio determination, a semiquantitative approach was used.[35,36,38] EELS measurements were performed in a FEI Tecnai F20 transmission electron microscope with a monochromated 200 keV electron beam of 100−150 meV energy spread (full-width-at-half-maximum, fwhm). EEL spectra were recorded in the STEM-EELS mode[58] with an energy dispersion of 10 meV/channel in a high resolution Gatan Imaging Filter equipped with a 2048 × 2048 pixel CCD camera. The EEL data shown in Figure 5 were further improved by a Richardson-Lucy deconvolution (MathWorks Matlab, deconvlucy function), implemented in a homemade analysis program.[61] All EEL maps shown in this work are integrated over an energy range of 100 meV.

■ ASSOCIATED CONTENT

Supporting Information

The Supporting Information is available free of charge on the ACS Publications website at DOI: 10.1021/acsami.6b13062.

Additional information and figures of 3D nanoprinting and interlacing; 3D nanoprinting examples; purification of planar FEBID Au-C deposits; and purification of freestanding 3D structures (PDF)

EEL map of a fully purified FEBID-gold nanoarchitecture (AVI)

■ AUTHOR INFORMATION

Corresponding Authors

*E-mail: prack@utk.edu.

*E-mail: harald.plank@felmi-zfe.at.

ORCID

Harald Plank: 0000-0003-1112-0908

Notes

The authors declare no competing financial interest.

■ ACKNOWLEDGMENTS

R.W., U.H., and H.P. gratefully acknowledge the valuable support by Prof. Dr. Ferdinand Hofer. The same authors also acknowledge financial support by the COST action CELINA (Nr. CM1301) and the EUROSTARS project TRIPLE-S (Nr. E! 8213). The research that led to these results has received funding from the EU FP7 programme [FP7/2007-2013] under Grant Agreement No. 312483 (ESTEEM2). P.D.R. and J.D.F. acknowledge that their contributions were supported by the Center for Nanophase Materials Sciences, which is sponsored at Oak Ridge National Laboratory by the Scientific User Facilities Division, Office of Basic Energy Sciences, U.S. Department of Energy. B.B.L. acknowledges support from the Chancellors Fellowship program at the University of Tennessee.

■ REFERENCES

(1) Barnes, W. L.; Dereux, A.; Ebbesen, T. W. Surface Plamons Subwavelength Optics. *Nature* **2003**, *424* (6950), 824−830.

(2) Okamoto, K.; Niki, I.; Shvartser, A.; Narukawa, Y.; Mukai, T.; Scherer, A. Surface-Plasmon-Enhanced Light Emitters Based on InGaN Quantum Wells. *Nat. Mater.* **2004**, *3* (9), 601−605.

(3) Lal, S.; Link, S.; Halas, N. J. Nano-Optics from Sensing to Waveguiding. *Nat. Photonics* **2007**, *1* (11), 641−648.

(4) Anker, J. N.; Hall, W. P.; Lyandres, O.; Shah, N. C.; Zhao, J.; Van Duyne, R. P. Biosensing with Plasmonic Nanosensors. *Nat. Mater.* **2008**, *7* (6), 442−453.

(5) Stipe, B. C.; Strand, T. C.; Poon, C. C.; Balamane, H.; Boone, T. D.; Katine, J. A.; Li, J.-L.; Rawat, V.; Nemoto, H.; Hirotsune, A.; Hellwig, O.; Ruiz, R.; Dobisz, E.; Kercher, D. S.; Robertson, N.; Albrecht, T. R.; Terris, B. D. Magnetic Recording at 1.5 Pb m−2 Using an Integrated Plasmonic Antenna. *Nat. Photonics* **2010**, *4* (7), 484−488.

(6) Atwater, H. A.; Polman, A. Plasmonics for Improved Photovoltaic Devices. *Nat. Mater.* **2010**, *9* (10), 865−865.

(7) Liz-Marzan, L. M. Tailoring Surface Plasmons through the Morphology and Assembly of Metal Nanoparticles. *Langmuir* **2006**, *22* (1), 32−41.

(8) Grzelczak, M.; Pérez-Juste, J.; Mulvaney, P.; Liz-Marzán, L. M. Shape Control in Gold Nanoparticle Synthesis. *Chem. Soc. Rev.* **2008**, *37* (9), 1783−1791.

(9) Utke, I.; Russell, P. E. *Nanofabrication Using Focused Ion and Electron Beams: Principles and Applications*; Oxford University Press: New York, 2012.

(10) Utke, I.; Hoffmann, P.; Melngailis, J. Gas-Assisted Focused Electron Beam and Ion Beam Processing and Fabrication. *J. Vac. Sci. Technol. B Microelectron. Nanom. Struct.* **2008**, *26* (4), 1197−1276.

(11) Randolph, S. J.; Fowlkes, J. D.; Rack, P. D. Focused, Nanoscale Electron-Beam-Induced Deposition and Etching. *Crit. Rev. Solid State Mater. Sci.* **2006**, *31* (3), 55−89.

(12) Van Dorp, W. F.; Hagen, C. W. A Critical Literature Review of Focused Electron Beam Induced Deposition. *J. Appl. Phys.* **2008**, *104* (8), 081301−081342.

(13) Peinado, P.; Sangiao, S.; De Teresa, J. M. Focused Electron and Ion Beam Induced Deposition on Flexible and Transparent Polycarbonate Substrates. *ACS Nano* **2015**, *9* (6), 6139−6146.

(14) Gabureac, M.; Bernau, L.; Utke, I.; Boero, G. Granular Co-C Nano-Hall Sensors by Focused-Beam-Induced Deposition. *Nanotechnology* **2010**, *21* (11), 115503.

(15) Kolb, F.; Schmoltner, K.; Huth, M.; Hohenau, A.; Krenn, J.; Klug, A.; List, E. J. W.; Plank, H. Variable Tunneling Barriers in FEBID Based PtC Metal-Matrix Nanocomposites as a Transducing Element for Humidity Sensing. *Nanotechnology* **2013**, *24* (30), 305501.

(16) Gavagnin, M.; Wanzenboeck, H. D.; Belić, D.; Bertagnolli, E. Synthesis of Individually Tuned Nanomagnets for Nanomagnet Logic by Direct Write Focused Electron Beam Induced Deposition. *ACS Nano* **2013**, *7* (1), 777−784.

(17) Perentes, A.; Bachmann, A.; Leutenegger, M.; Utke, I.; Sandu, C.; Hoffmann, P. Focused Electron Beam Induced Deposition of a Periodic Transparent Nano-Optic Pattern. *Microelectron. Eng.* **2004**, *73-74*, 412−416.

(18) Utke, I.; Jenke, M. G.; Röling, C.; Thiesen, P. H.; Iakovlev, V.; Sirbu, A.; Mereuta, A.; Caliman, A.; Kapon, E. Polarisation Stabilisation of Vertical Cavity Surface Emitting Lasers by Minimally Invasive Focused Electron Beam Triggered Chemistry. *Nanoscale* **2011**, *3* (7), 2718−2722.

(19) Edinger, K.; Becht, H.; Bihr, J.; Boegli, V.; Budach, M.; Hofmann, T.; Koops, H. W. P.; Kuschnerus, P.; Oster, J.; Spies, P.; Weyrauch, B. Electron-Beam-Based Photomask Repair. *J. Vac. Sci. Technol., B: Microelectron. Process. Phenom.* **2004**, *22* (6), 2902−2906.

(20) Lassiter, M. G.; Liang, T.; Rack, P. D. Inhibiting Spontaneous Etching of Nanoscale Electron Beam Induced Etching Features: Solutions for Nanoscale Repair of Extreme Ultraviolet Lithography Masks. *J. Vac. Sci. Technol. B Microelectron. Nanom. Struct.* **2008**, *26* (3), 963−976.

(21) Schwalb, C. H.; Grimm, C.; Baranowski, M.; Sachser, R.; Porrati, F.; Reith, H.; Das, P.; Müller, J.; Völklein, F.; Kaya, A.; Huth, M. A Tunable Strain Sensor Using Nanogranular Metals. *Sensors* **2010**, *10* (11), 9847−9856.

(22) Porrati, F.; Sachser, R.; Schwalb, C. H.; Frangakis, A. S.; Huth, M. Tuning the Electrical Conductivity of Pt-Containing Granular Metals by Postgrowth Electron Irradiation. *J. Appl. Phys.* **2011**, *109* (6), 063715.

(23) Botman, A.; Mulders, J. J. L.; Hagen, C. W. Creating Pure Nanostructures from Electron-Beam-Induced Deposition Using Purification Techniques: A Technology Perspective. *Nanotechnology* **2009**, *20* (37), 372001.

(24) Klein, K. L.; Randolph, S. J.; Fowlkes, J. D.; Allard, L. F.; Meyer, H. M., III; Simpson, M. L.; Rack, P. D. Single-Crystal Nanowires Grown via Electron-Beam-Induced Deposition. *Nanotechnology* **2008**, *19*, 345705.

(25) Córdoba, R.; Sesé, J.; De Teresa, J. M.; Ibarra, M. R. High-Purity Cobalt Nanostructures Grown by Focused-Electron-Beam-Induced Deposition at Low Current. *Microelectron. Eng.* **2010**, *87* (5−8), 1550−1553.

(26) Shawrav, M. M.; Taus, P.; Wanzenboeck, H. D.; Schinnerl, M.; Stöger-Pollach, M.; Schwarz, S.; Steiger-Thirsfeld, A.; Bertagnolli, E. Highly Conductive and Pure Gold Nanostructures Grown by Electron Beam Induced Deposition. *Sci. Rep.* **2016**, *6*, 34003.

(27) Mulders, J. J. L.; Belova, L. M.; Riazanova, A. Electron Beam Induced Deposition at Elevated Temperatures: Compositional Changes and Purity Improvement. *Nanotechnology* **2011**, *22* (5), 055302.

(28) Langford, R. M.; Ozkaya, D.; Sheridan, J.; Chater, R. Effects of Water Vapour on Electron and Ion Beam Deposited Platinum. *Microsc. Microanal.* **2004**, *10* (S02), 1122−1123.

(29) Roberts, N. A.; Fowlkes, J. D.; Magel, G. A.; Rack, P. D. Enhanced Material Purity and Resolution via Synchronized Laser Assisted Electron Beam Induced Deposition of Platinum. *Nanoscale* **2013**, *5* (1), 408−415.

(30) Roberts, N. A.; Magel, G. A.; Hartfield, C. D.; Moore, T. M.; Fowlkes, J. D.; Rack, P. D. In Situ Laser Processing in a Scanning Electron Microscope. *J. Vac. Sci. Technol., A* **2012**, *30* (4), 041404.

(31) Botman, A.; Mulders, J. J. L.; Weemaes, R.; Mentink, S. Purification of Platinum and Gold Structures after Electron-Beam-Induced Deposition. *Nanotechnology* **2006**, *17* (15), 3779−3785.

(32) Langford, R. M.; Wang, T.-X.; Ozkaya, D. Reducing the Resistivity of Electron and Ion Beam Assisted Deposited Pt. *Microelectron. Eng.* **2007**, *84* (5−8), 784−788.

(33) Frabboni, S.; Gazzadi, G. C.; Felisari, L.; Spessot, A. Fabrication by Electron Beam Induced Deposition and Transmission Electron Microscopic Characterization of Sub-10-Nm Freestanding Pt Nanowires. *Appl. Phys. Lett.* **2006**, *88* (21), 213113−213116.

(34) Plank, H.; Kothleitner, G.; Hofer, F.; Michelitsch, S. G.; Gspan, C.; Hohenau, A.; Krenn, J. Optimization of Postgrowth Electron-Beam Curing for Focused Electron-Beam-Induced Pt Deposits. *J. Vac. Sci. Technol. B* **2011**, *29* (5), 051801−051807.

(35) Mehendale, S.; Mulders, J. J. L.; Trompenaars, P. H. F. A New Sequential EBID Process for the Creation of Pure Pt Structures from MeCpPtMe3. *Nanotechnology* **2013**, *24* (14), 145303.

(36) Plank, H.; Noh, J. H. J. H.; Fowlkes, J. D. J. D.; Lester, K.; Lewis, B. B. B.; Rack, P. D. P. D. Electron-Beam-Assisted Oxygen Purification at Low Temperatures for Electron-Beam-Induced Pt Deposits: Towards Pure and High-Fidelity Nanostructures. *ACS Appl. Mater. Interfaces* **2014**, *6* (2), 1018−1024.

(37) Stanford, M. G.; Lewis, B. B.; Noh, J. H.; Fowlkes, J. D.; Roberts, N. A.; Plank, H.; Rack, P. D. Purification of Nanoscale Electron-Beam-Induced Platinum Deposits via a Pulsed Laser-Induced Oxidation Reaction. *ACS Appl. Mater. Interfaces* **2014**, *6* (23), 21256−21263.

(38) Geier, B.; Gspan, C.; Winkler, R.; Schmied, R.; Fowlkes, J. D.; Fitzek, H.; Rauch, S.; Rattenberger, J.; Rack, P. D.; Plank, H. Rapid and Highly Compact Purification for Focused Electron Beam Induced Deposits: A Low Temperature Approach Using Electron Stimulated H2O Reactions. *J. Phys. Chem. C* **2014**, *118* (25), 14009−14016.

(39) Burbridge, D. J.; Gordeev, N. Proximity Effects in Free-Standing EBID Structures. *Nanotechnology* **2009**, *20*, 285308.

(40) Plank, H.; Gspan, C.; Dienstleder, M.; Kothleitner, G.; Hofer, F. The Influence of Beam Defocus on Volume Growth Rates for Electron Beam Induced Platinum Deposition. *Nanotechnology* **2008**, *19* (48), 485302−485309.

(41) Fowlkes, J. D.; Randolph, S. J.; Rack, P. D. Growth and Simulation of High-Aspect Ratio Nanopillars by Primary and Secondary Electron-Induced Deposition. *J. Vac. Sci. Technol., B: Microelectron. Process. Phenom.* **2005**, *23*, 2825−2832.

(42) Fowlkes, J. D.; Winkler, R.; Lewis, B. B.; Stanford, M. G.; Plank, H.; Rack, P. D. Simulation-Guided 3D Nanomanufacturing via Focused Electron Beam Induced Deposition. *ACS Nano* **2016**, *10* (6), 6163−6172.

(43) Schmidt, F.-P.; Ditlbacher, H.; Hohenester, U.; Hohenau, A.; Hofer, F.; Krenn, J. R. Dark Plasmonic Breathing Modes in Silver Nanodisks. *Nano Lett.* **2012**, *12* (11), 5780−5783.

(44) Mølhave, K.; Madsen, D. N.; Dohn, S.; Bøggild, P. Constructing, Connecting and Soldering Nanostructures by Environmental Electron Beam Deposition. *Nanotechnology* **2004**, *15* (8), 1047−1053.

(45) Bret, T.; Utke, I.; Hoffmann, P.; Abourida, M.; Doppelt, P. Electron Range Effects in Focused Electron Beam Induced Deposition of 3D Nanostructures. *Microelectron. Eng.* **2006**, *83* (4−9), 1482−1486.

(46) Winkler, R.; Fowlkes, J.; Szkudlarek, A.; Utke, I.; Rack, P. D.; Plank, H. The Nanoscale Implications of a Molecular Gas Beam during Electron Beam Induced Deposition. *ACS Appl. Mater. Interfaces* **2014**, *6* (4), 2987−2995.

(47) Winkler, R.; Szkudlarek, A.; Fowlkes, J. D.; Rack, P. D.; Utke, I.; Plank, H. Toward Ultraflat Surface Morphologies During Focused Electron Beam Induced Nanosynthesis: Disruption Origins and Compensation. *ACS Appl. Mater. Interfaces* **2015**, *7* (5), 3289−3297.

(48) Schmied, R.; Fowlkes, J. D.; Winkler, R.; Rack, P. D.; Plank, H. Fundamental Edge Broadening Effects during Focused Electron Beam Induced Nanosynthesis. *Beilstein J. Nanotechnol.* **2015**, *6* (1), 462−471.

(49) Arnold, G.; Timilsina, R.; Fowlkes, J. D.; Orthacker, A.; Kothleitner, G.; Rack, P. D.; Plank, H. Fundamental Resolution Limits during Electron Induced Direct Write Synthesis. *ACS Appl. Mater. Interfaces* **2014**, *6*, 7380−7387.

(50) Plank, H.; Smith, D. A.; Haber, T.; Rack, P. D.; Hofer, F. Fundamental Proximity Effects in Focused Electron Beam Induced Deposition. *ACS Nano* **2012**, *6* (1), 286−294.

(51) Winkler, R.; Geier, B.; Plank, H. Spatial Chemistry Evolution during Focused Electron Beam-Induced Deposition: Origins and Workarounds. *Appl. Phys. A: Mater. Sci. Process.* **2014**, *117* (4), 1675−1688.

(52) Plank, H.; Smith, D. A.; Haber, T.; Rack, P. D.; Hofer, F. Fundamental Proximity Effects in Focused Electron Beam Induced Deposition. *ACS Nano* **2012**, *6* (1), 286−294.

(53) Stockman, M. Nanofocusing of Optical Energy in Tapered Plasmonic Waveguides. *Phys. Rev. Lett.* **2004**, *93* (13), No. 137404, DOI: 10.1103/PhysRevLett.93.137404.

DOI: 10.1021/acsami.6b13062
ACS Appl. Mater. Interfaces 2017, 9, 8233−8240

(54) Hohenau, A.; Ditlbacher, H.; Lamprecht, B.; Krenn, J. R.; Leitner, A.; Aussenegg, F. R. Electron Beam Lithography, a Helpful Tool for Nanooptics. *Microelectron. Eng.* **2006**, *83* (4−9), 1464−1467.
(55) Nelayah, J.; Kociak, M.; Stéphan, O.; García de Abajo, F. J.; Tencé, M.; Henrard, L.; Taverna, D.; Pastoriza-Santos, I.; Liz-Marzán, L. M.; Colliex, C. Mapping Surface Plasmons on a Single Metallic Nanoparticle. *Nat. Phys.* **2007**, *3* (5), 348−353.
(56) Schaffer, B.; Hohenester, U.; Trügler, A.; Hofer, F. High-Resolution Surface Plasmon Imaging of Gold Nanoparticles by Energy-Filtered Transmission Electron Microscopy. *Phys. Rev. B: Condens. Matter Mater. Phys.* **2009**, *79* (4), No. 41401, DOI: 10.1103/PhysRevB.79.041401.
(57) Haberfehlner, G.; Trügler, A.; Schmidt, F. P.; Hörl, A.; Hofer, F.; Hohenester, U.; Kothleitner, G. Correlated 3D Nanoscale Mapping and Simulation of Coupled Plasmonic Nanoparticles. *Nano Lett.* **2015**, *15* (11), 7726−7730.
(58) Jeanguillaume, C.; Colliex, C. Spectrum-Image: The next Step in EELS Digital Acquisition and Processing. *Ultramicroscopy* **1989**, *28* (1−4), 252−257.
(59) Schmidt, F.-P.; Ditlbacher, H.; Hohenester, U.; Hohenau, A.; Hofer, F.; Krenn, J. R. Universal Dispersion of Surface Plasmons in Flat Nanostructures. *Nat. Commun.* **2014**, *5*, No. 3604, DOI: 10.1038/ncomms4604.
(60) Bosman, M.; Zhang, L.; Duan, H.; Tan, S. F.; Nijhuis, C. A.; Qiu, C.-W.; Yang, J. K. W. Encapsulated Annealing: Enhancing the Plasmon Quality Factor in Lithographically-Defined Nanostructures. *Sci. Rep.* **2014**, *4*, No. 5537, DOI: 10.1038/srep05537.
(61) Schmidt, F.-P.; Hofer, F.; Krenn, J. R. Spectrum Image Analysis Tool − A Flexible MATLAB Solution to Analyze EEL and CL Spectrum Images. *Micron* **2017**, *93*, 43−51.

Supporting Information

Direct-Write 3D-Nanoprinting of Plasmonic Structures

Robert Winkler[1], Franz-Philipp Schmidt[1,2], Ulrich Haselmann[1], Jason D. Fowlkes[3,4], Brett B. Lewis[3,4], Gerald Kothleitner[1,5], Philip D. Rack[3,4,+], Harald Plank[1,5,]*

[1] Graz Centre for Electron Microscopy, Steyrergasse 17, 8010 Graz, AUSTRIA

[2] Institute of Physics, Karl-Franzens-University, Universitätsplatz 5, 8010 Graz, AUSTRIA

[3] Center for Nanophase Materials Sciences, Oak Ridge National Laboratory, Oak Ridge, Tennessee 37831, USA

[4] Department of Materials Science and Engineering, University of Tennessee, Knoxville, Tennessee 37996, USA

[5] Institute of Electron Microscopy and Nanoanalysis, Graz University of Technology, 8010 Graz, AUSTRIA

* corresponding author: E-mail: harald.plank@felmi-zfe.at

* co-corresponding author: E-mail: prack@utk.edu

Supporting Information 1: 3D Nanoprinting

While free-standing FEBID-pillars were often used for fundamental studies[1–4] only very few studies focused on real 3D fabrication[5–13]. The reason for that are the manifold challenges, namely unwanted effects like co-deposition, structure bending[14] and reproducibility.

One critical aspect is the dynamic change in precursor coverage during the deposition process. The actual situation is described by the working regime, reflecting the ratio between dissociating electrons and available precursor molecules[2,15–17]. For a controlled 3D fabrication on the nanoscale, the establishment of very similar precursor coverages for any addressed pixel point at any time is necessary. This is a very challenging task as there is a complex interplay regarding depletion and replenishment mechanisms[15,18–20]. While the depletion is linked to the beam settings, the local replenishment mechanisms can be classified in three main components: (1) diffusion from the surrounding substrate; (2) diffusion from the deposit; and (3) direct gas flux adsorption. While (1) decays with growing heights, (2) is driven by (3) in close proximity to the new growth areas. However, also (3) is not constant for all regions has and can have a strong directional component given by the technical setup[18–20]. The ideal conditions are thus the electron limited working regime (**ELR**)[21–23]. ELR conditions are achieved by using high primary energies (low dissociation cross-section) and low beam currents (low local depletion). Here, one also profits from the smallest possible electron probe diameter, resulting in smallest possible FEBID elements[21].

Inclined/suspended deposition is obtained by reducing the patterning velocity to a range of about 0.05 nm/ms. Lower patterning speeds lead to steeper deposit angles, faster velocities resulting in more and more horizontal elements up to the point where they collapse. The suitable pattern velocities obviously strongly depend on the beam settings (primary energy, beam current, focal settings) as well as precursor type and gas injection system alignment[19,20].

The most time consuming part is the proper preparation of dwell time, pixel coordinates and patterning sequence in a stream file. Up to now and for the experiments in this manuscript these

files were created via a self-written C++ and Matlab code. Fowlkes et al.[12] recently developed an easy-to-use software, which is based on hybrid Monte Carlo-continuum simulations and takes proximity deposition during 3D-FEBID into account. With increasing complexity of the structures it is necessary to use a special patterning sequence which will be discussed in the following section.

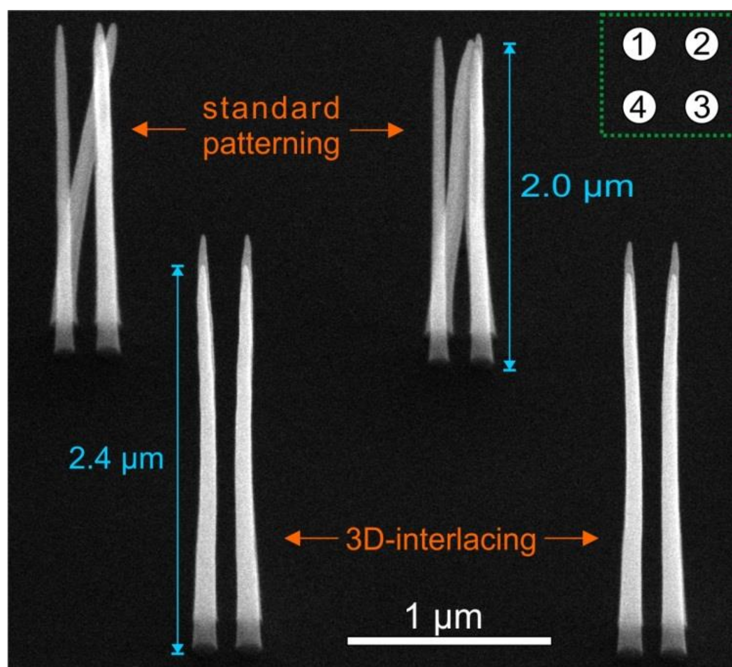

Figure S 1: Four-pillar arrangements to demonstrate the benefits of 3D-interlacing in contrast to standard patterning. Four Pt-C pillars, each grown for 30 seconds with 30 keV/21 pA, were fabricated in a continuous manner (standard patterning, top row) and with alternating point sequence (3D-interlacing, bottom row). The top right inset indicates the fabrication order in top view. For the standard patterning, pillar 1 was exposed for 30 seconds before proceeding with pillar 2, 3 and 4 respectively. On the contrary, for the 3D-interlacing approach first pillar 1 was exposed for 25 ms, followed by 25 ms on position 2, 3 and 4. This procedure was continued until a total exposure time of 30 s was achieved for each pillar. The pillar array fabricated via standard patterning exposes unwanted effects (pillar bending, inhomogeneous thicknesses and lower growth rates) that are solved via the presented 3D-interlacing approach.

3D-Interlacing: An alternating point sequence approach

One of the most serious problems during fabrication of freestanding 3D geometries is the bending of structures during deposition. Especially, for long side branches this effect strongly limits the possibility to create more complex geometries including multiple elements as discussed in more detail by Burbridge et al.[1]. For example, considering a simple geometry with 4 pillars in a squared arrangement (Figure S 1, inset top right) a sequential deposition of pillar 1, afterwards pillar 2, then pillar 3 and finally pillar 4 leads to a bending of pre-existing pillars (Figure S 1, top row). In addition to bending, forward and backscattered electrons escape from the side walls of a growing pillar and trigger deposition on previous pillars. As a consequence, first-built pillars get slightly thicker than final ones. Both effects, bending and non-homogeneous thicknesses are highly unwanted. These problems can now be mitigated with a suitable patterning sequence. For that, we follow the basic idea of an interlacing approach, which was already successfully introduced in different fields like the FIB processing of polymer by avoiding heat accumulation[23] or the improvement of growth rates during FEBID[16]. This interlacing approach was adapted to the fabrication of freestanding 3D structures, which we further consequently denote as “3D-interlacing”. The main idea is schematically shown in Figure 2 (top schemes) of the main manuscript. Instead of the deposition of single structural elements sequentially, all branches are patterned in parallel. This alternating point sequence approach of the 3D-interlacing solves the discussed problems in Figure S 1. With 3D-interlacing all four pillars are growing in parallel. The unavoidable effect of bending still appears as can be slightly seen in Figure S 1 but the effect is now distributed homogeneously to all four pillars. Furthermore, all four pillars show the same thickness. One noticeable advantage of 3D-interlacing over the standard sequential patterning is the significantly larger pillar height. After one DT pulse (25 ms in Figure S 1, bottom row) the electron beam jumps to the other 3 pillars. As a consequence, the 3D-interlacing provides an intrinsic refresh time to a just exposed area (here 75 ms) before it is irradiated again. This enhanced replenishment with new precursor molecules leads to an enhanced growth rate (20%) despite equal process times as for standard patterning. By that the electron

limited precursor regime is maintained. A significant problem for real 3D fabrication are drift problems, whether due to mechanical stage drift, charging drift (beam, specimen) or temperature gradients. The SEM images in main manuscripts Figure 2a clearly show that it is impossible to deposit a tetragonal bipyramid (**TBP**) geometry with a sequential patterning sequence under such conditions. By introducing the 3D-interlacing (top scheme in main manusripts Figure 2b) the TBP is connected even despite drift (see SEM images in main manuscripts Figure 2b).

Particularly noteworthy is the nanometer precision of FEBID when applying the interlacing strategy. Figure S 2 shows a tilted SEM image of an interlaced tetragonal-bipyramid (large image) with a fully closed tip region. To test the accuracy we changed the stream file in such a ways that growth stops before the tip is fully closed. The result can be seen in the top row of Figure S 2 where stopping distances of 4 nm, 8 nm and 12 nm were introduced. As evident there is clearly an increasing gap at the top region according to the aimed growth stop which clearly demonstrates the achievable precision of the fabrication process.

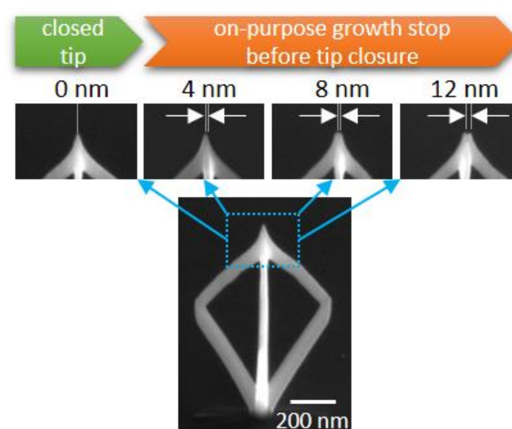

Figure S 2: precision testing at the tip region of a tetragonal-bipyramid as shown by a tilted SEM image (center). The top row shows the tip regions for fully closed situations (left) as well as for fabrication situation in which the growth has been stopped 4 nm, 8 nm and 12 nm before a full closure was achieved. As evident, there is an increasing nanoscale gap at the top regions which clearly demonstrates FEBID´s fabrication precision.

Concerning the reproducibility, Figure S 3 gives a series of free standing diving boards (a) and more complex tetragonal-bipyramids (b) which have been fabricated right after each other with total experimental times of more than an hour. For the diving board geometry a critical setup towards horizontal branch angles were used as small deviations during the fabrication getting more obvious in that case. Nevertheless, the structures remain very similar for ideal beam conditions. Note, that such intrinsic reproducibility is only possible under stable working regime conditions and therefore strongly depends on the technical setup of the system.

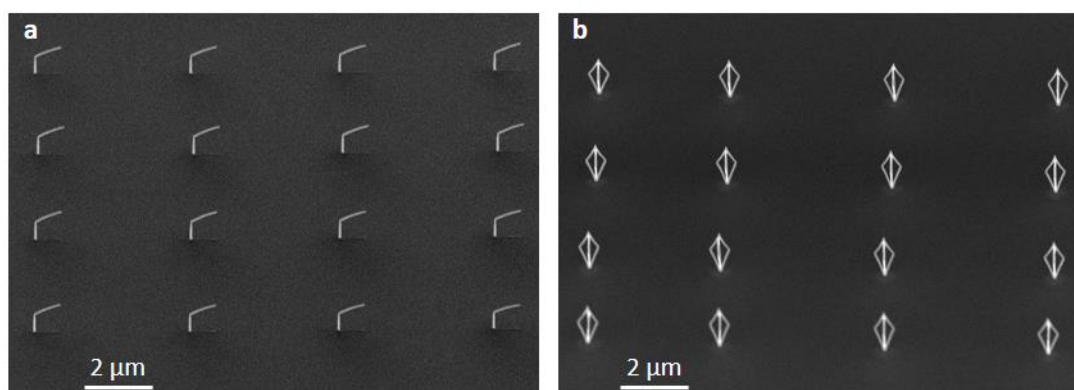

Figure S 3: reproducibility testing during FEBID based 3D nanoprinting for simple (a) and more complex 3D structures (b) to reveal both, reproducibility and stability for total experimental times on an hour scale.

For plasmonic investigations via STEM-EELS, it is necessary to fabricate the TBPs on a TEM grid, which is possible due to FEBID´s ability to deposit on almost any substrate morphology/material. A split copper grid was structured via Focused Ion Beam milling to prevent shadowing by edge contaminations during the TEM investigations. Furthermore, for a better assignment and visibility in the ESEM and TEM, slits and markers were cut (Figure S 4a). To inhibit electrical contact between Au-TBP and copper TEM grid, an insulating 300 nm thick SiO_X pad was deposited from TEOS precursor. This minimizes any coupling of the TBP structure to the copper grid which could otherwise obscure the plasmonic signatures. Usually, plasmonic structures for TEM investigations are conducted on a

thin membrane as also done for FEBID disks discussed in this manuscript. In those cases, the plasmonic behaviour is strongly determined by the interface between the metal particle and the substrate. With the novel aspect of freestanding 3D nano-structures, new possibilities for plasmonic investigations arise as there is no additional medium between metal structure and vacuum. Figure S 4b-e shows a purified TBP in side view rotated from 0° to 45° in 15° steps. These bright field TEM images emphasize the achievable precision of FEBID´s 3D-printing possibilities by exhibiting almost perfect rotation symmetry. Please note, the length differences between lower and upper branches are deliberate to provide asymmetry in that direction.

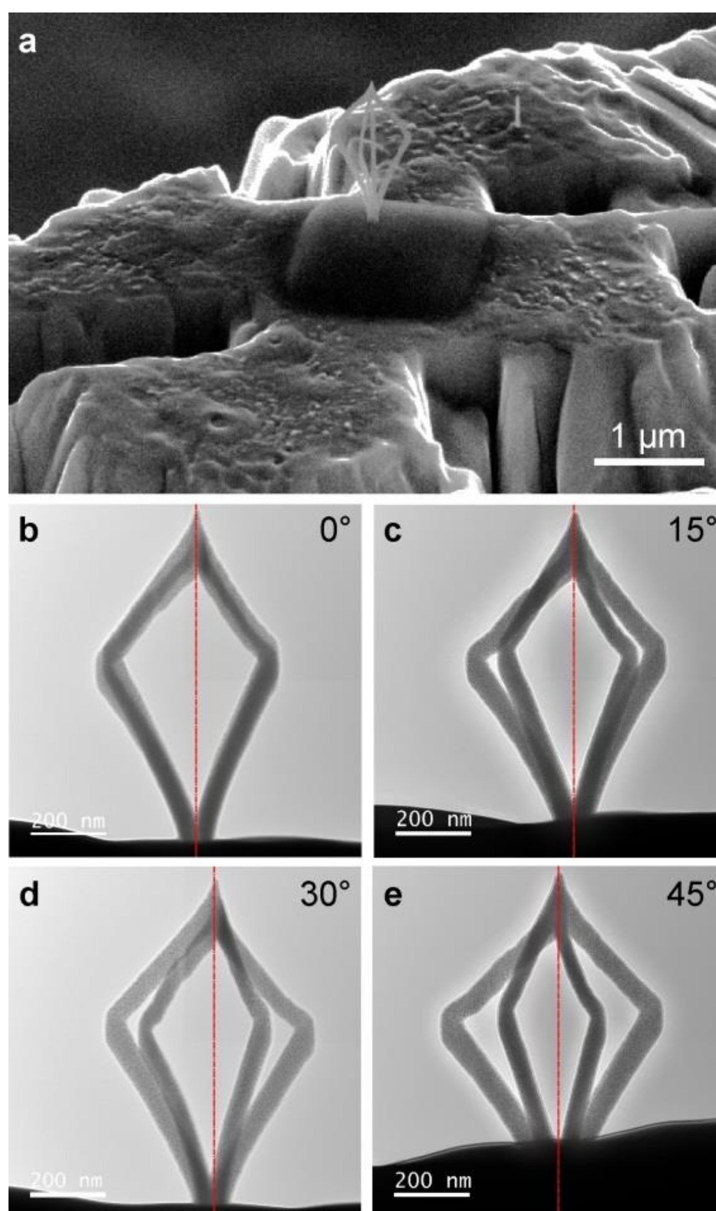

Figure S 4: TBP structure fabricated on a TEM grid. (a) shows a SEM image of a FIB-cut copper TEM grid on which a 1.5×1.5 µm² large TEOS pad with a height of 300 nm was deposited. On top of this insulating basement a TBP was fabricated. (b-e), representatively give such a TBP as TEM bright field images after a purification of 5 C/cm². The sample rotation from 0° (a) to 15° (b), to 30° (d), and 45° (e) demonstrates the rotational symmetry of the structure.

Supporting Information 2: 3D Nanoprinting Examples

The TBP design for this study was chosen based on plasmonic considerations, but much more complex architectures are possible (see also Figure 1 in the main manuscript). In the following we want to emphasize the novel and unique possibilities of the presented 3D-nanoprinting technique. Figure S 5 shows some FEBID architectures to demonstrate ***1)*** the accuracy in nano-fabrication enabling complex 3D structures and ***2)*** the flexibility in the choice of substrates (see Figure S 5a and e). Concerning structural dimensions freestanding branch thicknesses down to 20 nm are possible, justifying the term 3D-nano-printing. To give a hint to potential optical experiments, a TBP structure is pin-pointed on top of a light fibre shown in Figure S 5a and magnified in Figure S 5b. In contrast to lithography based techniques, 3D-nanoprinting is also possible on biological samples as demonstrated in Figure S 5e, which displays a hexagonal meshed tower fabricated on a wasp´s facet eye. Regarding plasmonic investigations, antennas with defined dimensions and shapes are of interest as representatively shown in Figure S 5f. Furthermore, complex multi-branch architectures can be realized (Figure S 5c, g, h). An architecture on a larger length scale including several structural elements like meshed grids, gothic arches, quadrupeds and squared and hexagonal tubes is presented Figure S 5h proving the applicability of 3D-printing to larger surface areas. We also want to highlight, that the 3D fabrication is not limited to the used gold precursor. Most of the presented structures in Figure S 5 were fabricated from $MeCpPt(IV)Me_3$ precursor. Fowlkes et al.[12] also demonstrated the applicability to tungsten precursor tungsten hexacarbonyl. Additionally FEBID allows the fabrication of multi material stacks which further opens up new possibilities such as insulating-metallic 3D material stacks which are extremely complicated to fabricate with other techniques on that scale.

The most time consuming and challenging part is the proper preparation of dwell time, pixel coordinates and patterning sequence in an executable stream file. Up to now these files were usually created via a self-made code written in C++ and Matlab. Fowlkes et al.[12] recently presented a

simulation taking proximity deposition during 3D-FEBID also into account and enable very complex geometries as representatively shown in Figure S 5c,d,g and h.

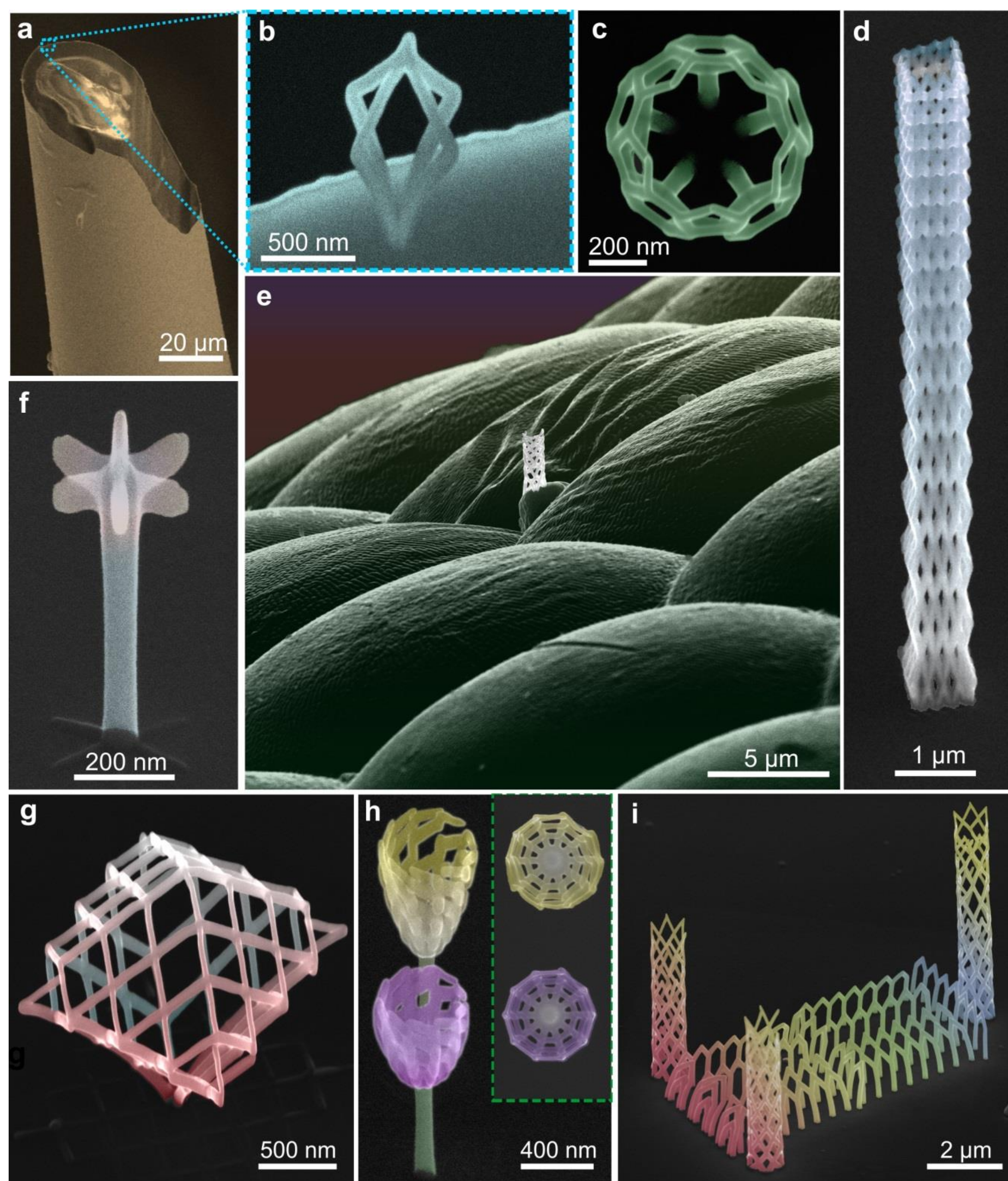

Figure S 5: 3D nano-printing representatives. (a) light fibre with a tetragonal-bipyramid shown in (b) with higher magnification. (c) open buckyball in top view. (d) Hollow skyscraper with a squared basement (860×860 nm²) and a height of more than 10 µm. (e) meshed FEBID-tower on a biological sample (wasp facet eye, C sputtered). (f) nano-antenna with hexagonal apex. (g) freestanding nano-cage. (h) tulips in side view and from the top (inset right). (i) gothic FEBID cathedral. (a,b) are fabricated from $Me_2Au(acac)$ precursor (c-i) from $MeCpPt(IV)Me_3$ precursor and shown in 52° tilt.

Supporting Information 3: Purification of Planar FEBID Au-C Deposits

In 2014, the purification of the organometallic platinum precursor MeCpPt(IV)Me_3 was demonstrated by Geier et al. where planar FEBID pads were irradiated with electrons in the presence of water vapor introduced into an environmental scanning electron microscope (**ESEM**)[24]. Due to the nanogranular composition after deposition - small platinum grains are embedded in a carbon matrix - water molecules are able to diffuse into the deposit. There, they are dissociated under e-beam irradiation into reactive products[25] which bind to carbon and leave the deposit as volatile compounds. The gold precursor used for this study (Me_2Au(acac)) (acetylacetonate- dimethyl-gold(III) also exhibit such a metal/carbon composition. Therefore the same purification mechanism was expected to work for this precursor type as well.

First purification investigations on gold-precursor based deposits were performed with 2×2 μm^2 pads on bulk substrates, mimicking experimental setup and parameters from Geier et al[24]. Purification is performed by a scanning e-beam in a 10 Pa H_2O ambient in an environmental scanning electron microscope (**ESEM**). Figure S 6a shows scanning electron microscopy (**SEM**) based energy dispersive X-ray spectroscopy (**EDXS**) spectra of an initially 120 nm thick Au-C FEBID deposit before (red) and after (green) full purification together with an Au (blue) and Si (black) reference spectra. Clearly the carbon peak (around 0.3 keV) after purification (green) is negligible and the Au-N (blue) and the Si-L (black) lines are more pronounced which confirms the successful carbon removal (see also EELS measurements in Figure S 8). The corresponding morphologies of a representative 2×2 μm^2 deposits before and after full purification are summarized in Figure S 6b by atomic force microscopy (**AFM**) height images at the left and right, respectively, revealing pore- and crack-free, highly compact surfaces with root-mean-square (**RMS**) roughness of 0.3 nm and 1.1 nm, respectively. While the deposit height is decreased from 120 nm to 40 nm as a consequence of the carbon removal (initial C content ~95 at.%[26]), the qualitative cross-sectional profile is maintained and reveals a lateral reduction < 4 rel.% as shown in Figure S 6c by normalized AFM line-sections.

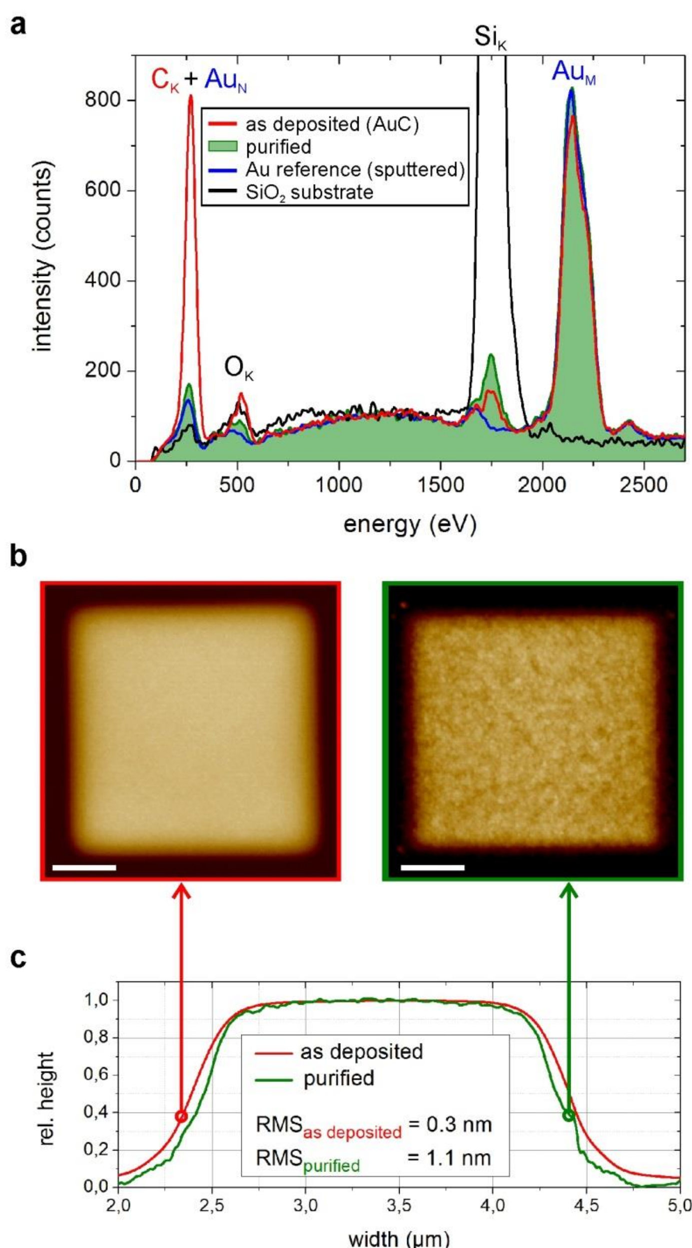

Figure S 6: Carbon removal of $Me_2Au(acac)$ based FEBID materials. (a) EDX spectra before (red) and after purification (green) together with reference spectra of sputtered Au (blue) and SiO_2 (black), confirming the successful carbon removal. (b) AFM height images of a 2×2 μm^2 deposit before (left) and after (right) purification revealing pore- and crack-free surfaces with RMS roughness of 0.3 nm and 1.1 nm, respectively (scale bar is 500 nm; height scales are normalized to compare the surface details). (c) normalized AFM cross-sections of deposits shown in (b) (see arrows and corresponding colours) revealing qualitatively maintained surfaces with lateral shrinkage of < 4 rel.%.

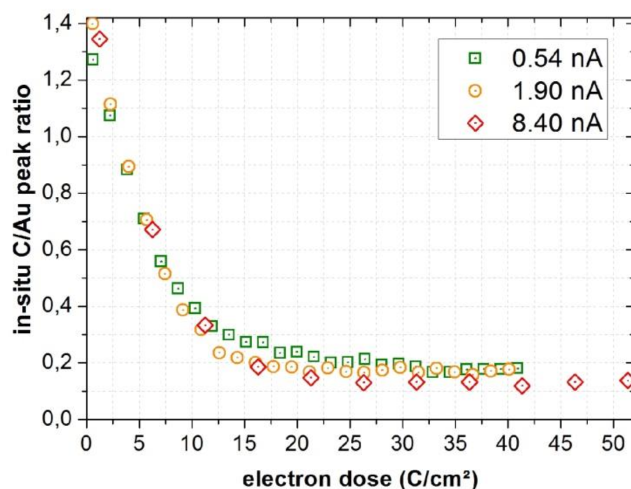

Figure S 7: Purification progress in dependency on the electron dose for different beam currents. 2×2 µm² Au-C pads with a height of 120 nm were purified with a primary energy of 5 keV at 10 Pa water vapour pressure. The initially high carbon-to-gold peak ratio is decreasing with increasing electron dose. This is independent on the applied beam currents and the ratio saturates at an electron dose around 20 C/cm², indicating fully purification.

Purification and acquisition of EDX spectra were performed simultaneously. Thus, the purification progress is trackable live during the purification. For the determination of C/Au ratio we followed the semi-quantitative EDXS approach for thin films[27,28,24].

From the recorded spectra (see Figure S 6a) and after subtraction of the substrate reference spectrum, this C/Au ratio is calculated by dividing the x-ray intensity in a range from 170-410 eV by the intensity from 2000-2350 eV. First range (further denoted as carbon peak) contains the not separately resolved C-K peak (277 eV) and Au-N peak (334 eV), the second range contains the Au-M peak (2123 eV, further denoted as gold peak). With a decrease of the carbon peak in relation to the gold peak the status of the purification progress can be tracked. Full purification is achieved when the purified spectrum does not differ from a sputtered Au reference sample. Figure S 7 reveals a fast decrease of Carbon in an early stage of the purification process, followed by saturation behaviour for electron doses around 20 C/cm². Experiments with varying deposit thicknesses and purification beam

currents (Figure S 7) revealed no major influence of those two parameter to the final chemical composition.

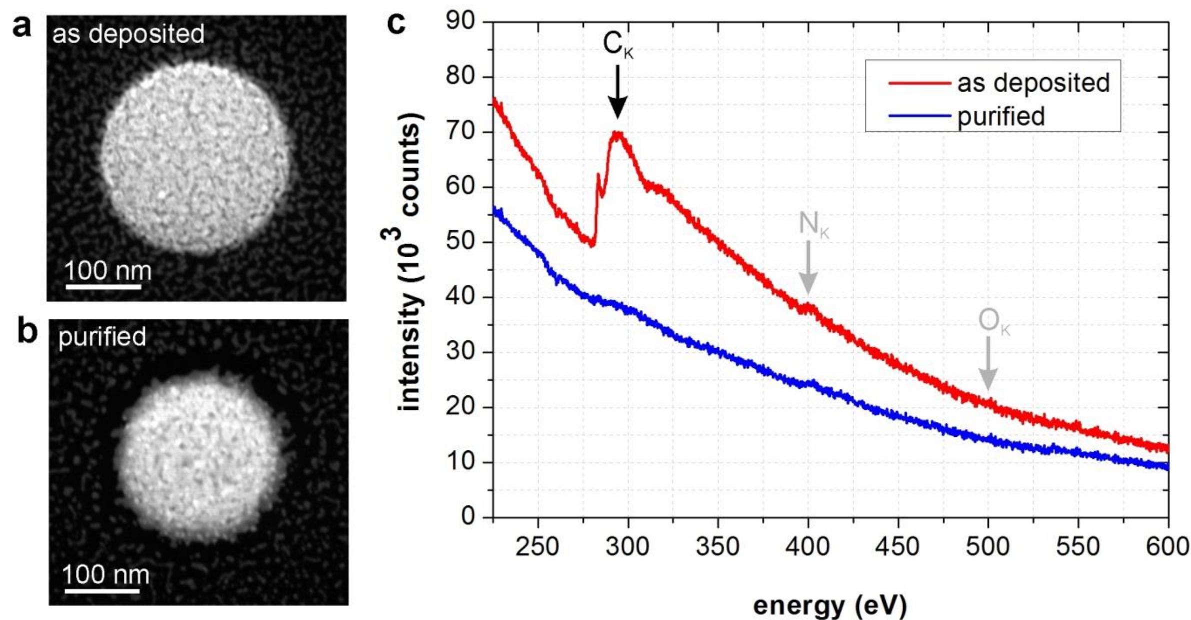

Figure S 8: Comparison of as-deposited and purified Au disks. (a) shows a HAADF image of an as-deposited Au-FEBID disk with a diameter of 250 nm on a Si_3N_4TEM grid. The same disk after a full purification is displayed in (b), exposing a compact morphology with an increased edge roughness and lateral shrinkage. Related AFM measurements revealed a height reduction from 60 nm to 30 nm. (c) EELS characterization of the disk center proves the total elimination of the carbon after the purification step. While the carbon-K peak is still prominent for as-deposited disks, this peak has vanished after the purification and an oxygen plasma step. The small nitrogen peak arises from the Si_3N_4TEM grid, the oxygen peak can be assigned to an oxygen content from the gold precursor.

In addition to in-situ EDXS measurements in the ESEM the chemical purity of the gold disks was confirmed via EELS characterization in the TEM (Figure S 8b) showing the absence of a carbon signal of purified disks in comparison to as-deposited disks. The removal of carbon implies a volume loss[29] which was measured by taking AFM height images before and after the purification. For fully purified 2×2 µm² pads a mean volume loss of 63% was found. Geometrically only a minimal lateral shrinkage

(~ 3%) was obtained and roughness analyses show a value of 1 nm (see Fig. 1b and 1c in the main article). By changing the geometry from pads (2×2 μm^2) to small disks (150 - 400 nm) on a Si_3N_4 TEM grid much stronger lateral shrinkages (30-43%) were observed while the expected volume losses of about 67 % is similar**.** As a consequence of disk contraction also the edge roughness increased after purification as can be seen in Figure S 8b in comparison to as deposited disks (Figure S 8a) and EBL disks.

Supporting Information 4: Purification of freestanding 3D structures

While the purification process for planar structures is straightforward and similar as reported by Geier et al.[24], the applicability to freestanding 3D elements is more challenging as the strong volume loss has to be considered. This can lead to deformation, breaking or detachment of fragile freestanding nano-architectures. TBPs were fabricated on a silicon wafer for preliminary tests of the purification process parameters: 1) water vapour pressure, 2) pixel dwell time, 3) primary energy, 4) beam current, and 5) electron dose. The variation of the pixel dwell time did not have a major influence on the purification results within the used range between 0.5 µs – 10 µs.

The water vapour pressure in the ESEM strongly affects the amount of electron scattering[30,31] and supports the purification of pillars in top view. For the used TBP geometry, a variation of water vapour pressure (10 Pa – 100 Pa) revealed no significant differences on the purification results. In contrast, purification efficiency was increased by lowering the primary electron energy to 5 keV and 2 keV.

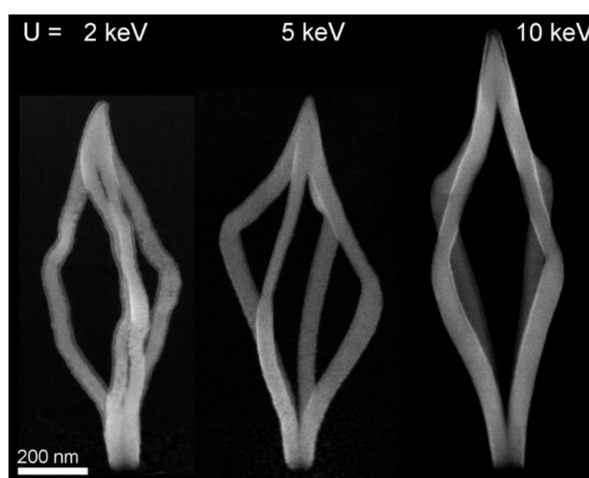

Figure S 9: TBPs after purification with different primary energies. While TBPs purified at 10 keV still look similar to as-deposited ones, for low purification energies (2 keV and 5 keV) the size of the gold grains increased. Furthermore, as a consequence of the carbon removal the shrinkage of the structures dimensions indicates a progressive purification stage, which leads to morphological distortions at 2 keV. Other parameters were kept constant for all three TBPs (beam current of 3 nA, water vapour pressure of 10 Pa, dose 50 C/cm², dwell time 1 µs, point pitch 4 nm).

This is assigned to the confined interaction volume for lower electron energies as described by Lewis et al.[29]. Figure S 9 visualizes the dependency on the primary energy at otherwise same process parameter via SEM images.

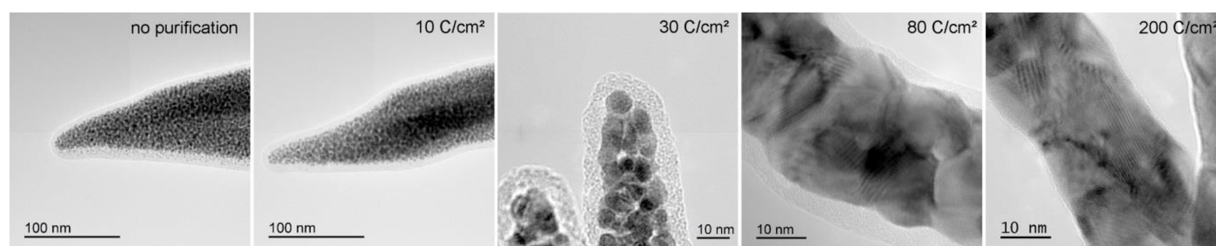

Figure S 10: High-resolution Bright Field TEM images on TBPs after different purification doses. As-deposited and low-dose purified Au TBPs exhibit small gold grains embedded in a carbon matrix. At an electron dose of 30 C/cm² the grains have already started to coalescence. After purification with an electron dose of 80 C/cm² the gold grain size has dramatically increased and an already compact composition is revealed. The purification with 200 C/cm² confirms a densely packed gold core. Please note, the carbon contaminations mainly origin from imaging before and after the purification step. For TBPs intended for plasmonic investigations SEM imaging was reduced to a minimum resulting in a carbon surface contaminations lower than 1 nm as shown the last micrograph. A thick carbon layer would implicate a high damping of plasmon peaks and has to be avoided.

Beside the higher purification efficiency for 2 keV, the high density of secondary electrons also leads to charging and preferentially strong bending of the initial structure. Therefore, as a compromise between efficiency and mechanical stability a purification energy of 5 keV was chosen for further processing. In general, it turned out that a slower purification process is beneficial in terms of shape retention. By using high beam currents the purification process time can be reduced but as a drawback, most of those structures collapse or are strongly deformed. For the plasmonic investigations the deposits were purified with low beam current (1.2 nA) at 5 keV to maintain the TBP shape. The most significant parameter is the electron dose, similar to the purification of planar gold deposits (Figure S 7). In contrast to two-dimensional deposits, freestanding 3D structures

require much higher electron doses to achieve comparable metal content. The dose dependency is demonstrated with High-Resolution TEM images in Figure S 10. A strong indication for a progressed purification status is the increase of gold grain size. For a compact gold core with coalescent grains, doses around 80 C/cm^2 are necessary. To ensure full purification, even higher doses (up to 200 C/cm^2) were applied for the TBP on the TEM grid. The downsides of too high doses are morphological distortions. Please note, the TBP design is already a very fragile geometry as they are mounted on a single spot to the substrate. Architectures with several contact points to the substrate are much more stable.

Supporting Informationary Videos

Supporting Informationary Video: EEL map of a fully purified FEBID-gold nano-architecture (D = 120 C/cm²)

References

(1) Burbridge, D. J.; Gordeev, S. N. Proximity Effects in Free-Standing EBID Structures. *Nanotechnology* **2009**, *20* (28), 285308–6.

(2) Plank, H.; Gspan, C.; Dienstleder, M.; Kothleitner, G.; Hofer, F. The Influence of Beam Defocus on Volume Growth Rates for Electron Beam Induced Platinum Deposition. *Nanotechnology* **2008**, *19* (48), 485302–485309.

(3) Randolph, S. J.; Fowlkes, J. D.; Rack, P. D. Effects of Heat Generation during Electron-Beam-Induced Deposition of Nanostructures. *J. Appl. Phys.* **2005**, *97*, 124312–124318.

(4) Klein, K. L.; Randolph, S. J.; Fowlkes, J. D.; Allard, L. F.; Meyer, H. M.; Simpson, M. L.; Rack, P. D. Single-Crystal Nanowires Grown via Electron-Beam-Induced Deposition. *Nanotechnology* **2008**, *19*, 345705–345708.

(5) Mølhave, K.; Madsen, D. N.; Rasmussen, A. M.; Carlsson, A.; Appel, C. C.; Brorson, M.; Jacobsen, C. J. H.; Bøggild, P. Solid Gold Nanostructures Fabricated by Electron Beam Deposition. *Nano Lett.* **2003**, *3* (11), 1499–1503.

(6) Ueda, K.; Yoshimura, M. Fabrication of Nanofigures by Focused Electron Beam-Induced Deposition. *Thin Solid Films* **2004**, *464*, 331–334.

(7) Bret, T.; Utke, I.; Hoffmann, P. Influence of the Beam Scan Direction during Focused Electron Beam Induced Deposition of 3D Nanostructures. *Microelectron. Eng.* **2005**, *78*, 307–313.

(8) Bret, T.; Utke, I.; Hoffmann, P.; Abourida, M.; Doppelt, P. Electron Range Effects in Focused Electron Beam Induced Deposition of 3D Nanostructures. *Microelectron. Eng.* **2006**, *83* (4–9), 1482–1486.

(9) Fernández-Pacheco, A.; De Teresa, J. M.; Córdoba, R.; Ibarra, M. R. Magnetotransport Properties of High-Quality Cobalt Nanowires Grown by Focused-Electron-Beam-Induced Deposition. *J. Phys. D. Appl. Phys.* **2009**, *42* (5), 55005-6.

(10) Fernández-Pacheco, A.; Serrano-Ramón, L.; Michalik, J. M.; Ibarra, M. R.; De Teresa, J. M.; O'Brien, L.; Petit, D.; Lee, J.; Cowburn, R. P. Three Dimensional Magnetic Nanowires Grown by Focused Electron-Beam Induced Deposition. *Sci. Rep.* **2013**, *3*, 1492-5.

(11) Esposito, M.; Tasco, V.; Cuscuná, M.; Todisco, F.; Benedetti, A.; Tarantini, I.; Giorgi, M. De; Sanvitto, D.; Passaseo, A. Nanoscale 3D Chiral Plasmonic Helices with Circular Dichroism at Visible Frequencies. *ACS Photonics* **2015**, *2* (1), 105–114.

(12) Fowlkes, J. D.; Winkler, R.; Lewis, B. B.; Stanford, M. G.; Plank, H.; Rack, P. D. Simulation-Guided 3D Nanomanufacturing via Focused Electron Beam Induced Deposition. *ACS Nano* **2016**, *10* (6), 6163–6172.

(13) Gazzadi, G. C.; Frabboni, S.; Menozzi, C. Suspended Nanostructures Grown by Electron Beam-Induced Deposition of Pt and TEOS Precursors. *Nanotechnology* **2007**, *18* (44), 445709-7.

(14) Burbridge, D. J.; Gordeev, N. Proximity Effects in Free-Standing EBID Structures. *Nanotechnology* **2009**, *20 (28)*, 285308-6.

(15) Szkudlarek, A.; Szmyt, W.; Kapusta, C.; Utke, I. Lateral Resolution in Focused Electron Beam-Induced Deposition: Scaling Laws for Pulsed and Static Exposure. *Appl. Phys. A* **2014**, *117* (4), 1715–1726.

(16) Plank, H.; Smith, D. A.; Haber, T.; Rack, P. D.; Hofer, F. Fundamental Proximity Effects in Focused Electron Beam Induced Deposition. *ACS Nano* **2012**, *6* (1), 286–294.

(17) Plank, H.; Haber, T.; Gspan, C.; Kothleitner, G.; Hofer, F. Chemical Tuning of PtC Nanostructures Fabricated via Focused Electron Beam Induced Deposition. *Nanotechnology* **2013**, *24* (17), 175305-8.

(18) Friedli, V.; Utke, I. Optimized Molecule Supply from Nozzle-Based Gas Injection Systems for Focused Electron- and Ion-Beam Induced Deposition and Etching: Simulation and Experiment. *J. Phys. D. Appl. Phys.* **2009**, *42* (12), 125305-11.

(19) Winkler, R.; Fowlkes, J.; Szkudlarek, A.; Utke, I.; Rack, P. D.; Plank, H. The Nanoscale Implications of a Molecular Gas Beam during Electron Beam Induced Deposition. *ACS Appl. Mater. Interfaces* **2014**, *6* (4), 2987–2995.

(20) Winkler, R.; Szkudlarek, A.; Fowlkes, J. D.; Rack, P. D.; Utke, I.; Plank, H. Toward Ultraflat Surface Morphologies During Focused Electron Beam Induced Nanosynthesis: Disruption Origins and Compensation. *ACS Appl. Mater. Interfaces* **2015**, *7* (5), 3289–3297.

(21) Arnold, G.; Timilsina, R.; Fowlkes, J. D.; Orthacker, A.; Kothleitner, G.; Rack, P. D.; Plank, H. Fundamental Resolution Limits during Electron Induced Direct Write Synthesis. *ACS Appl. Mater. Interfaces* **2014**, *6*, 7380–7387.

(22) Schmied, R.; Fowlkes, J. D.; Winkler, R.; Rack, P. D.; Plank, H. Fundamental Edge Broadening Effects during Focused Electron Beam Induced Nanosynthesis. *Beilstein J. Nanotechnol.* **2015**, *6* (1), 462–471.

(23) Orthacker, A.; Schmied, R.; Chernev, B.; Fröch, J. E.; Winkler, R.; Hobisch, J.; Trimmel, G.; Plank, H. Chemical Degradation and Morphological Instabilities during Focused Ion Beam Prototyping of Polymers. *Phys. Chem. Chem. Phys.* **2014**, *16* (4), 1658–1666.

(24) Geier, B.; Gspan, C.; Winkler, R.; Schmied, R.; Fowlkes, J. D.; Fitzek, H.; Rauch, S.; Rattenberger, J.; Rack, P. D.; Plank, H. Rapid and Highly Compact Purification for Focused Electron Beam Induced Deposits: A Low Temperature Approach Using Electron Stimulated H2O Reactions. *J. Phys. Chem. C* **2014**, *118* (25), 14009–14016.

(25) Fowlkes, J. D.; Geier, B.; Lewis, B. B.; Rack, P. D.; Stanford, M. G.; Winkler, R.; Plank, H. Electron Nanoprobe Induced Oxidation: A Simulation of Direct-Write Purification. *Phys. Chem. Chem. Phys.* **2015**, *17* (28), 18294–18304.

(26) Botman, A.; Mulders, J. J. L.; Weemaes, R.; Mentink, S. Purification of Platinum and Gold Structures after Electron-Beam-Induced Deposition. *Nanotechnology* **2006**, *17* (15), 3779–3785.

(27) Mehendale, S.; Mulders, J. J. L.; Trompenaars, P. H. F. A New Sequential EBID Process for the Creation of Pure Pt Structures from MeCpPtMe3. *Nanotechnology* **2013**, *24* (14), 145303-7.

(28) Plank, H.; Noh, J. H. J. H.; Fowlkes, J. D. J. D.; Lester, K.; Lewis, B. B. B.; Rack, P. D. P. D. Electron-Beam-Assisted Oxygen Purification at Low Temperatures for Electron-Beam-Induced Pt Deposits: Towards Pure and High-Fidelity Nanostructures. *ACS Appl. Mater. Interfaces* **2014**, *6* (2), 1018–1024.

(29) Lewis, B. B.; Stanford, M. G.; Fowlkes, J. D.; Lester, K.; Plank, H.; Rack, P. D. Electron-Stimulated Purification of Platinum Nanostructures Grown via Focused Electron Beam Induced Deposition. *Beilstein J. Nanotechnol.* **2015**, *6*, 907–918.

(30) Rattenberger, J.; Wagner, J.; Schröttner, H.; Mitsche, S.; Zankel, A. A Method to Measure the Total Scattering Cross Section and Effective Beam Gas Path Length in a Low-Vacuum SEM. *Scanning* **2009**, *31* (3), 107–113.

(31) Danilatos, G. D. Foundations of Environmental Scanning Electron Microscopy. *Advances in Electronics and Electron Physics* **1988**; 71 (C), 109-250

6.7 Appendix 7 - Curriculum Vitae

Curriculum Vitae

Curriculum Vitae

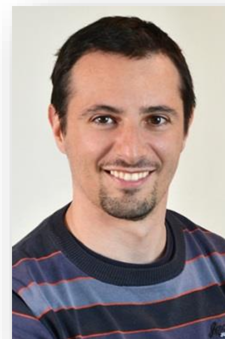

	Personal Data
Name	Robert Winkler
Academic degree	Dipl.-Ing. Mag. art. BSc.
Address	Dr. Robert-Sieger-Straße 13/20 8010 Graz AUSTRIA
Email	Robert.winkler@felmi-zfe.at
Tel. Nr.	43 (0)316 873 8334
Date and place of birth	December 27th, 1979; Vorau, Austria
Nationality	Austrian

	Professional Experience
5 / 2015 – 6 / 2015	• Guest scientist at the University of Tennessee and at the Oak Ridge National Labs (Tennessee, USA) • Research activities in the field of *3D-nanoprinting via focused electron beam induced deposition* • 3 weeks in total
2 / 2015	• Guest scientist at the Ecole polytechnique fédérale de Lausanne (EPFL, Switzerland) • Research activities in the field of *Atomic force microscopy via self-sensing cantilever* • 2 weeks in total

	Education
2 / 2014 - to date	PhD thesis *(Fabrication of functional, freestanding 3D nano-architectures via Focused Electron Beam induced Deposition)* at the *Graz Centre for Electron Microscopy* (Austria) supervised by Ass. Prof. Dr. Harald Plank
1 / 2014	Master degree in “Technical Physics” at the *Graz University of Technology*
10 / 2012 – 1 / 2014	Diploma thesis at the *“Graz Centre of Electron Microscopy”* (FELMI-ZFE, Austria) supervised by Ass. Prof. Dr. Harald Plank
11 / 2011	Bachelor degree in “Technical Physics” at the *Graz University of Technology*
10 / 2006	Master degree in “Guitar” at the University of music and performing arts Graz
10 / 2005 – 7 / 2012	Studies of “Music education” at University of music and performing arts Graz (Austria)
10 / 1999 – 1 /2014	Studies of “Technical Physics” at the *Graz University of Technology* (Austria)
10 / 1999 –10 / 2006	Studies of “Guitar” at University of music and performing arts Graz (Austria)
10 / 1998 – 6 / 1999	Military service
10 / 1993 – 7 / 1997	preparation course Hochschule for Music and performing art in Oberschützen (Austria)
9 / 1986 – 7 / 1998	Elementary & secondary school

	Peer Review Publications **178 citations, h-index 8, 2018-01-02**
18.	*High-Fidelity 3D-Nanoprinting Using a Focused Electron Beam: Growth Characteristics.* R. Winkler, B.B.B. Lewis, J.D. Fowlkes, P.D. Rack, H. Plank *ACS Nano* (2017), in review.
17.	*High-Fidelity 3D-Nanoprinting Using a Focused Electron Beam: Computer-Aided Design (CAD).* J.D. Fowlkes, R. Winkler, B.B. Lewis, A. Fernández-Pacheco, L. Skoric, D. Sanz Hernandez, M. Stanford, E. Mutunga, P.D. Rack, and H. Plank *ACS Nano* (2017), in review.
16.	*Free-Standing Quasi-1D Resonators for Gas-Sensing Applications.* G. Arnold, R. Winkler, M. Stermitz, A. Orthacker, S. Sax, A. Klug, J.H. Noh, J.D. Fowlkes, P.D. Rack, H. Plank (2017) in submission.
15.	*Comparing Postdeposition Reactions of Electrons and Radicals with Pt Nanostructures Created by Focused Electron Beam Induced Deposition.* J.A. Spencer, M. Barclay, M.J. Gallagher, R. Winkler, I. Unlu, Y.-C. Wu, H. Plank, L. McElwee-White, D.H. Fairbrother *Beilstein J. Nanotechnol.* (2017), 8, 2410–2424.
14.	*Direct-Write of Free-Form 3D Nanostructures with Controlled Magnetic Frustration.* L. Keller, M.K.I. Al Mamoori, J. Pieper, C. Gspan, I. Stockem, C. Schröder, S. Barth, R. Winkler, H. Plank, M. Pohlit, J. Müller, M. Huth *Nat. Commun.* (2017), accepted, arXiv:1709.05847.
13.	*Probing the Morphology and Evolving Dynamics of 3D Printed Nanostructures Using High-Speed Atomic Force Microscopy.* C. Yang, R. Winkler, M. Dukic, J. Zhao, H. Plank, G.E. Fantner *ACS Appl. Mater. Interfaces* (2017), 9 (29), 24456–24461.
12.	*Direct-Write 3D-Nanoprinting of Plasmonic Structures* R. Winkler, F.-P. Schmidt, U. Haselmann, J.D. Fowlkes, B.B. Lewis, G. Kothleitner, P.D. Rack, H. Plank *ACS Appl. Mater. Interfaces.* (2017), 9 (9), 8233-8240
11.	*3D Nanoprinting Via Laser-Assisted Electron Beam Induced Deposition: Growth Kinetics, Enhanced Purity and Electrical Resistivity* B.B. Lewis, R. Winkler, X. Sang, P.R. Pudasaini, M.G. Stanford, H. Plank, R.R. Unocic, J.D. Fowlkes, P.D. Rack *Beilstein J. Nanotechnol.* (2017), 8, 801-812.
10.	Simulation-Guided 3D Nanomanufacturing via Focused Electron Beam Induced Deposition. J.D. Fowlkes, R. Winkler, B.B.Lewis, M.G. Stanford, H. Plank, P.D. Rack *ACS Nano* (2016) 10, 6163-6172.

9.	Direct-Write Fabrication of Cellulose Nano-Structures via Focused Electron Beam Induced Nanosynthesis. T. Ganner, J. Sattelkow, B. Rumpf, M. Eibinger, D. Reishofer, R. Winkler, B. Nidetzky, S. Spirk, H. Plank *Nat. Sci. Rep.* (2016) 6, 32451.
8.	Focus electron beam induced deposition as a tool to create electron vortices. A. Béché, R. Winkler, H. Plank, F. Hofer, J. Verbeeck *Micron* (2016) 80 (34).
7.	Toward Ultraflat Surface Morphologies During Focused Electron Beam Induced Nanosynthesis: Disruption Origins and Compensation. R. Winkler, A. Szkudlarek, J.D. Fowlkes, P.D. Rack, I. Utke, H. Plank *ACS Appl. Mater. Interfaces* (2015) 7 (5), 3289.
6.	Fundamental edge broadening effects during focused electron beam induced nanosynthesis. R. Schmied, J.D. Fowlkes, R. Winkler, P.D. Rack, H. Plank Beilstein. J. Nanotechn. (2015) 6 (1), 462, invited.
5.	Electron nanoprobe induced oxidation: a simulation of direct-write purification. J.D. Fowlkes, B. Geier, B.B. Lewis, P.D. Rack, M.G. Stanford, R. Winkler, H. Plank *Phys.Chem. Chem. Phys.* (2015) 17, 18294.
4.	The Nanoscale Implications of a Molecular Gas Beam during Electron Beam Induced Deposition. R. Winkler, J.D. Fowlkes, A. Szkudlarek, U. Utke, P.D. Rack, H. Plank *ACS Appl. Mater. Interfaces* (2014) 6 (4), 2987.
3.	Spatial chemistry evolution during focused electron beam-induced deposition: origins and workarounds. R. Winkler, B. Geier, H. Plank *Applied Physics A* (2014) 117 (4), 1675, invited.
2.	Chemical degradation and morphological instabilities during focused ion beam prototyping of polymers. A. Orthacker, R. Schmied, B. Chernev, J.E. Fröch, R. Winkler, J. Hobisch, G. Trimmel, H. Plank *Phys.Chem. Chem. Phys.* (2014) 16, 1658.
1.	Rapid and Highly Compact Purification for Focused Electron Beam Induced Deposits: A Low Temperature Approach Using Electron Stimulated H_2O Reactions. B. Geier, C. Gspan, R. Winkler, R. Schmied, J.D. Fowlkes, H. Fitzek, H. Plank *J. Phys. Chem. C* (2014) 118 (25), 14009.

	Conference Contributions
25.	*3D-Nano-Printing via Focused Electron Beams: From a Concept Towards Stable Nano-Fabrication.* R. Winkler, J. Sattelkow, J. D. Fowlkes, B. B. Lewis, P. D. Rack and H. Plank Invited Tutorial at the "*EUFN workshop*", July 2017, Graz, Austria
24.	*FEBID Based Direct-Write of 2D and 3D Plasmonic Gold Structures* R. Winkler, F. Schmidt, U. Haselmann, U. Radeschnig, P. Falthansl, J. D. Fowlkes, B. B. Lewis, P. D. Rack, M. D. Thomson, F. Bürkle, M. Wiecha, F. Walla, R. Sachser, M. Huth, H. G. Roskos and H. Plank

	Contributed talk at the "*EUFN workshop*", July 2017, Graz, Austria
23.	*FEBID Based Direct-Write of 2D and 3D Plasmonic Gold Structures* R. Winkler, F. Schmidt, U. Haselmann, U. Radeschnig, P. Falthansl, J. D. Fowlkes, B. B. Lewis, P. D. Rack, M. D. Thomson, F. Bürkle, M. Wiecha, F. Walla, R. Sachser, M. Huth, H. G. Roskos and H. Plank Contributed talk at the "*61th EIPBN*", May 2017, Orlando, USA
22.	*Direct-Write Fabrication of Electric and Thermal High-Resolution Nanoprobes on Self-Sensing AFM Cantilever* J. Sattelkow, J. Fröch, R. Winkler, U. Radeschnig, M. Winhold, A. Deutschinger, T. Strunz, V. Stavrov, E.J. Fantner, C. Schwalb, G.E. Fantner, H. Plank Contributed talk at the "*61th EIPBN*", May 2017, Orlando, USA
21.	*Research on Novel Precursor Using a Versatile Gas Injection System* R. Winkler*, S. Rauch, U. Haselmann, H. Stüger, C. Gspan, M. Rohdenburg, P. Swiderek, H. Plank Contributed talk at the "*4th Kleindiek User Meeting*", April 2017, Reutlingen, Germany
20.	*FEBID Based Direct-Write of 3D Plasmonic Gold Structures* R. Winkler*, F. Schmidt, U. Haselmann, J. Fowlkes, P. Rack, H. Plank Contributed talk at the "*ASEM Meeting*", April 2017,Vienna, Austria
19.	*3D Nanoprinting. Von der Idee bis zur Umsetzung.* R. Winkler*, J. Sattelkow, J. Fröch, U. Radeschnig, G. Arnold, B. Eicher, U. Haselmann, F. Schmidt, F. Kolb, M. Stermitz, A. Orthacker, E. J. Fantner, C. Schwalb, M. Winhold, G. E. Fantner, J. D. Fowlkes, B. B. Lewis, P. D. Rack, M. Huth, H. Plank Contributed talk at the "*Workshop 65 years Electron Microscopy in Graz*", November 2016, Graz, Austria
18.	*Plasmonic activity of freestanding and purified 3D-FEBID architectures.* R. Winkler*, F. Schmidt, U. Haselmann, J. Fowlkes, P. Rack, H. Plank Contributed poster at the "*MNE*", September 2016, Vienna, Austria
17.	*Fabrication of Cellulose Structures via Focused Electron Beam Induced Conversion: Approaching the Nanoscale.* T. Ganner, J. Sattelkow, B. Rumpf, M. Eibinger, D. Reishofer, R. Winkler*, B. Nidetzky, S. Spirk, H. Plank Contributed talk at the "*MNE*", September 2016, Vienna, Austria
16.	*FEBID Based 3D Nanoprinting of Plasmonic Gold Structures: Beyond Current Limitations.* R. Winkler*, F. Schmidt, U. Haselmann, J. Fowlkes, P. Rack, G. Kothleitner, F. Hofer, H. Plank: Contributed talk at the "*FEBIP 2016*", July 2016, Vienna, Austria
15.	*3D Nanoprinting of Plasmonic Structures: new Pathways Towards Free-Standing Nanoarchitectures.* R. Winkler, F. Schmidt, U. Haselmann, J. Fowlkes, P. Rack, G. Kothleitner, F. Hofer, H. Plank* Contributed talk at the "*MRS Spring Meeting*", April 2016, Phoenix, US
14.	*AFM Based High-Speed Tomography in Electron and Ion Beam Microscopes.* R. Winkler, C. Yang, C. H. Schwalb, A. Deutschinger, G. E. Fantner, E. J. Fantner, H. Plank* Contributed talk at the "*MRS Spring Meeting*", April 2016, Phoenix, US
13.	*Plasmonic activity of freestanding and purified 3D-FEBID architectures.* R. Winkler*, F.-P. Schmidt, U. Haselmann, J.D. Fowlkes, B.B.Lewis, G. Kothleitner, P.D. Rack, H. Plank Contributed poster at the "*MNE*", September 2016, Vienna, Austria
12.	*Novel investigation possibilities on FEBID deposits by combining dual-beam capabilities with in-situ high-speed AFM* R. Winkler*, C. Yang, C. H. Schwalb, M. Winhold, A. Deutschinger, G. E. Fantner, E. J. Fantner, H. Plank Contributed poster at the "*FEBIP 2016*", July 2016, Vienna, Austria

11.	*Pure FEBID Gold Deposits for Plasmonic Applications.* U. Haselmann, R. Winkler*, F. Schmidt, H. Plank Contributed poster at the "*FEBIP 2016",* July 2016, Vienna, Austria
10.	*High-Fidelity Shapes and Disruption Mechanism during Focused Electron Beam Induced Deposition.* R. Winkler*, G. Arnold, R. Schmied, J.D. Fowlkes,. A. Szkudlarek, A. Orthacker, R. Timilsina, G. Kothleitner, P.D. Rack, I. Utke, H. Plank Contributed talk at the "*ASEM Meeting*", May 2015, Graz, Austria
9.	*Focused Ion Beam Processing of Polymers.Pushing the Limits by Alternative Patterning Strategies.* R. Schmied, A. Orthacker, J. Kraxner, R. Winkler*, B. Chernev, C. Mayrhofer, J. E. Fröch, J. Hobisch, G. Trimmel, H. Plank Contributed talk at the "*EIPBN*", San Diego, USA, May 2015
8.	*Focused Electron Beam Induced Processing: An Application Perspective.* H. Plank, R. Winkler* Invited talk at the "*EIPBN*", May 2015, San Diego, USA
7.	*High-Fidelity Shapes and Disruption Mechanism during Focused Electron Beam Induced Deposition.* R. Winkler*, G. Arnold, R. Schmied, J.D. Fowlkes,. A. Szkudlarek, A. Orthacker, R. Timilsina, G. Kothleitner, P.D. Rack, I. Utke, H. Plank Contributed poster at the "*EIBPN",* April 2015, San Diego, USA
6.	*Lateral gradients in precursor working regimes and its consequences on the surface morphology of focused electron beam induced deposits.* R. Winkler*, J. Fowlkes, A. Szkudlarek, I. Utke, P.D. Rack, H. Plank Contributed talk at the "*FEBIP 2014*", July 2014, Frankfurt, Germany
5.	*Property tuning of free standing, quasi-1D resonators fabricated via focused electron beam induced Pt deposition.* M. Stermitz, R. Winkler*, S. Nau, J.-H. Noh, A. Orthacker, S. Rauch, G. Kothleitner, P.D. Rack, S. Sax, E.J.W. List-Kratochvil, H. Plank Contributed talk at the "*ASEM Meeting*", April 2014, Vienna, Austria
4.	*Consequences of gas dynamics on morphology and chemistry during Electron Beam Induced Deposition.* R. Winkler*, J. Fowlkes, A. Szkudlarek, A. Melischnig, I. Utke, P.D. Rack, H. Plank Contributed poster at the "*IMC 2014",* September 2014, Prague, Czech Republic
3.	*Focused electron beam induced deposition - From fundamental to application as humidity sensor.* R. Winkler*, A. Szkudlarek, I. Utke, F. Kolb, K. Schmoltner, M. Huth, A. Hohenau, J. Krenn, A. Klug and H. Plank Contributed talk at the "*Materialsday TU Graz*", October 2013, Graz, Austria
2.	*Precursor Gas Dynamics as Crucial Element during Focused Electron Beam Induced Deposition of Functional Nanostructures.* R. Winkler*, H. Plank Contributed talk at the "*8th DACH FIB-Workshop*", June 2013, Unterpremstätten, Austria
1.	*Precursor Gas Dynamics as Crucial Element during Focused Electron Beam Induced Deposition of Functional Nanostructures.* R. Winkler*, A. Szkudlarek, I. Utke, H. Plank Contributed poster at the "*MNE",* September 2013, London, UK

	Other
4.	*Journal Cover Page for ACS Appl. Mater. Interfaces* (2017), 9, issue 9 and 10
3.	*Best Image Award* Received at the *"FEBIP 2016"*, July 2016, Vienna, Austria
2.	*Digital Micrograph Contest Winner* Received at the „*EIBPN*", April 2015, San Diego, USA
1.	*Cover Page of Papers from the 59th International Conference on Electron, Ion, and Photo Beam Technology and Nanofabrication 2015* Received at the *"EIPBN*", April 2015, San Diego, USA